

**NUMERICAL MODELING OF EQUIAXED SOLDIFICATION IN DIRECT
CHILL CASTING**

by

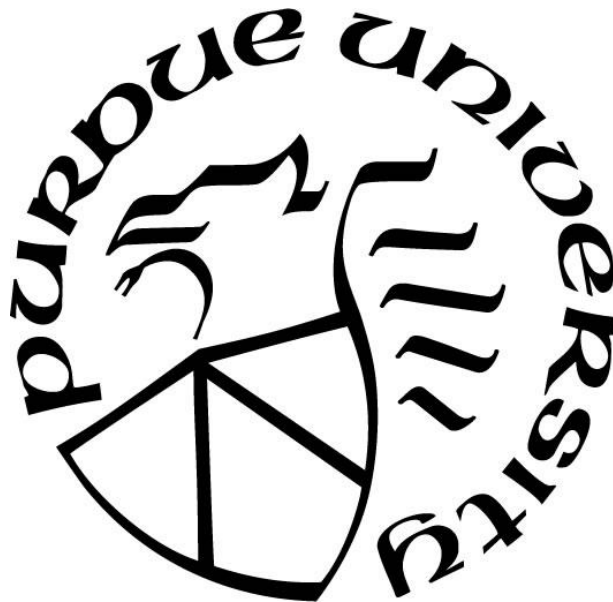
John S. Coleman

A Dissertation

Submitted to the Faculty of Purdue University

In Partial Fulfillment of the Requirements for the degree of

Doctor of Philosophy



School of Materials Engineering

West Lafayette, Indiana

December 2020

**THE PURDUE UNIVERSITY GRADUATE SCHOOL
STATEMENT OF COMMITTEE APPROVAL**

Dr. Matthew J.M. Krane, Chair

School of Materials Engineering

Dr. David Johnson

School of Materials Engineering

Dr. Amy Marconnet

School of Mechanical Engineering

Dr. Kevin Trumble

School of Materials Engineering

Approved by:

Dr. David Bahr

This work is dedicated to my parents, and especially to my wife, Lyndsay, whose support and encouragement through graduate school was invaluable.

ACKNOWLEDGMENTS

First, I would like to acknowledge my parents and wife, Lyndsay. This work would not have been possible without their support and encouragement. I would also like to thank my adviser, Matthew J.M. Krane, who has mentored me in my personal, academic, and professional development over the last several years. His guidance inspired confidence in my abilities, especially during the dissertation writing process. I am forever grateful to him for both encouraging and providing the opportunity for me to attend graduate school, a decision which has changed the trajectory of my life. Additional thanks to my graduate committee: Professors Kevin Trumble, David Johnson, and Amy Marconnet for their time, valuable contributions, and patience throughout this process.

I would like to express my sincere gratitude to Robert Wagstaff, who was the advocate for the financial gift from Novelis Solatens Technology Center that made this work possible. Bob made sure that I was provided enough time and funding to learn the numerical methods, theoretical background, and computational science necessary for the success of this work. This unique learning experience has guided my personal development as a researcher. I could not thank him enough. I would also like to thank Sam Wagstaff for our many conversations about direct chill casting. The experimental results in Chapter 9. of this dissertation were performed by Sam during his doctoral research. Without their contributions, this dissertation would lack industrial relevance and be incomplete.

Additionally, I want to thank my friends and colleagues, Alex Plotkowski and Kyle Fezi. Both were always available and willing to discuss problems related to material science and mathematical modeling. I am grateful for the mentorship throughout my graduate studies and personal development. Technical support was provided by Chris Greenshields and Henry Weller at CFD Direct. Special thanks to Henry, who took the time to guide me through the development and understanding of some of the numerical methods used in this work.

I would like to thank my coworkers who made it a pleasure to come to work each day including Paul Mather, Scott Wells, and Matthew Binkley. Final thanks are owed to the staff of the School of Materials Engineering who enabled this research, especially to Vicki Cline and Rosemary Son for their academic advising and continual patience.

TABLE OF CONTENTS

LIST OF TABLES	9
LIST OF FIGURES	10
NOMENCLATURE	16
ABSTRACT.....	21
1. INTRODUCTION	23
1.1 Background and Rationale	23
1.2 Physical Phenomena in Alloy Solidification	26
1.2.1 Equilibrium Phase Diagrams and Solidification Structures	26
1.2.2 Fluid Flow and the Development of Macrosegregation	30
1.2.3 Experimental Investigations of Macrosegregation in DC Casting	34
1.3 Mathematical Modeling of Alloys Solidification	36
1.3.1 Multiphase Models	37
1.3.2 Mixture Models	39
1.3.3 Mathematical Investigations of DC Casting.....	40
1.4 Research Objectives.....	43
2. PHYSICAL MODEL.....	46
2.1 Volume Averaging.....	47
2.2 Multiphase Model	50
2.3 Continuum Mixture Model	55
2.3.1 Conservation of Mass	57
2.3.2 Conservation of Momentum	58
Slurry Regime	59
Rigid Mush Regime	60
Single Domain Model	61
Momentum Closure.....	63
2.3.3 Conservation of Energy	65
2.3.4 Conservation of Species	67
2.4 Summary of Equations.....	68
3. MICROSEGREGATION MODEL.....	70

3.1	Analytical Microsegregation Model	70
3.1.1	Extension to Multicomponent Solidification.....	73
3.2	Volume-Averaged Microsegregation Model	75
3.2.1	Clarification of Interfacial Balances	78
3.2.2	Interfacial Closure Relationships.....	79
3.2.3	Verification	82
4.	NUMERICAL METHODS	85
4.1	Finite Volume Method.....	85
4.1.1	Face Interpolation	86
4.1.2	Gradients.....	88
4.1.3	Source Terms	89
4.1.4	Time Integration	89
4.1.5	Solution Methods for Linear Algebraic Systems.....	91
4.2	Pressure-Velocity Coupling	92
4.2.1	The PISO Algorithm.....	94
4.2.2	Cell-Based Drag Method	95
4.2.3	Face-Based Drag Method	96
4.2.4	Pressure Oscillations.....	97
4.3	Phase Flux Discretization	99
4.3.1	Mixture Flux Method.....	102
4.3.2	Phase Flux Method	103
5.	THERMODYNAMIC SOLUTION ALGORITHM	106
5.1	Semi-Implicit Source Term Linearization	106
5.2	Analytical Microsegregation Algorithm.....	108
5.3	Volume-Averaged Microsegregation Algorithm.....	109
5.4	Summary of Algorithms	111
6.	NUMERICAL EXERCISES AND VERIFICATION.....	114
6.1	Porous Plug.....	114
6.2	Settling Column	116
6.3	Solidification Numerical Benchmarks.....	120
6.3.1	Columnar Solidification Benchmark	122

6.3.2	Equiaxed Solidification Verification	128
	Macrosegregation Evolution	128
	Grid Dependence Study	132
	Nature of Composition Artifact Formation	135
6.4	DC Casting Verification	140
6.5	Summary	143
7.	SENSITIVITY OF MACROSCALE PREDICTIONS TO UNCERTAIN MICROSCALE PARAMETERS	144
7.1	Description of Transport Phenomena	144
7.2	Influence of Undercooling on Macrosegregation	145
7.3	Influence of Grain Structure on Macrosegregation	149
7.4	Simplified Grain Morphology Model	153
7.5	Sensitivity Study	158
7.6	Influence of Undercooling on DC Casting Predictions	160
7.7	Summary	162
8.	INVESTIGATION OF GRAIN TRANSPORT IN HORIZONTAL DIRECT CHILL CASTING	163
8.1	Background	163
8.2	Influence of Different Transport Phenomena	164
8.3	Grain Suspension Due to Forced Convection	167
8.4	Comparison of 2-D and 3-D Calculations	170
9.	INVESTIGATION OF JET-STIRRED DIRECT CHILL CASTING	174
9.1	Motivation for Jet-Stirred Casting	174
9.2	Experimental Trials	175
9.2.1	Experimental Results	178
9.2.2	Experimental Discussion	181
9.3	Numerical Investigation	183
9.3.1	Characterization of the Inflow Jet	183
9.3.2	Numerical Results	186
9.3.3	Characterization of the Flow Field	192
9.3.4	Influence of Different Transport Mechanisms	195

9.3.5 Conclusions.....	197
10. CONCLUSIONS AND FUTURE WORK	198
10.1 Recommendations for Future Work	199
APPENDIX A. THERMOPHYSICAL PROPERTIES AND BINARY PHASE DIAGRAM INFORMATION.....	201
APPENDIX B. EXTENSION OF MODEL TO DYNAMIC MESHES	202
REFERENCES	207
VITA.....	218

LIST OF TABLES

Table 2.1: Summary of volume-averaged balance equations	54
Table 2.2: Summary of volume-averaged constitutive interfacial transfer relationships	54
Table 2.3: Summary of continuum mixture conservation equations	69
Table 2.4: Summary of hydrodynamic relationships used in mixture momentum model.....	69
Table 5.1: Solution algorithm for the analytical microsegregation model	112
Table 5.2. Solution algorithm for the volume-averaged dendritic microsegregation model	113
Table 6.1. Relationships for the drag coefficient of as a function of liquid volume fraction and grain Reynolds number	118
Table A.1 Thermophysical properties and phase diagram data for different alloys investigated in this dissertation	201

LIST OF FIGURES

Figure 1.1: Illustration of the DC casting process with two inlet variations: a.) hot-top, and b.) bi-level with a combo-bag.	25
Figure 1.2: Generic binary eutectic equilibrium phase diagram with approximated linear solidus and liquidus lines.	29
Figure 1.3: Equiaxed grain types encountered in DC casting for Al-4.5wt%Cu: global grains (grain size $\approx 100 \mu\text{m}$), dendritic grains (grain size $\approx 250 \mu\text{m}$), and the morphological grain envelope model. Micrographs courtesy of Sam Wagstaff.	30
Figure 1.4: Various types of relative motion during equiaxed solidification induced by a.) solidification shrinkage, b.) natural convection, c.) grain motion, and d.) mushy zone deformation. The positive and negative signs indicate the regions of positive and negative segregation which form due to the relative solid-liquid motion in hypoeutectic alloys.	32
Figure 1.5: Typical relative flows and resulting macrosegregation profile in DC casting.	33
Figure 1.6: Comparison of experimental macrosegregation profiles in ingot slices for conventional and jet-stirred casting at a cast length of 1800 mm. The composition was previously measured using X-ray fluorescence (XRF) by Wagstaff and Allamore [9] and contour plots are reproduced here assuming two-fold symmetry of the measured ingot quadrant indicated by the black lines. 36	
Figure 2.1: A schematic of the temperature and composition fluxes near the solid-liquid interface.	53
Figure 3.1: Computed temperature vs. solid volume fraction curves (left) and the corresponding liquid composition curves (right) for an Al-4.5 wt% Cu alloy where $\beta = 1$, $\lambda = 0.118$ is the lever rule and $\beta = 0$, $\lambda = 0$ is the Gulliver-Scheil equation.	74
Figure 3.2: Computed temperature vs. solid volume fraction curves (left) and the corresponding liquid composition curves (right) for AA7050 where $\beta = 1$, $\lambda = 0.09$ is the lever rule and $\beta = 0$, $\lambda = 0$ is the Gulliver-Scheil equation.	75
Figure 3.3: The physical model of an equiaxed dendrite enclosed by an envelope. The fluid inside the envelope (interdendritic) is assumed to be well-mixed. The solid and extradendritic liquid compositions both decrease with distance from their respective interfaces.	77
Figure 3.4: Comparison of the inverse Ivantsov function for small supersaturations using different dendrite tip geometry assumptions (left). Grain diffusion coefficient as a function of solid fraction for various grain sizes and morphologies (right).	82
Figure 3.5: Effect of the dendrite tip geometry assumption on the predicted recalescence curves with the final grain radii of (A) $100 \mu\text{m}$, (B) 1 mm , (C) 10 mm . The predictions of Wang and Beckermann [67] and Rappaz and Thevoz [76] are coincident with the complete model.	84

Figure 3.6: Effect of the dendrite tip geometry assumption on the predicted grain fraction with the final grain radii of (A) 100 μm , (B) 1 mm, (C) 10 mm. The predictions of Wang and Beckermann [67] are coincident with the complete model with the exception of $g_g > 0.95$ due to the limiting used here for numerical stability. 84

Figure 4.1. Illustration of a finite control volume with a single neighbor on a co-located grid. ... 85

Figure 4.2. Illustration of the interpolation of the cell-center values (W, P) to the face-center value (w). 88

Figure 4.3: Simplified example of the pressure profiles given across a discontinuous volumetric force at control volume P for the cell-based drag and face-based drag methods. The latter is free of oscillations. 99

Figure 4.4: Schematic of the problematic “stair-step” cell which tend to produce composition artifacts during simulations of equiaxed solidification on co-located grids. Packed cells are indicated in grey, slurry cells in white. 101

Figure 6.1: Illustration of the numerical domain for the porous plug verification case 115

Figure 6.2: Steady state velocity field calculated for the porous plug test case ($Da = 10^{-5}$ and $Re = 25$) using different momentum formulations. 115

Figure 6.3: Centerline normalized x-component velocity for the porous plug test case with $Da = 10^{-5}$ (left) and 10^{-3} (right) using different drag formulations. The velocities magnitudes are linearly interpolated to the face-centers to represent the oscillation of the flux. The results from Aguerre et al. [94] are coincident with those obtained here. 116

Figure 6.4: Solid volume fraction field and solid velocity streamlines at different times for the settling validation case. The top block line indicates the solid-liquid interface and the bottom black line indicates the packing interface. The mixture upwind method of ref. [73] predicts unphysical settling and accumulation behavior, while the phase-flux method proposed in Section 4.3.2 predicts the physically correct solution. 119

Figure 6.5: Comparison of the (left) drag coefficients and (right) the evolution of the solid-liquid interface and the packing interface for various drag models. 120

Figure 6.6: Description of the SMACS benchmark case and domain including thermal conditions and locations used for evaluating model predictions. 122

Figure 6.7: The bold solid line show the columnar dendrite tip front and the light lines are streamlines varying from -0.06 to -0.01 kg/s with constant increments. 125

Figure 6.8: Final composition profiles of the Hebditch-Hunt benchmark case for different mesh spacings ($\Delta x = 2, 1, 0.5,$ and 0.025 mm) and momentum schemes. 126

Figure 6.9: Comparison of composition profiles at various grid spacings, and the mesh convergence of the global macrosegregation index for the cell-drag and face-drag momentum formulations. 127

Figure 6.10: Pb composition fields at intermediate times during solidification for the cell-based drag and face-based drag formulations evaluated with different levels of diffusion in the solid flux, $\eta = 0.0$ and $\eta = 1.0$. The bold line show the packing interface and the light lines are streamlines varying from 0.05 to 0.3 kg/s in increments of 0.025 kg/s. Simulations were performed with a grid spacing of 1 mm and a critical packing fraction of $g_g^c = 0.15$ 130

Figure 6.11: Pb composition fields at intermediate times during solidification for the cell-based drag and face-based drag formulations evaluated with different levels of diffusion in the solid flux, $\eta = 0.0$ and $\eta = 1.0$. The bold line show the packing interface and the light lines are streamlines varying from 0.05 to 0.3 kg/s in increments of 0.025 kg/s. Simulations were performed with a grid spacing of 1 mm and a critical packing fraction of $g_g^c = 0.30$ 131

Figure 6.12: Histograms of the depleted composition artifacts for the cell-based and face-based drag formulations. Simulations were performed with a grid spacing of 1 mm. 132

Figure 6.13: Comparison of the grid dependence of the final Pb segregation field for the cell-drag formulation and the face-based drag formulation evaluated with different levels of diffusion in the solid flux, $\eta = 0.0$ and $\eta = 1.0$. The packing fraction was $g_g^c = 0.15$ for each case..... 133

Figure 6.14: Comparison of the grid dependence of the final Pb segregation field for the cell-drag formulation and the face-based drag formulation evaluated with different levels of diffusion in the solid flux, $\eta = 0.0$ and $\eta = 1.0$. The packing fraction was $g_g^c = 0.30$ for each case..... 134

Figure 6.15: Pb composition fields in the rigid mush and velocity fields in the slurry near the packing interface for the cell-based drag formulation. Problematic “stair-step” cells which have a propensity to form composition artifacts are shown in red, paired with the outflow velocity vector. Simulations were performed with a grid spacing of 1 mm. 137

Figure 6.16: Pb composition fields in the rigid mush and velocity fields in the slurry near the packing interface for the face-based drag formulation. Problematic “stair-step” cells which have a propensity to form composition artifacts are shown in red, paired with the outflow velocity vector. Simulations were performed with a grid spacing of 1 mm. 138

Figure 6.17: Pb composition fields in the rigid mush and velocity fields in the slurry near the packing interface for the face-based drag formulation and the blended solid-flux method ($\eta = 1.0$). Problematic “stair-step” cells which have a propensity to form composition artifacts are shown in red, paired with the outflow velocity vector. Simulations were performed with a grid spacing of 1 mm. 139

Figure 6.18: Copper (wt. fr.) for different values of the solid-flux diffusion coefficient. The contours in decreasing order of z-position are the liquidus, the packing interface, the demarcation of the loose packed grain region, and the solidus. Simulations were performed with a critical packing fraction of $g_g^c = 0.15$ (top) and $g_g^c = 0.30$ (bottom). 142

Figure 6.19: Profiles of Cu segregation from simulations with different values of the solid-flux diffusion coefficient. The model predictions are compared to the experimental profiles of Vreeman et al [47]. 143

Figure 7.1: Evolution of the composition fields, flow field, and packing interface using the Scheil microsegregation model compared to volume-averaged microsegregation with input parameters showing the best agreement (hemispherical tip, $R_f = 37.5 \mu\text{m}$, and $D_l = 1 \times 10^{-8} \text{m}^2\text{s}$) and input parameters showing the poorest agreement (paraboloidal tip, $R_f = 125 \mu\text{m}$, and $D_l = 2 \times 10^{-9} \text{m}^2\text{s}$) at different times. 147

Figure 7.2: The mean absolute percent error (MAPE) measuring deviation of the macrosegregation predictions using the volume-averaged microsegregation models from the Gulliver-Scheil predictions for different values of liquid mass diffusivity and final grain size in microsegregation model..... 148

Figure 7.3: Temperature and liquid fraction histories at a location 1mm from the chill at the midheight of the cavity for a case equiaxed solidification using variation microsegregation models. The maximum deviation from Scheil (maximum MAPE) shows a recalescence curve and about 1 K of undercooling. 148

Figure 7.4: Internal solid fraction at packing for each tip geometry models for different final grain radii. 151

Figure 7.5: Evolution of the Pb composition fields, flow field, and packing interface using the hemispherical tip and paraboloidal tip models to control the grain morphology using $R_f = 75 \mu\text{m}$, and $D_l = 2 \times 10^{-9} \text{m}^2\text{s}$ 152

Figure 7.6: Probability density of the internal solid fraction at packing predicted by each tip geometry model for $R_f = 75 \mu\text{m}$ and $D_l = 2 \times 10^{-9} \text{m}^2\text{s}$ (left) and the range of inverse permeabilities restricting interdendritic liquid flow across these packing fractions..... 153

Figure 7.7: A. Experimental grain morphologies taken from ref. [117] B. Average calculated internal solid fraction at the onset of packing for both tip geometry models and the primary inputs to the microsegregation model (R_f, D_l)..... 155

Figure 7.8: Evolution of the composition fields and packing interface using the hemispherical tip model $R_f = 500 \mu\text{m}$, and $D_l = 6 \times 10^{-9} \text{m}^2\text{s}$ with the calculated morphological conditions compared using a constant packing fraction obtained from the linear fit in Eqn. (7.2) for the equivalent volume-averaged and Scheil microsegregation models. 156

Figure 7.9: Evolution of the composition fields and packing interface using the paraboloidal tip model $R_f = 37.5 \mu\text{m}$, and $D_l = 6 \times 10^{-9} \text{m}^2\text{s}$ with the calculated morphological conditions compared using a constant packing fraction obtained from the linear fit in Eqn. (7.3) for the equivalent volume-averaged and Scheil microsegregation models. 157

Figure 7.10: Sensitivities of the internal solid fraction at packing to the grain growth model input. 159

Figure 7.11: Sensitivities of macrosegregation predictions to uncertain microscale model input. 159

Figure 7.12: Copper distribution in the billet for different microsegregation models. The contours in decreasing order of y-position are the liquidus, the packing interface, the demarcation of the loose packed grain region, and the solidus. Simulations were performed with a critical packing fraction of $g_g^c = 0.30$ and volume-averaged calculations used a final grain radius of $R_f = 125 \mu\text{m}$	161
Figure 7.13: Profiles of Cu concentration from simulations with different microsegregation models. The model predictions are compared to the experimental profiles of Vreeman et al. [47] (left). Comparison of predicted and measured temperature profiles (right).	162
Figure 8.1: Schematic of horizontal direct chill (HDC) casting. The red outline indicates the position of the domain used for 2-D calculations.	164
Figure 8.2: Steady state composition fields and streamlines for various transport mechanisms in HDC with two different inlet positions. Bold black lines denote liquidus, packing interface, and solidus.	166
Figure 8.3: Effect of inlet position and grain size on grain suspension and the steady state composition profiles in HDC casting.....	168
Figure 8.4: Comparison of macrosegregation profiles in HDC for a center and bottom jet. Lowering the jet position in the model significantly reduces the macrosegregation in the ingot by suspending grains.....	169
Figure 8.5: Steady state streamlines and sump shape for the 400 mm width HDC cast slab.	169
Figure 8.6: Steady state composition fields and flow vectors a 2-D simulation and 3-D simulations at the centerline slabs with increasing width. Bold black lines denote liquidus and solidus, and dotted line denotes packing interface.....	171
Figure 8.7: Comparison of 2-D and 3-D steady state composition profiles along the centerline of HDC cast slabs.....	172
Figure 8.8: Comparison of final macrosegregation fields in the ingot slice for HDC castings with different model widths are inlet configurations.....	172
Figure 8.9: Influence of slab width on steady state sump profiles at centerline of HDC cast slabs (left). Comparison of 2-D (dotted) and 3-D (solid) results for different slab thicknesses (right). Each case have a midheight inlet.	173
Figure 9.1: Schematic of the low-head, jet-stirred DC caster and computational domain with a bi-level feeding scheme.....	177
Figure 9.2: Schematic of the ingot cross section used for cutting quadrants for metallographic and XRF analysis.....	178
Figure 9.3: Comparison of the grain size and macrosegregation profiles for conventional casting and jet-stirred Al-4.5wt%Cu.....	179
Figure 9.4: Micrographs etched with HBF ₄ showing the final grain structure along the mid-length of convectional cast (top) and jet-stirred (bottom) Al-4.5wt%Cu slabs.....	180

Figure 9.5: Histograms of macrosegregation measured across the ingot quadrant as-cast (left) and after scalping the surface (right).	182
Figure 9.6: Comparison of histograms for final grain size (left) and dendritic arm spacing (right) measured across the ingot quadrant.	182
Figure 9.7: Solid fraction isocontours for conventional and jet-stirred casting. The white line surrounding the inflow marks the liquidus surface and the other white line marks the packing interface. A was taken at upon the composition field reaching steady-state and B was taken 500 s later.	185
Figure 9.8: Comparison of the experimental segregation contours (left) to the numerical prediction (right) using the average grain size and morphology parameters for conventional and jet-stirred casting.	189
Figure 9.9: Comparison of macrosegregation profiles across the quadrant thickness for convectional casting (left) and jet-stirred casting (right). The experimental data indicated by the solid black markers was averaged over a representative area extending 115 mm from the mid-width.	189
Figure 9.10: Comparison of final macrosegregation fields in the conventional ingot quadrant for various grain size and morphology parameters within the uncertainty band of the experimental data.	190
Figure 9.11: Comparison of final macrosegregation fields in the jet-stirred ingot quadrant for various grain size and morphology parameters within the uncertainty band of the experimental data.	191
Figure 9.12: Contour plots of the z-component velocity at different depths in the sump for conventional and jet-stirred casting where a negative component (blue) indicates downward flow in the direction of casting. The vectors are plotted as unit vectors of the x-component and y-component to highlight the direction of the secondary flow field. The solid black lines mark the solidus and liquidus surfaces, while the dotted black line marks the packing interface.....	193
Figure 9.13: Contour plots of the segregation and solid fraction fields at the x-z plane at the centerline and y-z plane at the midwidth. The top solid line marks the liquidus surface while the bottom solid line marks the eutectic surface. The dotted line indicates the packing interface..	194
Figure 9.14: Segregation formation along the thickness for various transport mechanisms The top solid line marks the liquidus surface while the bottom solid line marks the eutectic surface. The dotted line indicates the packing interface. Streamlines are calculated in the ingot frame of reference. Three cases are provided: natural convection only (NC), natural convection and grain motion (NC+GM), and natural convection, grain motion, and shrinkage (NC+GM+SH).....	196
Figure 9.15: Cu segregation profiles along the thin face of rolling slabs for different transport mechanisms.....	197

NOMENCLATURE

Latin symbols

a_P	Diagonal coefficients in FVM solution matrix
a_N	Off-diagonal coefficients in FVM solution matrix
[A]	Solution matrix in FVM linear algebraic system
A	Area
A_i	Area of microscopic interface
c_p	Constant pressure specific heat
\mathbf{b}	Collection of sources in FVM linear algebraic system
[b]	Source vector in FVM linear system
C	Composition
C_{eut}	Eutectic composition
C_{max}^α	Maximum composition of the primary solid phase α
C_D	Drag coefficient
$\bar{C}_{k,i}$	Average interfacial composition for phase k along microscopic interface i
Co	Courant number
\mathbf{d}	Vector between the center of control volume P and its neighbor N
d_g	Local grain diameter used in the relative solid-liquid velocity term
d_g^f	Final grain diameter used in the relative solid-liquid velocity term
D	Solutal mass diffusivity, drag coefficient
E_k	Interfacial energy transfer into phase k
f_x	Weighting factor for central differencing
F_f	Mixture flux at face f
$F_{D,f}$	Numerical diffusion flux at face f
$F_{l,f}$	Liquid mass flux at face f
$F_{r,f}$	Relative solid-liquid mass flux at face f
$F_{s,f}$	Solid mass flux at face f
Fo	Fourier number

g_k	Volume fraction of phase k
g_g^c	Grain volume fraction upon coalescence
g_s^t	Solid volume fraction from transport stage used in operator splitting method
g_{si}	Internal solid fraction
g_{si}^H	Internal solid fraction predicted from hemispherical tip model
g_{si}^P	Internal solid fraction predicted from paraboloidal tip model
\mathbf{g}	Gravity vector
GMI	Global macrosegregation index
\mathbf{h}	Displacement vector in the direction of gravity from some reference point
h	Specific enthalpy
\mathbf{H}_P	Collection of vectors at control volume P used in the PISO algorithm
\mathbf{I}	Identity tensor
I_v	Ivantsov function
\mathbf{j}	Diffusion flux vector
J_k	Interfacial solute transfer into phase k
k	Thermal conductivity
k_p	Solute partition coefficient
k_p^*	Mass-weighted solute partition coefficient
K	Permeability of the rigid mush
L_f	Latent heat of fusion
m	Marker function
m_{liq}	Linearized liquidus slope
m_{sol}	Linearized solidus slope
\mathbf{M}_k	Interfacial momentum transfer into phase k
\mathbf{M}_k^d	Interfacial momentum transfer into phase k due to drag
$MAPE$	Mean absolute percent error
\mathbf{n}	Normal vector
\mathbf{n}_k	Normal vector at the microscale interface pointing into phase k
p	Total pressure

p^R	Reduced pressure
$\bar{p}_{k,i}$	Average interfacial pressure for phase k along microscopic interface i
\mathbf{q}_k	Heat diffusion flux vector for phase k
\dot{R}_k	General interfacial transfer into phase k
R	Local grain radius used in volume-averaged microsegregation model
R_f	Final grain radius used in volume-averaged microsegregation model
Re_g	Grain Reynolds number
\mathbf{s}_k	Species diffusion flux vector for phase k
S	Source term, surface
\mathbf{S}_f	Outward surface area vector of face f
S_i	Interfacial area per unit volume for microscopic interface i
t	Time
Δt	Time step
T	Temperature
T_{eut}	Eutectic temperature
$\bar{T}_{k,i}$	Average interfacial temperature for phase k along microscopic interface i
T_{liq}	Liquidus temperature
T_{sol}	Solidus temperature
\mathbf{u}	Velocity vector
\mathbf{u}_i	Velocity normal to the microscopic interface
\mathbf{u}_m	Mesh velocity
\mathbf{u}_r	Relative solid-liquid velocity vector
\tilde{u}_r	Relative solid-liquid velocity coefficient
\mathbf{u}_{ref}	Reference velocity of the rigid mush
V	Volume
V_g	Volume of grain
\bar{w}_{ni}	Average normal growth velocity of interface i
\mathbf{x}	Position vector
$[\mathbf{x}]$	Column vector in FVM linear algebraic system

Δx	Grid spacing in x-direction
X_k	Indicator function for phase k

Greek symbols

β	Solutal back diffusion parameter
Γ	General diffusion coefficient
Γ_{GT}	Gibbs-Thomson coefficient
Γ_k	Mass generation rate of phase k due to phase change
δ_i	Species diffusion length at microscopic interface i
δ_i^T	Thermal diffusion length at microscopic interface i
Δ	Growth constraint in the volume-averaged microsegregation model
ζ	Indicator function for packing interface cells with a mixture outflow
η	Numerical diffusion coefficient for phase mass flux at packing interface
λ	Characteristic length scale of the rigid mush, shrinkage coefficient
μ	Dynamic viscosity of the slurry
μ^*	Mean sensitivity in elementary effects method
μ_{eff}	Effective dynamic viscosity
ν	Kinematic viscosity
ρ	Density
ρ_{eff}^B	Effective density in the buoyancy term
ρ_k^B	Density from Boussinesq approximation for phase k
σ_k	Material stress tensor of phase k
τ_k	Deviatoric momentum stress tensor
ϕ_k	General transport quantity of phase k
ω	Blending factor for face-based drag method
Ω	Supersaturation

Superscripts

*	Effective, auxiliary, previous iteration
o	Previous time

Subscripts

CD	central differencing
d	Interdendritic liquid
e	Extradendritic liquid
f	Face
g	Grain
i	Interface, constituent
k	Phase
l	Liquid
N	Neighboring control volume
o	Reference value
P	Control volume of interest
UD	upwind differencing

Other supplementary symbols

$\max(\cdot)$	Maximum operator
$\min(\cdot)$	Minimum operator
$\text{pos}(\cdot)$	Positive operator
$\langle \phi \rangle$	Volume average of quantity ϕ
$\langle \phi_k \rangle^k$	Intrinsic volume average for quantity ϕ of phase k
$\hat{\phi}_k$	Fluctuating component for quantity ϕ of phase k

Acronyms

CFD	Computational fluid dynamics
DC	Direct chill
FVM	Finite volume method
HDC	Horizontal direct chill
PISO	Pressure-implicit with splitting of operators
VDC	Vertical direct chill

ABSTRACT

Direct chill (DC) casting is the main production method for wrought aluminum alloys. In this semi-continuous process, significant heat is extracted through a narrow, solidified shell by impinging water jets. A combination of rapid cooling and inoculation of the liquid metal with heterogeneous nucleation sites (grain refiner) produces the proper conditions for equiaxed solidification. As equiaxed grains nucleate and grow in the slurry, they are transported by natural convection until their eventual coalescence into a rigid mush. The preferential accumulation of these solute-depleted grains in localized regions of the casting can lead to long range composition differences known as macrosegregation. Because macrosegregation cannot be mitigated by subsequent processing, it is critical to understand and prevent its development during casting.

Numerical models are often used to gain insight into the interplay of the different transport phenomena that cause macrosegregation. The formation of mobile equiaxed grains creates a multiphase system with many moving interfaces, causing several modeling challenges. In principle, a model could be formulated in terms of local instantaneous variables describing the evolution of these interfaces, however the associated computational cost prohibits its extension to the length scale of industrial castings. For this reason, macroscopic transport equations are mathematically formulated using volume averaging methods. Two different volume-averaged model formulations can be distinguished in the solidification literature. The first approach is the multiphase formulation, which solves separate sets of governing equations for each phase that are coupled using microscale interfacial balances. While this approach retains closure models to describe the behavior of the sub-grid interfaces, these interfacial models introduce significant uncertainty that is propagated through the model. The second approach is the mixture formulation, which solves a single set of governing equations for the mixture and utilizes more pragmatic closure relationships. While this approach significantly reduces the complexity and computational cost of the model, previous formulations have oversimplified the microscale transport. Recognizing the advantages and disadvantages of both formulations, a mixture model is rigorously derived, retaining appropriate relationships for the grain structure and microsegregation behavior in equiaxed solidification

Implementation of this model into a 3-D finite volume method (FVM) code using a co-located grid is discussed along with appropriate treatment of the discontinuous body forces and phase mass

fluxes across the interface between the slurry and rigid mush. More specifically, body forces in the momentum equation are treated at the face-centers of a control volume to prevent erroneous velocity oscillations near this interface, and a diffuse phase flux method is proposed to reduce the sensitivity of composition predictions to the numerical grid. The proposed methods are verified across a wide range of conditions present in equiaxed solidification.

This model is then used to investigate the role of grain motion on macrosegregation development in equiaxed solidification, specifically in horizontal and vertical DC casting. In horizontal DC casting, the casting axis is perpendicular to gravity and there is a tendency for grains to accumulate along the bottom of the ingot. Feeding liquid metal through a constrained inlet near the bottom suspends grains in the slurry, both reducing the overall macrosegregation and improving the macrosegregation symmetry in the ingot. In vertical DC casting, the casting axis is parallel to gravity and there is a tendency for grains to accumulate in the center of the ingot. It is determined by a combination of simulations in the current work and previous experimental results that a strong localized jet at the centerline can suspend grains in the slurry and reduce negative centerline segregation. The change in segregation is attributed to a combination of reducing the accumulation of solute-depleted grains near the centerline and thinning the rigid mush where solidification shrinkage pulls enriched liquid away from the centerline. The strong localized jet also causes significant refinement and homogenization of the grain structure, which improves the mechanical properties of the ingot. These studies indicate that it is beneficial for DC casting practices to move towards agitated or stirred melts, and away from conventional practices which promote thermal stratification and localized accumulation of equiaxed grains.

1. INTRODUCTION

1.1 Background and Rationale

The use of aluminum and its alloys has significantly expanded in the last few decades. The annual world production of primary aluminum grew from about 20 million tons in the early 2000s to 64 million tons in 2019 [1], making aluminum the second most economically important metal after iron. It is estimated that more than half of the global production of aluminum is used as rolled and extruded product in applications where light weight and corrosion resistance are required, including transportation (e.g. aerospace and automotive), construction, and packaging (e.g. foil and cans). Direct chill (DC) casting is the primary processing method for wrought aluminum ingots used as starting stock for these formed products, representing a multibillion dollar economic activity.

The technology behind DC casting is well developed with a long history dating back to the 1930s when it was invented almost simultaneously and independently in Germany and the USA. A number of excellent reviews on the historical development of the modern DC casting process are available [2,3]. A distinguishing feature of DC casting from other casting methods (e.g. permanent mold casting, die casting, and sand casting) is that the majority of heat is extracted through a narrow solidified shell by impinging water jets (hence “direct chill”) rather than indirectly through the mold walls. The increased cooling rate promotes a finer and more uniform grain structure desired for subsequent deformation processing.

A schematic of vertical DC casting, the most common variant of the process, is shown in Figure 1.1. Molten metal is poured from the furnace into a transfer trough and enters the mold either through a gap in the trough (known as a hot-top system), or through a down spout where it is then distributed through a combo-bag (known as a bi-level system). At the beginning of the process, a bottom block mounted to a hydraulic ram closes the mold. Once a solid shell forms along the bottom block and near the mold walls, the bottom block is lowered into a casting pit. At this stage, the inner core of the ingot still contains a solid-liquid mixture, from which heat is extracted through the solid shell with water jets as the ingot exits the mold. This secondary cooling stage accounts for 80-90% of the total heat extraction during the DC casting process. Casting stops when the ram reaches the bottom of the casting pit, making the process semi-continuous.

The most severe defect in DC casting is the formation of hot and cold cracks resulting from the residual stresses that accumulate due to uneven thermal contractions and expansions during cooling. Inoculation of the melt with titanium-based grain refiner promotes the heterogenous nucleation of equiaxed grains which exhibit improved uniformity in mechanical properties and reduced hot cracking susceptibility. These equiaxed grains form a slurry of solid grains suspended in the liquid metal. As the particles grow and interact, they connect to form a permeable rigid mush. The demarcation between the slurry and the rigid mush is referred to as the packing interface, indicated by the dotted line in Figure 1.1.

A less severe but commonly observed defect in DC casting is macrosegregation, defined as chemical inhomogeneity on the length scale of the ingot. Because wrought aluminum alloys obtain most of their strength by precipitating secondary phases, macrosegregation plays a direct role in the distribution of microstructure and mechanical properties of the ingot. This casting defect is problematic because it reduces the efficiency of the subsequent heat treatment and deformation processes. In the most severe cases, the chemical composition in a significant portion of the ingot can be outside of the material specification limits of the alloy and it must be scrapped. Although this defect causes scrapping in less than 1% of all ingots produced [2], recent industrial needs require larger ingots in which macrosegregation tends to be more severe.

Although research into the transport phenomena causing macrosegregation has been extensively studied since the advent of DC casting, progress towards mitigating its severity has only been achieved in recent years. The purpose of this work is to improve modeling capabilities of the DC casting process, allowing better prediction of the transport phenomena known to cause macrosegregation. A model scalable to 3-D simulations of large rolling slabs is required to investigate industrially relevant problems. This model is used to investigate the role that forced convection from the liquid metal distribution system can have on macrosegregation.

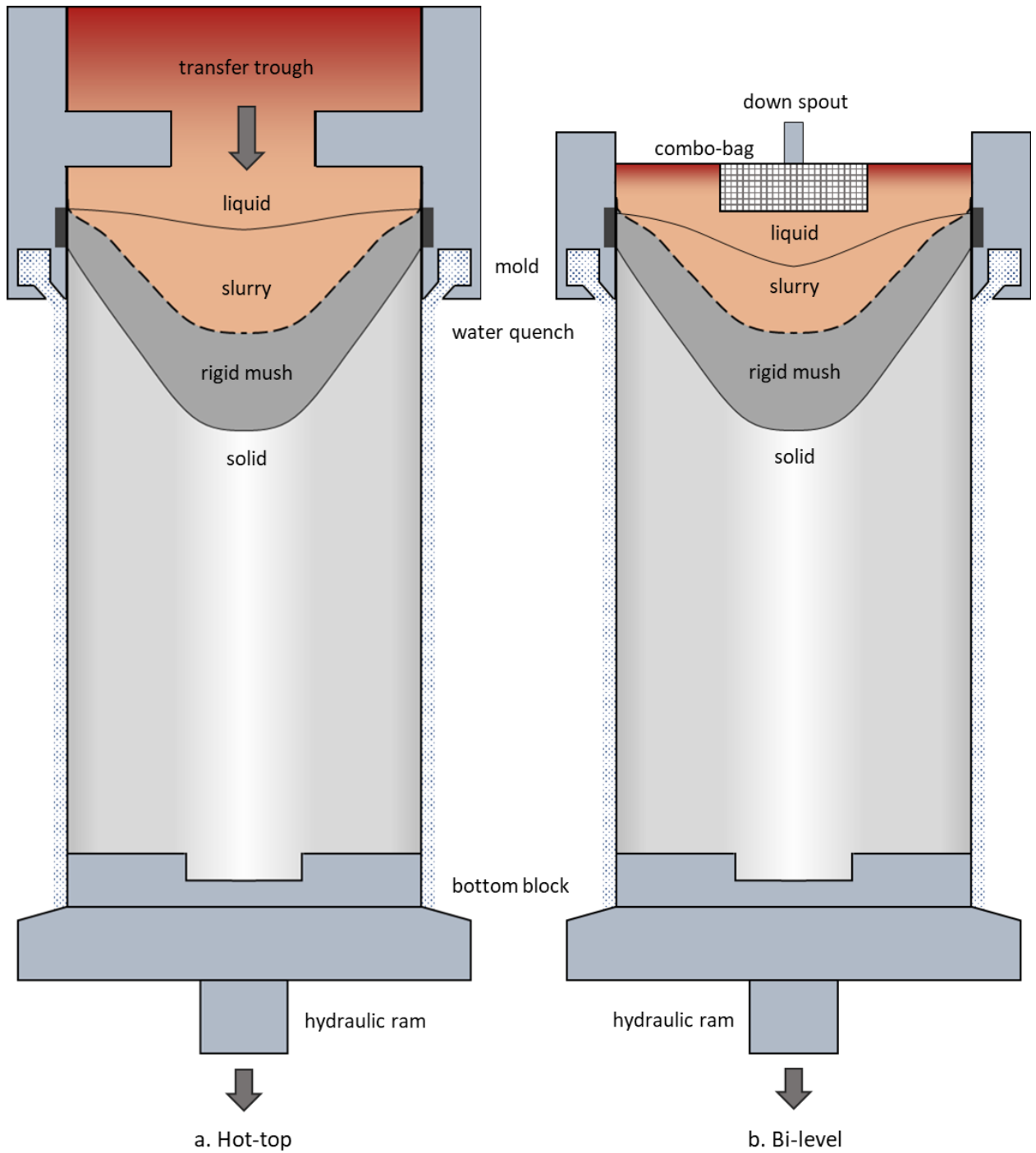


Figure 1.1: Illustration of the DC casting process with two inlet variations: a.) hot-top, and b.) bi-level with a combo-bag.

1.2 Physical Phenomena in Alloy Solidification

1.2.1 Equilibrium Phase Diagrams and Solidification Structures

One of the most powerful tools for the exposition of segregation development during alloy solidification is the binary eutectic phase diagram. This diagram shows the types and quantities of thermodynamic phases present at equilibrium as a function of temperature and composition. A generic diagram for solute A and B is shown in Figure 1.2 at constant pressure. Composition is plotted on the x-axis and temperature on the y-axis. The primary divisions on this diagram are the liquidus and solidus lines. At temperatures above the liquidus line, only liquid is present, and at temperatures below the solidus line, only solid is present. There will either be one or two solid phases depending on the temperature and composition. The α solid phase has a crystal structure of pure A (face-centered-cubic for Al) with B in solution. Likewise, β is a solid solution with the structure of pure B. At the eutectic point, which occurs at the eutectic temperature T_{eut} and composition C_{eut} , all three phases (L , α , and β) coexist in equilibrium. The wrought alloys studied in this work are all hypoeutectic, meaning that they solidify on the α -side of the diagram.

Between the solidus and liquidus is a two-phase region where a single solid phase coexists in equilibrium with the liquid. In this temperature range, the solid and liquid will have different compositions due to the difference in solute solubilities. For equilibrium solidification (i.e. lever rule), the individual phase compositions fall on the solidus and liquidus lines. When calculating the phases fractions and phase compositions, it is often convenient to represent the solidus and liquidus curves as straight lines:

$$T_{liq} = T_m + m_{liq}C_l \quad (1.1)$$

and

$$T_{sol} = T_m + m_{sol}C_s \quad (1.2)$$

where T_m is the melting temperature of the pure solvent, m_{liq} and m_{sol} are the slopes of the liquids and solidus, and C_l and C_s are the compositions of the liquid and solid phases. The composition ratio of the solid and liquid at the equilibrium interface is the partition coefficient:

$$k_p = \frac{C_s}{C_l} = \frac{C_{max}^\alpha}{C_{eut}} \quad (1.3)$$

which can be approximated using maximum composition of the primary solid phase C_{max}^{α} and the eutectic composition C_{eut} . It is necessary for hypoeutectic alloys to have a partition coefficient less than one, indicating that solute is rejected into the liquid phase during solidification.

Using the phase diagram, the process of solidification can be described for an alloy with the initial composition C_o . The path begins in the liquid at some temperature $T > T_{liq}$ and liquid composition $C_l = C_o$. As heat is extracted, the temperature drops until $T = T_{liq}$ and solidification begins. The composition of the first solid to form is $C_s = k_p C_o$. With more heat removal, the temperature drops and the equilibrium solid and liquid compositions move down the solidus and liquidus curves, respectively, until solidification ends at the solidus temperature, $T_{sol} = T_m + m_{sol} C_o$.

Although the phase diagram provides a significant amount of information, it assumes that the system is in thermal and solutal equilibrium. The wrought aluminum alloys studied in this work are substitutional alloys, meaning that the atoms from each element can occupy the same lattice sites in the crystal structure. Therefore, the atomic mobility is significantly lower in the solid than in the liquid and the rate of solute diffusion, characterized by the mass diffusivity coefficient D , is several orders of magnitude less. A more appropriate assumption for substitutional alloys might be the Gulliver-Scheil assumption which assumes thermal and solutal equilibrium at the solid-liquid interface, complete solute diffusion into the liquid, and no solute diffusion into the solid during solidification. The consequence of this final assumption is that the average solid composition lags behind the interfacial solid composition, and thus, the solid fraction at a given temperature is lower than under equilibrium conditions. Additionally, solidification persists down to the eutectic temperature which widens the freezing range of the alloy. The appropriate solute diffusion assumption will depend on the interfacial area available for solute diffusion (i.e. the microstructure) and the time scale of the solidification process. Because the evolution of phase fractions and compositions predicted by these different microsegregation models will tend to differ, proper understanding of the microstructure and solidification conditions are required.

Two important insights concerning alloys solidification affecting macroscopic transport can be established from the previous description of solidification reactions. The first is that alloys freeze over a finite temperature range, resulting in a two-phase region where solid and liquid coexist, commonly referred to as a mushy zone. The second is that the solid and liquid phases have different compositions which change as a function of temperature and are both different than

the initial composition. These two effects result in temperature and composition gradients in the mushy zone which can induce relative solid-liquid motion, translating segregation to the macroscale.

In most commercial applications, the mushy zone will consist of solid dendrites with interdendritic liquid. Dendrites are tree-like structures consisting of primary and secondary arms, which grow in the preferred growth direction, e.g. $\langle 100 \rangle$ for cubic crystal structures. The growth of a dendrite is driven by undercooling at the dendrite tip. Undercooling refers to the phenomenon of solidification to occur at some temperature below the equilibrium liquidus temperature due to combined thermal, curvature, and solutal effects. The growth velocity of the dendrite tip increases as the undercooling increases. For cubic systems, the secondary arms will tend to branch orthogonal to the primary dendrite to fill the space between primary arms. When these structures grow from a fixed surface against a unidirectional (at least locally) heat flux, they are classified as columnar dendrites. Columnar dendrites do not generally have enough space to grow in DC casting due to the heterogenous nucleation of grains in the undercooled region ahead of the columnar dendrites. The grains that nucleate and grow in this region are classified as equiaxed grains and can have several different types of structures.

The two most important structures in DC casting are globular grains and dendritic grains, shown in Figure 1.3. A globular microstructure occurs when solutal or thermal instabilities are unable to develop during solidification, e.g. when the grain radius is small with respect to a characteristic instability wavelength of the interface [4]. The primary phase will tend to grow with a nearly spherical solid-liquid interface. Under similar thermal conditions, the same alloy may develop a dendritic microstructure when the final grain size is large, which occurs when the number of heterogenous nucleation sites is decreased. A simple morphological model used to describe equiaxed grains is the grain envelope model of Rappaz and Thévoz [5]. The grain envelope is a hypothetical, smooth surface that connects the tips of the primary dendrite arms. The morphology, or dendricity, of the grain is characterized by the ratio of the solid and grain fraction volume fractions:

$$g_{s,i} = \frac{g_s}{g_g} = \frac{g_s}{g_s + g_d} \quad (1.4)$$

Where the grain volume fraction (g_g) is the sum of the solid volume fraction (g_s) and the interdendritic liquid volume fraction (g_d). This morphological parameter is commonly known as

the internal solid fraction ($g_{s,i}$) and is used throughout this work to characterize grain morphologies. Globular grains will therefore have an internal solid fraction slightly less than one, while dendritic grains will have an internal solid fraction much less than one.

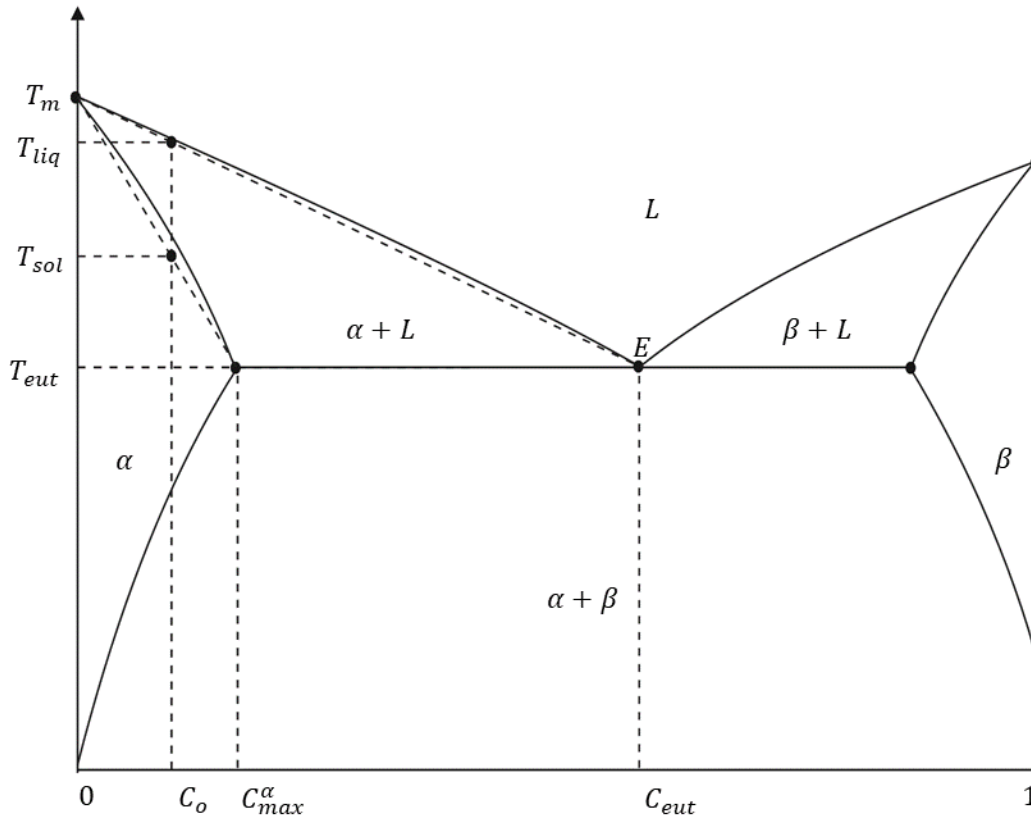


Figure 1.2: Generic binary eutectic equilibrium phase diagram with approximated linear solidus and liquidus lines.

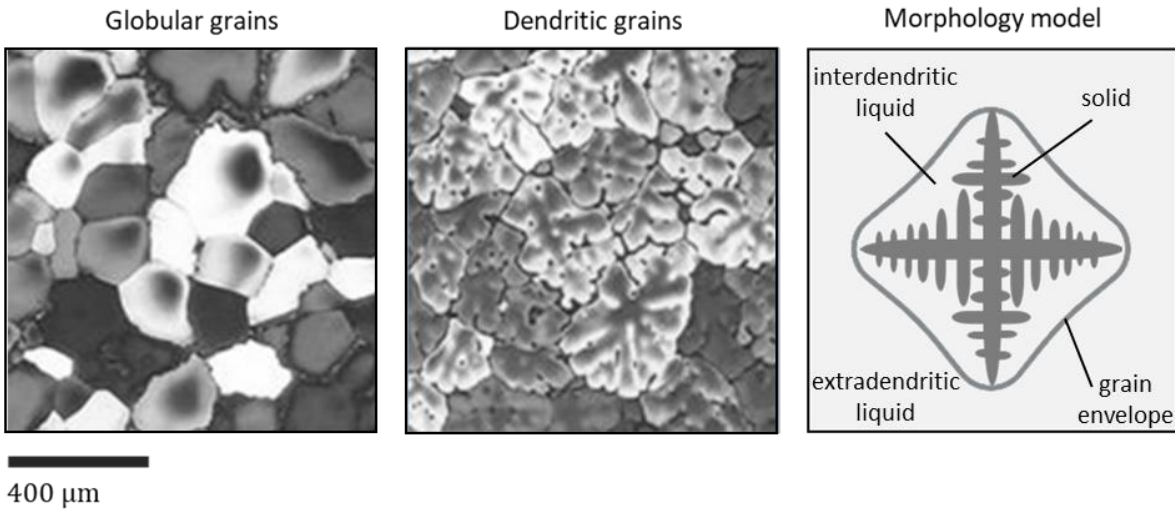


Figure 1.3: Equiaxed grain types encountered in DC casting for Al-4.5wt%Cu: global grains (grain size $\approx 100 \mu\text{m}$), dendritic grains (grain size $\approx 250 \mu\text{m}$), and the morphological grain envelope model. Micrographs courtesy of Sam Wagstaff.

1.2.2 Fluid Flow and the Development of Macrosegregation

Due to solute rejection into the liquid at the grain interface, any macroscopically significant relative motion of the enriched liquid and the depleted solid grains causes the macroscopic transport of the solute. This phenomenon is known as macrosegregation. The four main causes of relative motion during equiaxed solidification [4], illustrated in Figure 1.4, are:

1. **Shrinkage induced flow:** The density of the solid phases is generally higher than the liquid. The volume contraction upon solidification causes suction of the liquid, generally perpendicular to the solid fraction isocontours. This flow is most significant deep in the mushy where other flow effects are negligible due to strong drag forces. Although the liquid velocities may be small, they can cause significant solute redistribution due to the liquid being highly enriched in this region.
2. **Natural convection:** Temperature and composition gradients produce buoyancy forces that drive enriched liquid through permeable regions in the rigid mush
3. **Grain motion:** Suspended equiaxed grains in the slurry tend to move (settle or float) depending on the density difference between the solid and liquid. The amount of relative solid-liquid motion depends on balance of buoyancy and drag forces, which both depend

on the morphology of the grain. Globular grains tend to settle more quickly than dendritic grains due to the larger volume to surface area ratio.

4. **Mushy zone deformation:** The deformation of the solid skeleton of the rigid mush causes motion of the enriched interdendritic liquid. It is primarily caused by thermal or mechanical stresses which can expel enriched liquid under compression, or pull in liquid under tension

Macrosegregation in DC casting is caused by the net contribution from each source of relative phase motion, illustrated in Figure 1.5. The flow in the slurry region is primarily driven by thermosolutal natural convection caused by the rapid cooling at the ingot surface which drives flow along a narrow boundary layer near the packing interface. Natural convection tends to transport enriched liquid in the rigid mush towards the centerline, the degree to which depends on the permeability of the rigid mush and the dimensions of the ingot. Natural convection also tends to sweep solute-depleted grains toward the centerline where they settle in a region of thermal and solutal stratification. The accumulation of depleted grains contributes to negative segregation at the centerline and positive segregation in the slurry, the degree to which depends on both the grain size and internal solid fraction. Finally, shrinkage induced flow in the rigid mush is directed orthogonal to the solid fraction isocontours, pulling liquid from the centerline to the surface. The degree to which shrinkage flow effects macrosegregation primarily depends on the orientation of the solid fraction isocontours in the rigid mush.

Shrinkage generally causes two distinct macrosegregation segregation features, the first is a depleted centerline due to the enriched liquid pulled from this location being replaced with liquid closer to the nominal composition from the slurry. The second is a depleted region adjacent to a narrow band of enrichment at the surface. The enriched surface is due to a phenomenon known as liquation. As the surface solidifies it pulls away from the mold, enriched liquid is driven by the hydrostatic head through the permeable rigid mush to the surface where it freezes. Due to the poor surface quality and the severe amount of localized segregation, the surface is generally scalped before subsequent treatment. Because the depleted centerline cannot be modified by any such downstream process, it is the most concerning and prominent macrosegregation feature in DC cast ingots. With this macrosegregation feature in mind, experimental investigations of macrosegregation and grain structure are reviewed in the following section to demonstrate efforts made towards understanding the origin and mitigation of its formation.

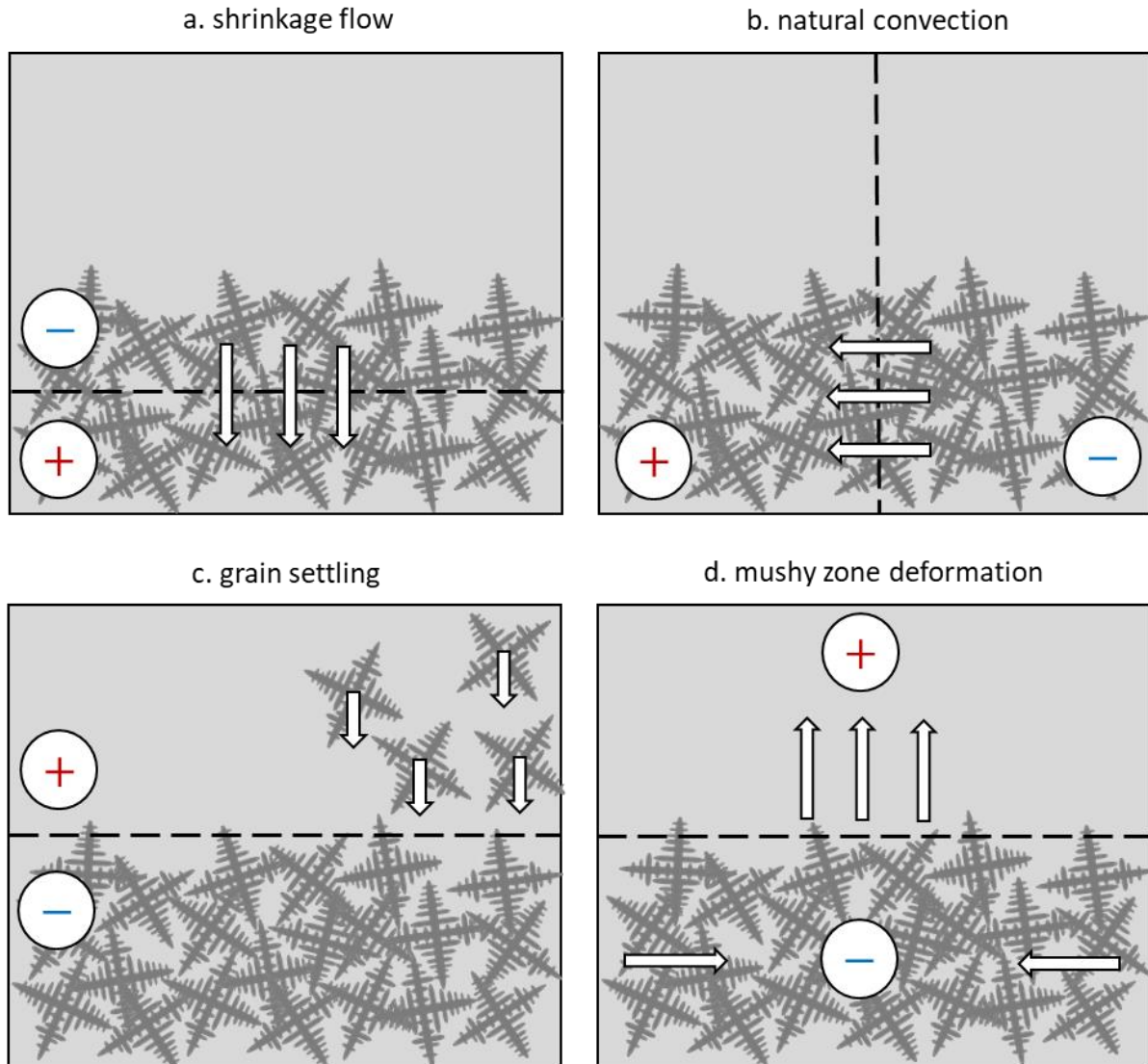


Figure 1.4: Various types of relative motion during equiaxed solidification induced by a.) solidification shrinkage, b.) natural convection, c.) grain motion, and d.) mushy zone deformation. The positive and negative signs indicate the regions of positive and negative segregation which form due to the relative solid-liquid motion in hypoeutectic alloys.

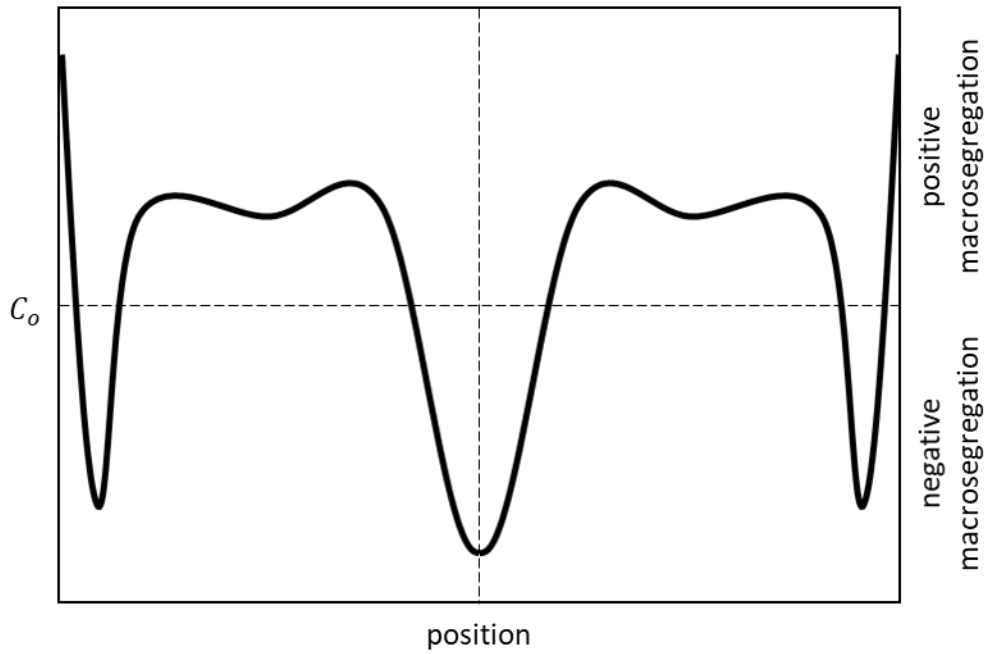
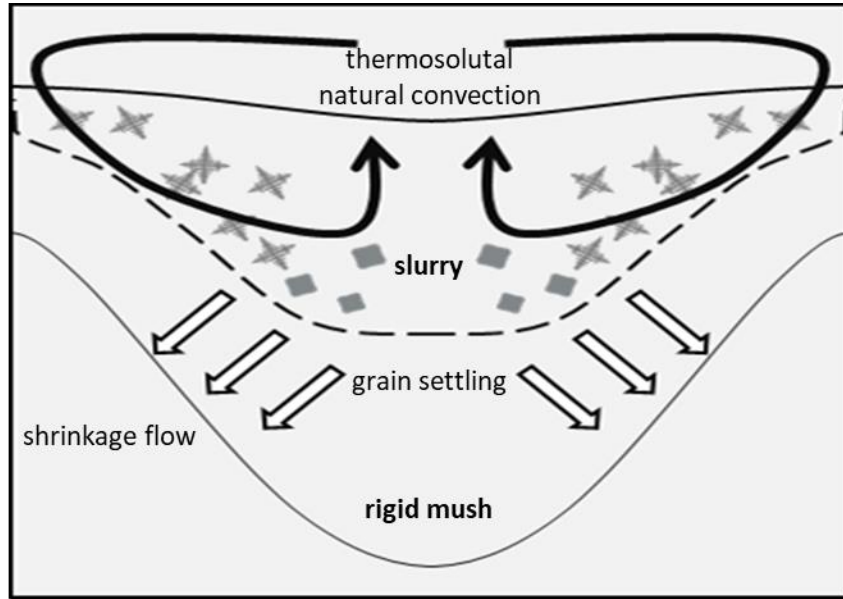


Figure 1.5: Typical relative flows and resulting macrosegregation profile in DC casting.

1.2.3 Experimental Investigations of Macrosegregation in DC Casting

One of the earliest attempts to explain mechanisms for macrosegregation in DC casting was performed by Yu and Granger in 1986 [6] on Al-Cu-Mg slabs. The authors found positive segregation towards the surface and negative segregation at the centerline (similar to Figure 1.5) and concluded that the former was due to shrinkage induced flow while the latter was due to grain accumulation. A duplex grain structure was observed near the centerline consisting of both fine and coarse cell dendrites. The spatially varying microstructure indicates different thermal histories for the two structures since the dendrite cell size depends on the cooling rate, and therefore, the coarse cell dendrites must have grown at much smaller cooling rates. Electron microprobe measurements of the composition profiles in the grains showed that these coarse cell grains grew in near isothermal conditions close to the centerline, while the fine dendrites grew under higher cooling rates as they were swept along the packing interface. The negative centerline segregation was attributed primarily to the accumulation of solute-depleted coarse cell dendrites.

This hypothesis was generally supported by Gariepy and Caron [7] in their investigation of 51 different rolling slabs (AA3014 and AA5182) cast with various metal distribution systems, casting speeds, and levels of grain refinement. The authors found that the level of centerline solute depletion generally increased with the amount of added grain refiner and suggested that grain refinement practices should be optimized to only supply the amount necessary to prevent hot-cracking, but prevent the morphological transition to globular grains that tend to accumulate at the centerline. The authors also demonstrated the significant role that the liquid metal distribution had on macrosegregation. The authors concluded that adding combo-bags to the bi-level transfer system (see Figure 1.1) could reduce the bulk segregation by up to 30 – 40% by preventing forced convection down the centerline. However, no specific mechanism describing how attenuated forced convection led to the reduction of macrosegregation was provided. The practical conclusion of this work were that both grain refinement and liquid metal distribution practices could have a significant effect on macrosegregation, and the design of these practices should be improved.

Under the European EMPACT project, Joly et al. [8] characterized the macrosegregation and grain structure formation in ingots (AA5182) cast with and without grain refiner and combo-bags. An ingot cast with a combo-bag exhibited more severe centerline depletion when grain refined (−9.2% Mg) than non-grain refined (−4.2% Mg). This observation was attributed to the increased settling tendency and packing fraction for globular grains in the grain refined case

compared to dendritic grains in the non-grain refined case. The morphology of the grain appeared to play a larger role than the grain size in the accumulation of solute-depleted grains near the centerline. The grain refined ingot had a significantly smaller average grain size ($198 \pm 41 \mu\text{m}$ compared to $399 \pm 52 \mu\text{m}$) while having a more solute-depleted centerline. The interplay of grain morphology on hydrodynamics explains why trends in centerline macrosegregation as a function of grain size cannot be well established because large grains will tend to undergo a globular-to-dendritic morphological transition. In contrast to Garipey and Caron [7], the authors observed that removal of the combo-bag led to the overall reduction in centerline depletion, however no mechanism was suggested.

More recently, Wagstaff and Allanore [9–12] used a strong localized jet to feed liquid metal down the centerline of Al-4.5wt%Cu slabs to prevent the accumulation of solute-depleted grains at the centerline. The authors proposed an optimal jet condition strong enough to suspend grains locally, but weak enough to minimize the erosion of the rigid mush, which would tend to increase the horizontal component of shrinkage driven flow. For the first time, the authors demonstrated the ability to refine and globularize the grain structure, while simultaneously preventing the accumulation of solute-depleted grains at the centerline. A considerable reduction in the depleted centerline for this “jet-stirred” process compared to conventional casting with a combo-bag is shown in Figure 1.6, where the casting direction is into the page. The use of a numerical model to elucidate details of the change in transport phenomena leading to this different macrosegregation pattern is one of the primary goals of this dissertation.

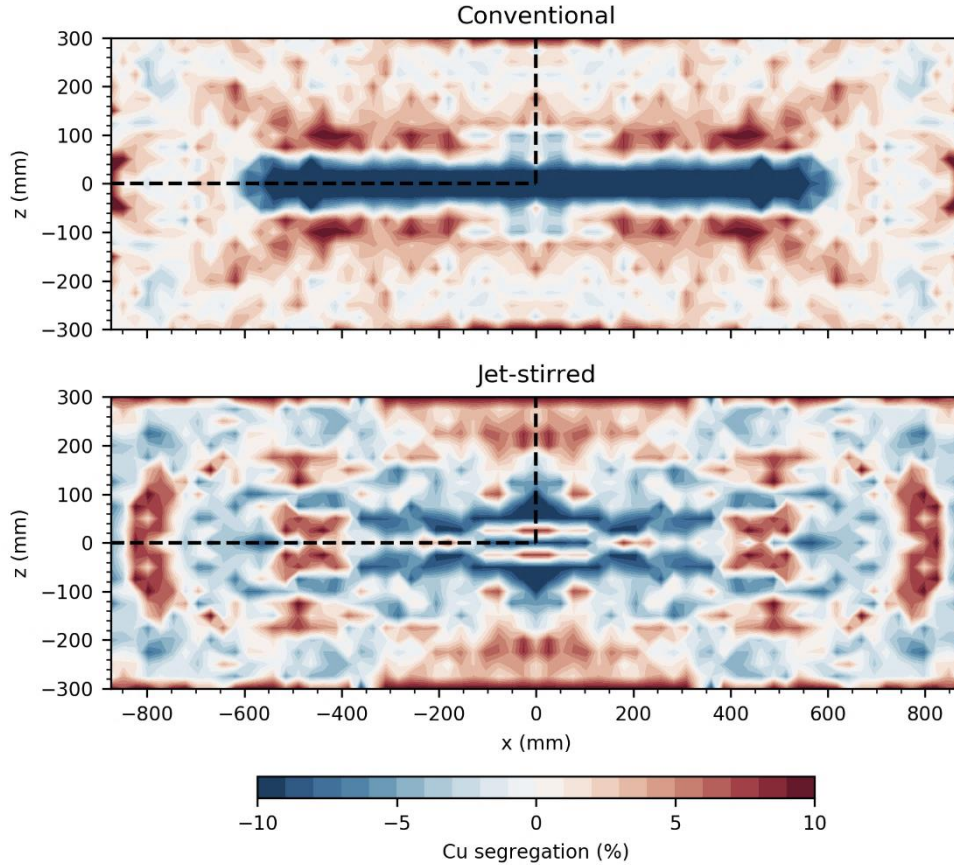


Figure 1.6: Comparison of experimental macrosegregation profiles in ingot slices for conventional and jet-stirred casting at a cast length of 1800 mm. The composition was previously measured using X-ray fluorescence (XRF) by Wagstaff and Allamore [9] and contour plots are reproduced here assuming two-fold symmetry of the measured ingot quadrant indicated by the black lines.

1.3 Mathematical Modeling of Alloys Solidification

Having identified the various micro- and macroscopic transport phenomena that contribute to macrosegregation development during solidification and in DC casting, focus is shifted towards the development and use of mathematical models of macrosegregation. Among the first studies to model macrosegregation during alloy solidification were published in the 1960s by Flemings and his coworkers [13,14]. Flemings and Nereo [13] derived a local solute redistribution equation; an ordinary differential equation based on solute mass conservation and the Scheil assumption for local solute partitioning. This equation was used to determine the macrosegregation caused by shrinkage-induced flow in Al-Cu castings cooled from the bottom. The analytical model enabled

the authors to study the effects of varying heat transfer rates and casting cross-sections to qualitatively explain macrosegregation development in castings. This model was later extended by Mehrabian et al. [15] to include the effect of buoyancy driven flows in the interdendritic liquid. A temperature gradient was imposed, and steady state velocity and compositional fields in the mushy zone were calculated. A parametric study suggested that channels of highly enriched liquid during columnar solidification were the result of buoyancy, and not shrinkage.

The first attempt to calculate, rather than prescribe, the interactions between the mushy zone and bulk fluid, was performed by Szekely and Jassal [16]. A multi-domain approach was used where separate conservation equations modeled were solved for the heat and momentum transfer in the mush, liquid, and solid. An iterative procedure was used to couple the different regions using the solutions on their boundaries. Ridder et al. [17] used a similar model to study macrosegregation in an axisymmetric ingot, with Flemings solute redistribution equation in the mushy zone. The macrosegregation predictions of the model qualitatively agreed with experiments.

Substantial progress in solidification modeling began in the mid-1980s with the advent of single-domain models. Such models eliminated the computational difficulties associated with coupling and remeshing near interfaces by solving the same set of equations over the entire fixed computational domain, regardless of the location of phase fronts. Two different modeling approaches can be distinguished from the single domain models: the multiphase models of Beckermann and coworkers [18,19], and the mixture model of Bennon and coworkers [20–22].

1.3.1 Multiphase Models

Ni and Beckermann [18] were the first to use the volume-averaging approach to propose a two-phase model for transport phenomena occurring during globular equiaxed solidification. In this approach, the microscale transport equations for the solid and liquid phases are averaged over a representative volume element (RVE). The formal averaging procedure, was based on the method of Drew [23] for incorporating microscopic phenomena into macroscopic balance equations. These macroscopic balances are formulated for each phase and coupled by interphase transfer terms that reflect the transport phenomena such as grain nucleation and growth, solutal undercooling and backdiffusion, and interfacial drag occurring on the microscopic scale. The interphase transfer terms are dependent on the solid-liquid interfacial area per unit volume, which characterizes the geometry of the interface lost during the averaging process. Expressions for the

interfacial area per unit volume generally require the number density of grains, determined either from some type of nucleation model [24] or are taken to be uniform and constant. The solid growth rate in the representative volume is approximated by a growing sphere model controlled by a solute mass balance at the solid-liquid interface, assumed to be at thermodynamic equilibrium. The interphase drag of a sphere is calculated according to the generalized expression of Agarwal and O'Neill [25], approaching Stoke's law for a single sphere at low solid volume fractions and the Kozeny-Carman expression for the permeability of a packed bed of spheres at high solid volume fractions. The solid phase is treated as a pseudo fluid with an effective viscosity that approaches an infinite value at a predefined packing fraction of 0.637, corresponding to the random close packing of spheres [26]. This implies that the macroscopic velocity gradients in the solid vanish at solid fractions above the packing limit so that the rigid solid assumes a uniform velocity equal to the system velocity.

Wang and Beckermann [19] expanded the previous multiphase model to dendritic grain morphologies using the concept of a grain envelope (see Figure 1.3). Because this hypothetical interface separates the inter- and extradendritic liquid, it provides the ability to incorporate microscopic phenomena related to the grain morphology into the macroscopic equations [27]. The growth of the envelope is governed by the velocity of the primary dendrite tips using an Ivantsov-based growth model [28], which requires a further assumption about the geometry of the dendrite tip (e.g. hemisphere [29] or paraboloid [30]). The evolution of the solid phase inside the envelope is controlled by solute diffusion on the length scale of the secondary dendrite arms, assuming local thermodynamic equilibrium at the solid-liquid interface. Thus, the morphology of the dendritic grain is determined by the competitive growth of the primary and secondary dendrite arms and the internal solid fraction can then be calculated. For the limiting case where the internal solid fraction reaches unity, the model reduces to the two-phase formulation of Ni and Beckermann [18].

Perhaps, the most important aspect of this model is that the internal fraction solid can be tracked to account for the influence of grain morphology on the hydrodynamic behavior of the system. For example, the effective viscosity used to transition between the slurry and rigid mush is dependent on the grain fraction, Eqn. (1.4), so that grains can coalesce with a solid fraction less than the theoretical packing limits for its ideal shape. This phenomenon is supported by ample experimental evidence from Arnberg and coworkers [31,32] which shows that the packing fraction for aluminum alloys is in the solid fraction range of 0.1 – 0.55, depending of the grain

morphology. Additionally, the use of the grain envelope model better accounts for the influence of grain morphology on the buoyancy and drag forces exerted on the grain. In this regard, an interphase drag model based on settling experiments involving a wide range of realistically shaped models of dendrites [33,34] was proposed by Wang et al. [35]. Combeau et al. [36] compared the macrosegregation and grain structure predictions using a similar multiphase model to explore the influence of grain morphology on macrosegregation in steel castings. Notably, the authors showed that dendritic grains settled slower and carried less solute-depleted mass to the centerline than globular grains. A significant improvement in the prediction of centerline segregation was observed by accounting for the grain dendricity in the numerical model.

1.3.2 Mixture Models

While the multiphase approach theoretically resolves the microscopic and macroscopic features of equiaxed solidification in significant detail, it requires model inputs for the interphase transfer terms for which experimental data can be scarce, introducing additional uncertainty into the model predictions. Furthermore, the use of separate conservation equations for each phase can be computationally expensive and difficult to implement into standard CFD procedures. Bennon and Incropera [21,37] proposed an alternative approach, known as the continuum mixture model, which cast the previous transport equations in terms of mixture quantities to reduce the number of equations to be solved and negating the need for uncertain interphase transfer terms. When necessary, individual phase contributions are found by postulating *ad hoc* algebraic relationships. An example of such a relationship is using lever rule to calculate the phase fractions and compositions rather than using the complicated multiphase growth kinetics model. The relative simplicity of these models has led to the development of robust and efficient solution procedures for coupling the various transport equations [38–40], making them well suited to upscaling to the length and time scales of industrial systems. Recognizing these benefits, Ni and Incropera [41,42] extended the mixture model to include solutal undercooling and solid motion, although no calculations were performed.

Vreeman et al. [43,44] used some of the previous developments to propose a binary mixture model accounting for grain motion during equiaxed solidification. The model uses different source terms in the momentum equations for the slurry and packed zones. Compared to the pseudo-viscosity model, this approach requires a method for tracking the evolution of the packing interface

to properly transition terms from expressions in the slurry to the rigid mush. Using a discrete transition between slurry and rigid mush regions can have a significant artificial influence on the composition predictions [45,46] and must be treated carefully. The supplementary relationship used to predict the relative solid-liquid velocity assumes a constant, characteristic grain diameter and spherical, globular grains. The only morphological consideration of the model is the *ad-hoc* selection of the characteristic packing fraction which invokes an implicit assumption about the grain morphology which is not included in the relative velocity model. Although this model has been used with some success in DC casting [47–49], there have been few attempts to reformulate the mixture model to incorporate a more realistic description of the grain size and morphology in equiaxed solidification. Development of a continuum mixture model for dendritic equiaxed solidification is one of the primary goals of this dissertation.

1.3.3 Mathematical Investigations of DC Casting

The earliest attempts at modelling DC casting process were by Flood et al. in 1991 [50]. The model, which assumed an entirely rigid mush (no solid-liquid slurry) moving at the casting speed and neglected solidification shrinkage, was applied to an Al-4.5wt%Cu billet with a diameter of 420 mm. Without settling solid grains or shrinkage driven flow, the authors observed positive segregation at the center of the ingot due to solutal convection in the rigid mush. Reddy and Beckermann [51] made the first attempt to model grain motion in DC casting of a Al-4.5wt%Cu billet with a diameter of 533 mm. The authors compared cases with and without grain motion and compared preliminary results to the experiments of Finn et al. [37]. Although neither case showed good quantitative agreement with experiments, it was demonstrated that incorporation of grain motion into the numerical model allowed for the prediction of a depleted centerline. For the same alloy and casting conditions, Reddy and Beckermann [52] studied competition between thermosolutal natural convection and shrinkage induced flow. The former relies on the permeability of the rigid mush, while the latter does not, so that shrinkage flow fills the volume deficit from solidification regardless of the solid structure via continuity. A rigid mush with relatively high permeability allowed natural convection to dominate shrinkage flow in the rigid mush causing positive centerline segregation. On the other hand, a rigid mush with a low permeability damped natural convection and shrinkage flow dominated causing negative centerline segregation.

Vreeman et al. [43] studied macrosegregation formation in 400 mm diameter billets using a continuum mixture model that considered grain motion, thermosolutal convection, and shrinkage. Two different alloys were considered: Al-4.5wt%Cu, which has cooperating negative thermal and solutal buoyancy (i.e. Cu is lighter than Al) and Al- 6wt%Mg, which has competing thermal and solutal buoyancy (Mg is heavier than Al). The first parametric study on the role of grain motion on macrosegregation showed that both the grain diameter and packing fractions had a significant impact on predictions. It was also shown that a region of loosely packed grains formed in the center of the ingot that increased in volume with increasing grain size due to the increased sedimentation rate of the larger grains. The authors demonstrated the different flow patterns in the slurry for the two alloys. Since Mg is lighter than Al, the natural convection flow tended to recirculate up towards the inlet before interacting with the incoming liquid. In the other alloy, Cu is heavier than Al, and the recirculation cell was constrained to a region below the thermally stratified hot-top reservoir.

Later, Vreeman et al. [47] used the same simplified model to compare the model predictions to experiments for a 450 mm diameter grain-refined Al-6wt%Cu billets. The comparison showed sufficient agreement in temperature profiles, composition profiles, and sump shape to explain general trends in the process. The authors concluded that the experimental packing fraction could be somewhere in the range of 0.2-0.25 solid fraction based on the comparison of the composition profiles but noted that this value most likely depends on the position in the casting and casting parameters.

Flood and Davidson [53] presented an analytical model of DC casting and performed a scaling analysis on the flow patterns in the sump. The authors showed that, as the liquid metal is uniformly introduced at the top of the mold, it is immediately pulled towards the chilled surface and is driven down by thermal buoyancy forces in a narrow boundary layer along the rigid mush. As the cooling liquid moves radially inward and down the rigid mush, the fluid is continually entrained into the mush and solidifies. When the remaining fluid reaches the centerline, it is redirected upwards as part of a shear-driven recirculation cell that is mostly isothermal. The scaling analysis was further used to demonstrate that general flow structure was a weak function of billet radius and superheat, so that there is only a narrow range of buoyancy driven velocities possible.

Rappaz and coworkers [54,55] studied macrosegregation formation in an Al-Mg sheet ingot (275 mm thick) based on the experiments of the EMPACT project [8] using a 2-D model that did not account for grain motion. Jalanti [54] concluded that the combined thermosolutal

natural convection for Al-Mg alloys had an insignificant role compared to shrinkage on the macrosegregation formation. Comparison with experiments showed reasonable qualitative agreement in the prediction of a depleted centerline, but did not predict enrichment in the mid-section, attributed to the lack of grain motion model. The conclusions from this study suggest that shrinkage driven flow is the most important transport mechanism contributing to the depleted centerline in DC cast slabs.

Zaloznik et al. [56] performed the most detailed investigation to date regarding the relative importance of transport mechanisms on the macrosegregation. A 350 mm thick sheet ingot of aluminum alloy 7449 was simulated using a 2-D multiphase model. The authors found that shrinkage and grain motion were the two most important transport mechanisms contributing to the formation of negative centerline segregation, with shrinkage flow being the most important by a wide margin. The authors also identified two mechanisms for grain coalescence. Near the chill and along the inclined packing interface grains coalesce by a growth and impingement mechanism, whereas near the centerline grains coalesce by sedimentation. This latter mechanism causes a flat, loosely packed bed similar to the previous observations of Vreeman et al. [43]. Although the model did not predict grain morphologies (i.e. a fully globular structure was prescribed), various trends can be concluded from the reported undercoolings and growth rates. As the grains are swept along the packing interface they rapidly grow in a region of large undercooling and will tend to be dendritic and increase in size towards the centerline. The grains that do not coalesce are carried into the sump where they are either carried to regions above the liquidus temperature, and remelt, or remain in the core of the slurry. This region exhibits low undercoolings and growth velocities which can explain the formation of coarse dendrites intermixed with fine equiaxed dendrites, as has been observed experimentally [6,8].

Heyvaert et al. [57] attempted to simultaneously predict the grain structure and macrosegregation using a version of the Wang and Beckermann multiphase model [19]. The model was compared to the results from the combined numerical and experimental investigation of Vreeman et al. [47]. Although the authors claim better agreement with experiments, the macrosegregation predictions using different input parameters for nucleation density, envelope packing fraction, and tip geometry assumption are all within the experimental uncertainty band. Although the model is sophisticated, it does not seem to shed much light on the transport phenomena occurring in DC casting not already captured by more simplified approaches. Instead

the general conclusions seem to characterize the behavior of the multiphase model as a function of model input. For example, it was demonstrated that assuming paraboloidal dendrite tips led to the prediction of a globular-to-dendritic transition depending on the nucleation parameters prescribed to the model, while the hemispherical tip model consistently predicted globular grains. Therefore, the authors concluded that there is still a need for improved microstructure modeling before these models can reliably predict grain structure evolution and be confidently used to model DC casting. Some recent efforts towards this goal have been made by Torabi et al. [58].

In each of the preceding studies, liquid metal was introduced from a sufficiently wide inlet so that the inflow was immediately entrained towards the mold. Although several numerical studies have examined the flow field behavior for different inlet configurations in DC casting [49,59–62], few studies have calculated the macrosegregation in 3-D slabs. Pakanati [63] applied a version of the Wang and Beckermann multiphase model [19] to 3-D simulations of DC casting including a centerline jet to promote grain suspension. However, the computational expense of the multiphase approach prevented the model from assisting in process design decisions because a limited number of simulations could be performed. A similar conclusion was reached by Mortensen et al. [64] and their multiphase model [65] was simplified by prescribing a constant grain size and packing fraction, and the Gulliver-Scheil assumption was used to model microsegregation. Nevertheless, the model still included all relevant macroscopic transport phenomena including forced convection from a constrained inlet, natural convection, grain motion, and mushy zone deformation. The macrosegregation in the AA5182 ingots previously cast and characterized by Joly et al. [8] was investigated. The authors observed the same qualitative results as the experiments: removal of the combo-bag reduced the negative centerline segregation; however the flow field was not examined and no mechanism for this change in segregation was suggested.

1.4 Research Objectives

The formation of macrosegregation in DC casting has been investigated for many years, but a full understanding is still developing. Due to the complexity of the physical phenomena involved and the opacity of the metal, a merely experimental approach cannot provide enough clarity and must be complimented with numerical studies. Previous efforts to perform numerical studies for DC casting point towards the need to bridge the gap between the multiphase and mixture models.

The former resolves a significant amount of detail regarding the grain structure; however, the current implementations of these models require prohibitive computational resources to use them for 3-D parametric studies of industrial scale processes. In contrast, current implementations of mixture models are sufficiently scalable, but do not include enough detail of the grain structure to apply these models to realistic cases.

Extension and generalization of the mixture model is presented in Chapter 2, formulated from the volume-averaged multiphase equations. Information regarding the grain structure is retained in the hydrodynamic considerations of the model. The model is further extended to more realistic microsegregation models with finite solute diffusion in Chapter 3. Two different microsegregation models are formulated with a varying level of complexity. The first is an analytical model based on the work of Clyne and Kurz [66] which gives an algebraic expression for phase fractions and compositions. This expression can be directly incorporated into the efficient thermodynamic coupling procedures developed by Voller and coworkers [38–40]. The second is based on the multiphase model of Wang and Beckermann [67] which attempts to simultaneously predict both the microsegregation and microstructure development. An efficient thermodynamic coupling procedure is developed for the multiphase microsegregation model in Chapter 5. As a result, the computational expense of the two microsegregation models are similar and can be evaluated in terms of their ability to predict various microscale phenomena in Chapter 7. It is of general interest to determine if the multiphase microsegregation model: (1) can reliably predict grain structure using the latest closure relationships, and (2) changes the macroscale transport predictions compared to the more simplified analytical approach.

The most important aspects of any numerical model are related to the discretization procedures used to solve the transport equations. The finite volume method on co-located grids is reviewed in Chapter 4, and novel treatments of the discontinuous body forces and phase mass fluxes across the packing interface are proposed. The numerical model is verified against benchmark solutions in Chapter 6 to characterize its behavior and select discretization procedures that are free from erroneous numerical artifacts.

The final objective of this work is to investigate the role that forced convection has on grain transport and macrosegregation in DC casting using the verified numerical model. In horizontal DC casting, the casting axis is perpendicular to gravity and there is a tendency for grains to accumulate along the bottom of the ingot. Feeding liquid metal through a constrained inlet near

the bottom in an effort to suspend grains is investigated in Chapter 8. In vertical DC casting, the casting axis is parallel to gravity and there is a tendency for grains to accumulate in the center of the ingot. The influence of a strong vertical jet down the centerline on the transport mechanisms contributing to macrosegregation development is investigated in Chapter 9. The grain structure data previously measured by Wagstaff and Allamore [9] in industrial scale vertical DC cast ingots is used a model input to properly account for the microstructure variation under different flow conditions.

2. PHYSICAL MODEL

This chapter is dedicated to formulating a mathematical model describing equiaxed solidification and deriving the corresponding conservation equations. This model uses a single-domain approach to account for both flow regimes present during equiaxed solidification: the slurry and the rigid mush. In the slurry regime, the solid phase is mobile, and the flow behaves as a solid-liquid suspension. This is classified as a multiphase flow because two-way coupling exists between the phase structures and the local flow conditions. In the rigid mush, the solid phase is coalesced into a nondeformable solid matrix moving at the system velocity. This is classified as a single-phase flow through a saturated permeable medium because the local flow conditions do not directly influence the solid structure. The purpose of this model is to capture the effects that the combined relative solid-liquid motion in the different flow regimes have on the development of macrosegregation in castings.

Although models have been formulated to describe the microscopic details of solidification interfaces, the length scale disparity between these interfaces and industrial scale castings prohibits their use. For example, a model that could theoretically capture the grain-scale phenomena in grain refined DC casting would require a computational grid spacing of about 10 μm . Calculation of the governing equations via the finite volume method (FVM) in three dimensions for a single cubic meter casting would require 10^{15} (one quadrillion) control volumes, an amount that is not feasible at any point in the foreseeable future. For this reason, macroscopic transport equations are formulated using volume averaging methods to replace instantaneous descriptions on the grain interface with approximated averages over a length scale that bridges the disparity between microscale phenomena and industrial systems. In this case, a grid spacing which provides meaningful averages of the microscale interfaces and accurate approximations of the discrete macroscale transport equations is on the order of 1-10 mm. Therefore, the volume averaging method can reduce the control volume requirement to about 10^6 (one million), which is reasonable for current computing systems available in both academia and industry.

The development of the current model relates the previous work of Drew [23] for volume averaging procedures, Beckermann and coworkers for its application to multiphase models of solidification [18,19], and Bennon and Incropera [20] for the formulation of mixture equations. Insight into the relationship between multiphase and mixture equations is also taken from Prescott

et al. [22], Ni and Incropera [41], and Manninen [68]. Therefore, the model developed in this chapter is the continuation of long-standing ideas used to provide the necessary framework for mathematical model formulation of solidification processes. The resulting mixture model retains relationships for the grain morphology and size which were oversimplified in previous mixture formulations for equiaxed solidification.

2.1 Volume Averaging

Volume averaging is a procedure used to derive macroscopic continuum equations for individual phases in a multiphase system. Consider a representative volume consisting of solid grains and liquid, as shown in Figure 2.1. The formal definition of the volume average of the transport quantity ϕ_k over this representative volume V is

$$\langle \phi_k \rangle = \frac{1}{V} \int_V X_k \phi_k dV \quad (2.1)$$

where the phase function X_k indicates if the phase exists at a certain position \mathbf{x} and time t

$$X_k(\mathbf{x}, t) = \begin{cases} 1 & \text{if } \mathbf{x} \text{ is in phase } k \text{ at time } t \\ 0 & \text{else} \end{cases} \quad (2.2)$$

The volume average of the phase function,

$$\langle X_k \rangle = \frac{1}{V} \int_V X_k dV = \frac{V_k}{V} = g_k \quad (2.3)$$

is equal to the phase volume fraction g_k of phase k present in the representative volume and conservation of total volume requires that the phase volume fractions sum to unity:

$$\sum_k g_k = 1 \quad (2.4)$$

The fluctuating component of the quantity for phase k in the representative volume is defined as

$$\hat{\phi}_k = \phi_k - \langle \phi_k \rangle \quad (2.5)$$

where $\langle \phi_k \rangle^k$ is referred to as the *intrinsic* volume average. However, when the fluctuating component is neglected ($\hat{\phi}_k = 0$), this value is mathematically equivalent to its microscopic counterpart, ϕ_k . Therefore, the volume average of some quantity is simply the product of the volume fraction and the microscopic quantity for that phase,

$$\langle \phi_k \rangle = g_k \phi_k \quad (2.6)$$

The material derivative of the phase function, also known as the topological function,

$$\frac{\partial X_k}{\partial t} + \mathbf{u}_i \cdot \nabla X_k = 0 \quad (2.7)$$

is utilized to provide the necessary relationship between the time varying component and spatially varying component of X_k . Here, \mathbf{u}_i is the velocity normal to the interface and the gradient of the phase function ∇X_k has properties of a Dirac δ -function since it is zero everywhere except at the interface. The magnitude of ∇X_k at the interface is equivalent to the normal derivative and its direction points into the direction of phase, which gives

$$\nabla X_k = \frac{\partial X_k}{\partial n} \mathbf{n}_k = \delta(\mathbf{x} - \mathbf{x}_i) \mathbf{n}_k \quad (2.8)$$

Because the collection of all points on the interface defines the interfacial surface area, the volume integral of $\phi_k \nabla X_k$ is equivalent to the surface integral of the interfacial value

$$\int_V \phi_k \nabla X_k dV = \int_{A_i} \phi_{k,i} \mathbf{n}_k dA \quad (2.9)$$

The previous volume averaging relationships can be applied to the general equation for transport of quantity ϕ_k :

$$\underbrace{\frac{\partial}{\partial t} (\rho_k \phi_k)}_{\text{transient term}} + \underbrace{\nabla \cdot (\rho_k \phi_k \mathbf{u}_k)}_{\text{advection term}} = - \underbrace{\nabla \cdot (\mathbf{j}_k)}_{\text{diffusion term}} + \underbrace{S_k}_{\text{source terms}} \quad (2.10)$$

where each term has been labeled with its physical representation. The first step in deriving volume-averaged transport equations is to multiply the microscale balance by the phase indicator

function, such that:

$$\underbrace{X_k \frac{\partial}{\partial t} (\rho_k \phi_k)}_{\text{transient term}} + \underbrace{X_k \nabla \cdot (\rho_k \phi_k \mathbf{u}_k)}_{\text{advection term}} = - \underbrace{X_k \nabla \cdot (\mathbf{j}_k)}_{\text{diffusion term}} + \underbrace{X_k S_k}_{\text{source terms}} \quad (2.11)$$

Applying the chain rule to the transient, advection, and diffusion terms,

$$\begin{aligned} & \underbrace{\frac{\partial}{\partial t} (X_k \rho_k \phi_k) - \rho_k \phi_k \frac{\partial X_k}{\partial t}}_{\text{transient term}} \\ & + \underbrace{\nabla \cdot (X_k \rho_k \phi_k \mathbf{u}_k) - \rho_k \phi_k \mathbf{u}_k \cdot \nabla X_k}_{\text{advection term}} = \\ & - \underbrace{\nabla \cdot (X_k \mathbf{j}_k) + \mathbf{j}_k \cdot \nabla X_k}_{\text{diffusion term}} + \underbrace{X_k S_k}_{\text{source terms}} \end{aligned} \quad (2.12)$$

and averaging the microscopic equations over the representative volume, gives

$$\begin{aligned} & \underbrace{\frac{\partial}{\partial t} \left(\frac{1}{V} \int_V (X_k \rho_k \phi_k) dV \right) + \frac{1}{V} \int_V (\rho_k \phi_k \mathbf{u}_i \cdot \nabla X_k) dV}_{\text{transient term}} \\ & + \underbrace{\frac{1}{V} \int_V \nabla \cdot (X_k \rho_k \phi_k \mathbf{u}_k) dV - \frac{1}{V} \int_V \nabla \cdot (\rho_k \phi_k \mathbf{u}_k \cdot \nabla X_k) dV}_{\text{advection term}} = \\ & - \underbrace{\frac{1}{V} \int_V \nabla \cdot (X_k \mathbf{j}_k) dV + \frac{1}{V} \int_V \mathbf{j}_k \cdot \nabla X_k}_{\text{diffusion term}} + \underbrace{\frac{1}{V} \int_V X_k S_k}_{\text{source terms}} \end{aligned} \quad (2.13)$$

Using the definition of the volume-averaged normal derivative of X_k in Eqn. (2.8) gives

$$\begin{aligned} & \underbrace{\frac{\partial}{\partial t} (g_k \rho_k \phi_k) - \frac{1}{V} \int_{A_i} \rho_k \phi_{k,i} \mathbf{u}_i \cdot \mathbf{n}_k dA}_{\text{transient term}} \\ & + \underbrace{\nabla \cdot (g_k \rho_k \phi_k \mathbf{u}_k) + \frac{1}{V} \int_{A_i} \rho_k \phi_{k,i} \mathbf{u}_k \cdot \mathbf{n}_k dA}_{\text{advective term}} = \\ & - \underbrace{\nabla \cdot (g_k \mathbf{j}_k) + \frac{1}{V} \int_{A_i} \mathbf{j}_k \cdot \mathbf{n}_k dA}_{\text{diffusion term}} + \underbrace{g_k S_k}_{\text{source terms}} \end{aligned} \quad (2.14)$$

Collecting the area integral terms gives a general macroscale balance equation which can be used to describe the average behavior of a phase quantity in a representative volume:

$$\frac{\partial}{\partial t}(g_k \rho_k \phi_k) + \nabla \cdot (g_k \rho_k \phi_k \mathbf{u}_k) = -\nabla \cdot (g_k \mathbf{j}_k) + g_k S_k + \dot{R}_k \quad (2.15)$$

where \dot{R}_k is a collection of the microscale interfacial transfer terms:

$$\dot{R}_k = \underbrace{\frac{1}{V} \int_{A_i} \rho_k \phi_{k,i} (\mathbf{u}_i - \mathbf{u}_k) \cdot \mathbf{n}_k dA}_{\text{interface transfer due to phase change}} + \underbrace{\frac{1}{V} \int_{A_i} \mathbf{j}_k \cdot \mathbf{n}_k dA}_{\text{interface transfer due to diffusion}} \quad (2.16)$$

The generation of a transport quantity in one phase must come at the annihilation of the quantity in the other phases, so that the net contribution of the interfacial transfer terms sum to zero:

$$\sum_k \dot{R}_k = 0. \quad (2.17)$$

2.2 Multiphase Model

Macroscopic conservation equations can be specified for a certain system by making relevant assumptions which simplify the interfacial transfer expressions. Although exact expressions for the interfacial transfers are provided in Eqn. (2.16), they are not useful for closure of the model because their length scale is not resolved after averaging. In view of the mean value theorem for integrals, the interfacial transfer terms can be modeled as the product of an interfacial area concentration (i.e. $S_i = A_i/V$) and a mean interfacial flux. Hence, the interfacial transfer due to phase change becomes:

$$\frac{1}{V} \int_{A_i} \rho_k \phi_{k,i} (\mathbf{u}_i - \mathbf{u}_k) \cdot \mathbf{n}_k dA = S_i \rho_k \bar{w}_{ni} \bar{\phi}_{k,i} \quad (2.18)$$

where \bar{w}_{ni} represents the average normal velocity of the interface relative to phase k . For $\bar{\phi}_{k,i} = 1$, the mass exchange due to phase change is obtained

$$\Gamma_k = S_i \rho_k \bar{w}_{ni} \quad (2.19)$$

Similarly, an exact expression for the interfacial stress due to diffusion is provided. These terms physically represent transport phenomena caused by microscopic gradient on either side of the interface. Similar to the interface motion transfer, diffusion transfers can generally be modeled as the product of the interfacial area concentration and a mean interfacial flux. For momentum, the diffusion flux vector $\mathbf{j}_k = -\boldsymbol{\sigma}_k$, represents the general material stress tensor and can be decomposed into isotropic and deviatoric components, $\boldsymbol{\sigma}_k = -p_k \mathbf{I} + \boldsymbol{\tau}_k$. The diffusion and interfacial stress terms become

$$\nabla \cdot (g_k \boldsymbol{\sigma}_k) - \frac{1}{V} \int_{A_i} \boldsymbol{\sigma}_k \cdot \mathbf{n}_k dA = -\nabla \cdot (g_k p_k) + \bar{p}_{k,i} \nabla g_k + \nabla \cdot (g_k \boldsymbol{\tau}_k) + \mathbf{M}_k^d \quad (2.20)$$

where the deviatoric part of the interfacial stress \mathbf{M}_k^d , represents the effect of viscous drag caused by the relative motion of the phases on either side of the interface. Constitutive models for modeling this term are addressed in later sections. In principle the average interfacial pressure of can be modeled using $(\bar{p}_{k,i} - \bar{p}_{j,i}) = \sigma \bar{\kappa}$, where $\bar{\kappa}$ is the average curvature of the interface. However, for solid-liquid systems the assumption of mechanical equilibrium on the length scale of the control volume is generally valid (i.e. $\bar{p}_{k,i} = p_k = p$) and is used here [18,20,23,68].

For species, the flux vector is written in terms of Fick's first law, $\mathbf{j}_k = -\rho_k D_k \nabla C_k$, where D_k is the solute mass diffusivity. Similarly, the heat flux vector is written in terms of Fourier's law, $\mathbf{j}_k = -k_k \nabla T_k$, where k_k is the thermal conductivity. The interfacial transfer due to these fluxes can be evaluated using a small representative volume near the solid-liquid interface [4], shown in Figure 2. It is generally assumed that these fluxes can be approximated by the difference between the interfacial average and the volume-averaged quantities over some characteristic length. Hence, the interfacial mass transfer due to diffusion for species and heat are

$$\nabla \cdot (g_k \mathbf{s}_k) + \frac{1}{V} \int_{A_i} \mathbf{s}_k \cdot \mathbf{n}_k dA = \nabla \cdot (g_k \rho_k D_k \nabla C_k) + S_i \rho_k \frac{D_k}{\delta_i} (\bar{C}_{k,i} - C_k) \quad (2.21)$$

and

$$\nabla \cdot (g_k \mathbf{q}_k) + \frac{1}{V} \int_{A_i} \mathbf{q}_k \cdot \mathbf{n}_k dA = \nabla \cdot (g_k k_k \nabla T_k) + S_i \frac{k_k}{\delta_i^T} (\bar{T}_{k,i} - T_k) \quad (2.22)$$

where δ_i is the diffusion length characterizing the resistance to diffusion and is generally a complicated function of the microscopic phenomena. Its determination for equiaxed solidification requires a more formal analysis which is addressed in the application of a volume-averaged microsegregation model in Chapter 3. Applying these constitutive relationships to the general transport equation provides macroscale balance equations for mass, momentum, temperature, and species, summarized in Table 2.1. The interfacial transfer terms and balances are provided in Table 2.2.

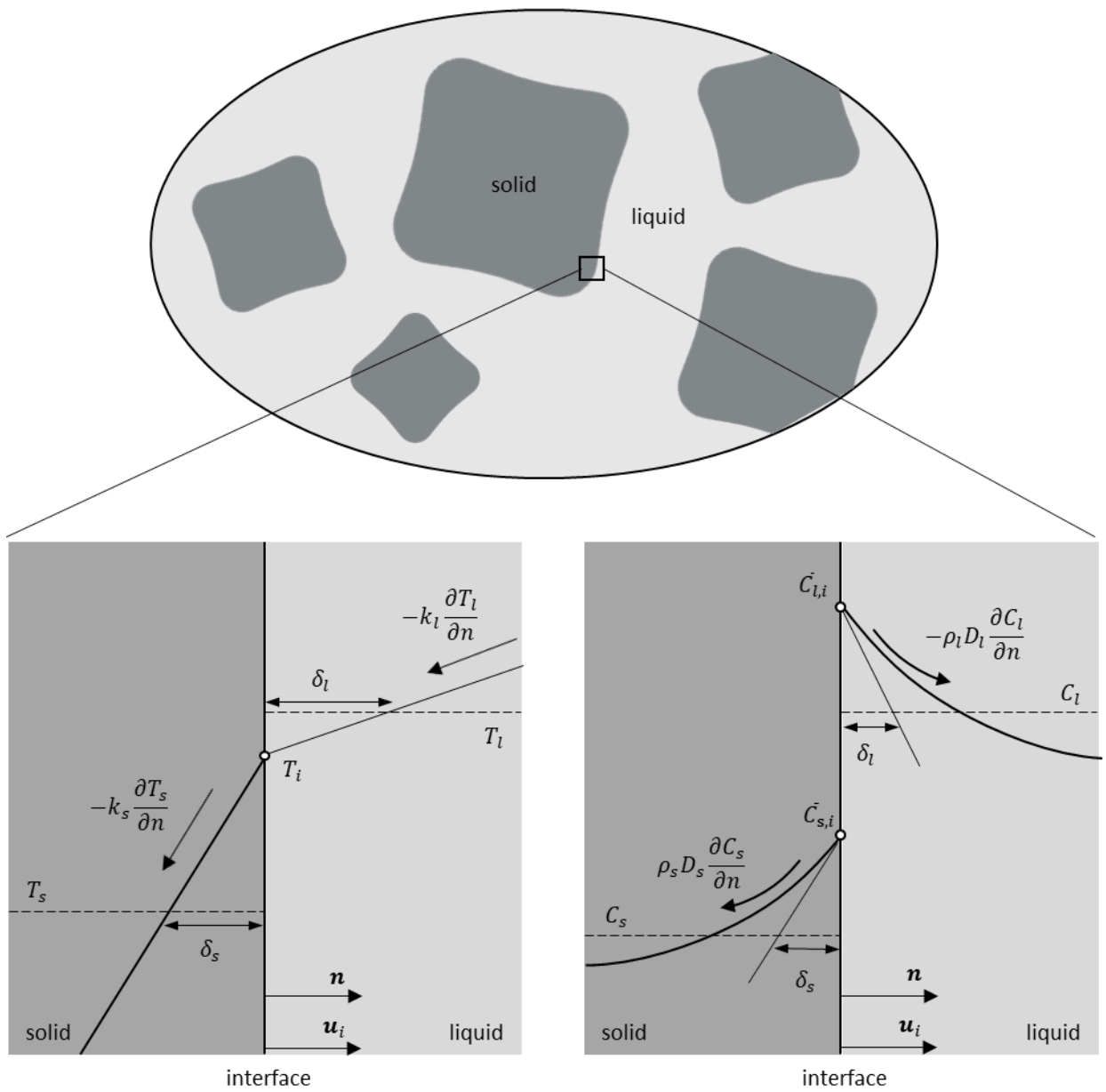


Figure 2.1: A schematic of the temperature and composition fluxes near the solid-liquid interface.

Table 2.1: Summary of volume-averaged balance equations

Quantity	Volume-Averaged Equations	Eqn.
Mass	$\frac{\partial}{\partial t}(g_k \rho_k) + \nabla \cdot (g_k \rho_k \mathbf{u}_k) = \Gamma_k$	(2.23)
Momentum	$\frac{\partial}{\partial t}(g_k \rho_k \mathbf{u}_k) + \nabla \cdot (g_k \rho_k \mathbf{u}_k \mathbf{u}_k) = \nabla \cdot (g_k \boldsymbol{\tau}_k) - g_k \nabla p + g_k \rho_k^B \mathbf{g} + \mathbf{M}_k$	(2.24)
Energy	$\frac{\partial}{\partial t}(g_k \rho_k h_k) + \nabla \cdot (g_k \rho_k \mathbf{u}_k h_k) = \nabla \cdot (g_k k_k \nabla T_k) + E_k$	(2.25)
Species	$\frac{\partial}{\partial t}(g_k \rho_k C_k^i) + \nabla \cdot (g_k \rho_k \mathbf{u}_k C_k^i) = \nabla \cdot (g_k \rho_k D_k^i \nabla C_k^i) + J_k$	(2.26)

Table 2.2: Summary of volume-averaged constitutive interfacial transfer relationships

Quantity	Interfacial Transfers	Eqn.
Mass	$\Gamma_k = S_i \rho_k \bar{w}_{ni}$	(2.27)
Momentum	$\mathbf{M}_k = \Gamma_k \bar{\mathbf{u}}_{k,i} + \mathbf{M}_k^d$	(2.28)
Energy	$E_k = \Gamma_k \bar{h}_{k,i} + S_i \frac{k_k}{\delta_i} (\bar{T}_{k,i} - T_k)$	(2.29)
Species	$J_k = \Gamma_k \bar{C}_{k,i} + S_i \rho_k \frac{D_k}{\delta_i} (\bar{C}_{k,i} - C_k)$	(2.30)

2.3 Continuum Mixture Model

Although widely adopted within the solidification modeling community, the formal averaging procedure completed in the previous section is not necessary to obtain volume-averaged conservation equations. Bennon and Incropera [20] obtained nearly identical equations using continuum theory, which suggests that if the phase is continuous within the control volume, the differential surface area dA_k and volume dV_k of the phase are equal to $g_k dA$ and $g_k dV$, respectively. Since the integrands are continuous and differentiable functions, the integral theorems of Leibnitz and Gauss can be applied to the microscale conservation equation,

$$\begin{aligned} \frac{\partial}{\partial t} \left(\frac{1}{V} \int_V \rho_k \phi_k dV_k \right) + \frac{1}{V} \int_V \nabla \cdot (\rho_k \mathbf{u}_k) dV_k &= \int_V \nabla \cdot (\mathbf{J}_k) dV_k \\ &+ \int_V S_k dV_k + \int_V \dot{R}_k dV \end{aligned} \quad (2.31)$$

and an expression identical to Eqn. (2.15) is obtained. Although this approach does not provide any insight into the mathematical representation of the interfacial transfer terms, \dot{R}_k , Bennon and Incropera [20] cast the conservation equations in terms of the mixture by summing the individual phase equations, and these terms cancel according to conservation ($\sum_k \dot{R}_k = 0$). Due to the relative simplicity of this method, it is the goal of the subsequent sections to derive mixture forms of the governing equations for mass, momentum, energy, and species to describe equiaxed solidification. These expressions will be derived from the summation of the multiphase volume-averaged conservation equations provided in Table 2.1.

A volumetric mixture variable is defined as the summation of the phase fraction and the phase quantity:

$$\phi = \sum_k g_k \phi_k \quad (2.32)$$

A similar expression is given for mass quantities by the additional consideration of the phase density:

$$\phi = \frac{1}{\rho} \sum_k \rho_k g_k \phi_k \quad (2.33)$$

where ρ is the mixture density:

$$\rho = \sum_k \rho_k g_k \quad (2.34)$$

An expression for the mixture velocity is obtained using $\phi = \mathbf{u}$ in Eqn. (2.33)

$$\mathbf{u} = \frac{1}{\rho} \sum_k \rho_k g_k \mathbf{u}_k \quad (2.35)$$

To facilitate the formulation of continuum mixture equations, a relationship for the summation of phase mass fluxes is used based on decomposing the advective term into contributions from the mean mixture motion and the relative phase motion:

$$\sum_k \rho_k g_k \mathbf{u}_k \phi_k = \rho \mathbf{u} \phi + \sum_k \rho_k g_k (\mathbf{u}_k - \mathbf{u})(\phi_k - \phi) \quad (2.36)$$

Here, $(\mathbf{u}_k - \mathbf{u})$ is commonly referred to as diffusion velocity, i.e., the velocity of phase k relative to the mass center of the mixture. In general, the solidification microstructure will consist of three distinct hydrodynamic phases: the solid grain, the interdendritic liquid, and the extradendritic liquid. The permeability of interdendritic structure is typically low enough that flow tends to move around the grain envelope until the grains coalesce into a rigid mush. Modeling the partitioning of liquid flow between inter- and extradendritic regions presents significant modeling difficulties. Although models exist that include these effects [19,35], the current model makes no attempt to do so. Instead, it is assumed the inter- and extradendritic liquid acts a single hydrodynamic phase ($\mathbf{u}_d = \mathbf{u}_e = \mathbf{u}_l$), which leads to the following mixture relationship:

$$\sum_k \rho_k g_k \mathbf{u}_k \phi_k = \rho \mathbf{u} \phi + \rho_s g_s (\mathbf{u}_s - \mathbf{u})(\phi_s - \phi) + \rho_l g_l (\mathbf{u}_l - \mathbf{u})(\phi_l - \phi) \quad (2.37)$$

This assumption will overpredict segregation in the slurry when the inter- and extra- dendritic liquid are at different compositions because the mass flux of enriched liquid away from the solid grain is over-estimated. However, it will generally have a negligible effect on segregation predictions due to the small supersaturations of the alloys investigated in this work, defined as the ratio of the difference between the inter- and extradendritic liquid compositions to the difference

between the interdendritic liquid and solid compositions. Despite this simplification of liquid flow partitioning, the influence of grain morphology will still be included through the combination of an effective viscosity model, a marker function m used to transition terms for the slurry and the rigid mush in the momentum equation, and the calculation of the relative solid-liquid velocity.

2.3.1 Conservation of Mass

The conservation of mass for phase k is expressed in Eqn. (2.23). Summing this equation over each phase,

$$\frac{\partial}{\partial t} \left(\sum_k \rho_k g_k \right) + \nabla \cdot \left(\sum_k \rho_k g_k \mathbf{u}_k \right) = \sum_k \Gamma_k \quad (2.38)$$

and utilizing the definitions of mixture density and the mixture velocity gives a continuity equation for the mixture:

$$\frac{\partial \rho}{\partial t} + \nabla \cdot (\rho \mathbf{u}) = 0 \quad (2.39)$$

Formulation of this mixture equation replaces the phase quantities with mixture quantities as the dependent variables of the partial differential equations used to describe macroscopic transport. In this example, the phase volume fraction is replaced with the mixture density. Thus, it is a requirement of the mixture method that the individual phase quantities can be obtained from some *ad hoc* relationships specified in terms of mixture quantities. For alloy solidification, relationships describing the phase fractions and compositions as a function of local temperature and composition are well-established based on analytical microsegregation models (e.g. lever rule and Scheil model), making these systems amenable to the mixture method. The assumptions made in obtaining such closure relationships are addressed in Chapter 3.

2.3.2 Conservation of Momentum

The conservation of momentum for phase k is expressed in Eqn. (2.24). Summing this equation over each phase,

$$\begin{aligned} \frac{\partial}{\partial t} \left(\sum_k \rho_k g_k \mathbf{u}_k \right) + \nabla \cdot \left(\sum_k \rho_k g_k \mathbf{u}_k \mathbf{u}_k \right) &= \nabla \cdot \left(\sum_k g_k \boldsymbol{\tau}_k \right) \\ &- \sum_k g_k \nabla p + \sum_k g_k \rho_k^B \mathbf{g} + \sum_k \mathbf{M}_k \end{aligned} \quad (2.40)$$

and applying the mixture relationships and interfacial balances gives a mixture momentum expression for an arbitrary multiphase system

$$\begin{aligned} \frac{\partial}{\partial t} (\rho \mathbf{u}) + \nabla \cdot (\rho \mathbf{u} \mathbf{u}) &= \nabla \cdot \left(\sum_k g_k \boldsymbol{\tau}_k \right) \\ &- \nabla \cdot \left(\sum_k \rho_k g_k (\mathbf{u}_k - \mathbf{u})(\mathbf{u}_k - \mathbf{u}) \right) - \nabla p + \rho^B \mathbf{g} \end{aligned} \quad (2.41)$$

The second term of the right-hand side originate from the viscous stress generated from the relative phase motion and therefore is sometimes referred to as the diffusion stress tensor. Under the assumption of the simplified hydrodynamic model used in this work, the solid and liquid diffusion velocities can be related by the relationship:

$$\rho_l g_l (\mathbf{u}_l - \mathbf{u}) + \rho_s g_s (\mathbf{u}_s - \mathbf{u}) = 0 \quad (2.42)$$

Substitution of Eqn. (2.42) into Eqn. (2.41) gives the following momentum equation for a solid-liquid mixture:

$$\begin{aligned} \frac{\partial}{\partial t} (\rho \mathbf{u}) + \nabla \cdot (\rho \mathbf{u} \mathbf{u}) &= \nabla \cdot (g_s \boldsymbol{\tau}_s + g_l \boldsymbol{\tau}_l) \\ &- \nabla \cdot \left(\rho \frac{\rho_s g_s}{\rho_l g_l} (\mathbf{u}_s - \mathbf{u})(\mathbf{u}_s - \mathbf{u}) \right) - \nabla p + \rho^B \mathbf{g} \end{aligned} \quad (2.43)$$

Consideration must be given to the treatment of the phase stress tensors ($g_s \boldsymbol{\tau}_s$, $g_l \boldsymbol{\tau}_l$) to account for the two flow regimes present during equiaxed solidification: the slurry and the rigid mush.

Slurry Regime

The general form of the macroscopic stress tensor for a Newtonian fluid is defined as

$$\boldsymbol{\tau}_k = \mu_k [\nabla \mathbf{u}_k + (\nabla \mathbf{u}_k)^T] - \frac{2}{3} \mu_k (\nabla \cdot \mathbf{u}_k) I \quad (2.44)$$

where I is the identity tensor. According to the scaling analysis of Vreeman et al. [44], contribution from the spatial variation in phase fraction is negligible compared to the velocity gradients in the slurry region, justifying expression of the gradient as $\nabla \mathbf{u}_k$ and not $\nabla g_k \mathbf{u}_k$ as in Prescott et al. [22]. While expressions for the effective viscosity of slurries have been widely studied dating back to the seminal theory of Einstein in 1908 [69], determination of the individual phase viscosities have been left to volume-averaged interpretations of the mixture relations. The derivation of the mixture stress tensor, $\boldsymbol{\tau}$, from the summation of the volume-averaged components leads to the creation of several algebraic source terms that do not have any direct physical meaning. Because the macroscopic viscosity of a slurry is an intrinsic property of the mixture, the mixture stress tensor can be specified directly in terms of mixture quantities:

$$\nabla \cdot (g_s \boldsymbol{\tau}_s + g_l \boldsymbol{\tau}_l) = \nabla \cdot \left(\mu [\nabla \mathbf{u} + (\nabla \mathbf{u})^T] - \frac{2}{3} \mu (\nabla \cdot \mathbf{u}) I \right) \quad (2.45)$$

where μ is the macroscopic mixture viscosity of the mixture which can be calculated according to:

$$\mu = \mu_l \left(1.0 - \min \left(\frac{g_g}{g_g^c}, 0.7 \right) \right)^{-2.5 g_g^c} \quad (2.46)$$

This is a modified form of the expression proposed by Ishii and Zuber [70], which only considers the linear portion of the dynamic viscosity curve for suspensions. Although many other forms of the mixture viscosity are available, it is necessary to avoid functions which approach an infinite viscosity during coalescence because such functions would remove any mixture velocity gradients near the packing interface. Substitution of Eqn. (2.45) into Eqn.(2.43) gives an expression for the momentum transport in the slurry regime:

$$\begin{aligned} \frac{\partial}{\partial t}(\rho \mathbf{u}) + \nabla \cdot (\rho \mathbf{u} \mathbf{u}) &= \nabla \cdot \left(\mu [\nabla \mathbf{u} + (\nabla \mathbf{u})^T] - \frac{2}{3} \mu (\nabla \cdot \mathbf{u}) \mathbf{I} \right) \\ &\quad - \nabla \cdot \left(\rho \frac{\rho_s g_s}{\rho_l g_l} (\mathbf{u}_s - \mathbf{u})(\mathbf{u}_s - \mathbf{u}) \right) - \nabla p + \rho^B \mathbf{g} \end{aligned} \quad (2.47)$$

Rigid Mush Regime

The previous assumptions regarding viscous stress are not valid in the rigid mush because the solid phase is nondeformable. Assuming that the liquid kinematic viscosity is locally invariant ($\nabla v_l = 0$) and the solid phase is rigid ($\nabla \cdot (\nabla \mathbf{u}_s) = 0$), the liquid stress tensor is defined as:

$$\nabla \cdot (g_l \boldsymbol{\tau}_l) = \rho v_l [\nabla \mathbf{u} + (\nabla \mathbf{u})^T] - \frac{2}{3} \rho v_l (\nabla \cdot \mathbf{u}) \mathbf{I}. \quad (2.48)$$

The solid stress tensor is obtained by rearranging Eqn. (2.24) for the solid phase

$$\nabla \cdot (g_s \boldsymbol{\tau}_s) = \frac{\partial}{\partial t} (\rho_s g_s \mathbf{u}_s) + \nabla \cdot (\rho_s g_s \mathbf{u}_s \mathbf{u}_s) + g_s \nabla p - g_s \rho_s^B \mathbf{g} - \mathbf{M}_l^d. \quad (2.49)$$

The first two terms on the right-hand side are zero in a stationary bed and negligible in a moving bed. The interfacial drag is modeled according to Darcy's Law:

$$\mathbf{M}_l^d = -g_l^2 \frac{\mu_l}{K} (\mathbf{u}_l - \mathbf{u}_s) \quad (2.50)$$

where K is the permeability of the structure, often determined from the Blake-Kozeny model as a function of some characteristic length scale λ :

$$K = \frac{\lambda^2}{180} \frac{g_l^3}{(1 - g_l)^2}. \quad (2.51)$$

Applying the mixture relationship to the relative velocity in the drag term gives

$$\nabla \cdot (g_s \boldsymbol{\tau}_s) = g_s \nabla p - g_s \rho_s^B \mathbf{g} - g_l \rho \frac{v_l}{K} (\mathbf{u} - \mathbf{u}_s) \quad (2.52)$$

Substituting the divergence of the phase stress tensors into Eqn. (2.43) gives a continuum mixture relationship for the flow through the rigid mush:

$$\begin{aligned}
\frac{\partial}{\partial t}(\rho \mathbf{u}) + \nabla \cdot (\rho \mathbf{u} \mathbf{u}) &= \nabla \cdot \left(\rho v_l [\nabla \mathbf{u} + (\nabla \mathbf{u})^T] - \frac{2}{3} \rho v_l (\nabla \cdot \mathbf{u}) \mathbf{I} \right) \\
&\quad - \nabla \cdot \left(\rho \frac{\rho_s g_s}{\rho_l g_l} (\mathbf{u}_s - \mathbf{u})(\mathbf{u}_s - \mathbf{u}) \right) - g_l \nabla p + g_l \rho_l^B \mathbf{g} \\
&\quad - g_l \rho \frac{v_l}{K} (\mathbf{u} - \mathbf{u}_s)
\end{aligned} \tag{2.53}$$

Since one of the primary objectives of the continuum mixture model is to develop equations amenable to numerical procedures for single phase flow, a final step must be taken to prevent the scaling of the pressure gradient by g_l in Eqn. (2.53). When the solid fraction is sufficiently high to form a continuous structure, it is assumed that the only significant terms in Eqn. (2.53) are those associated with the pressure gradient, the liquid buoyancy force, and the interfacial drag force.

$$g_l \nabla p - g_l \rho_l^B \mathbf{g} - g_l \rho \frac{v_l}{K} (\mathbf{u} - \mathbf{u}_s) = 0 \tag{2.54}$$

Dividing these terms by g_l does not change their identity with zero and the continuum mixture momentum equation for the rigid mush becomes:

$$\begin{aligned}
\frac{\partial}{\partial t}(\rho \mathbf{u}) + \nabla \cdot (\rho \mathbf{u} \mathbf{u}) &= \nabla \cdot \left(\rho v_l [\nabla \mathbf{u} + (\nabla \mathbf{u})^T] - \frac{2}{3} \rho v_l (\nabla \cdot \mathbf{u}) \mathbf{I} \right) \\
&\quad - \nabla \cdot \left(\rho \frac{\rho_s g_s}{\rho_l g_l} (\mathbf{u}_s - \mathbf{u})(\mathbf{u}_s - \mathbf{u}) \right) - \nabla p + \rho_l^B \mathbf{g} - \rho \frac{v_l}{K} (\mathbf{u} - \mathbf{u}_s)
\end{aligned} \tag{2.55}$$

Single Domain Model

Comparing the momentum conservation in the slurry regime and rigid mush regime, a single momentum equation is attainable through the specification of an effective viscosity μ_{eff} and effective buoyant density ρ_{eff}^B . These effective properties can be formulated as linear combinations of each flow regime value following the definition of a marker function m , which indicates the local condition of the solid structure. A discrete transition model is used in this work, where the marker function is defined as:

$$m(\mathbf{x}, t) = \begin{cases} 1 & \text{if } \mathbf{x} \text{ is in rigid mush at time } t \\ 0 & \text{else} \end{cases} \tag{2.56}$$

An iterative rules-based method for tracking the local position of the packing interface on a numerical grid similar to Vreeman et al. [43] is applied. This method states that a point in space is packed if the local grain fraction is greater than or equal to the critical packing fraction, i.e. $g_g(\mathbf{x}, t) \geq g_g^c(\mathbf{x}, t)$, and has a neighboring point that is also packed. Therefore, the propagation of the packing front from some initial point or collection of points, generally prescribed as a boundary of the numerical domain, is physically representative of the evolution of the packing front during equiaxed solidification. Using this marker method, the effective viscosity and density are defined as:

$$\mu_{eff} = (1 - m)\mu + m\rho v_l \quad (2.57)$$

and

$$\rho_{eff}^B = (1 - m)(g_s \rho_s^B + g_l \rho_l^B) + m\rho_l^B \quad (2.58)$$

where the densities are obtained by the Boussinesq approximation including both thermal and solutal effects:

$$\rho_l^B = \rho_l [1 - \beta_{T,l}(T - T_o) - \beta_{c,l}(C_l - C_{l,o})] \quad (2.59)$$

and

$$\rho_s^B = \rho_s [1 - \beta_{T,s}(T - T_o) - \beta_{c,s}(C_s - C_{s,o})] \quad (2.60)$$

In these expressions, β_T and β_c are the thermal and solutal expansion coefficients, and T_o and $C_{k,o}$ are the reference temperatures and compositions.

Substituting and collection of similar terms gives a single equation for momentum transport in equiaxed and columnar solidification, simultaneously modeling transport of mobile grains in the slurry and liquid flow in the rigid mush:

$$\begin{aligned} \frac{\partial}{\partial t}(\rho \mathbf{u} \mathbf{u}) + \nabla \cdot (\rho \mathbf{u} \mathbf{u}) &= \nabla \cdot \left(\mu_{eff} [\nabla \mathbf{u} + (\nabla \mathbf{u})^T] - \frac{2}{3} \mu_{eff} (\nabla \cdot \mathbf{u}) \mathbf{I} \right) \\ &\quad - \nabla \cdot \left(\rho \frac{\rho_s g_s}{\rho_l g_l} (\mathbf{u}_s - \mathbf{u})(\mathbf{u}_s - \mathbf{u}) \right) - \nabla p + \rho_{eff}^B \mathbf{g} \\ &\quad - m\rho \frac{v_l}{K} (\mathbf{u} - \mathbf{u}_s) \end{aligned} \quad (2.61)$$

Momentum Closure

Closure of mixture momentum model requires an expression for the solid velocity. Although empirical correlations exist for the settling velocity of dispersed solid in a suspension, it is more common to formulate relationships in terms of the relative solid-liquid velocity, i.e.

$$\mathbf{u}_r = \mathbf{u}_s - \mathbf{u}_l \quad (2.62)$$

The one-dimensional equation of motion for a single porous grain in a fluid under gravity is:

$$\rho_g^B V_g \frac{d}{dt} (\mathbf{u}_s - \mathbf{u}_l) = V_g (\rho_g^B - \rho_l^B) \mathbf{g} + \frac{1}{2} \rho_l^B A_g C_D |\mathbf{u}_s - \mathbf{u}_l| (\mathbf{u}_s - \mathbf{u}_l) \quad (2.63)$$

where V_g is the volume of the grain, A_g is the surface area of the grain, and C_D the drag coefficient. The left-hand side represents the acceleration of the grain relative to the liquid, while the right-hand side represents the buoyancy and drag forces acting on the grain. A scaling analysis shows the relative importance of each term in Eqn. (2.63):

$$\underbrace{\frac{\rho_g^B}{(\rho_g^B - \rho_l^B)} \frac{u_r}{gt}}_{\text{inertia}} \sim \underbrace{1}_{\text{buoyancy}} \sim \underbrace{\frac{\rho_l^B}{(\rho_g^B - \rho_l^B)} \frac{A_g C_D u_r^2}{V_g g}}_{\text{drag}} \quad (2.64)$$

The grain will reach a constant terminal relative velocity when the buoyancy force is balanced by drag, such that:

$$u_r \sim \sqrt{\frac{(\rho_g^B - \rho_l^B) V_g g}{\rho_l^B A_g C_D}} \quad (2.65)$$

If it can be shown that this condition is attained over relatively short time scales, then the inertial term can be neglected altogether. The terminal velocity is attained at times when the inertial term is much smaller than the buoyancy term, or

$$t \ll \rho_g^B \sqrt{\frac{V_g}{\rho_l^B (\rho_g^B - \rho_l^B) g A_g C_D}} \approx \sqrt{\frac{\rho_l^B d_g}{(\rho_g^B - \rho_l^B) g C_D}} \quad (2.66)$$

For equiaxed solidification in DC casting, these terms have the following approximate orders of magnitude $\rho_l^B \approx \mathcal{O}(1000 \text{ kg m}^{-3})$, $\rho_g^B - \rho_l^B \approx \mathcal{O}(100 \text{ kg m}^{-3})$, $g \approx \mathcal{O}(10 \text{ m s}^{-2})$,

$C_D \approx \mathcal{O}(100)$, $d_g \approx \mathcal{O}(1 \times 10^{-4} \text{ m})$. The resulting characteristic time to reach terminal velocity is $t \approx \mathcal{O}(0.01 \text{ s})$ for 100 μm spherical grains in the dilute slurry, and therefore, acceleration can be safely neglected. Introducing the grain Reynolds number, which represents the ratio of inertial and viscous forces on the particle due to the relative velocity:

$$Re_g = \frac{\rho_l d_g |\mathbf{u}_s - \mathbf{u}_l|}{\mu_l} \quad (2.67)$$

and assuming spherical grains ($A_g/V_g = 3/2d_g$), the relative velocity for a single grain can be expressed as:

$$(\mathbf{u}_s - \mathbf{u}_l) = \frac{4(\rho_g^B - \rho_l^B)d_g^2}{3C_D Re_g \mu_l} \mathbf{g} \quad (2.68)$$

where relative density can also be specified defined in terms of the internal solid fraction:

$$\rho_g^B - \rho_l^B = g_{s,i}(\rho_s^B - \rho_l^B) \quad (2.69)$$

In the slurry, viscous interactions of multiple grains will tend to reduce the relative velocity by a factor equal to the volume of surrounding liquid, resulting in the following general expression for the relative velocity:

$$(\mathbf{u}_s - \mathbf{u}_l) = \frac{4(1 - g_g)g_{s,i}(\rho_s^B - \rho_l^B)d_g^2}{3C_D Re_g \mu_l} \mathbf{g} \quad (2.70)$$

While many different models have been proposed for modeling drag in suspensions, one similarity is that each can be arranged as an expression of $C_D Re_g$. In Chapter 6, different $C_D Re_g$ relationships for popular drag models used in equiaxed solidification models are introduced and compared for an isothermal settling experiment. Using the mixture relationships and the marker function, an expression for the solid velocity in the single domain model is:

$$\mathbf{u}_s = (1 - m) \left[\mathbf{u} + \frac{\rho_l g_l}{\rho} \mathbf{u}_r \right] + m \mathbf{u}_{ref} \quad (2.71)$$

Although grain nucleation model and growth models exist for calculating the grain diameter, these models generally depend on highly uncertain nucleation and growth kinetics parameters. Since the

average grain size at the end of solidification, d_g^f , is generally well-known for a particular casting process and is an easy to measure quantity (via optical microscopy), it is used to calculate the local grain diameter appearing in the relative velocity expression.

$$d_g = \left(\frac{g_g}{g_g^c} \right)^{\frac{1}{3}} d_g^f \quad (2.72)$$

Scaling the local grain fraction by the grain packing fraction assumes that the grain diameter observed in post-mortem metallographic analysis is approximately equal to the grain diameter at packing.

2.3.3 Conservation of Energy

Assuming local thermal equilibrium ($T_k = T$), the enthalpy conservation equation for phase k is

$$\frac{\partial}{\partial t} (\rho_k g_k h_k) + \nabla \cdot (\rho_k g_k \mathbf{u}_k h_k) = \nabla \cdot (g_k k_k \nabla T) + \dot{E}_k \quad (2.73)$$

The last term represents the energy exchange rate between phases which sum to zero according to conservation of energy, $\sum_k \dot{E}_k = 0$. The general expression for the enthalpy of phase k is:

$$h_k = h_k^o + \int_{T^o}^T c_k dT \quad (2.74)$$

where h_k^o is the reference enthalpy at the reference temperature T^o . The reference temperature $T^o = 0 \text{ K}$ can be used so that $h_s^o = 0$ and $h_l^o = L_f$, where L_f is the latent heat of phase change. Taking the specific heats as constants, the following expressions are obtained for the solid and liquid phase enthalpies:

$$h_s = c_{p,s} T \quad (2.75)$$

and

$$h_l = c_{p,l} T + L_f \quad (2.76)$$

It is noted that both Bennon and Incropera and Wang and Beckermann [71] previously used the eutectic temperature as a reference for the liquid (i.e. $T^o = T_{eut}$) which results in $h_l^o = c_{p,s}T_{eut} + L_f|_{T_{eut}}$ for the reference enthalpy of the liquid, where $L_f|_{T_{eut}}$ is the latent heat evaluated at the eutectic temperature. Since all terms related to the reference state are constants, the change in reference temperature can be accounted for using a modified form of the latent heat without any loss of generality of the current mixture method:

$$L_f = (c_{p,s} - c_{p,l})T_{eut} + L_f|_{T_{eut}} \quad (2.77)$$

Although this form of the latent heat definition is not implemented in this work, the nature of these additional terms appearing in previous studies are clarified here and can be applied if desired.

Summing (2.73) over both phases,

$$\frac{\partial}{\partial t}(\rho_s g_s h_s + \rho_l g_l h_l) + \nabla \cdot (\rho_s g_s \mathbf{u}_s h_s + \rho_l g_l \mathbf{u}_l h_l) = \nabla \cdot ((g_l k_l + g_s k_s) \nabla T) \quad (2.78)$$

and substituting the definition of phase enthalpies with rearrangement gives:

$$\begin{aligned} \frac{\partial}{\partial t}(\rho c_p T) + \nabla \cdot ((\rho_s g_s \mathbf{u}_s c_{p,s} + \rho_l g_l \mathbf{u}_l c_{p,l}) T) &= \nabla \cdot (k \nabla T) \\ &+ \left[\frac{\partial}{\partial t} (g_s \rho_s) + \nabla \cdot (g_s \rho_s \mathbf{u}_s) \right] L_f \end{aligned} \quad (2.79)$$

where the mixture specific heat capacity c_p and mixture thermal conductivity k are defined as:

$$c_p = \frac{1}{\rho} \sum_k \rho_k g_k c_{p,k} \quad (2.80)$$

and

$$k = \sum_k g_k k_k \quad (2.81)$$

Eqn. (2.79) is identical to the form specified for the multiphase model developed by Wang and Beckermann when the definition of latent heat is replaced with Eqn. (2.77). Finally, using the mixture relationship for the average liquid velocity ($\rho_l g_l \mathbf{u}_l = \rho \mathbf{u} - \rho_s g_s \mathbf{u}_s$) gives the following mixture energy equation specified in terms of temperature:

$$\begin{aligned} \frac{\partial}{\partial t}(\rho c T) + \nabla \cdot (\rho \mathbf{u} c_{p,l} T) &= \nabla \cdot (k \nabla T) + \nabla \cdot (\rho_s g_s \mathbf{u}_s (c_{p,l} - c_{p,s}) T) \\ &+ \left[\frac{\partial}{\partial t}(\rho_s g_s) + \nabla \cdot (\rho_s g_s \mathbf{u}_s) \right] L_f \end{aligned} \quad (2.82)$$

2.3.4 Conservation of Species

Two different microsegregation models are used in this work to describe the evolution of phase fractions and compositions: (1) a volume-averaged microsegregation model which includes the effect of finite diffusion in both the solid and liquid phases, and (2) a simplified analytical model which includes finite diffusion in the solid, but considers the liquid to be solutally well-mixed. For the volume-averaged microsegregation model, the phase composition equations must be calculated in their multiphase form provided in Table 2.1, and so a conservation equation for the mixture composition is not needed. Therefore, the form of the solute conservation equation will depend on the chosen microsegregation model.

Several insights can be used to simplify modeling the composition field. First, the solutal Péclet number ($Pe_c = Lu/D$), which is the ratio of the solutal advection and diffusion rates over the characteristic length scale L , is generally large enough to justify neglecting the macroscopic solute diffusion terms altogether [4]. Several researchers have adopted this simplified approach without any change to the numerical predictions of the model. This is true even for solutions of columnar solidification on relatively fine grids (about 0.25 mm) [72]. The multiphase solute conservation equations for the solid and liquid become

$$\frac{\partial}{\partial t}(g_s \rho_s C_s) + \nabla \cdot (g_s \rho_s \mathbf{u}_s C_s) = \Gamma_s k_p \bar{C}_{l,i} + \frac{S_{s,l} \rho_s D_s}{\delta_s} (k_p \bar{C}_{l,i} - C_s) \quad (2.83)$$

and

$$\frac{\partial}{\partial t}(g_l \rho_l C_l) + \nabla \cdot (g_l \rho_l \mathbf{u}_l C_l) = - \left[\Gamma_s k_p \bar{C}_{l,i} + \frac{S_{s,l} \rho_s D_s}{\delta_s} (k_p \bar{C}_{l,i} - C_s) \right] \quad (2.84)$$

where the interfacial area concentration of the solid-liquid interface is $S_{s,l}$ and the solid composition at the interface is $\bar{C}_{s,i} = k_p \bar{C}_{l,i}$. Because the solutal interfacial transfer terms must sum to zero (i.e. $J_s = -J_l$), only the solid transfers are used to prevent over-constraining the problem. If the liquid is treated as two distinct hydrodynamic phases, an additional advection

source term accounting for the flow partitioning of inter- and extra- dendritic liquid is required in Eqn. (2.84). Summing these multiphase species equations gives:

$$\frac{\partial}{\partial t}(\rho C) + \nabla \cdot (\rho_s g_s \mathbf{u}_s C_s + \rho_l g_l \mathbf{u}_l C_l) = 0 \quad (2.85)$$

Although the mixture relationship for the summation of advection terms, i.e. Eqn. (2.37), can be applied here, Vreeman and Incropera [73] showed that the composition predictions are sensitive to the numerical discretization of the advection source term in this method. In the original work of Bennon and Incropera [20], the mixture advection term was discretized by upwind differencing, while the advection source term was discretized by central differencing causing erroneous segregation predictions. To avoid confusion between mathematical formulation and numerical discretization, the advection terms for each phase are left in their original form. Although this form of the mixture species equation requires an explicit time discretization, and is therefore only conditionally stable, the time steps needed to resolve the time accuracy of the solution are generally small enough that this will not affect the solution [40,74,75]. Features of the numerical methods used to solve the phase fluxes appearing in each solute conservation equation are discussed in detail in Chapter 4.

2.4 Summary of Equations

The system of equations for the continuum mixture model are summarized in Table 2.3 and Table 2.4. However, relationships are required for the phase fractions (g_s, g_l) , and phase compositions (C_s, C_l) to close the mathematical model. In the next chapter, two different microsegregation models with varying degrees of complexity are formulated to provide expressions for these phase quantities.

Table 2.3: Summary of continuum mixture conservation equations

Quantity	Mixture Conservation Equation	Eqn.
Mass	$\frac{\partial \rho}{\partial t} + \nabla \cdot (\rho \mathbf{u}) = 0$	(2.39)
Momentum	$\frac{\partial}{\partial t} (\rho \mathbf{u} \mathbf{u}) + \nabla \cdot (\rho \mathbf{u} \mathbf{u}) = \nabla \cdot \left(\mu_{eff} [\nabla \mathbf{u} + (\nabla \mathbf{u})^T] - \frac{2}{3} \mu_{eff} (\nabla \cdot \mathbf{u}) \mathbf{I} \right)$ $- \nabla \cdot \left(\rho \frac{\rho_s g_s}{\rho_l g_l} (\mathbf{u}_s - \mathbf{u})(\mathbf{u}_s - \mathbf{u}) \right)$ $- \nabla p + \rho_{eff}^B \mathbf{g} - m \frac{v_l}{K} \rho (\mathbf{u} - \mathbf{u}_s)$	(2.61)
Energy	$\frac{\partial}{\partial t} (\rho c T) + \nabla \cdot (\rho \mathbf{u} c_{p,l} T) = \nabla \cdot (k \nabla T) + \nabla \cdot (\rho_s g_s \mathbf{u}_s (c_{p,l} - c_{p,s}) T)$ $+ \left[\frac{\partial}{\partial t} (\rho_s g_s) + \nabla \cdot (\rho_s g_s \mathbf{u}_s) \right] L_f$	(2.82)
Species	$\frac{\partial}{\partial t} (\rho C) + \nabla \cdot (\rho_s g_s \mathbf{u}_s C_s + \rho_l g_l \mathbf{u}_l C_l) = 0$	(2.85)

Table 2.4: Summary of hydrodynamic relationships used in mixture momentum model

Property	Relationship	Eqn.
Effective viscosity	$\mu_{eff} = (1 - m)\mu + m\rho v_l$	(2.57)
Mixture viscosity	$\mu = \mu_l \left(1.0 - \min \left(\frac{g_g}{g_g^c}, 0.7 \right) \right)^{-2.5 g_g^c}$	(2.46)
Solid density (buoyancy)	$\rho_s^B = \rho_s [1 - \beta_{T,s}(T - T_o) - \beta_{c,s}(C_s - C_{s,o})]$	(2.59)
Liquid density (buoyancy)	$\rho_l^B = \rho_l [1 - \beta_{T,l}(T - T_o) - \beta_{c,l}(C_l - C_{l,o})]$	(2.60)
Effective density (buoyancy)	$\rho_{eff}^B = (1 - m)(g_s \rho_s^B + g_l \rho_l^B) + m \rho_l^B$	(2.58)
Permeability	$K = \frac{\lambda^2}{180} \frac{g_l^3}{(1 - g_l)^2}$	(2.51)
Grain diameter	$d_g = \left(\frac{g_g}{g_g^c} \right)^{\frac{1}{3}} d_g^f$	(2.72)
Solid velocity	$\mathbf{u}_s = (1 - m) \left[\mathbf{u} + \frac{\rho_l g_l}{\rho} \mathbf{u}_r \right] + m \mathbf{u}_{ref}$	(2.71)
Relative velocity	$\mathbf{u}_r = \frac{4(1 - g_g) g_{s,i} (\rho_s^B - \rho_l^B) d_g^2}{3 C_D Re_g \mu_l} \mathbf{g}$	(2.70)

3. MICROSEGREGATION MODEL

In this chapter, microsegregation models are developed to provide closure to the macroscale equations formulated in the previous chapter. It is desirable for these microsegregation models to account for the various solute profiles that can develop due to the interaction of solute rejection during solidification with solute diffusion in both the liquid and solid phases. A scaling analysis performed by Dantzig and Rappaz [4] showed that interdendritic liquid can be safely assumed as well-mixed over a wide range of solidification conditions. However, it is not yet clear if consideration of finite diffusion in the solid and extradendritic liquid are required to obtain reasonable predictions of macroscale transport during equiaxed solidification. Towards this understanding, two different microsegregation models are formulated in this chapter. The first is an analytical model which accounts for finite diffusion in the solid phase but assumes the extradendritic liquid to be well-mixed. This model is based on the work of Clyne and Kurz [66] and is extended to account for different solid and liquid densities in a conservative manner. The second is a volume-averaged model for equiaxed dendrites which accounts for finite diffusion in both the solid and extradendritic liquid. This model is based on the original work of Wang and Beckermann [67] but is applied here using interfacial closure relationships which are easier to implement into standard numerical procedures. In particular, the complicated nucleation models are avoided altogether by assuming a constant grain number density (n) during solidification. The nucleation and growth of an equiaxed dendrite is approximated as a function of the local grain volume fraction (g_g), the initial grain radius during nucleation (R_o), and the final grain radius at the end of solidification (R_f). This model is verified against the more complicated approach [67] for the solidification of an Al-5wt.%Si alloy based on the case proposed by Rappaz and Thevoz [76].

3.1 Analytical Microsegregation Model

Assuming thermal equilibrium (i.e. $T_k = \bar{T}_{k,i} = T$) and a solutally well-mixed liquid (i.e. $C_l = \bar{C}_{l,i}$) on the length scale of the representative volume implies that the liquidus surface of the equilibrium phase diagram (see Figure 1.2) provides the relationship between the liquid composition and temperature:

$$T = T_m + m_{liq}C_l \quad (3.1)$$

The fundamental requirement for closure of this microsegregation model is a relationship for the liquid composition as a function of the local solid volume fraction, i.e. $C_l = f(g_s)$, which is derived in this section using the same approach as Clyne and Kurz [66]. The mixture composition in the representative volume is:

$$\rho C = \rho_s g_s C_s + \rho_l g_l C_l \quad (3.2)$$

In the case of a uniform solid morphology and constant phase densities, Eqn. (3.3) can be written as:

$$\rho C = \rho_s \int_0^{g_s} C_s d\theta + \rho_l g_l C_l \quad (3.3)$$

where θ is a place-holder for integration [66]. The time derivative can be expressed as

$$\frac{\partial}{\partial t}(\rho C) = \rho_s k_p C_l \frac{dg_s}{dt} + \rho_s \int_0^{g_s} \frac{\partial C_s}{\partial t} d\theta + \rho_l \frac{\partial}{\partial t}(g_l C_l) \quad (3.4)$$

where the second term on the right-hand side is the solute “back diffusion” rate. This term can be represented in the following manner

$$\rho_s \int_0^{g_s} \frac{\partial C_s}{\partial t} d\theta = \beta \rho_s g_s k_p \frac{\partial C_l}{\partial t} \quad (3.5)$$

where k_p is the equilibrium partition coefficient and β is the “back diffusion” parameter in the range $0 \leq \beta \leq 1$. This parameter allows for a simplified treatment of solute diffusion into the solid phase between the limits of zero back diffusion ($\beta = 0$, the Scheil assumption) and complete back diffusion ($\beta = 1$, the lever rule). Substitution of Eqn. (3.5) into Eqn. (3.4) with rearrangement gives:

$$\frac{d}{dt}(\rho C) = \rho_s k_p C_l \frac{dg_s}{dt} + \beta g_s \rho_s k_p \frac{dC_l}{dt} + \rho_l C_l \frac{dg_l}{dt} + g_l \rho_l \frac{dC_l}{dt} \quad (3.6)$$

At this point, the Clyne and Kurz model [66] assumed equal solid and liquid densities to simplify the resulting expression for the solute concentration in the liquid. However, this assumption leads to discrepancies between phase volume fractions and phase mass fractions when the solid and liquid densities are different, a situation that is required for calculating shrinkage induced flow in the macroscale transport model. Therefore, the assumption of equal phase densities is relaxed by expanding of the time derivative of the left-hand side of Eqn. (3.6):

$$\rho \frac{dC}{dt} + C \frac{d\rho}{dt} = \rho_s k_p C_l \frac{dg_s}{dt} + \beta g_s \rho_s k_p \frac{dC_l}{dt} + \rho_l C_l \frac{dg_l}{dt} + g_l \rho_l \frac{dC_l}{dt} \quad (3.7)$$

The first term in Eqn. (3.7) is zero due to conservation of the mixture species during phase change in a closed system, however the second term is nonzero due the varying mixture density during solidification. Using the mixture relationship for density (i.e. $\rho = \rho_s g_s + \rho_l g_l$) and the conservation of volume (i.e. $dg_s/dt = -dg_l/dt$), the following expression is obtained after rearrangement:

$$\frac{dg_s}{\rho_l - (\rho_l - \rho_s \beta k_p) g_s} = \frac{dC_l}{C(\rho_s - \rho_l) + [\rho_l - \rho_s k_p] C_l} \quad (3.8)$$

Both sides of this equation can be integrated using the identity:

$$\int_{x_1}^{x_2} \frac{dx}{a + bx} = \frac{1}{b} \left[\ln \left(1 + \frac{bx_2}{a} \right) - \ln \left(1 + \frac{bx_1}{a} \right) \right] \quad (3.9)$$

with the definite integral limits ($x_1 = 0, x_2 = g_s$) for the left-hand side and ($x_1 = C, x_2 = C_l$) for right-hand side. Solving the integrand in terms of the liquid composition with rearrangement gives:

$$C_l = C \left[\left(\frac{\lambda}{(1 - k_p^*)} + 1 \right) \left[1 - (1 - k_p^* \beta) g_s \right]^{\frac{k_p^* - 1}{1 - k_p^* \beta}} - \frac{\lambda}{(1 - k_p^*)} \right] \quad (3.10)$$

where k_p^* is the mass-weighted partition coefficient:

$$k_p^* = \frac{\rho_s}{\rho_l} k_p \quad (3.11)$$

and λ is the shrinkage coefficient:

$$\lambda = \frac{\rho_s - \rho_l}{\rho_l} \quad (3.12)$$

Substitution of Eqn. (3.10) into Eqn. (3.1) with rearrangement provides an expression for the solid volume fraction as a function of the local temperature:

$$g_s = \frac{1}{(1 - k_p^* \beta)} \left[1 - \left(\frac{(T - T_m)(1 - k_p^*) + \lambda m_l C}{m_l C (1 - k_p^* + \lambda)} \right)^{\frac{1 - k_p^* \beta}{k_p^* - 1}} \right] \quad (3.13)$$

This equation recovers the Clyne and Kurz model [66] for $\rho_s = \rho_l$, Scheil assumption when $\rho_s = \rho_l$ and $\beta = 0$, and the lever rule when $\rho_s \neq \rho_l$ and $\beta = 1$. Figure 3.1 compares the solid volume fraction calculated using the Eqn. (3.13) and liquid composition using Eqn. (3.10) for an Al-4.5 wt% Cu alloy. The dotted lines indicate the correction in volume fraction due to unequal phase densities.

3.1.1 Extension to Multicomponent Solidification

A major advantage of this the analytical microsegregation model is its simple extension to multicomponent solidification of dilute alloys. For most dilute alloys, the liquidus surface can be reasonably be approximated as the summation of the binary liquidus lines:

$$T = T_m + \sum_{i=1}^n m_l^i C_l^i \quad (3.14)$$

where m_l^i is liquidus slope of species i and C_l^i is the liquid composition of species i . Recognizing the properties of summations, the local solid fraction expression provided in (3.13) may be used for multicomponent systems by replacing the effective partition coefficient k_p^* and $m_l C$ term with the summation of each constituent, i.e.

$$k_p^* = \frac{\rho_s}{\rho_l} \sum_{i=1}^n k_p^i \quad (3.15)$$

and

$$m_l C = \sum_{i=1}^n m_i^i C^i \quad (3.16)$$

Figure 3.2 compares the solid fraction and copper composition of the liquid for aluminum alloy AA7050. The partition coefficients and liquidus slopes were taken from Fezi et al. [48], determined using the thermodynamic database program ThermocalcTM with the TCAL1 database. In the case of this commercial wrought alloy, the incorporation of shrinkage into microsegregation model has an insignificant effect on the solidification curve and liquid composition evolution. However, properly accounting for the limited diffusion in the solid phase significantly increases the alloy freezing range and the enrichment of the liquid at the end of solidification where shrinkage driven flow can significantly affect the macrosegregation.

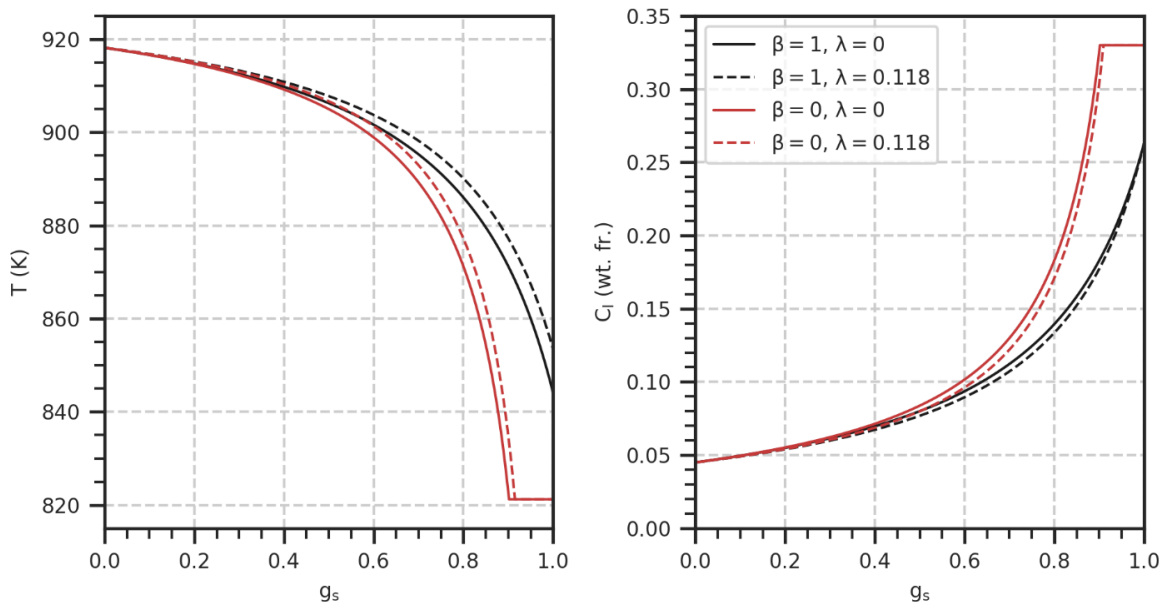


Figure 3.1: Computed temperature vs. solid volume fraction curves (left) and the corresponding liquid composition curves (right) for an Al-4.5 wt% Cu alloy where $\beta = 1, \lambda = 0.118$ is the lever rule and $\beta = 0, \lambda = 0$ is the Gulliver-Scheil equation.

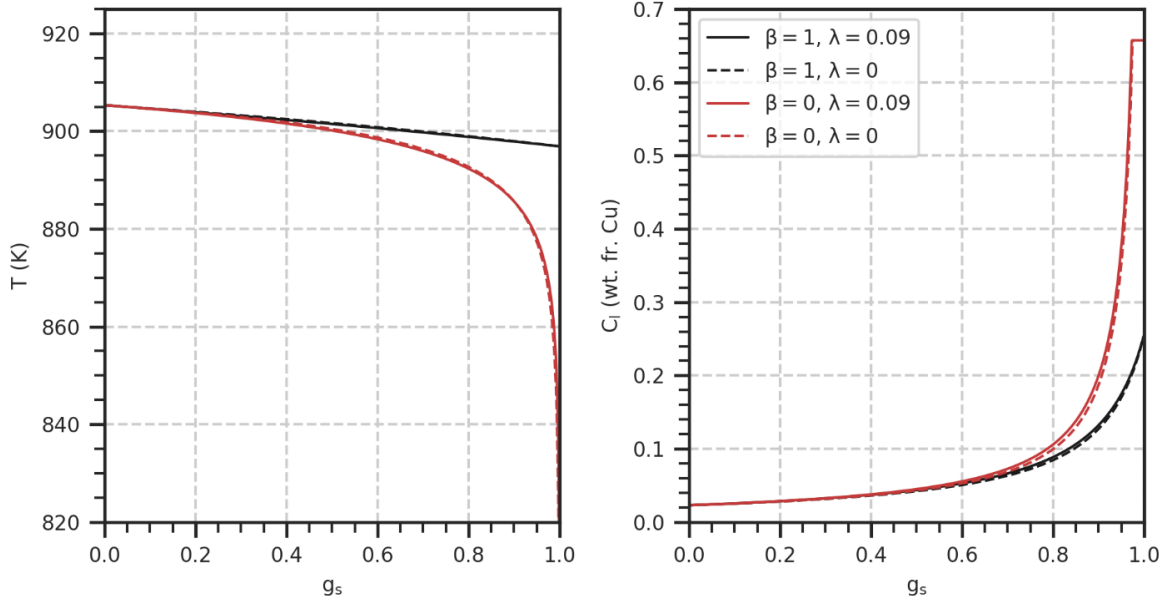


Figure 3.2: Computed temperature vs. solid volume fraction curves (left) and the corresponding liquid composition curves (right) for AA7050 where $\beta = 1$, $\lambda = 0.09$ is the lever rule and $\beta = 0$, $\lambda = 0$ is the Gulliver-Scheil equation.

3.2 Volume-Averaged Microsegregation Model

The primary limitation of the previous analytical model is the neglect of finite diffusion in the extradendritic liquid. This phenomenon is important for predicting the recalescence and grain growth during equiaxed of solidification. Wang and Beckermann [67] developed a more general approach to the microsegregation problem based on volume averaging to account for the previous microsegregation phenomena as well as finite diffusion in the extradendritic liquid. Three different regions are defined using the concept of a grain envelope [5]: the solid dendrite (s), interdendritic liquid (d), and extradendritic liquid (e), shown in Figure 3.3. The interdendritic liquid is still assumed to be well-mixed; but the additional interface allows for the treatment of finite diffusion in the extradendritic liquid. Assuming the representative volume is closed and isothermal, the densities of the solid and liquid are constant, the solute balance for the interdendritic liquid is [4]:

$$\begin{aligned} \rho_l \frac{d}{dt} (g_d \bar{C}_{l,i}) &= \rho_l \frac{dg_d}{dt} \bar{C}_{l,i} - \rho_s \frac{dg_s}{dt} k_p \bar{C}_{l,i} - \frac{\rho_l S_g D_l}{\delta_l} (\bar{C}_{l,i} - C_e) \\ &\quad - \frac{\rho_s S_{s,l} D_s}{\delta_s} (k_p \bar{C}_{l,i} - C_s) \end{aligned} \quad (3.17)$$

where the last two terms represent solute diffusion into the extradendritic and solid phase, respectively. The corresponding solute diffusion rates are controlled by the interfacial area concentrations of the grain interface (S_g) and the solid-liquid interface ($S_{s,l}$), and the characteristic diffusion lengths in the extradendritic liquid (δ_e) and solid (δ_s). The time derivative of the left-hand side can be expanded and combined with the first two terms on the right-hand side using the interfacial balance relationships provided in Table 2.2:

$$\rho_l g_d \frac{d\bar{C}_{l,i}}{dt} = \rho_s \frac{dg_s}{dt} (1 - k_p) \bar{C}_{l,i} - \frac{\rho_l S_g D_l}{\delta_e} (\bar{C}_{l,i} - C_e) - \frac{\rho_s S_{s,l} D_s}{\delta_s} (k_p \bar{C}_{l,i} - C_s) \quad (3.18)$$

Rearranging this expression in terms of the solid phase change rate gives:

$$\rho_s (1 - k_p) \bar{C}_{l,i} \frac{dg_s}{dt} = \frac{\rho_l S_g D_l}{\delta_e} (\bar{C}_{l,i} - C_e) + \frac{\rho_s S_{s,l} D_s}{\delta_s} (k_p \bar{C}_{l,i} - C_s) + \rho_l g_d \frac{d\bar{C}_{l,i}}{dt} \quad (3.19)$$

For a closed system, this equation states that the species flux rejected into the interdendritic liquid due to phase change is either diffused into the extradendritic region, diffused into the solid region, or stored in the interdendritic region [19]. The volume average of total liquid in the representative volume is specified as:

$$g_l C_l = g_d \bar{C}_{l,i} + g_e C_e \quad (3.20)$$

and therefore, an equivalent expression for the phase change rate (i.e. $\Gamma_s = dg_s/dt$) in terms of the volume-averaged solid and liquid compositions is:

$$\frac{dg_s}{dt} = \Gamma_s = \frac{\frac{S_{s,l} \rho_s D_s}{\delta_s} (k_p \bar{C}_{l,i} - C_s) + \frac{S_g \rho_l D_l}{\delta_e} \frac{g_l}{(1 - g_g)} (\bar{C}_{l,i} - C_l) + \rho_l g_d \frac{d\bar{C}_{l,i}}{dt}}{(1 - k_p) \bar{C}_{l,i}} \quad (3.21)$$

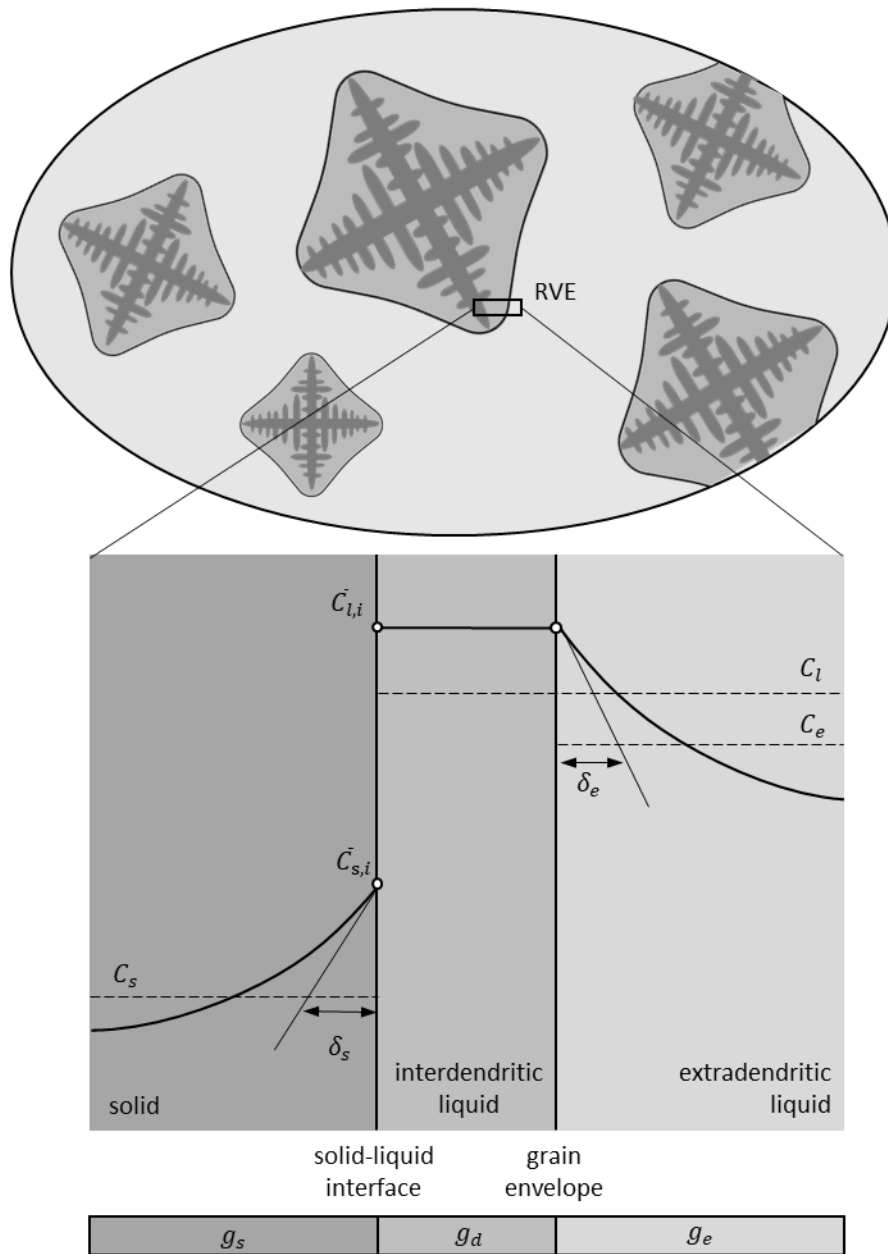


Figure 3.3: The physical model of an equiaxed dendrite enclosed by an envelope. The fluid inside the envelope (interdendritic) is assumed to be well-mixed. The solid and extradendritic liquid compositions both decrease with distance from their respective interfaces.

3.2.1 Clarification of Interfacial Balances

When the volume-averaged microsegregation model was extended to consider advection by Wang and Beckermann [19], the phase change rate was obtained from the macroscale species balance in the interdendritic liquid phase:

$$\begin{aligned} \frac{\partial}{\partial t}(\rho_l g_d \bar{C}_{l,i}) + \nabla \cdot (\rho_l g_d \mathbf{u}_d \bar{C}_{l,i}) = & -\Gamma_s k_p \bar{C}_{l,i} + \Gamma_g \bar{C}_{l,i} \\ & - \frac{\rho_s S_{s,l} D_s}{\delta_s} (k_p \bar{C}_{l,i} - C_s) - \frac{\rho_l S_g D_l}{\delta_e} (\bar{C}_{l,i} - C_e) \end{aligned} \quad (3.22)$$

The phase change rate of the grain envelope Γ_g was replaced with an equivalent expression from the interdendritic continuity equation:

$$\frac{\partial}{\partial t}(\rho_l g_d) + \nabla \cdot (\rho_l g_d \mathbf{u}_d) = \Gamma_g - \Gamma_s \quad (3.23)$$

resulting in the following expression upon substitution:

$$\begin{aligned} \frac{\partial}{\partial t}(\rho_l g_d \bar{C}_{l,i}) + \nabla \cdot (\rho_l g_d \mathbf{u}_d \bar{C}_{l,i}) = & -\Gamma_s k_p \bar{C}_{l,i} + \left[\frac{\partial}{\partial t}(\rho_l g_d) + \nabla \cdot (\rho_l g_d \mathbf{u}_d) + \Gamma_s \right] \bar{C}_{l,i} \\ & - \frac{\rho_s S_{s,l} D_s}{\delta_s} (k_p \bar{C}_{l,i} - C_s) - \frac{\rho_l S_g D_l}{\delta_l} (\bar{C}_{l,i} - C_e) \end{aligned} \quad (3.24)$$

Isolating the solid phase change rate on the left-hand side and using the chain rule for the time derivatives and divergence terms gives:

$$\Gamma_s = \frac{\frac{\rho_s S_{s,l} D_s}{\delta_s} (k_p \bar{C}_{l,i} - C_s) + \frac{\rho_l S_g D_l}{\delta_l} \frac{g_l}{(1 - g_g)} (\bar{C}_{l,i} - C_l) + \rho_l g_d \frac{\partial \bar{C}_{l,i}}{\partial t} + \rho_l g_d \mathbf{u}_d \nabla \bar{C}_{l,i}}{(1 - k_p) \bar{C}_{l,i}} \quad (3.25)$$

The additional term, $\mathbf{u}_d \nabla \bar{C}_{l,i}$, accounts for the advection of interdendritic liquid across of the RVE. However, it is not clear if formulating the interfacial species balances from macroscale equations is a theoretically consistent approach. An interfacial species balance on the length scale of the microscopic interface would show $\nabla \bar{C}_{l,i} = 0$, due to the assumption of a well-mixed interdendritic liquid, and the relationship for the solid phase change rate would be equivalent to Eqn. (3.21). Therefore, the interfacial species balances should be performed under the assumption of a closed

system on the approximate length scale of the microstructure to prevent the generation of extraneous terms originating from the volume averaging procedure. The solid growth rate provided is Eqn. (3.21) is used for the remainder of this dissertation.

3.2.2 Interfacial Closure Relationships

Closure of the previous volume-averaged microsegregation model requires auxiliary relationships for the interfacial parameters. To simplify notation, the phase change rate is expressed as:

$$\Gamma_s = \frac{a(k_p \bar{C}_{l,i} - C_s) + b(\bar{C}_{l,i} - C_l) + \rho_l g_d \frac{d\bar{C}_{l,i}}{dt}}{(1 - k_p)\bar{C}_{l,i}} \quad (3.26)$$

where a is the diffusion rate coefficient in the solid:

$$a = \frac{S_{s,l} \rho_s D_s}{\delta_s} \quad (3.27)$$

and b is the effective diffusion rate coefficient in the extradendritic liquid:

$$b = \frac{S_g \rho_l D_l}{\delta_e} \frac{g_l}{(1 - g_g)} \quad (3.28)$$

The solid diffusion coefficient, a , is assumed to be zero in this dissertation to focus exclusively on the effect that finite diffusion in the extradendritic liquid has on the macroscale transport phenomena. The liquid diffusion coefficient, b , is a function of interfacial parameters yet to be defined, namely the grain fraction g_g , interfacial area of the grain S_g , and liquid diffusion length δ_e .

In general, the formulation of the interfacial expressions begins with a nucleation model to prescribe a grain number density, n . This approach is avoided here due to the uncertainties involved in nucleation model inputs. Instead, a final effective grain radius R_f is prescribed, which invokes the assumption that the grain number density is constant. This assumption is justified by evaluating the relationship between the two parameters for spherical grains:

$$R = \left(\frac{3}{4\pi n} \right)^{\frac{1}{3}} \quad (3.29)$$

which indicates that the grain radius is insensitive variations in n . To include the effect of nucleating spherical grains, a lower limit for the grain fraction is used that is equal to the assumed volume fraction of nucleated grains:

$$g_g^* = \max \left(g_g, \left(\frac{R_o}{R_f} \right)^3 \right) \quad (3.30)$$

where R_o is the radius of the nucleated grains, assumed to be $R_o = 0.5 \mu\text{m}$ in this work. The local grain radius is then calculated according to:

$$R = g_g^{*\frac{1}{3}} R_f \quad (3.31)$$

and is used to evaluate the interfacial area per unit volume of the grain:

$$S_g = \min \left(\frac{1 - g_s}{1 - \pi\sqrt{3}/8}, 1 \right) 3g_g^{*\frac{2}{3}} R_f^{-1} \quad (3.32)$$

The first term inside the $\min(\cdot)$ operator, which return the minimum of the two arguments, is an Avrami-like factor that accounts for grain impingement for FCC structures [77].

The growth of the dendritic grain is assumed to be governed by the growth of isolated dendrite tips. According to the Lipton-Glicksman-Kurz (LGK) model [30], the velocity the dendrite tips are:

$$\bar{w}_{ng} = \frac{D_l m_l (k_p - 1) \bar{C}_{Li}}{\pi^2 \Gamma_{GT}} [\text{Iv}^{-1}(\Omega)]^2 \quad (3.33)$$

where Γ_{GT} is the Gibbs-Thomas coefficient. The form of the inverse Ivantsov function $\text{Iv}^{-1}(\Omega)$ depends on the geometric approximation made for the tip. Assuming a hemispherical dendrite tip [29], the inverse Ivantsov function is

$$\text{Iv}^{-1}(\Omega) = \Omega \quad (3.34)$$

where Ω is the supersaturation

$$\Omega = \frac{\bar{C}_{l,i} - C_e}{\bar{C}_{l,i}(1 - k_p)} = \left(\frac{g_l}{1 - g_g^*} \right) \frac{\bar{C}_{l,i} - C_l}{\bar{C}_{l,i}(1 - k_p)} \quad (3.35)$$

Instead, if the tip is assumed to be paraboloid of revolution (hereinafter “paraboloidal”), the inverse Ivantsov function is approximated by [67]:

$$\text{IV}^{-1}(\Omega) = 0.4567 \left(\frac{\Omega}{1 - \Omega} \right)^{1.195} \quad (3.36)$$

A comparison of these geometric tip approximations (Figure 3.4) shows that hemispherical tip model predicts higher growth velocities for typical supersaturations ($10^{-4} - 10^{-1}$), and therefore, will tend to predict more dendritic grain morphologies compared to the paraboloidal tip model for the same conditions [57,78].

With the grain radius (R) and grain growth velocity (\bar{w}_{ng}) defined, the liquid diffusion length can be calculated. The smoothly varying analytical solution of Bedel [79],

$$\delta_e = \left[\frac{1}{R} + \frac{\frac{(R_f^2 - R^2)}{2\Delta}}{\frac{(R_f^2 - R^2)}{2} - \Delta \left(R_e + \Delta - (R_f + \Delta) e^{\frac{R-R_f}{\Delta}} \right)} \right]^{-1} \quad (3.37)$$

based on the original work of Martorano et al. [80] is used in this dissertation. Numerical experimentation found this expression to be well-behaved across a wide range of morphological and cooling conditions. Additionally, Eqn. (3.37) is easy to implement into a numerical model because it does not require numerical integration, and obeys the growth restraint:

$$\delta_e \leq \Delta = \frac{D_l}{\bar{w}_{ng}} \quad (3.38)$$

under which dC_l/dt is greater than zero.

Finally, an additional phase transport equation for the grain is solved,

$$\frac{\partial}{\partial t} (\rho_g g_g) + \nabla \cdot (\rho_g g_g \mathbf{U}_s) = \rho_g S_g \bar{w}_{ng} \quad (3.39)$$

at which point all interfacial parameters in the liquid diffusion coefficient b in Eqn. (3.28) are defined. In Figure 3.4 the liquid diffusion coefficient is plotted as a function internal solid fraction $g_{s,i}$ and the final grain radius R_f to illustrate the effect of grain morphology and size on solute diffusion into the extradendritic liquid. The diffusion coefficient reaches a maximum value when the grain fraction goes to unity, enforcing the condition of complete mixing in the liquid. Additionally, the magnitude of the term depends on the final grain radii supplied as an input parameter and will tend to force mixing of the extradendritic liquid as the grain size is reduced.

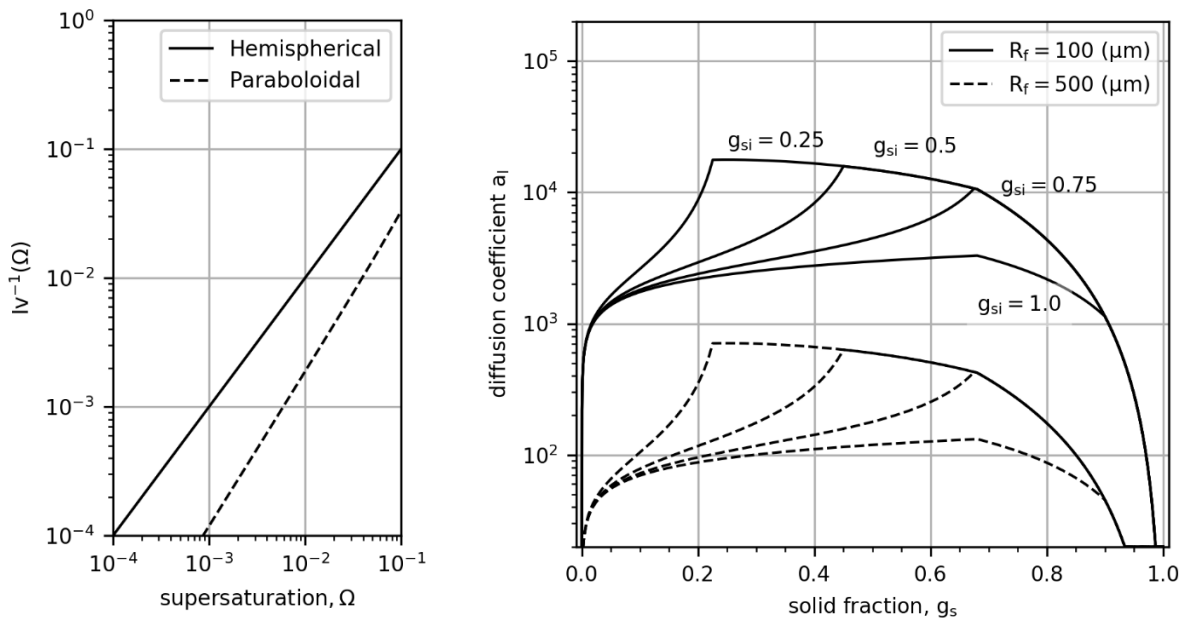


Figure 3.4: Comparison of the inverse Ivantsov function for small supersaturations using different dendrite tip geometry assumptions (left). Grain diffusion coefficient as a function of solid fraction for various grain sizes and morphologies (right).

3.2.3 Verification

In order to verify the volume-averaged model and its closure relationships for equiaxed dendritic growth, solidification of an Al-5wt%Si alloy is simulated, based on Rappaz and Thévoz [76]. Predicted cooling curves are compared to the results from Wang and Beckermann [67] in Figure 3.5 for a cooling rate of 45 Ks^{-1} and three different final grain radii (R_f). The calculations are in excellent agreement with the benchmark solutions. It is demonstrated that hemispherical

model tends to predict shallower recalescence curves due to the increased grain growth rates (see Figure 3.4). Therefore, the hemispherical model will systematically predict more dendritic grains than the paraboloidal model (Figure 3.6) and will have a total liquid composition closer to the interfacial liquid composition $\bar{C}_{l,i}$ due to the increased amount of interdendritic liquid during solidification. The numerical procedure used for calculating the previous system of equations describing volume-averaged microsegregation and grain growth is presented in Chapter 5. The influence that the undercooling predicted by the volume-averaged model has on transport phenomena during equiaxed solidification is investigated in Chapter 7. Further the reliability of the predicted grain structures is also evaluated.

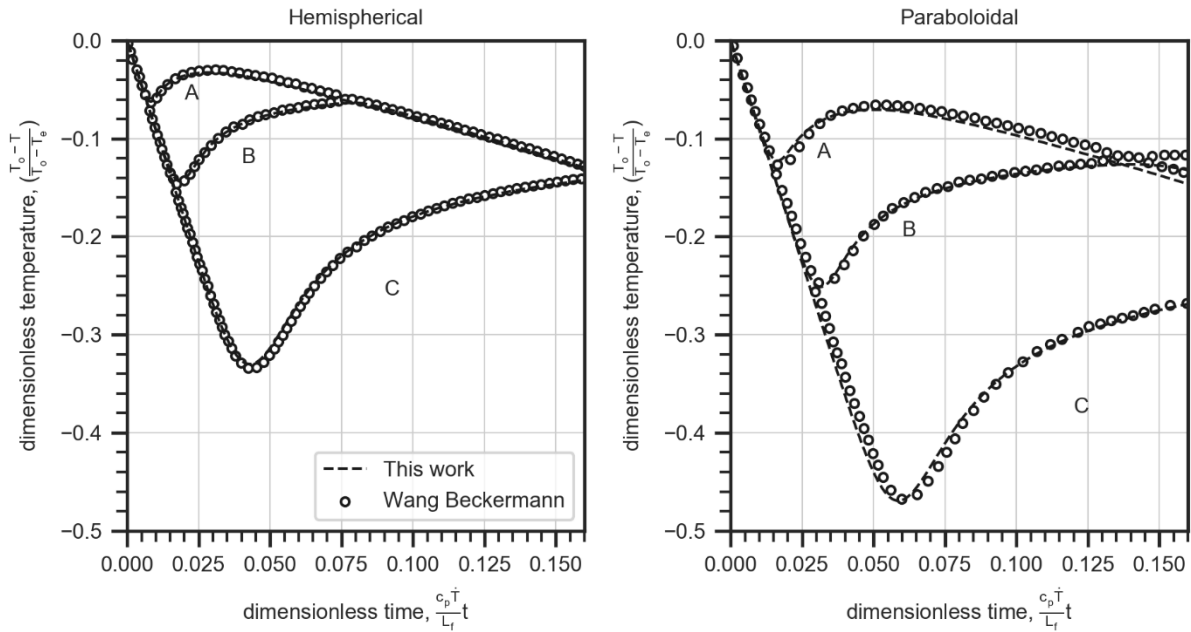


Figure 3.5: Effect of the dendrite tip geometry assumption on the predicted recalescence curves with the final grain radii of (A) 100 μm , (B) 1 mm, (C) 10 mm. The predictions of Wang and Beckermann [67] and Rappaz and Thevoz [76] are coincident with the complete model.

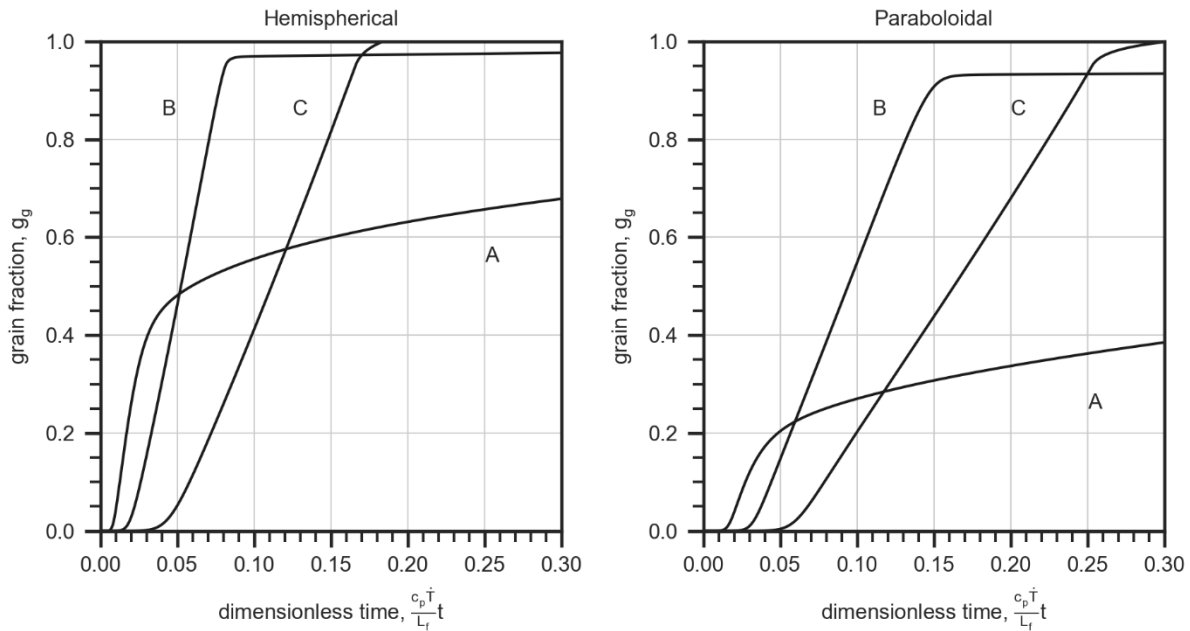


Figure 3.6: Effect of the dendrite tip geometry assumption on the predicted grain fraction with the final grain radii of (A) 100 μm , (B) 1 mm, (C) 10 mm. The predictions of Wang and Beckermann [67] are coincident with the complete model with the exception of $g_g > 0.95$ due to the limiting used here for numerical stability.

4. NUMERICAL METHODS

In this chapter, the numerical methods used for solving the model equations developed in the previous chapters are described. The finite volume method (FVM) on co-located is used to solve the continuum transport equations. The purpose of numerical discretization is to transform differential equations into a system of linear algebraic equations which can be solved by an appropriate method. The implementation and solution of the linear system of equations is done using OpenFOAM, an open-source computational fluid dynamics (CFD) platform based on the finite volume method (FVM). A brief description of the finite volume method on co-located grids is provided following Jasak [81] and Rusche [82]. Then, coupling of pressure and velocity and the formulation of phase mass fluxes are discussed in detail and novel methods for handling discontinuities across the discrete packing interface are developed.

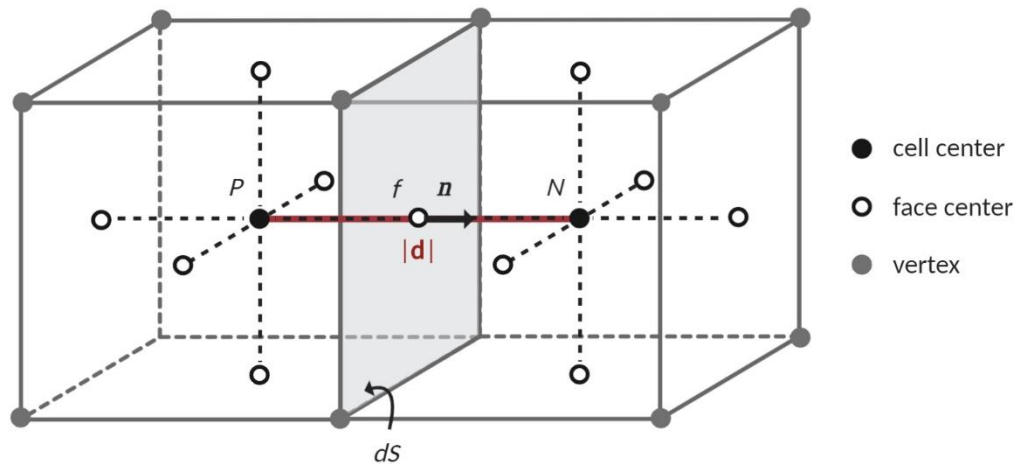


Figure 4.1. Illustration of a finite control volume with a single neighbor on a co-located grid.

4.1 Finite Volume Method

The main principle of the finite volume method is the subdivision of the problem domain into control volumes (CVs) over which the equations are integrated (Figure 4.1). Integrations over

each CV are approximated by numerical integration using field values represented at control volume centers. Using the transport equation for a general transport quantity ϕ ,

$$\underbrace{\frac{\partial}{\partial t}(\rho\phi)}_{\text{storage}} + \underbrace{\nabla \cdot (\rho\mathbf{u}\phi)}_{\text{advection}} = \underbrace{\nabla \cdot (\Gamma\nabla\phi)}_{\text{diffusion}} + \underbrace{\sum}_{\text{source}} \quad (4.1)$$

a finite volume discretization is formulated by integrating over the local volume V_P and time:

$$\int_t^{t+\Delta t} \left[\underbrace{\int_{V_P} \frac{\partial \rho\phi}{\partial t} dV}_{\text{storage}} + \underbrace{\int_{V_P} \nabla \cdot (\rho\mathbf{u}\phi) dV}_{\text{advection}} \right] dt = \int_t^{t+\Delta t} \left[\underbrace{\int_{V_P} \nabla \cdot (\Gamma\nabla\phi) dV}_{\text{diffusion}} + \underbrace{\int_{V_P} S dV}_{\text{source}} \right] dt \quad (4.2)$$

where the subscript P denotes index of the current control volume and Δt the time step. The advection and diffusion terms are converted from volume integrals to surface integrals using the Gauss's theorem for both divergence and gradient operations:

$$\int_{V_P} \nabla \otimes \phi dV = \int_{S_P} \phi \otimes \mathbf{n} dS \quad (4.3)$$

where the symbol \otimes is used to represent any tensor product. In order to evaluate these surface integrals on a numerical grid, the values of ϕ must be interpolated from the cell-centers to the face-centers bounding the control volume [82]. The methods used to approximate the volume integrals in Eqn. (4.2) are discussed in the following sections.

4.1.1 Face Interpolation

Interpolation of cell-centered values to the face-centers is a fundamental requirement of the finite volume method to evaluate surface integrals. Many face interpolation schemes exist, however the two most important for this work are central differencing and upwind differencing. Central differencing is a second order accurate method defined as:

$$\phi_{f(CD)} = f_x \phi_P + (1 - f_x) \phi_N \quad (4.4)$$

where $f_x = |\mathbf{x}_f - \mathbf{x}_N| / (|\mathbf{x}_f - \mathbf{x}_N| + |\mathbf{x}_f - \mathbf{x}_P|)$ is a weighting factor and \mathbf{x} is the position vector, shown in Figure 4.2. This method is used to interpolate all thermophysical properties from cell-centers to face-centers, and is also used to define the mass flux through a face when approximating the advection terms:

$$\mathbf{F}_f = (\rho\mathbf{u})_{f(CD)} \cdot \mathbf{S}_f \quad (4.5)$$

where $\mathbf{S}_f = \mathbf{n}dS$ is the outward facing surface area vector of face f . The scheme can be subject to numerical instabilities when interpolating quantities during evaluation of the advection terms [83].

The most common remedy to numerical instabilities of higher-order methods is first-order upwind differencing. In this method, the value of ϕ at the face is approximated by the upstream cell-center value, and thus, depends on the direction of the mass flux across the face:

$$\phi_{f(UD)} = \text{pos}(\mathbf{F}_f)\phi_P + \text{pos}(-\mathbf{F}_f)\phi_N \quad (4.6)$$

where the operator $\text{pos}(\cdot)$ returns one if the value is greater than zero and returns zero otherwise. The convention used for the orientation of mass fluxes in this work is that a positive flux indicates flow out of cell P across face f and a negative flux indicates flow into cell P across face f . This convention is chosen based on the orientation of the outward facing surface area vector \mathbf{S}_f .

The previous two interpolation schemes are illustrated in Figure 4.2. It can be shown that the leading truncation error of upwind differencing resembles a diffusive flux [83], however, it guarantees boundedness of the solution and the numerical diffusion can be mitigated to some extent by grid refinement. Following the definition of these face interpolation methods, the advection terms used throughout this work can be defined according to the approximation:

$$\int_V \nabla \cdot (\rho\mathbf{u}\phi)dV = \int_S (\rho\mathbf{u}\phi) \cdot \mathbf{n}dS \approx \sum_f (\rho\mathbf{u})_{f(CD)}\phi_{f(UD)} \cdot \mathbf{S}_f \approx \sum_f \mathbf{F}_f\phi_{f(UD)} \quad (4.7)$$

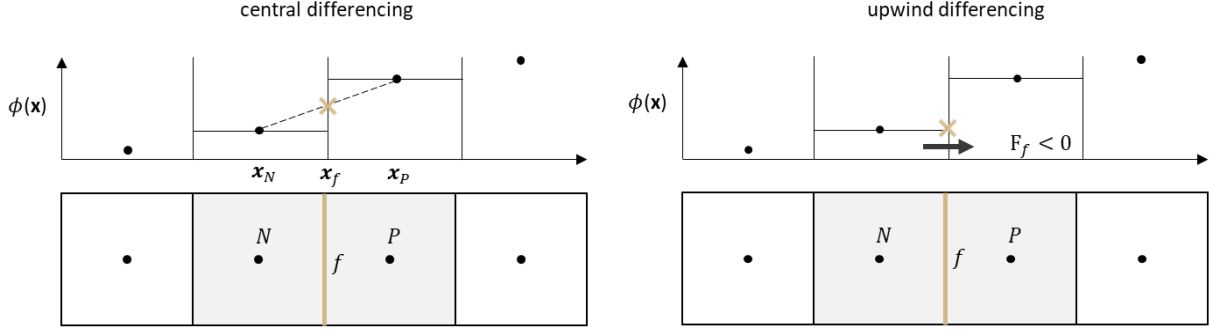


Figure 4.2. Illustration of the interpolation of the cell-center values (W, P) to the face-center value (w).

4.1.2 Gradients

Two different evaluations of the gradient terms are used in this work. The first operation produces a cell-centered gradient of ϕ using Gauss integration. The discretization is performed by applying Gauss's theorem to the volume integral:

$$\int_V \nabla \phi dV = \int_S \phi \mathbf{n} dS \approx \sum_f \phi_{f(CD)} \mathbf{S}_f \quad (4.8)$$

where the face value of $\phi_{f(CD)}$ is evaluated by central differencing. The second operation produces a face-centered normal gradient that is approximated using:

$$\nabla_f^\perp \phi = \frac{\phi_N - \phi_P}{|\mathbf{d}|} \quad (4.9)$$

where the \mathbf{d} is the vector between the center of cell P and its neighbor N. This approximation is second order accurate on the orthogonal grids. In the case of non-orthogonal grids, a correction term can be introduced by interpolating the previous Gauss method [81,82].

Following the definition of gradient operators for orthogonal grids, discretization of the diffusion terms is performed similarly to the previous advection terms:

$$\int_V \nabla \cdot (\Gamma \nabla \phi) dV = \int_S (\Gamma \nabla \phi) \cdot \mathbf{n} dS \approx \sum_f \Gamma_{f(CD)} \nabla_f^\perp \phi = \sum_f \left(\Gamma_{f(CD)} \frac{\phi_N - \phi_P}{|\mathbf{d}|} \right) \quad (4.10)$$

where Γ is the diffusion coefficient at the face-center evaluated by central differencing.

4.1.3 Source Terms

Before proceeding to the development of basic rules for time integration, some attention is given to the source term appearing in Eqn. (4.2). When the source term depends on ϕ , it is desirable to include this dependence when constructing the discretized equation [84]. Since the techniques used for the linear system of equations can only formally account for linear dependences, the source term must be linearized according to:

$$S = S_P \phi_P + S_C \quad (4.11)$$

where S_P is a coefficient of ϕ_P (not S evaluated at P) and S_C is the constant part of S . Iterative methods can be used to handle such situations by splitting a given expression in terms of S_P and S_C , which are calculated from the new values of ϕ at each iteration. How these terms are evaluated depends on their interaction with other terms in the transport equation and its influence on the boundedness and accuracy of the solution. The rules for constructing these expressions are covered in detail by Patankar [84].

4.1.4 Time Integration

Discretization of the unsteady term is performed using Euler time differencing. For a static mesh, a linear variation of ϕ over the time step Δt is:

$$\int_{V_p} \frac{\partial \rho \phi}{\partial t} dV \approx \frac{\rho_P \phi_P - \rho_P^o \phi_P^o}{\Delta t} \quad (4.12)$$

where o denotes old values from the previous time step. Using the definitions of the spatial and temporal terms, the discrete form of the transport equations can be written as:

$$\begin{aligned} \int_t^{t+\Delta t} \left[\frac{\rho_P \phi_P - \rho_P^o \phi_P^o}{\Delta t} V_p + \sum_f F_f \phi_{f(UD)} \right] dt \\ = \int_t^{t+\Delta t} \left[\sum_f \left(\Gamma_{f(CD)} \frac{\phi_N - \phi_P}{|\mathbf{d}|} \right) + S_P \phi_P V_p + S_C V_p \right] dt \end{aligned} \quad (4.13)$$

There are two methods used in this work for treating the time integrals of transport equations: explicit and implicit methods. Explicit time discretization is a first order accurate method which evaluates the spatial terms from the previous time. For the advection terms, this method becomes unstable if the Courant number,

$$Co = \frac{u\Delta t}{\Delta x} \quad (4.14)$$

is greater than 1. Therefore, a strict time step limit is required for numerical stability of the solution. A similar time step limit for the diffusion terms based on the Fourier number is also enforced [84]. The explicitly discretized equation reads:

$$\frac{\rho_P\phi_P - \rho_P^o\phi_P^o}{\Delta t}V_p + \sum_f F_f\phi_{f(UD)}^o = \sum_f \Gamma_{f(CD)} \frac{\phi_N^o - \phi_P^o}{|\mathbf{d}|} + S_P\phi_P V_p + S_C V_p \quad (4.15)$$

Again, there is some freedom in choosing how to evaluate $S_P\phi_P$ and S_C depending on the linearization method chosen. Therefore, these terms are written arbitrarily since $S_P\phi_P$ could be solved in the following ways: (1) using previous time value for ϕ_P , (2) using the previous iteration value for ϕ_P , or (3) being combined with the term $\rho_P\phi_P/\Delta t$ on the left hand side. The explicit solution for ϕ_P at the new time can be solved directly using:

$$\phi_P = \frac{\rho_P^o}{\rho_P}\phi_P^o + \frac{\Delta t}{\rho_P V_p} \left[\sum_f F_f\phi_{f(UD)}^o + \sum_f \Gamma_{f(CD)} \frac{\phi_N^o - \phi_P^o}{|\mathbf{d}|} + S_P\phi_P V_p + S_C V_p \right] \quad (4.16)$$

Alternatively, implicit time discretization is another first order accurate method which evaluates the spatial terms at the new time. This method is unconditionally stable and guarantees boundedness of the solution. The final implicitly discretized equation reads:

$$\frac{\rho_P\phi_P - \rho_P^o\phi_P^o}{\Delta t}V_p + \sum_f F_f\phi_{f(UD)} = \sum_f \left(\Gamma_{f(CD)} \frac{\phi_N - \phi_P}{|\mathbf{d}|} \right) + S_P\phi_P V_p + S_C V_p \quad (4.17)$$

Although $S_P\phi_P$ and S_C are still meant to be arbitrary, it is generally recommended for numerical stability to combine this term with $\rho_P\phi_P/\Delta t$ for implicit time discretization whenever possible. This is known as an implicit source term, and the rules for its use are explained in ref. [84]. The

implicit solution for ϕ_P cannot be evaluated directly since it depends on the values of neighboring cells ϕ_N :

$$\left(\frac{\rho_P}{\Delta t} - S_P\right) \phi_P V_P + \sum_f F_f \phi_{f(UD)} - \sum_f \left(\Gamma_{f(CD)} \frac{\phi_N - \phi_P}{|\mathbf{d}|}\right) = \frac{\rho_P^o \phi_P^o}{\Delta t} + S_C V_P \quad (4.18)$$

However, Eqn. (4.18) is a linear algebraic system which can be solved according to the methods described in the subsequent section.

4.1.5 Solution Methods for Linear Algebraic Systems

The discretization and linearization procedures outlined up to this point produce a linear algebraic equation for each control volume. The exact form of these linear algebraic equations depends on the governing equation and the discretization methods used, but can be written in the general form:

$$a_P \phi_P + \sum_N a_N \phi_N = b_P \quad (4.19)$$

The value of ϕ_P depends on the values of the neighboring cells (N), creating a system with one equation for each cell of the space domain. These systems can be expressed in a matrix form

$$[A][x] = [b] \quad (4.20)$$

where $[A]$ is a sparse square matrix with coefficients a_P on the main diagonal and a_N off the diagonal, $[x]$ is a column vector of the dependent variable and $[b]$ is the source vector. The description of these values as “vectors” comes from general matrix terminology, a list of values defined at the centers of the control volumes, and do not indicate the type of field it may contain.

The solution of this system is commonly achieved using iterative (as opposed to direct) methods. Iterative methods begin with an initial guess and subsequent iteration to improve the approximation until some specified tolerance it met. It is beyond the scope of this dissertation to discuss these methods in detail, however a variant of the original conjugate gradient (GC) method, proposed by Hestenes and Stiefel [85] is used to implicitly solve momentum and energy. In this method, conjugation of the residuals is used to construct search directions for the solution. Because

the residual is orthogonal to the previous search direction, it guarantees to always produce a new, linearly independent search direction until the residual is zero and the exact solution is obtained. The convergence rate depends on the dispersion of the eigenvalues of the matrix and can be improved through preconditioning. In this work, the Diagonal-based Incomplete LU (DILU in OpenFOAM) preconditioner is used for this purpose. The solver adopted for asymmetric matrices is then a preconditioner variant of the Bi-Conjugate Gradient Stabilized (PBiCGStab in OpenFOAM) by Van Der Vorst [86]. It will be demonstrated in the next section that a linear system for the pressure equation is also obtained. The method used to solve the pressure equation is GAMG (Geometric Algebraic Multi-Grid). The basic idea behind multi-grid solvers is to use a coarse grid with fast solution times to smooth high frequency errors and then generate an initial condition for finer grids. This solver was combined with a DIC (Diagonal-based Incomplete Cholesky) smoother.

4.2 Pressure-Velocity Coupling

In order to couple the pressure and velocity fields, segregated algorithms are commonly used. These methods solve the pressure and velocity equations separately using iterative solution procedures. In general, when the velocity fields are stored at the center of a control volume along with scalar quantities (i.e. co-location), the influence of pressure is not properly represented in the discretized momentum equation. This is known to cause oscillations in the velocity fields, sometimes referred to as “checker-boarding”. To mitigate this numerical issue, staggered grids [87] have been adopted in which the velocity fields are treated on a separate grid centered around the faces of the scalar variable control volumes. Given that the velocities are needed at the faces to calculate the advection terms in the conservation equations, this approach has some merit. The staggered grid approach has been widely used within the solidification modeling community but is no longer the standard method employed in most commercial CFD codes (e.g. Fluent, OpenFOAM, starCCM+) because it is not well-suited for parallelization and complex geometries due to the difficult bookkeeping of the multiple numerical grids.

Currently, the most common method to avoid pressure-velocity decoupling on co-located grids is the Rhie-Chow method [88], which interpolates velocities to the control volume faces when evaluating the continuity equation to imitate the staggered grid approach. The conservative field is the mass flux across control volume faces. Although this interpolation has been extremely

successful in solving decoupling issues on co-located grids, it was originally developed for flow fields without rapidly varying pressure gradients [89] or large body forces [90], and does not guarantee non-oscillatory fields for such systems. In particular, Zhang et al. [91] highlighted that the standard Rhie-Chow interpolation gives unsatisfactory results for buoyancy-driven flows in the vicinity of strong heat sources or large concentration gradients, and for flows through resistive materials with large gradients or discontinuities in the resistance. Because each of these situations are prevalent during solidification, corrections to the Rhie-Chow interpolation are necessary to accurately model solidification processes on co-located grids.

Several corrections to the Rhie-Chow interpolation have been presented in the literature. The most successful of these methods can be classified as *balanced-force* methods [92] where the pressure gradients and body forces are considered at the control volume faces, so that the body forces acting on the flow are more accurately balanced by the corresponding pressure gradients. Zhang et al. [91] proposed a correction for smoothing out the pressure gradient on cell faces by introducing body forces explicitly into the calculation. However, the explicit treatment of the momentum equation limits its application to certain flow conditions. A solution of this problem was proposed by Nordlund et al. [93] in which the drag coefficient in the cells near discontinuities was calculated by interpolation of the drag coefficient at the cell faces. Although this solution allows for an implicit velocity equation to be solved, the proposed formulation does not guarantee flux-velocity coupling and conservation errors can become prohibitively large despite producing a smooth velocity field. In another approach, Aguerre et al. [94] proposed to reconstruct the velocities from the conservative face flux inspired by a flux difference minimization to obtain an oscillation-free solution. However, the proposed reconstruction method used was only evaluated on cartesian, uniform meshes, so further studies are necessary for it to be considered a general improvement. Based on the development of these methods, a face-based drag and buoyancy formulation is developed here based on the PISO algorithm (Pressure-Implicit with Splitting of Operators) proposed by Issa [95].

4.2.1 The PISO Algorithm

The discretized forms of the mass and momentum equations are:

$$\frac{\rho_P - \rho_P^o}{\Delta t} + \sum_f F_f = 0 \quad (4.21)$$

and

$$a_P \mathbf{u}_P + \sum_N a_N \mathbf{u}_N = a_P^o \mathbf{u}_P^o - \nabla p_P + \mathbf{b}_P \quad (4.22)$$

where \mathbf{b}_P represents the collection of body forces:

$$\mathbf{b}_P = \rho_{eff,P}^B \mathbf{g} + D_P \mathbf{u}_P \quad (4.23)$$

The PISO algorithm [95] is a common procedure for coupling the velocity and pressure fields, which are both unknown upon evaluation of Eqn. (4.22). The first step of the PISO algorithm, known as the ‘‘momentum predictor’’, involves calculating the momentum field using an intermediate pressure field:

$$\mathbf{u}_p = \frac{\mathbf{H}_p}{a_p} - \frac{1}{a_p} \nabla p \quad (4.24)$$

As an initial guess in a given time step, p is the converged solution from the previous time step and \mathbf{H}_p includes the explicit temporal term, the off-diagonal terms, and the body forces:

$$\mathbf{H}_p = a_p^o \mathbf{u}_p^o - \sum_N a_N \mathbf{u}_N + \mathbf{b}_P \quad (4.25)$$

The continuity constraint is applied to the condition of a divergence-free mass flux in Eqn. (4.21), and therefore, a consistent method for interpolating the velocity field between the cell-centers and face-centers must be constructed. Interpolating the momentum predictor, Eqn. (4.24), to the faces gives an expression for the mass flux across the face:

$$F_f = [\rho_P]_f \left[\frac{\mathbf{H}_P}{a_P} \right]_f \cdot \mathbf{s}_f - \frac{[\rho_P]_f}{[a_P]_f} |\mathbf{s}_f| \nabla_f^\perp(p_P) \quad (4.26)$$

where the operator $[\cdot]_f$ will represent central differencing face-centered values to cell-centered values going forward, and $\nabla_f^\perp(\cdot)$ denotes the surface normal gradient at the given face approximated by Eqn. (4.9). Substitution of this expression into the continuity equation, Eqn. (4.21), gives the pressure correction equation:

$$\sum_f \left(\frac{[\rho_P]_f}{[a_P]_f} |\mathbf{S}_f| \nabla_f^\perp(p_P) \right) = \frac{\rho_P - \rho_P^o}{\Delta t} + \sum_f \left([\rho_P]_f \left[\frac{\mathbf{H}_P}{a_P} \right]_f \cdot \mathbf{S}_f \right) \quad (4.27)$$

the solution of which returns the pressure field that produces the conservative fluxes and corrected velocity fields when substituted into Eqn. (4.26) and Eqn. (4.24), respectively.

4.2.2 Cell-Based Drag Method

The method described in Section 4.2.1 is the standard Rhie-Chow interpolation [88], because the continuity constraint is applied to face-center values in Eqn. (4.27). The main shortcoming of this approach is that the explicit body forces \mathbf{b}_p are collected into \mathbf{H}_p and may not properly balance the pressure gradient across the face in the continuity constraint if large gradients in the body forces exist. To improve the interpolation of the buoyancy force, a reduced pressure is commonly employed, defined as the difference of the total pressure and the hydrostatic component:

$$p^R = p - \rho_{eff}^B \mathbf{g} \cdot \mathbf{h}$$

where \mathbf{h} is the displacement vector in the direction of gravity from some reference point. One benefit of performing calculations with the reduced pressure is that the buoyancy force in the continuity constraint is evaluated in terms of its surface normal gradient at the face-centers:

$$\nabla_f^\perp(p_P^R) + \rho^B \mathbf{g} \cdot \mathbf{h} = \nabla_f^\perp(p_P^R) + g \mathbf{h} \nabla_f^\perp(\rho_{eff,P}^B) \quad (4.28)$$

making it consistent with the pressure correction calculated in Eqn. (4.27). Because the buoyancy and pressure terms are evaluated at the face-centers in the continuity constraint, the cell-centered vector used to calculate the velocity field should be reconstructed from face-centered values. The expression of Weller et al. [96,97] is used for this operation:

$$\mathcal{R}[\phi_f] = \left(\sum_f \frac{\mathbf{S}_f \mathbf{S}_f}{|\mathbf{S}_f|} \right)^{-1} \cdot \sum_f \phi_f \frac{\mathbf{S}_f}{|\mathbf{S}_f|} = \boldsymbol{\phi}_P \quad (4.29)$$

where the operator $\mathcal{R}[\cdot]$ denotes the interpolation of a face-centered fields (Q_f) to a cell-centered vector ($\boldsymbol{\phi}_P$). If the drag term is evaluated at the cell-centers is either collected into a_P if evaluated as an implicit source term, or collected into \mathbf{H}_P if evaluated as an explicit source term and the momentum predictor becomes:

$$\mathbf{u}_P = \frac{\mathbf{H}_P}{a_P} - \frac{1}{a_P} \mathcal{R} \left[|\mathbf{S}_f| \nabla_f^\perp(p_P^R) + gh |\mathbf{S}_f| \nabla_f^\perp(\rho_{eff,P}^B) \right] \quad (4.30)$$

Since the buoyancy force is no longer specified as a source term in \mathbf{H}_P , the flux corrector is modified, such that:

$$\mathbf{F}_f = [\rho_P]_f \left\{ \left[\frac{\mathbf{H}_P}{a_P} \right]_f \cdot \mathbf{S}_f - \frac{1}{[a_P]_f} \left[|\mathbf{S}_f| \nabla_f^\perp(p_P^R) + gh |\mathbf{S}_f| \nabla_f^\perp(\rho_{eff,P}^B) \right] \right\} \quad (4.31)$$

4.2.3 Face-Based Drag Method

Although the previous cell-based drag scheme treats the buoyancy and pressure terms at the face-centers, a consistent method for evaluating all body forces at the faces would require the removal of the cell-centered drag term (D_P) from the diagonal of the solution matrix (a_P). A fully explicit formulation of the drag term similar to [91], i.e.:

$$\mathbf{u}_P = \frac{\mathbf{H}_P}{a_P} - \frac{1}{a_P} \mathcal{R} \left[|\mathbf{S}_f| \nabla_f^\perp(p_P^R) + gh |\mathbf{S}_f| \nabla_f^\perp(\rho_{eff,P}^B) + D_f \mathbf{F}_f \right] \quad (4.32)$$

would be prone to numerical instabilities due to the large value of the explicit source term $D_f \mathbf{F}_f$ compared to all other terms, where D_f is the drag coefficient evaluated at the face-center. In order to obtain a “face-based” drag approach while also retaining numerical stability gained by including the drag coefficient on the diagonal of the solution matrix, a semi-implicit formulation of the momentum predictor is proposed here, i.e.:

$$\mathbf{u}_P = \left(\frac{1}{1 + a_P^{-1} D_P} \right) \left\{ \frac{\mathbf{H}_P}{a_P} - \frac{1}{a_P} \left(\mathcal{R} \left[|\mathbf{S}_f| \nabla_f^\perp(p_P^R) + gh |\mathbf{S}_f| \nabla_f^\perp(\rho_{eff,P}^B) + D_f \mathbf{F}_f \right] - D_P \mathcal{R}[\mathbf{F}_f] \right) \right\} \quad (4.33)$$

This formulation assumes that $\rho_P \mathbf{u}_P \approx \mathcal{R}[\mathbf{F}_f]$ upon convergence, which is already a requirement to maintain consistency between the velocity and flux fields. Therefore, the cell-centered drag terms cancel each other upon convergence but provide numerical stability during the iterative procedure. A consistent form of the mass flux can be expressed as:

$$\mathbf{F}_f = \left(\frac{[\rho_P]_f}{1 + [a_P^{-1}]_f D_f} \right) \left\{ \left[\frac{\mathbf{H}_P}{a_P} \right]_f \cdot \mathbf{s}_f - \frac{1}{[a_P]_f} \left[|\mathbf{s}_f| \nabla_f^\perp(p_P^R) + gh |\mathbf{s}_f| \nabla_f^\perp(\rho_{eff,P}^B) \right] \right\} \quad (4.34)$$

where D_f is the drag coefficient calculated at the face.

An immediate advantage of this formulation is that D_f is no longer limited to the same interpolation method as a_P (i.e. central differencing). For solidification models, it is desirable to interpolate the solid fraction to the face-centers, and calculating the drag term using the interpolated value [98], which was previously not possible on co-located grid. This method for evaluating the drag coefficient at the face-centers is used for the remainder of this dissertation. Another advantage of this formulation is that the level of numerical diffusion introduced to the solution by the reconstruction operator can be controlled through modification of the final term in Eqn. (4.33) and (4.34). If a stronger bias towards the cell-based drag formulation is desired, then $D_P \mathcal{R}[\mathbf{F}_f]$ can be replaced with a blended formulation,

$$D_P \mathcal{R}[\mathbf{F}_f] \rightarrow D_P [\omega \mathcal{R}[\mathbf{F}_f] + (1 - \omega) \mathbf{u}_P] \quad (4.35)$$

where ω is the blending factor: From a theoretical standpoint, it appears that the proposed face-based drag scheme is an improvement across a wide range of possible flow conditions. For cases where the drag term dominates the momentum transport terms ($D_P \gg a_P$), the method approaches the face-based momentum scheme (i.e. $\rho_P \mathbf{u}_P = \mathcal{R}[\mathbf{F}_f]$), and therefore, tends towards a smoother velocity field in the presence of body force discontinuities. On the other hand, for cases the drag term is negligible ($D_P \ll a_P$), the method recovers the Rhie-Chow interpolation, and introduces no additional numerical diffusion.

4.2.4 Pressure Oscillations

The two methods for evaluating drag on co-located grids in Section 4.2.2 and Section 4.2.3 are applied to a simple 1-D Cartesian case with a uniform velocity in each control volume and a

body force F located only at control volume P , shown in Figure 4.3. This case is taken from Réthoré and Sørensen [99] and modified for application to the current methods. The discrete form of the 1-D velocity equation in control volume P is:

$$a_P u_P + \sum_N a_N u_N = 0.5(p_E - p_W)\Delta y + F_P \Delta x \Delta y \quad (4.36)$$

which simplifies by continuity ($u_P = u_N$) to give the pressure drop across cell P :

$$p_E - p_W = 2F_P \Delta x = 2F \Delta x \quad (4.37)$$

Applying this same procedure for cell W and E (where there is no volumetric force) gives:

$$p_P - p_{WW} = 2F_W \Delta x = 0 \quad \text{and} \quad p_{EE} - p_P = 2F_E \Delta x = 0 \quad (4.38)$$

These pressure profiles are oscillatory around cell P for the cell-based drag method, shown in Figure 4.3. However, when the body forces are determined at the faces, the following pressure profile is obtained for cell P

$$p_E - p_W = (F_w + F_e)\Delta x = 2F \Delta x \quad (4.39)$$

and similarly, for cell W and E :

$$p_P - p_{WW} = (F_{ww} + F_w)\Delta x = F \Delta x \quad \text{and} \quad p_{EE} - p_P = (F_e + F_{ee})\Delta x = F \Delta x \quad (4.40)$$

These pressure profiles correctly account the pressure drop across control volume P without oscillations in the adjacent cells, shown in Figure 4.3.

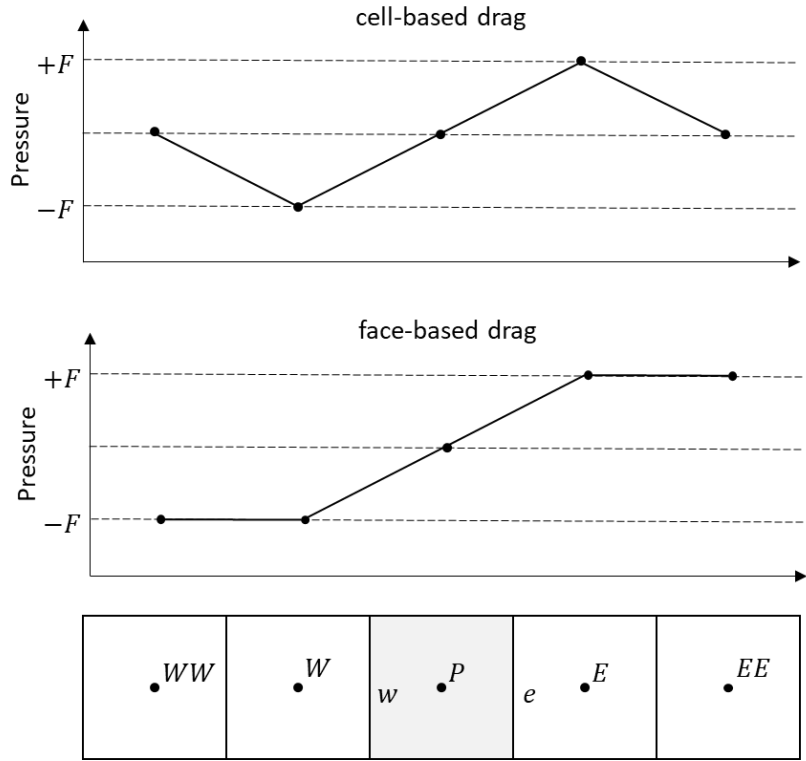


Figure 4.3: Simplified example of the pressure profiles given across a discontinuous volumetric force at control volume P for the cell-based drag and face-based drag methods. The latter is free of oscillations.

4.3 Phase Flux Discretization

Up to this point, the numerical discretization and the pressure-velocity coupling method have been formulated in a manner believed to be free of spurious oscillations of the mixture flux. However, departure of the phase flux from the mixture flux across the packing interface is still possible depending on the assumptions made upon its evaluation. This issue is addressed in the current section, and a correction method based on proper handling of the phase fluxes across this transition is proposed.

A common feature of equiaxed solidification models is the localized formation of highly solute depleted control volumes. Plotkowski and Krane [45,46] characterized the formation of these features using a continuum mixture model, similar to the one used in this work, but implemented on a staggered grid. The authors demonstrated a tendency for the discretization method to cause depleted control volumes near the chilled vertical wall where the buoyancy-driven flows are largest. The frequency and severity of these features were shown to increase with

refinement of the numerical grid, motivating their classification as numerical artifacts since their initiation and propagation do not occur on a physically representative length scale. The standard methodology also tended to suppress these artifacts as the drag force at the packing interface was increased, either by increasing the packing fraction or by decreasing the characteristic length scale used in Eqn. (2.51).

To further investigate the behavior of the mixture flux and phase fluxes across the packing interface, the discretization of the mixture composition equation,

$$\frac{\partial}{\partial t}(\rho C) + \nabla \cdot (\rho_s g_s \mathbf{u}_s C_s + \rho_l g_l \mathbf{u}_l C_l) = 0 \quad (2.85)$$

is evaluated. If the solid flux across each face of a packed cell is zero, explicit integration of the mixture composition in the rigid mush for constant density gives:

$$C_P = C_P^o + \frac{\Delta t}{\rho} \sum_f F_f C_{l,f(UD)} \quad (4.41)$$

The most problematic cells will be those along the packing interface that are permeable enough to allow the enriched liquid to be carried out of the packed cell and replaced with dilute liquid from the upwind slurry cell. This situation will tend to occur for cells with a “stair-step” configuration on 2-D co-located grids. To demonstrate this point further, this configuration is prescribed in Figure 4.4 for a uniform grid ($\Delta x = \Delta y$). An inflow across face n is balanced by the outflow across face w , such that $u_n \Delta x = -u_w \Delta y$ and:

$$C_P = [C_P^o + u_n \Delta x (C_{l,N} - C_{l,P})] \Delta t \quad (4.42)$$

Because the packed cell is at a higher liquid composition than the upwind slurry cell (i.e. $C_{l,P} > C_{l,N}$) a composition sink forms in cell P . The rate of depletion is a function of both the strength of the flow u_n , and the local composition difference ($C_{l,N} - C_{l,P}$). From this simplified analysis, it is demonstrated that these depleted cells will tend to form at finer grid spacings where the composition gradients increase, and when the permeability of the packing interface is higher. This composition sink will continue until either the local solid fraction in the packed cell becomes high enough to restrict liquid flow across the faces, or until sufficient heat is removed from either cell

N or cell W to cause the packing interface to move. Because composition depletion accelerates solidification in cell P , and delays solidification in cell W , the packing interface will stall in this configuration and further deplete cell P .

Previous authors [45,100–102] have attempted to artificially diffuse this transition over some predefined solid fraction range. However, this numerical phenomenon depends on both the source terms used in mixture momentum equation and the model chosen for transitioning the solid from a mobile to a packed states so these models are only situational corrections. An improved approach is to directly treat the solid fluxes across the packing interface. It is proposed here to formulate an artificial solid flux at the outflow face (F_w) which tends to limit the amount of enriched liquid advected out of the interface cells, i.e.:

$$C_P = [C_P^o + u_n \Delta x (C_{L,N} - C_{L,P}) + F_w C_{L,P}] \Delta t \quad (4.43)$$

This method remains local to the problematic “stair-step” cells, and thus, is not expected to change the overall macrosegregation trends. In addition to the previous numerical rationale, this method can also be justified using the same physical reasoning used to support transition function models [45,100–102]: the packing interface is a sub-grid feature, with part of the CV packed and the rest still free floating, so a numerically diffuse approach is a better representation than an interface strictly at the CV boundaries. In order to implement this method, the previous handling of the phase fluxes based on the work of Vreeman and Incropera [73] is reevaluated.

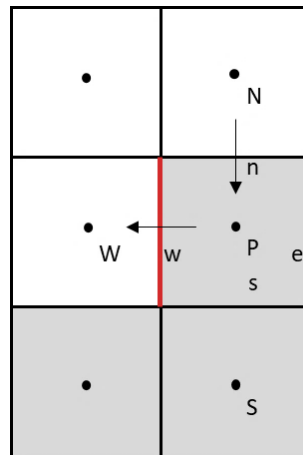


Figure 4.4: Schematic of the problematic “stair-step” cell which tend to produce composition artifacts during simulations of equiaxed solidification on co-located grids. Packed cells are indicated in grey, slurry cells in white.

4.3.1 Mixture Flux Method

Vreeman and Incropera [73] demonstrated that the macrosegregation predictions for equiaxed solidification can be extremely sensitive to the interpolation method used for calculating the phase mass fluxes in the species equation. Limiting attention to the slurry flow regime for now, the solid velocity is calculated as a function of the mixture and relative velocities.

$$\mathbf{u}_s = \mathbf{u} + \frac{\rho_l g_l}{\rho} \mathbf{u}_r \quad (4.44)$$

where

$$\mathbf{u}_r = \frac{4(1-g_g)g_{s,i}(\rho_s^B - \rho_l^B)d_g^2}{3C_D Re_g \mu_l} \mathbf{g} = \tilde{u}_r \mathbf{g} \quad (4.45)$$

The *intrinsic* solid mass phase flux across face f can be written as:

$$F_{s,f} = \frac{\rho_s}{[\rho]_f} ([\rho \mathbf{u}]_f + \rho_l g_{l,f} [\tilde{u}_r]_f \mathbf{g}) \cdot \mathbf{S}_f \quad (4.46)$$

where the gravity vector is separated from the relative velocity coefficient \tilde{u}_r in Eqn. (4.45). It is convenient to retain separation of the mixture mass flux, F_f , and the relative flux, $F_{r,f}$, when writing the volume-averaged solid mass phase flux, such that:

$$\langle F_{s,f} \rangle = \frac{\rho_s}{[\rho]_f} [g_{s,f} F_f + g_{s,f} \langle F_{r,f} \rangle] \quad (4.47)$$

where

$$\langle F_{r,f} \rangle = g_{l,f} F_{r,f} \quad (4.48)$$

and

$$F_{r,f} = \rho_l [\tilde{u}_r]_f \mathbf{g} \cdot \mathbf{S}_f \quad (4.49)$$

At this point, the solid and liquid fractions must be interpolated to the faces. Vreeman performed this interpolation by upwind differencing using the mixture flux, which give the following expression for the average solid flux:

$$\begin{aligned} \langle F_{s,f} \rangle &= \frac{\rho_s}{[\rho]_f} [\text{pos}(F_f)g_{s,P} + \text{pos}(-F_f)g_{s,N}]F_f \\ &+ \frac{\rho_s}{[\rho]_f} [\text{pos}(F_f)g_{s,P} + \text{pos}(-F_f)g_{s,N}]\langle F_{r,f} \rangle \end{aligned} \quad (4.50)$$

where

$$\langle F_{r,f} \rangle = \rho_l [\text{pos}(F_f)g_{l,P} + \text{pos}(-F_f)g_{l,N}]F_{r,f} \quad (4.51)$$

According to mass conservation, the average liquid mass flux is then:

$$\langle F_{l,f} \rangle = F_f - \langle F_{s,f} \rangle \quad (4.52)$$

The original motivation for the previous discretization scheme was to consistently interpolate the phase fractions with the mixture composition in their formulation of the species equation:

$$\frac{\partial}{\partial t}(\rho C) + \nabla \cdot (\rho \mathbf{u} C) = \nabla \cdot (\rho \mathbf{u} C - \rho_s g_s \mathbf{u}_s C_s + \rho_l g_l \mathbf{u}_l C_l) \quad (4.53)$$

However, the mixture advection terms must sum to zero for a conservative scheme, and this “mixture flux method” forces both the phase fractions and phase compositions to be interpolated in the direction of the mixture flux regardless of their individual flux orientations. This can lead to inconsistent interpolation of these terms, which can have unintended consequences on the numerical predictions.

4.3.2 Phase Flux Method

The most obvious alternative to the previous scheme is to interpolate each phase fraction by upwinding it in the direction of its corresponding flux, but this method does not guarantee boundedness or conservativeness of the phase fractions since continuity is solved in terms of the mixture [82]. Therefore, a combined interpolation of the phase fractions with respect to the mixture flux and the relative flux is desired. Recalling that $\mathbf{u}_r = \mathbf{u}_l - \mathbf{u}_s$, the liquid fraction can be interpolated with respect to $-F_{r,f}$ to approximate the direction its corresponding flux:

$$\langle F_{r,f} \rangle = \rho_l [\text{pos}(-F_{r,f})g_{l,P} + \text{pos}(F_{r,f})g_{l,N}]F_{r,f} \quad (4.54)$$

The solid fraction can then be interpolated with respect to F_f and $\langle F_{r,f} \rangle$:

$$\begin{aligned} \langle F_{s,f} \rangle &= \frac{\rho_s}{[\rho]_f} [\text{pos}(F_f)g_{s,P} + \text{pos}(-F_f)g_{s,N}]F_f \\ &+ \frac{\rho_s}{[\rho]_f} [\text{pos}(\langle F_{r,f} \rangle)g_{s,P} + \text{pos}(-\langle F_{r,f} \rangle)g_{s,N}]\langle F_{r,f} \rangle \end{aligned} \quad (4.55)$$

This interpolation method was originally proposed by Weller [103] and despite introducing numerical diffusion [82], it helps interpolate the phase fraction in the direction of its corresponding flux. During equiaxed solidification, this situation will tend to occur near the packing interface and in quiescent regions of the slurry where grains tend to settle.

The numerical diffusion introduced by the previous phase flux formulation is more obvious when evaluating the terms in the rigid mush. From the mixture relationships, the relative phase flux in the rigid mush is:

$$\langle F_{r,f} \rangle = -F_f \quad (4.56)$$

and therefore, the solid fraction interpolated with respect to both F_f and $-F_f$:

$$\begin{aligned} \langle F_{s,f} \rangle &= \frac{\rho_s}{[\rho]_f} [\text{pos}(F_f)g_{s,P} + \text{pos}(-F_f)g_{s,N}]F_f \\ &- \frac{\rho_s}{[\rho]_f} [\text{pos}(-F_f)g_{s,P} + \text{pos}(F_f)g_{s,N}]F_f \end{aligned} \quad (4.57)$$

which is nonzero wherever $g_{s,P} \neq g_{s,N}$. Because the flow of enriched liquid in the rigid mush is important to the macrosegregation development, it is not desirable for this diffusive flux to be applied everywhere in the rigid mush. Instead, it should be limited to the problematic faces which tend to cause highly solute depleted cells at the packing interface, shown in Figure 4.4. To perform this limiting, the interface of the rigid mush is first identified using the outward pointing normal of the marker function m interpolated to the cell-faces:

$$\mathbf{n}_{m,f} = - \left(\frac{[\nabla m]_f}{|[\nabla m]_f| + 1 \times 10^{-8}/\sqrt[3]{1}} \right) \cdot \mathbf{S}_f \quad (4.58)$$

where \bar{V} is the average volume of the control volume in the domain used to prevent division by zero. This term is zero everywhere except for the cells along the packing interface. To further identify faces with an outflow of the mixture flux, an indicator function, ζ , is defined:

$$\zeta = \eta \text{pos}(\mathbf{n}_{m,f} \mathbf{F}_f)$$

where $0 \leq \eta \leq 1$ is a coefficient which controls the amount of numerical diffusion introduced to the solid phase flux. When $\eta = 0$, the scheme is equivalent to a discretely packed interface. After combining terms and utilizing the marker function, the average solid flux at any face in the domain is:

$$\langle \mathbf{F}_{s,f} \rangle = \frac{\rho_s}{[\rho]_f} ([\text{pos}(\mathbf{F}_f)g_{s,P} + \text{pos}(-\mathbf{F}_f)g_{s,N}] \mathbf{F}_f + (1 - m_f) \langle \mathbf{F}_{r,f} \rangle + m_f \mathbf{F}_{D,f}) \quad (4.59)$$

where the newly introduced diffusion flux is:

$$\begin{aligned} \mathbf{F}_{D,f} = & \zeta [\text{pos}(-\mathbf{F}_f)g_{s,P} + \text{pos}(\mathbf{F}_f)g_{s,N}] \mathbf{F}_f \\ & - (1 - \zeta) [\text{pos}(\mathbf{F}_f)g_{s,P} + \text{pos}(-\mathbf{F}_f)g_{s,N}] \mathbf{F}_f \end{aligned} \quad (4.60)$$

Finally, it is noted that in order to ensure that no solid flows into an already packed cell, the marker function at the face-centers, m_f in Eqn. (4.59), must be evaluated using a local maximum scheme.

5. THERMODYNAMIC SOLUTION ALGORITHM

In the previous chapter the spatial and time discretization used for the finite volume method was discussed. In this chapter, the iterative procedure used to linearize the latent heat source term is addressed. A review of the open literature suggests that the most robust and efficient numerical procedures for solving the highly coupled thermodynamic equations describing solidification are based on the linearized source-based method of Swaminathan and Voller [38,39]. Such procedures generally require 2-4 iterations per time step to decrease the normalized residuals for solid fraction and temperature to values below 10^{-4} . For comparison, Wu et al. [104] report that their iterative procedure for solving volume-averaged microsegregation models can take up to 60 iterations for similar convergence criteria. It is of general interest to the solidification modeling community to understand what features of the linearized source-based method produce numerical stability and rapid convergence, and to what degree this method can be extended to more generalized microsegregation models. This iterative procedure is evaluated and applied to both the analytical and volume-averaged microsegregation models formulated in Chapter 3.

5.1 Semi-Implicit Source Term Linearization

Assuming a constant solid density, the solid transport equation will have the following form for an explicit time integration:

$$\rho_s \left(\frac{g_s - g_s^o}{\Delta t} \right) + \sum_f \langle F_{s,f} \rangle = \Gamma_s \quad (5.1)$$

where the average solid mass flux $\langle F_{s,f} \rangle$ is calculated using the methods described in Section 4.3.

The discrete form of the energy equation for an implicit time integration is then:

$$a_p T_p = a_p^o T_p^o + \sum_N a_N T_N + L_f \left[\rho_s (g_s - g_s^o) + \Delta t \sum_f \langle F_{s,f} \rangle \right] \quad (5.2)$$

The transient latent heat term can be linearized by approximating the solid fraction using a Taylor series expansion of the form:

$$g_s = g_s^* + \frac{dg_s}{dT}(T - T^*) \quad (5.3)$$

Substitution of this expression into the discrete energy equation yields:

$$\left[a_P - \rho_s L_f \frac{dg_s}{dT} \right] T_p = a_P^o T_P^o + \sum_N a_N T_N + L_f \left[\rho_s \left(g_s^* - g_s^o - \frac{dg_s}{dT} T^* \right) + \Delta t \sum_f \langle F_{s,f} \rangle \right] \quad (5.4)$$

The first beneficial feature of this method is that the latent heat source term now contains an implicit component which improves the numerical stability and convergence rate of the linear algebra solver [84]. Because the implicit method is unconditionally stable, the time step taken to solve the energy equation can theoretically be as large as the desired time accuracy of the solution. This time-stepping behavior can have a dramatic effect on the calculation time compared to previous multi-time step methods [105] or explicit time integration methods [74]. Both methods require relatively small time steps in the thermodynamic solution algorithm to assist convergence.

The second beneficial feature of this method is that it is a Newton-Raphson method, which exhibits quadratic convergence. Eliminating all terms in the energy equation that are not found in the Taylor's series expansion gives an expression for temperature that is more recognizable as a Newton-Raphson method:

$$T_p = T^* - \left[\frac{dg_s}{dT} \right]^{-1} g_s^* \quad (5.5)$$

Implementation of this iterative method requires an estimate of the solution (T^*) and an expression for solid fraction that is differentiable with respect to temperature to obtain the solid fraction slope (dg_s/dT). When latter requirement is not possible, the slope can be approximated using a finite difference approximation [40]. This approach is a known as a secant method and exhibits a slightly slower rate of convergence (about 1.6 times more iterations per time step [40]). Although these iterative methods are sensitive to the estimate of the solution, transient solidification problems are generally well behaved and a good initial estimate is made by calculating T^* as a function of previous iteration field values, in this case g_s^* . In the subsequent sections, expressions for dg_s/dT and T^* are derived for both the analytical microsegregation model and the volume-averaged microsegregation model.

5.2 Analytical Microsegregation Algorithm

Implementation of the previous method is straightforward when an algebraic expression for the solid fraction exists. For the generalized analytical model formulated in Chapter 3:

$$g_s = \frac{1}{(1 - k_p^* \beta)} \left[1 - \left(\frac{(T - T_m)(1 - k_p^*) + \lambda m_{liq} C}{m_{liq} C (1 - k_p^* + \lambda)} \right)^{\frac{1 - k_p^* \beta}{k_p^* - 1}} \right] \quad (3.13)$$

the solid fraction slope and temperature estimate can be evaluated directly, such that:

$$\frac{dg_s}{dT} = \frac{1}{\lambda m_{liq} C_o + (T - T_m)(1 - k_p^*)} \left(\frac{(T - T_m)(1 - k_p^*) + \lambda m_{liq} C}{m_{liq} C (1 - k_p^* + \lambda)} \right)^{\frac{1 - k_p^* \beta}{k_p^* - 1}} \quad (5.6)$$

and

$$T^* = T_m + m_{liq} C_l \quad (5.7)$$

where

$$C_l = C \left[\left(\frac{\lambda}{(1 - k_p^*)} + 1 \right) [1 - (1 - k_p \beta) g_s]^{\frac{k_p^* - 1}{1 - k_p^* \beta}} - \frac{\lambda}{(1 - k_p^*)} \right] \quad (5.8)$$

It is noted that the expression for the temperature estimate is equal to the liquidus surface and can be calculated from the liquid composition at the previous iteration, i.e. $T^* = T_m + m_{liq} C_l$. These expressions are valid during primary solidification between the liquidus and eutectic temperatures. During a eutectic reaction, the remaining liquid is assumed to solidify isothermally as an equilibrium eutectic. This type of reaction is isothermal and a large amount of latent heat can be released for alloys containing a significant eutectic fraction, g_s^{eut} . To improve numerical stability, the eutectic reaction is artificially spread over a numerically convenient range ΔT_{eut} , where a value of $\Delta T_{eut} = 0.1$ is used in this work. A linear expression for the solid fraction that meets the general requirement for a Newton-Raphson (i.e. a differentiable function of temperature) is used:

$$g_s = 1 - \left[\frac{g_s^{eut} - 1}{\Delta T_{eut}} \right] (T^* - T_{eut}) \quad (5.9)$$

Therefore, the solid fraction slope and temperature estimate are

$$\frac{dg_s}{dT} = \frac{g_s^{eut} - 1}{\Delta T_{eut}} \quad (5.10)$$

and

$$T^* = T_{eut} - \left[\frac{\Delta T_{eut}}{g_s^{eut} - 1} \right] (g_s^* - 1) \quad (5.11)$$

The rapid convergence rate of the iterative procedure during a eutectic reaction is maintained using this method and justifies the additional memory load of storing g_s^{eut} at each control volume. This field is calculated when the temperature drops below the eutectic temperature so that the solid fraction slope remains constant until the control volume is fully solidified. To facilitate remelting of the eutectic, the auxiliary eutectic fraction is limited to a maximum value of 0.99.

5.3 Volume-Averaged Microsegregation Algorithm

Implementation of this iterative method is slightly more complicated for the volume-averaged microsegregation models and has yet to be performed in the literature. This microsegregation model provides the phase change rate Γ_s , and therefore, does not contain an explicit relationship for g_s . In order to provide this relationship in a manner suitable to the semi-implicit source method, an operator splitting method is used. Založnik and Combeau [106] have formally shown that the influence of the advection term and the phase change term can be included separately without a significant loss of accuracy.

Operator splitting is a well-established concept in CFD and is explained here in the specific context of the phase transport equation. First, g_s is integrated over $[t_o, t_o + \Delta t]$ with the initial condition $g_s(t_o) = g_s^o$, without the influence of growth. The solid fraction obtained in this step is denoted as g_s^t . In a second stage, the growth contributions are integrated over the same time interval $[t_o, t_o + \Delta t]$ with the initial condition $g_s(t_o) = g_s^t$. The two contributions are summed to obtain the total variation. The discrete form of the solid transport equation using explicit time integration is

$$\rho_s \left(\frac{g_s - g_s^o}{\Delta t} \right) + \underbrace{\sum_f \langle F_{s,f} \rangle}_{\text{advection term}} = \underbrace{\frac{a(\bar{C}_{l,i} - C_l) + b(k_p \bar{C}_{l,i} - C_s) + \frac{\rho_l g_d}{\Delta t} (\bar{C}_{l,i} - \bar{C}_{l,i}^o)}{(1 - k_p) \bar{C}_{l,i}}}_{\text{phase change term}} \quad (5.12)$$

If the advection term is accounted for in a separate transport stage, i.e.:

$$g_s^t = g_s^o - \frac{\Delta t}{\rho_s} \sum_f \langle F_{s,f} \rangle \quad (5.13)$$

then an explicit solid fraction expression due to growth is obtained:

$$g_s = g_s^t + \frac{\Delta t}{\rho_s} \left[\frac{a(\bar{C}_{l,i} - C_l) + b(k_p \bar{C}_{l,i} - C_s) + \frac{\rho_l g_d}{\Delta t} (\bar{C}_{l,i} - \bar{C}_{l,i}^o)}{(1 - k_p) \bar{C}_{l,i}} \right] \quad (5.14)$$

This expression becomes a differentiable function of temperature once the condition of interfacial equilibrium, $T^* = T_m + m_{liq} \bar{C}_{l,i}$, is employed. The expression for the temperature estimate needed for the Newton-Raphson method is obtained following algebraic rearrangement of Eqn. (5.14), such that:

$$T^* = T_m + m_{liq} \Delta t \left[\frac{aC_l + bC_s + \frac{\rho_l g_d}{\Delta t} \bar{C}_{l,i}^o}{(k_p - 1)\rho_s(g_s - g_s^t) + \Delta t \left(a + b + \frac{\rho_l g_d}{\Delta t} \right)} \right] \quad (5.15)$$

Similarly, the derivative of Eqn. (5.14) provides the necessary the solid fraction slope:

$$\frac{dg_s}{dT} = \frac{\Delta t}{\rho_s} \left[m_l \frac{aC_l + bC_s - \frac{\rho_l g_d}{\Delta t} \bar{C}_{l,i}^o}{(1 - k_p)(T - T_m)^2} \right] \quad (5.16)$$

Finally, substitution of the solid fraction at the previous time in Eqn. (5.13) into the Eqn. (5.2) gives the following form of the energy conservation equation for the volume-averaged microsegregation model:

$$\left[a_P - \rho_s L_f \frac{dg_s}{dT} \right] T_P = a_P^o T_P^o + \sum_N a_N T_N + \rho_s L_f \left[g_s^* - g_s^t - \frac{dg_s}{dT} T^* \right] \quad (5.17)$$

Closure of the volume-averaged microsegregation model still requires the solution of the solid and liquid phase composition transport equations, Eqns. (2.83) and (2.84), which can be expressed in the following manner for an explicit time integration:

$$C_s = \frac{1}{(g_s + \varphi_s)} \left\{ (g_s^o + \varphi_s) C_s^o - \Delta t \left[\sum_f (\langle F_{s,f} \rangle C_{s,f(UD)}) - \frac{1}{\rho_s} J_s \right] \right\} \quad (5.18)$$

and

$$C_l = \frac{1}{(g_l + \varphi_l)} \left\{ (g_l^o + \varphi_l) C_l^o - \Delta t \left[\sum_f (\langle F_{l,f} \rangle C_{l,f(UD)}) + \frac{1}{\rho_l} J_s \right] \right\} \quad (5.19)$$

where φ_k is a stabilization coefficient used to bound the solution in the dilute limits of phase k :

$$\varphi_k = \max(1 \times 10^{-6} - g_k, 0) \quad (5.20)$$

For the current operator splitting method, the interfacial solute transfer into the solid phase due to phase change and diffusion can be expressed as:

$$J_s = \frac{\rho_s}{\Delta t} (g_s - g_s^t) k_p \bar{C}_{l,i} + a(k_p \bar{C}_{l,i} - C_s) \quad (5.21)$$

where $k_p \bar{C}_{l,i}$ is replaced with the solid composition at the previous time, C_s^o , for remelting and the liquid composition at the previous time, C_l^o , during a eutectic reaction to ensure solute conservation as the relevant phase fractions approaches zero.

5.4 Summary of Algorithms

At the beginning of a time step, all mixture properties are calculated and the iterative packing algorithm is performed to update the marker function m . Next, the source terms for the momentum equations are calculated and the PISO algorithm, outlined in Section 4.2, is solved for the mixture flux F_f and mixture velocity \mathbf{u} . The average solid phase flux $\langle F_{s,f} \rangle$ and average liquid flux $\langle F_{l,f} \rangle$ are then calculated using the discretization in Section 4.3. Finally, the thermodynamic algorithms based on the semi-implicit source scheme outlined in the current chapter are solved for temperature T , phase volume fractions (g_s, g_l) , and phase compositions (C_s, C_l) . The specific form of the algorithm depends on which microsegregation model is employed. The procedure is outlined in Table 5.1 for the analytical microsegregation model, and Table 5.2 for the dendritic multiphase

microsegregation model. Once these algorithms converge, the corresponding mixture composition is updated and the solution advances in time.

Table 5.1: Solution algorithm for the analytical microsegregation model

1. Calculate solid fraction slope and reference temperature [†] :	\
$\frac{dg_s}{dT} = \frac{1}{\lambda m_{liq} C_o + (T - T_m)(1 - k_p^*)} \left(\frac{(T - T_m)(1 - k_p^*) + \lambda m_{liq} C}{m_{liq} C(1 - k_p^* + \lambda)} \right)^{\frac{1 - k_p^* \beta}{k_p^* - 1}} \quad (5.6)$	
$T^* = T_m + m_{liq} C_l \quad (5.7)$	
2. Solve implicit energy equation:	
$\left[a_p - \rho_s L_f \frac{dg_s}{dT} \right] T_p = a_p^o T_p^o + \sum_N a_N T_N + \rho_s L_f \left[g_s^* - g_s^o - \frac{dg_s}{dT} T^* \right] + \Delta t L_f \sum_f \langle F_{s,f} \rangle \quad (5.4)$	
3. Update and bound the phase fractions due to phase change:	
$g_s = \min \left(\max \left(g_s^* + \frac{dg_s}{dT} (T - T^*), 0 \right), 1 \right) \quad (5.3)$	
$g_l = 1 - g_s \quad (2.4)$	
4. Explicitly calculate the composition equations:	
$C_l = C \left[\left(\frac{\lambda}{(1 - k_p^*)} + 1 \right) \left[1 - (1 - k_p \beta) g_s \right]^{\frac{k_p^* - 1}{1 - k_p^* \beta}} - \frac{\lambda}{(1 - k_p^*)} \right] \quad (5.8)$	
$C_s = \frac{(\rho_s g_s + \rho_l g_l) C - \rho_l g_l C_l}{\rho_s g_s} \quad (3.2)$	
5. Iterate steps 1 through 4 until residual convergence below tolerances	

[†] Replace with eutectic expressions when necessary

Table 5.2. Solution algorithm for the volume-averaged dendritic microsegregation model

1. Solve the bounded solid phase transport equation and update the liquid fraction:	\
$g_s = \min \left(\max \left(g_s^o - \frac{\Delta t}{\rho_s} \sum_f \langle F_{s,f} \rangle, 0 \right), 1 \right) \quad (5.13)$	
$g_l = 1 - g_s \quad (2.4)$	
2. Store the phase fractions from the transport stage: $g_s^t = g_s$ and $g_l^t = g_l$	
3. Calculate the interfacial relationships outlined in Section 3.2.2	
4. Calculate solid fraction slope and reference temperature [†] :	
$\frac{dg_s}{dT} = \frac{\Delta t}{\rho_s} \left[m_l \frac{aC_l + bC_s - c\bar{C}_{l,i}^o}{(1 - k_p)(T - T_m)^2} \right] \quad (5.16)$	
$T^* = T_m + m_l \Delta t \left[\frac{aC_l + bC_s + \frac{\rho_l g_d}{\Delta t} \bar{C}_{l,i}^o}{(k_p - 1)\rho_s(g_s - g_s^t) + \Delta t \left(a + b + \frac{\rho_l g_d}{\Delta t} \right)} \right] \quad (5.15)$	
5. Solve the implicit energy equation:	
$\left[a_p - \rho_s L_f \frac{dg_s}{dT} \right] T_p = a_p^o T_p^o + \sum_N a_N T_N + \rho_s L_f \left[g_s^* - g_s^t - \frac{dg_s}{dT} T^* \right] \quad (5.17)$	
6. Update and bound the phase fractions due to phase change:	
$g_s = \min \left(\max \left(g_s^* + \frac{dg_s}{dT} (T - T^*), 0 \right), 1 \right) \quad (5.3)$	
$g_l = 1 - g_s \quad (2.4)$	
7. Update and bound liquid interface composition:	
$\bar{C}_{l,i} = \min((T - T_m)/m_{liq}, C_{eut}) \quad (3.1)$	
8. Update the composition source term [†] :	
$J_s = \frac{\rho_s}{\Delta t} (g_s - g_s^t) k_p \bar{C}_{l,i} + a(k_p \bar{C}_{l,i} - C_s) \quad (5.21)$	
9. Explicitly calculate the composition equations:	
$C_s = \frac{1}{(g_s + \varphi_s)} \left\{ (g_s^o + \varphi_s) C_s^o - \Delta t \left[\sum_f (\langle F_{s,f} \rangle C_{s,f(UD)}) - \frac{1}{\rho_s} J_s \right] \right\} \quad (5.18)$	
$C_l = \frac{1}{(g_l + \varphi_l)} \left\{ (g_l^o + \varphi_l) C_l^o - \Delta t \left[\sum_f (\langle F_{l,f} \rangle C_{l,f(UD)}) + \frac{1}{\rho_l} J_s \right] \right\} \quad (5.19)$	
10. Iterate steps 4 through 9 until residual convergence below tolerances	

[†] Replace with eutectic expressions when necessary

6. NUMERICAL EXERCISES AND VERIFICATION

The purpose of this chapter is to verify the implementation of the fully coupled equiaxed solidification model on the OpenFOAM platform. Verification of the numerical methods used to formulate the drag term (Section 4.2) and the phase mass fluxes (Section 4.3) on collocated grids is first performed using reduced physics problems which neglect solidification. Next, the behavior of the solidification model including the thermodynamic solution algorithm (see Chapter 5) is studied for a static casting test case considering both columnar and equiaxed solidification. The nature of composition artifact formations on collocated grids is investigated and suggestions are made to mitigate their formation, specifically the use of the face-based drag formulation (see Section 4.2.3) and the diffuse phase flux transition model (see Section 4.3.2). Finally, predictions using the full DC casting model are compared to data taken from an industrial scale DC cast ingot [47].

6.1 Porous Plug

Before proceeding to the verification of the fully coupled solidification model, it is useful to demonstrate the behavior of the two drag formulations presented in the previous chapter on a simplified test case limited to incompressible forced convection through an isotropic porous plug. This case was originally proposed by Costa [107] and later evaluated by Nordlund et al. [93] and Aguerre et al. [94] on co-located grids. A schematic of the test case is provided in Figure 6.1. A 2-D channel of height $H = 50$ mm and length $L = 8H$ is fed by a fully developed parabolic flow on the left boundary with a mean velocity u_{in} . The Darcy number of the porous plug is defined as $Da = K/H^2$, where K is the isotropic permeability. A value of $Da = 10^{-5}$ was previously shown to cause spurious oscillations in the velocity field for the cell-based drag formulation and is used here for verification of the proposed face-based drag formulation [94]. Central differencing is used to interpolate the drag term to the face-centers for the face-based drag approach.

Figure 6.2 shows that each momentum formulation correctly predicts fully developed parabolic profile far from the plug and a uniform profile inside of the plug for a Reynolds number $Re = 25$. However, the cell-based drag formulation causes spurious velocities at the porous interface, while the face-based drag formulation predicts a smooth and continuous transition

between regions. A more detailed insight into the velocity profiles is presented in Figure 6.3, where the normalized x -component of the centerline velocity are compared for the different drag formulations. For the cell-based drag formulation, the amplitude of the velocity oscillation decreases as the Darcy number decreases to 10^{-3} , and therefore, drag becomes less dominant. From these results, it is demonstrated that the face-based drag formulation which exhibits a continuous variation of the velocity profiles across the interface regardless of the flow conditions.

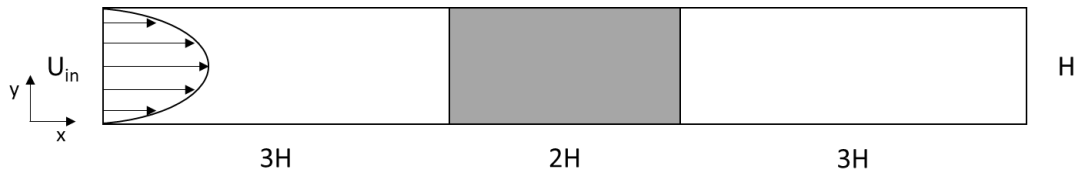


Figure 6.1: Illustration of the numerical domain for the porous plug verification case

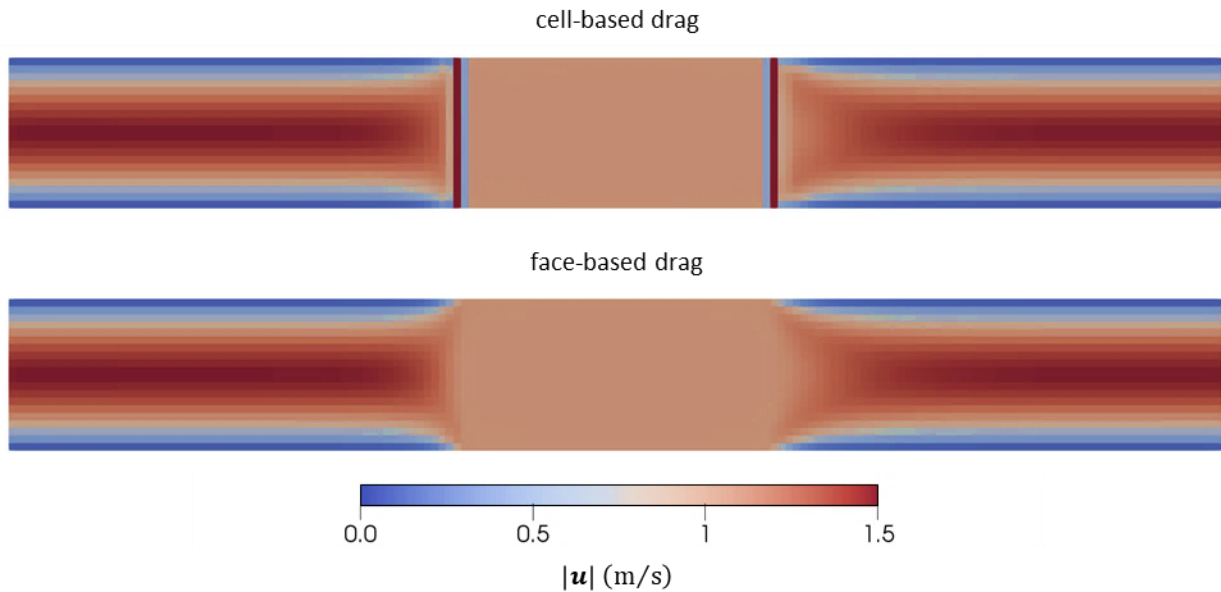


Figure 6.2: Steady state velocity field calculated for the porous plug test case ($Da = 10^{-5}$ and $Re = 25$) using different momentum formulations.

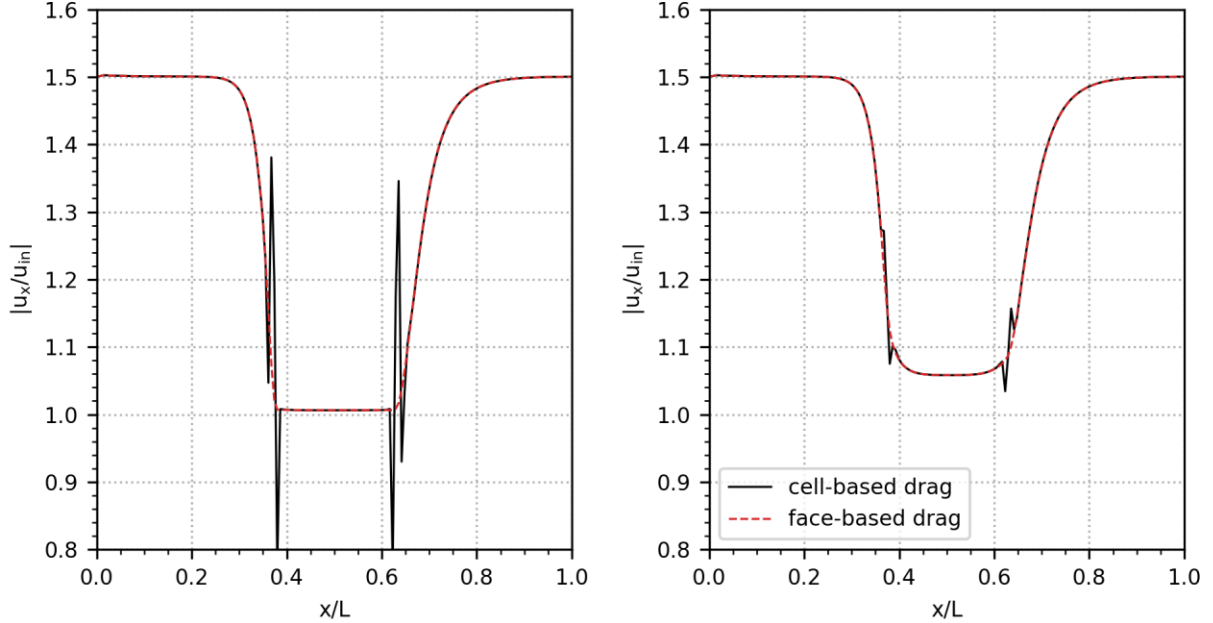


Figure 6.3: Centerline normalized x-component velocity for the porous plug test case with $Da = 10^{-5}$ (left) and 10^{-3} (right) using different drag formulations. The velocities magnitudes are linearly interpolated to the face-centers to represent the oscillation of the flux. The results from Aguerre et al. [94] are coincident with those obtained here.

6.2 Settling Column

In order to verify the implementation of the phase flux discretization method (Section 4.3.2), model predictions are compared to the settling experiment of Pham Van Bang et al. [108]. This experiment suspended polystyrene spheres ($d_g = 290 \pm 30 \mu\text{m}$, $\rho = 1.05 \text{ kg m}^{-3}$) in a $2.5 \times 10 \text{ cm}$ column of silicon oil ($\nu = 20 \text{ kg (m s)}^{-1}$, $\rho = 0.95 \text{ kg m}^{-3}$). Magnetic Resonance Imaging (MRI) tracked the evolution of the particle concentration in the column. The solid-liquid interface and the packing interface evolutions over time were reported. A mixing procedure was used to create a homogenous suspension with a volume fraction of 0.48 at an initial height of 5.5 cm. To simulate this case, a 2-D orthogonal mesh with a uniform grid spacing of 1 mm was used. It was assumed that the particles packed at a volume fraction of 0.6. Three different drag models that are commonly used in equiaxed solidification models are evaluated. The $CdRe$ expressions characterizing the generalized drag coefficient used in the relative solid-liquid velocity expression, Eqn. (2.70), are provided in Table 6.1.

Each drag model considers the effect of multiple spherical particles on the relative phase velocity. The Agarwal-O'Neil model [25] and the Gidaspow model [109] transition from semi-empirical correlations developed using the submerged object model in the dilute region to correlations developed using the porous medium approach (e.g. Kozeny-Carmen [110]) in the dense region. The Wang-Beckermann model [35] also transitions between these two regimes, however unlike the previous models, it does so in a continuous manner. While the model overpredicts the drag coefficient relative to all other models for solid spheres (see Figure 6.5), it was specifically developed for equiaxed dendrites. More complicated expressions of this term are available which can account for the permeability of the interdendritic structure and the sphericity of the dendrites.

Contour plots of the predicted solid fraction field and solid velocity streamlines at various times are provided in Figure 6.4 for the mixture flux method and the phase flux method formulated in Section 4.3. Both calculations were performed using the Wang-Beckermann drag model. The solid-liquid surface is indicated by the top black line and the packing interface is indicated by the remaining black lines. The phase flux method formulated in Section 4.3.2 predicts a continuous evolution of both the solid-liquid interface and the packing interface, in agreement with experimental observations. However, the mixture flux method predicts unphysical agglomeration of particles near the solid-liquid interface, and the formation of an inhomogeneous packed bed. It is noted that the same unphysical agglomeration near the solid-liquid interface is observed in another model of equiaxed solidification compared against the same case [111]. The results here suggest that the current phase flux model is an improvement over the previous method applied for equiaxed solidification [73] because it better captures the physics of settling and sedimentation of grains.

In Figure 6.5 the evolution of the solid-liquid interface and the packing interface for each drag model are compared to experiments [108]. The Agarwal and O'Neil model [25] overpredicts the sedimentation rate (indicated by the bottom line), the Wang et al. [35] model underpredicts the sedimentation rate, while the Gidaspow model [109] is in excellent agreement with experiments. While both the Wang et al. and the Gidaspow models predicted solid-liquid interface evolution agrees with experiments, the Agarwal and O'Neil model overpredicts the interface. These trends can be directly related to the drag coefficient predicted in the range of solid fractions of interest here, i.e. Wang-Beckermann gives the highest drag at a given solid fraction, Gidaspow gives intermediate

drag, and Agarwal and O’Neil gives the lowest drag. Despite the Gidaspow model’s good overall agreement with this experiment, it is emphasized that the conditions are not directly analogous to equiaxed solidification. Equiaxed dendrites can have a considerably higher surface area to volume ratio compared to spheres, so drag models developed for spherical particles may underestimate the drag induced on the free-floating dendritic structure. Because the Wang-Beckermann model was developed specifically for such structures and gives satisfactory predictions for the settling rates of perfect spheres, it is adopted for the remainder of this work.

Table 6.1. Relationships for the drag coefficient of as a function of liquid volume fraction and grain Reynolds number

Model	Drag coefficient, C_D
Agarwal and O’Neil (1988) [25]	$C_D = \frac{48C_{ke}g_g}{Re_g^*} + C_{ie}$ $C_{ke} = \begin{cases} \frac{1}{2} \left(\frac{(1-g_g)^3}{g_g} \right) \frac{1+4.7g_g}{1-1.83g_g} & \text{if } g_p \leq 0.5 \\ \frac{25}{6} & \text{if } g_p > 0.5 \end{cases}$ $C_{ie} = \begin{cases} \frac{24(10^E - 1)}{Re_g^* [1.0 - 0.9(0.75 - g_g)^{1/3} g_g^{2/3}]^3} & \text{if } g_p \leq 0.5 \\ \frac{7}{3} & \text{if } g_p > 0.5 \end{cases}$ $E = 0.261Re_g^{*0.369} - 0.105Re_g^{*0.431} - \frac{0.124}{1 + (\log_{10} Re_g^*)^2}$
Gidaspow (1994) [109]	$C_D = \begin{cases} \frac{24}{Re_g} (1 + 0.15Re_g^{*0.687}) g_g^{-2.65} & \text{if } g_p \leq 0.2 \\ \frac{4}{3} \left[150 \frac{g_p}{Re_g^*} + 1.75 \right] & \text{if } g_p > 0.2 \end{cases}$
Wang et al. (1995) [35]	$C_D = \frac{16 \beta^2 (1 - g_g)^2}{3 Re_g \frac{g_g}{g_g}}$ $\beta = \left[\frac{9}{2} g_g \frac{2 + 4/3 \eta^5}{2 - 3\eta + 3\eta^5 - 2\eta^6} \frac{1}{1.26 \log_{10} \left(\frac{1}{0.163} \right)} \right]^{1/2}$

†where $Re_g^* = (1 - g_g)Re_g$

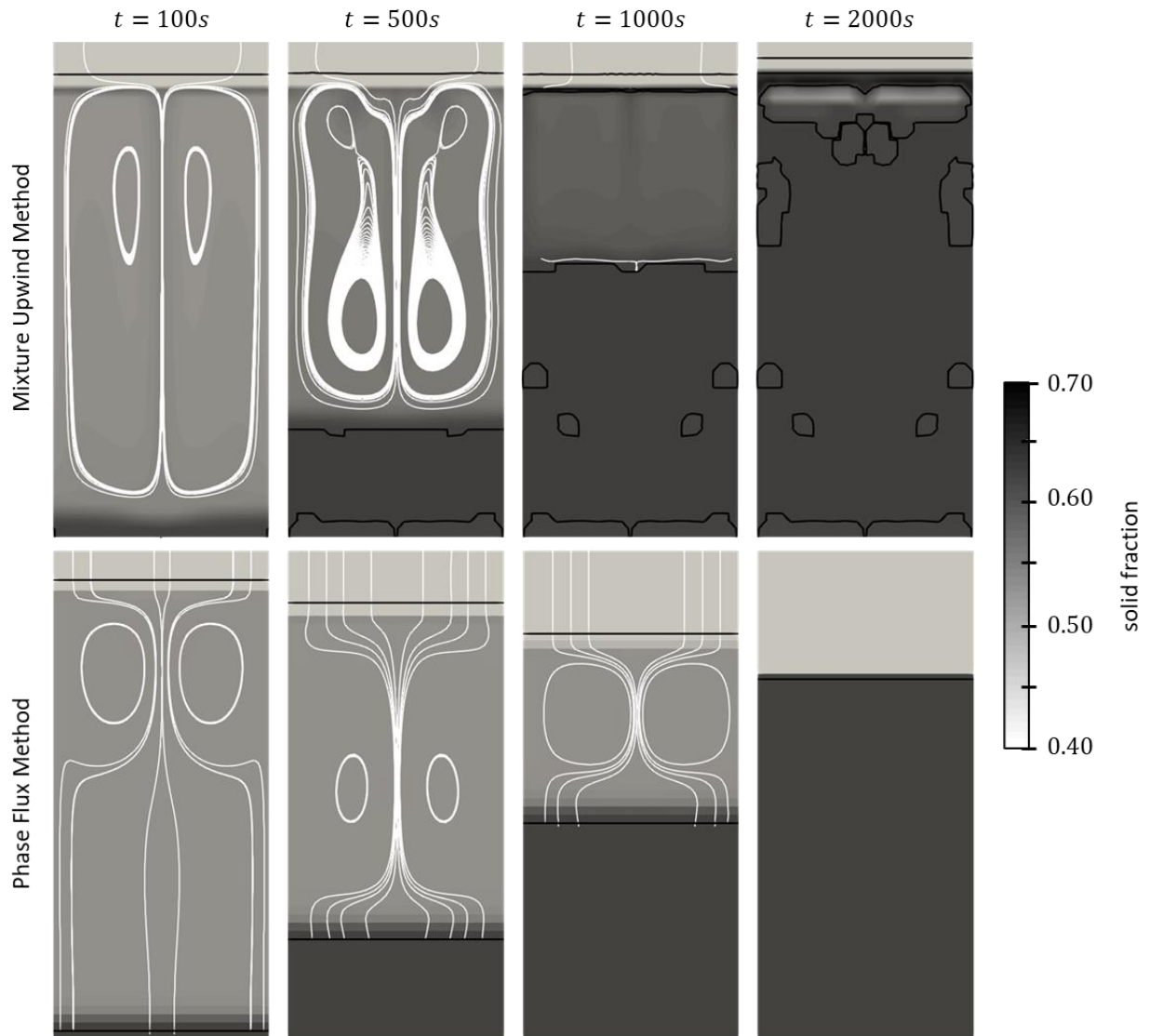


Figure 6.4: Solid volume fraction field and solid velocity streamlines at different times for the settling validation case. The top block line indicates the solid-liquid interface and the bottom black line indicates the packing interface. The mixture upwind method of ref. [73] predicts unphysical settling and accumulation behavior, while the phase-flux method proposed in Section 4.3.2 predicts the physically correct solution.

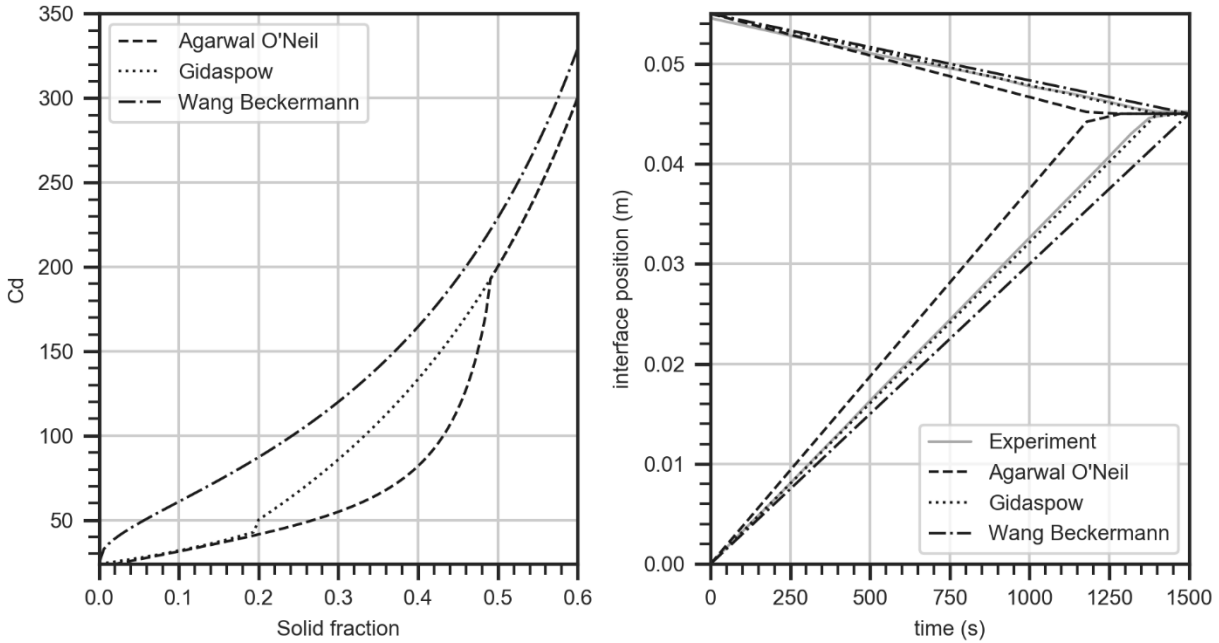


Figure 6.5: Comparison of the (left) drag coefficients and (right) the evolution of the solid-liquid interface and the packing interface for various drag models.

6.3 Solidification Numerical Benchmarks

Having verified the pressure-velocity coupling on co-located grids and the discretization of phase fluxes, the full solidification model is applied to the SMACS numerical benchmark problem [112]. This benchmark is based on the well-known Hebditch-Hunt experiment [113], where an insulated cavity is cooled from two vertical side walls. Because the casting is symmetric about its vertical centerline, only the right half of the domain is simulated using a 2-D domain that is $5 \text{ cm} \times 6 \text{ cm}$. A schematic of the test case is shown in Figure 6.6. Two different alloys are investigated: Pb-18wt%Sn and Sn-10wt%Pb. Thermophysical properties and phase diagram information are provided in . The analytical microsegregation is used in this study assuming no back-diffusion of solute into the solid phase (i.e. the Scheil assumption). It is noted that shrinkage is not considered in these numerical simulations. For columnar solidification, the solid phase is assumed fixed at the liquidus so the only source of relative motion causing macrosegregation is enriched interdendritic liquid motion driven by thermosolutal buoyancy. For equiaxed solidification, the solid phase is mobile until some critical solid fraction and an additional source of relative motion is the settling of depleted grains.

In Section 6.3.1, the solidification model is applied to columnar solidification of Pb-18wt%Sn. Reference solutions are available in ref. [72], focused on the prediction of channel segregates. Channel segregates are localized regions of intense segregation, presenting as thin columns. On an experimental micrograph cross-section, these highly enriched regions manifest themselves as small circles, so they are often referred to as “freckles”. Numerical simulation of freckle formation is difficult because the instability that initiate and propagate their formation occurs on a length scale below the resolution of volume-averaged models. Therefore, the numerical prediction of channel segregates will strongly depend on the mesh size and numerical methods used to solve the transport equations. Because previous authors [49,72,114] have been able to obtain reasonable predictions for this benchmark on co-located grids without special treatment of the drag term, it is of interest to investigate possible changes in the numerical predictions when the face-based drag formulation is used.

After the columnar benchmark, the solidification model is applied to a case of equiaxed solidification in Section 6.3.2. No reference solutions exist for this system, so Sn-10wt%Pb is chosen based on its cooperative thermal and solutal buoyancy forces. This alloy provides a closer analogue to the Al-Cu alloys investigated for DC casting later in this work. A comparison between the cell-based and face-based drag formulations, and a comparison between the discrete and diffuse phase flux transitions are made. Two different packing fractions for globular grains ($g_{si} = 1$) are examined, $g_{s,p} = 0.15$ and $g_{s,p} = 0.30$, to investigate situations where buoyancy forces drive flow across the packing interface cells, and situations where drag forces effectively damp flow across the packing interface cells.

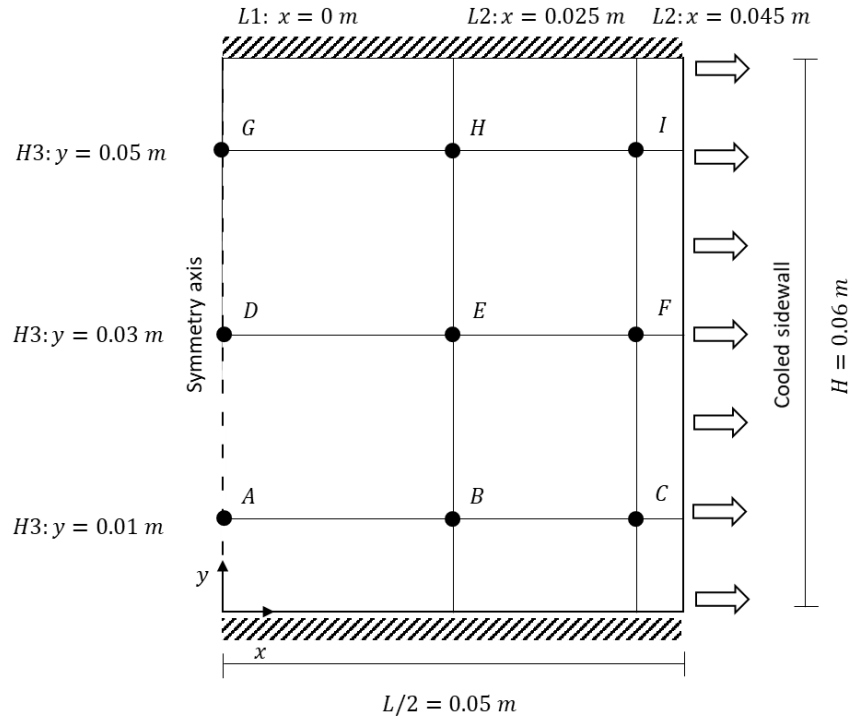


Figure 6.6: Description of the SMACS benchmark case and domain including thermal conditions and locations used for evaluating model predictions.

6.3.1 Columnar Solidification Benchmark

Before proceeding to the numerical results, the nature of composition channel formation is discussed. Composition channels are initiated by convective instabilities that form near the liquidus front. For most alloys, including the lead-tin alloy studied here, solute is rejected into the liquid during solidification which locally changes the liquid density and induces solutal buoyancy forces. If the solutal buoyancy forces are strong enough to overcome the drag force exerted by the mushy zone, enriched liquid will be transported by the local flow field. When the enriched liquid is driven towards regions of lower solid fraction (i.e. towards the liquidus front), solidification will be delayed or even reversed due to the thermodynamic conditions. The local permeability of the mushy zone will increase, allowing subsequent enriched liquid to flow in this direction and propagate a channel.

The evolution of channel propagation using the cell-drag formulation is shown in Figure 6.7. To remain consistent with the reference solutions [72], a grid spacing of 0.25 mm and constant time step of 0.005 s are used. In the rigid mush, positive solutal buoyancy dominates the

negative thermal buoyancy and a counterclockwise flow cell develops in the casting. Channel segregates are present in the upper right corner by 25 seconds. As solidification progresses, channels continue to initiate and propagate in the upper right quadrant of the casting. The extradendritic liquid is continuously enriched during solidification due to the transport of enriched interdendritic liquid out of the rigid mush. As a result, the upper left-hand corner, which is the last to solidify, is positively segregated. The bottom right region is negatively segregated due to the counterclockwise circulation of interdendritic liquid.

Figure 6.8 shows the final composition profiles for both drag formulations at different mesh spacings. The qualitative predictions of both formulations are similar and converge to approximately the same solution at a grid spacing of 0.25 mm. The face-drag formulation tends to predict more solute enriched channels than the cell-drag formulation on coarser grids. This is attributed to the different methods used to calculate permeability at the face. In the cell-drag formulation, the permeability term is interpolated by central differencing, while in the face-based drag formulation, the solid fraction is interpolated to the face by central differencing before permeability is calculated. Because permeability is a highly nonlinear function of solid fraction, the face-drag formulation will exert less resistance to the buoyancy driven flow near the liquidus front than the cell-drag formulation, which allows channel segregates to form more readily.

Figure 6.9 shows the composition profiles along $x = 0.005$ m at various grid spacings. The quantitative predictions of both formulations are very similar and converge to approximately the same solution at a grid spacing of 0.25 mm. As the grid is refined from 1 mm to 0.25 mm, the number of channels increases from three to five. Additionally, the average width of the channels decreases, and the level of positive segregation in the channels increases, as the grid is refined below the length scale of the channels. To investigate the grid dependence of the two models, the global macrosegregation index is used:

$$GMI = \frac{1}{V} \sum_{p=1}^n \left| \frac{C_p - C_o}{C_o} \right| dV \quad (6.1)$$

The agreement between the coarsest and finest grids is slightly worse for the face-based drag formulation compared to the cell-based drag formulation, attributed to the numerical diffusion introduced by the former method. However, a convenient feature of the proposed face-based drag

formulation is the ability to bias the solution towards a cell-based drag formulation using the blending factor in Eqn. (4.33). Either the blending factor or mesh refinement can be used to remove the numerical diffusion if desired. Nonetheless, the macrosegregation predicted by each drag formulation are essentially equivalent.

Since channel formation is highly dependent on the buoyancy-drag balance, it should be expected that any attempt to improve the consistency in handling these terms in the momentum formulation would improve the consistency in numerical predictions. In the porous plug case, it was demonstrated that the cell-based drag formulation can lead to spurious oscillations in the momentum field. Such oscillations could set up the proper conditions to initiate channels in the numerical solution. However, because the drag term is introduced continuously in columnar solidification, the cell-drag formulation does not suffer from this discretization error. In the next section, the two drag formulations are compared for equiaxed solidification where discontinuities in the drag term exist.

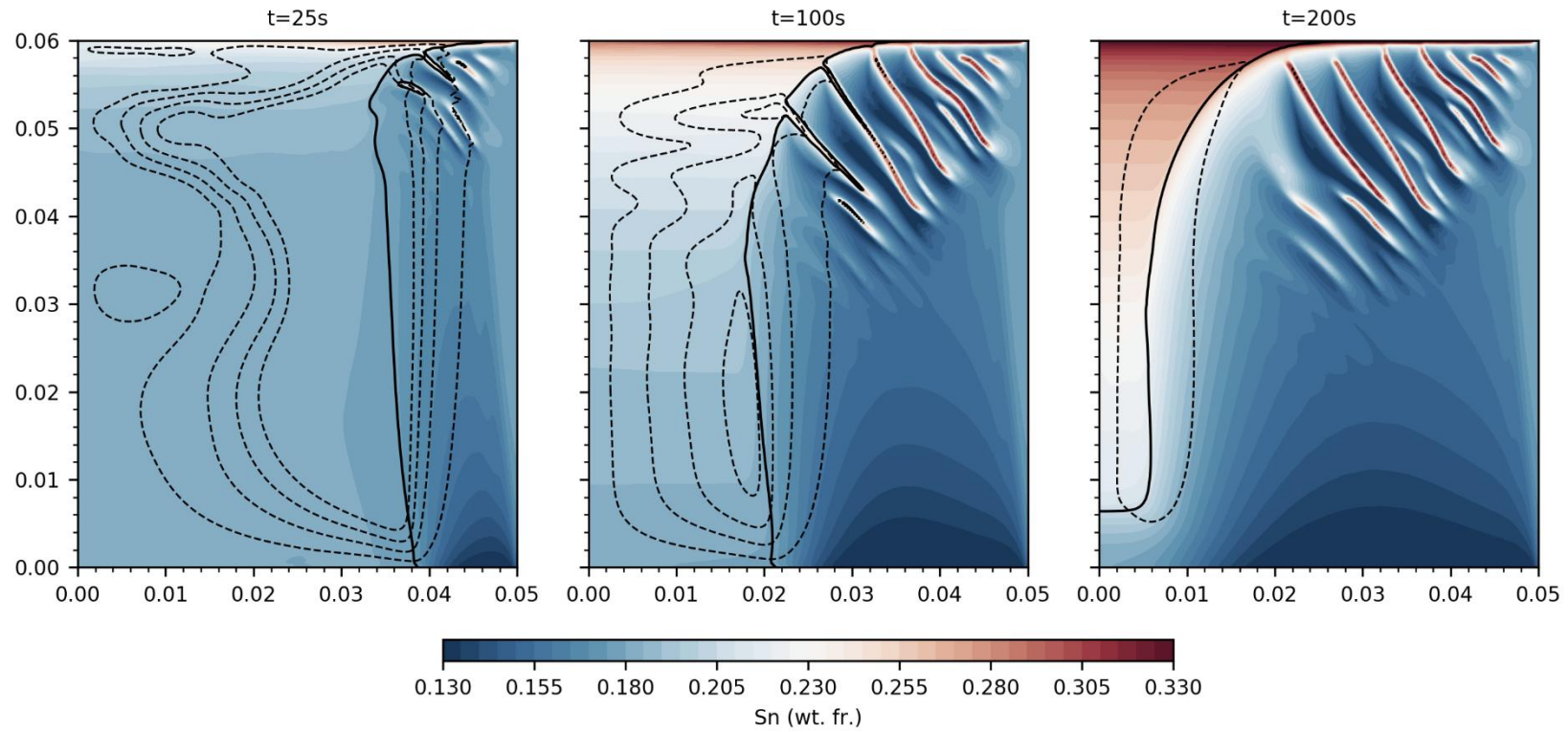


Figure 6.7: The bold solid line show the columnar dendrite tip front and the light lines are streamlines varying from -0.06 to -0.01 kg/s with constant increments.

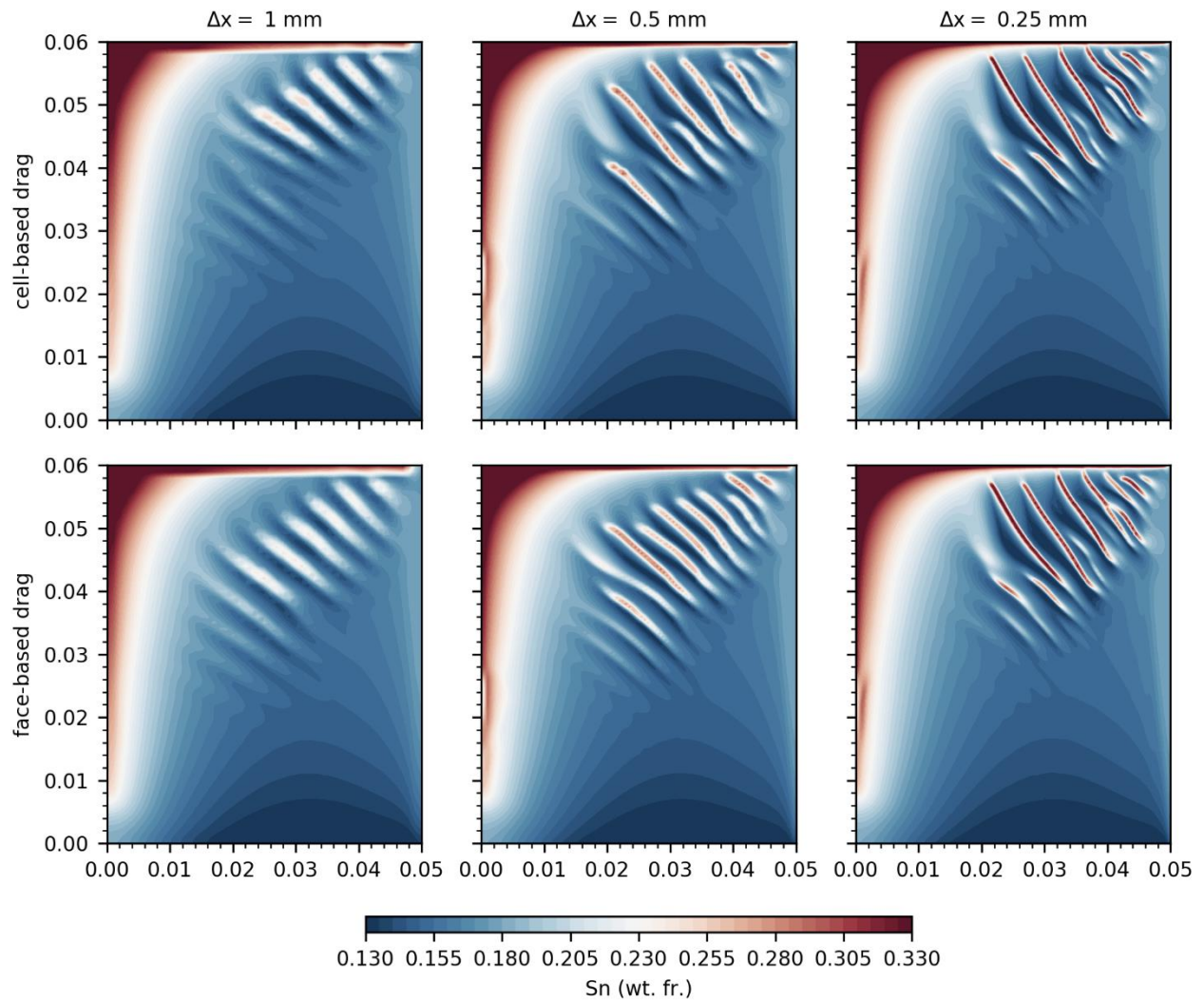


Figure 6.8: Final composition profiles of the Hebditch-Hunt benchmark case for different mesh spacings ($\Delta x = 2, 1, 0.5,$ and 0.025 mm) and momentum schemes.

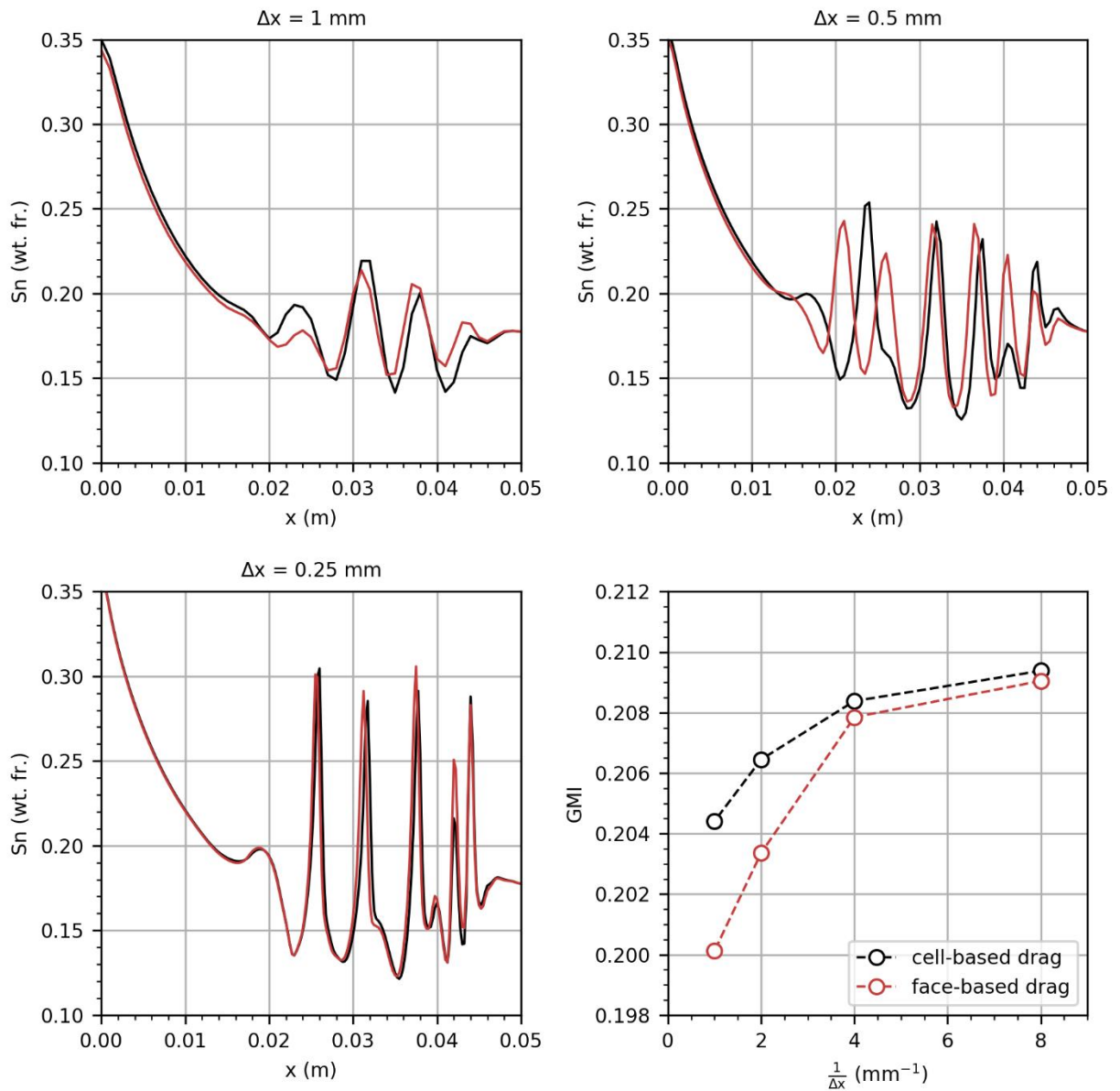


Figure 6.9: Comparison of composition profiles at various grid spacings, and the mesh convergence of the global macrosegregation index for the cell-drag and face-drag momentum formulations.

6.3.2 Equiaxed Solidification Verification

In this section, the SMACS numerical benchmark is performed for equiaxed solidification of Sn-10wt%Pb. The focus is shifted towards the formation of numerical artifacts in models of equiaxed solidification, presenting as localized regions of highly depleted cells. The two drag formulations are compared to investigate their behavior in the presence of a discontinuous drag term at the packing interface. For the cell-based drag formulation, a discrete transition ($\eta = 0$) of the solid phase flux is used. For the face-based drag formulation, both a discrete ($\eta = 0$) and a diffuse ($\eta = 1$) transition of the solid phase flux are investigated.

Macrosegregation Evolution

Figure 6.10 compares the predicted evolution of Pb composition fields, flow fields, and the packing interface for each method using a packing fraction of $g_{s,p} = 0.15$. Since no superheat is provided, the slurry region quickly occupies the entire domain upon cooling from the right wall. Buoyancy forces near the chill drive a clockwise flow cell. For the cell-based drag formulation, the control volumes along the bottom wall become packed after a few seconds. Similarly, the control volume along the chilled wall up to a height of 0.05 m are packed by 15 s. At the onset of packing, the strength of the natural convection along the vertical packing interface is high, indicated by the closely spaced streamlines. An area of severe depletion ($< -20\%$) forms near the right wall, due to the significant flow across the packing interface. The packing interface stalls in this region as the interface cells solidify and continue to shed solute. After 50s, thermal and solutal mixing of the slurry is sufficient enough to reduce the strength of the flow and the “L-shaped” packing moves towards the upper right corner. During this process, the slurry becomes positively segregated as depleted grains settle out of suspension. When the entire cavity is occupied by the rigid mush, the clockwise circulation of enriched interdendritic liquid causes a region of positive segregation along the bottom wall.

For the face-based drag formulation with a discrete solid flux transition ($\eta = 0$), the general development of macrosegregation is similar to the previous case, but with a few exceptions. The vertical wall packs slower and is 35 mm below the previous prediction at 15 s. As solidification progresses, the grains tend to accumulate along the horizontal packing interface at a higher rate causing a less angular packing interface. The region of positive segregation along the bottom wall

at the end of solidification is similar to the previous cause, however the positive segregation in the upper left quadrant is significantly less. This is attributed to the lower predicted volume of high depleted cells. Instead of composition artifacts manifesting as one large feature, the depleted cells are now distributed along the right wall and confined to a few local cells. The spacing between the depleted cells decreasing as solidification progresses and the thermosolutal buoyancy forces weakens. The formation of these artifacts are qualitatively similar to those reported for static casting of aluminum alloys on staggered grids by Plotkowski and Krane [45,46]. The macrosegregation predictions using the diffuse solid flux transition ($\eta = 1$) are nearly identical to the discrete case ($\eta = 0$), the only difference being the suppression of composition artifacts along the right wall.

If the proposed mechanism that these artifacts form due to the advection of enriched liquid out of the edge of the rigid mush is valid, then reducing the permeability of these cells would tend to suppress their formation. The previous calculations are repeated with a packing fraction of $g_{s,p} = 0.30$, shown in Figure 6.11. The permeability along the packing interface is several orders of magnitude less for this case, and thus, the flow across these control volumes should be negligible and the solution free from artifacts. While this is true for the face-based drag formulation, the volume of highly depleted control volumes is significantly increased for the cell-based drag formulation. The only possible explanation for this behavior is strong oscillations in the mixture flux across these control volumes, similar to those observed in the porous plug case in Section 6.1.

Figure 6.12 shows histograms of the artifact cells for each of the previous cases. Again, artifacts are defined as have segregation below -20% of the nominal value in this case. For the cell-drag formulation, an increased packing fraction noticeably increases the occurrence of artifacts but does not necessarily increase the severity. In the most extreme cells for a packing fraction of $g_g^c = 0.15$, the depletion is nearly 90% below the nominal value. For the face-drag formulation, only five artifact cells appear when a discrete transition is used for a packing fraction $g_g^c = 0.15$, and no artifacts form for a packing fraction of $g_g^c = 0.30$. The solution is completely free of artifacts when the diffuse solid flux transition is used.

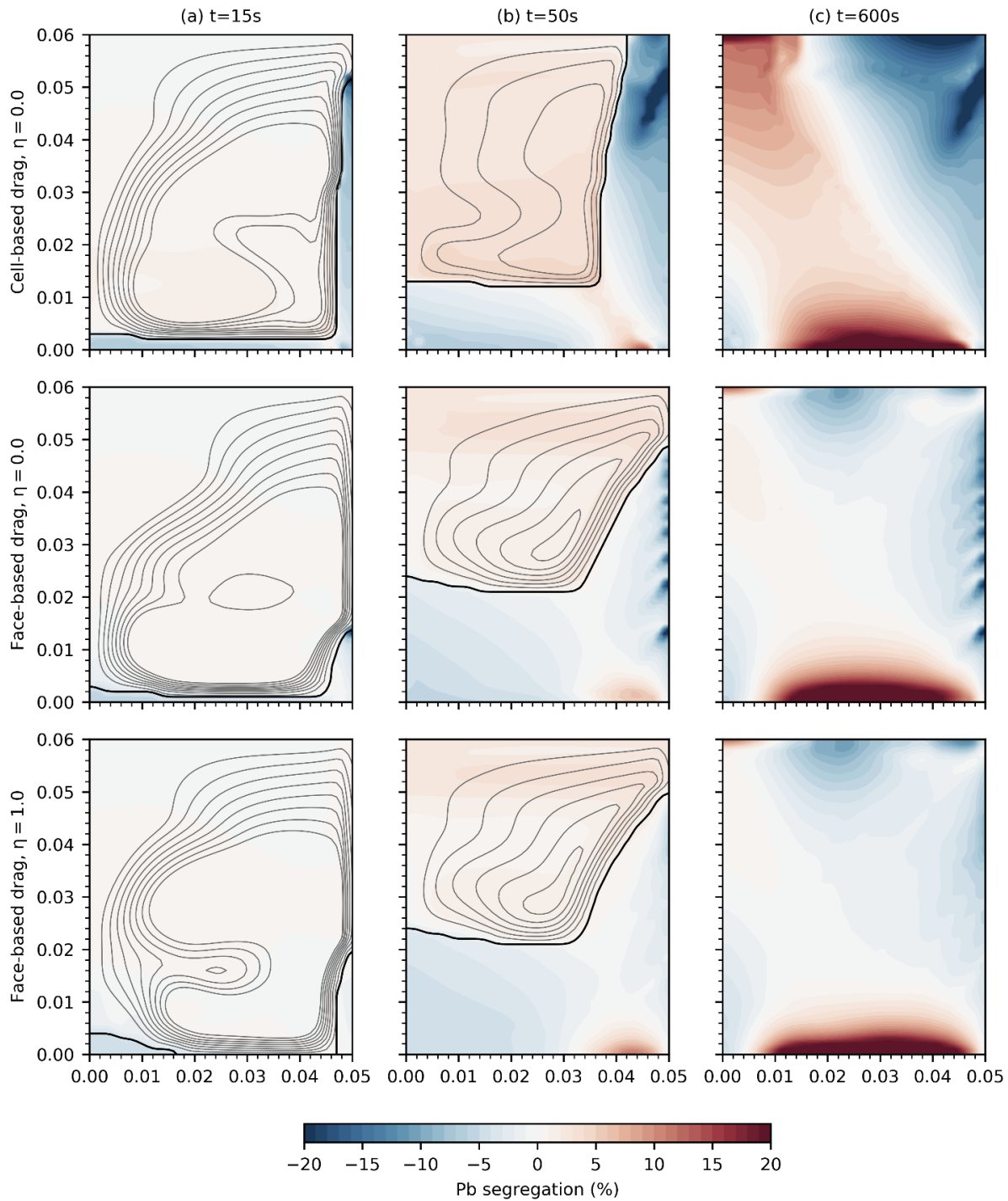


Figure 6.10: Pb composition fields at intermediate times during solidification for the cell-based drag and face-based drag formulations evaluated with different levels of diffusion in the solid flux, $\eta = 0.0$ and $\eta = 1.0$. The bold line show the packing interface and the light lines are streamlines varying from 0.05 to 0.3 kg/s in increments of 0.025 kg/s. Simulations were performed with a grid spacing of 1 mm and a critical packing fraction of $g_g^c = 0.15$.

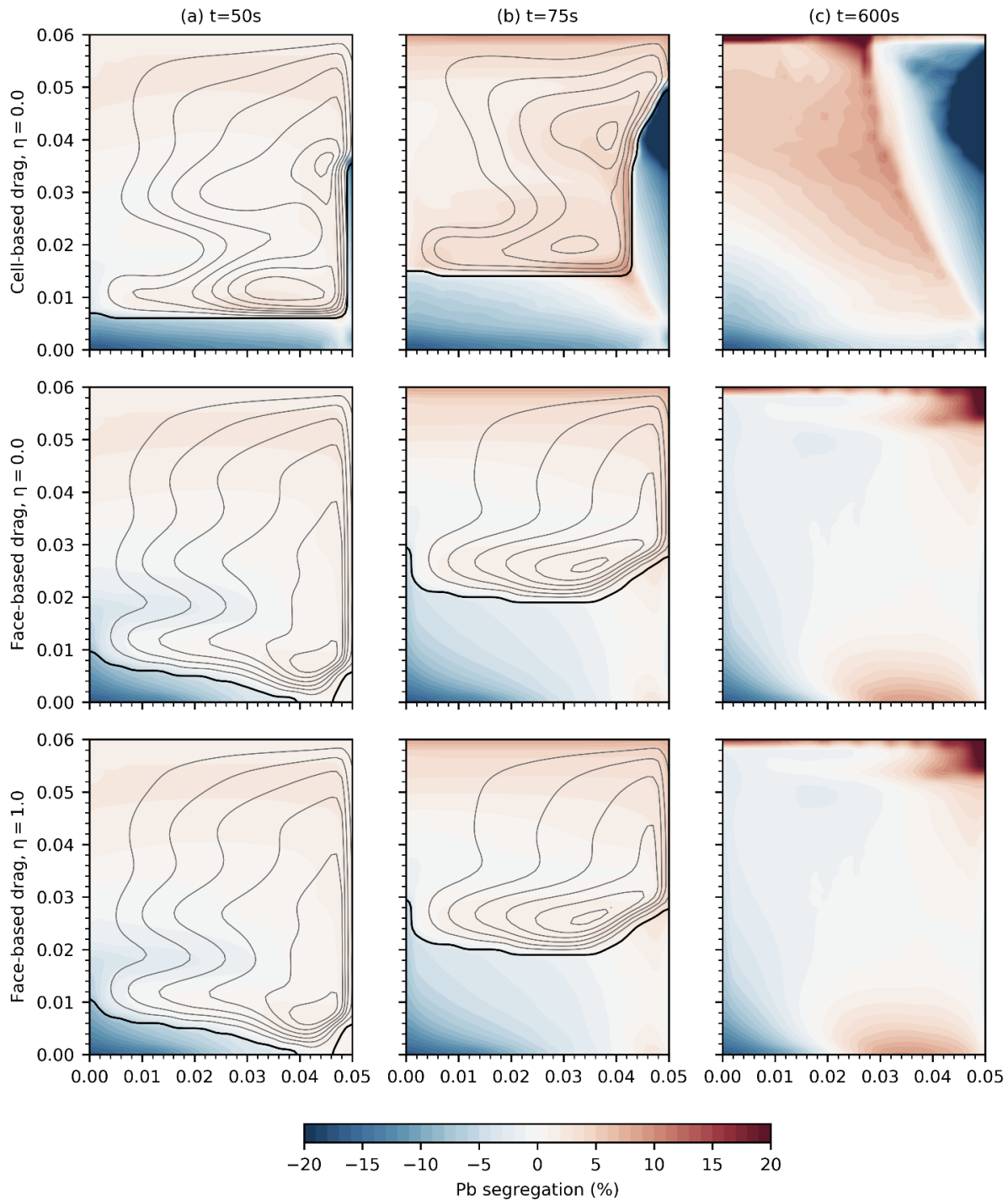


Figure 6.11: Pb composition fields at intermediate times during solidification for the cell-based drag and face-based drag formulations evaluated with different levels of diffusion in the solid flux, $\eta = 0.0$ and $\eta = 1.0$. The bold line show the packing interface and the light lines are streamlines varying from 0.05 to 0.3 kg/s in increments of 0.025 kg/s. Simulations were performed with a grid spacing of 1 mm and a critical packing fraction of $g_g^c = 0.30$.

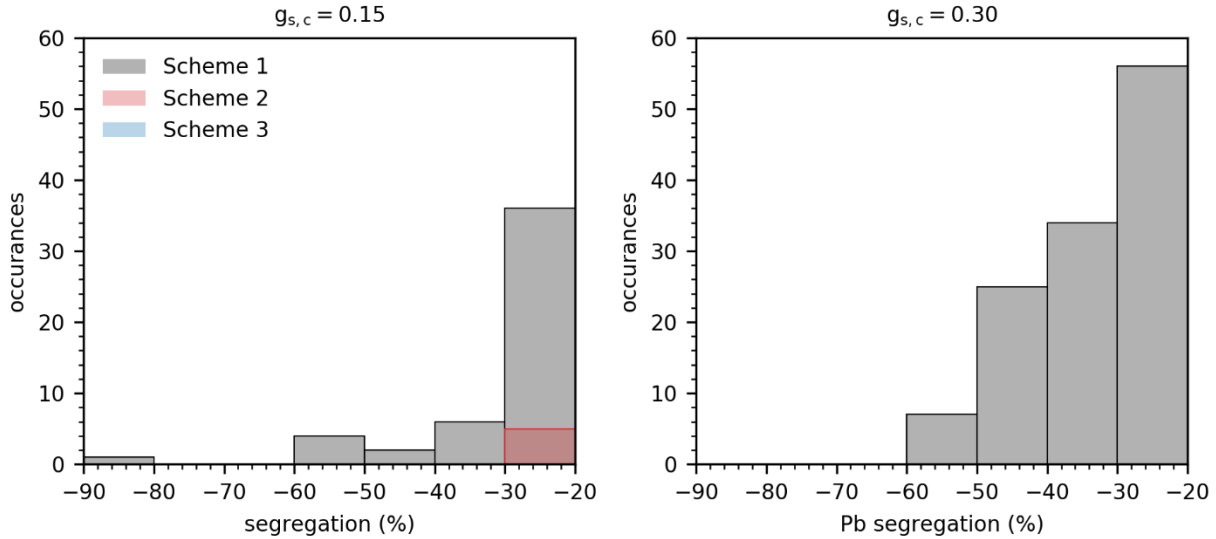


Figure 6.12: Histograms of the depleted composition artifacts for the cell-based and face-based drag formulations. Simulations were performed with a grid spacing of 1 mm.

Grid Dependence Study

A common feature of previous equiaxed solidification models is the inability to obtain composition predictions that are not highly sensitive to the numerical grid due to the formation of composition artifacts. Therefore, it is important to determine if the face-based drag formulation and the diffused solid flux transition improve the grid dependence of the solution. Three different grid sizes evaluated: 3 mm, 2 mm, and 1 mm.

The predicted Pb segregation fields are shown in Figure 6.13 for a packing fraction of $g_{s,p} = 0.1$, and in Figure 6.14 for a packing fraction of $g_{s,p} = 0.30$. The overall macrosegregation trends are similar for an individual case when the grid is refined. However, the size and severity of the depletion zone along the right wall demonstrates a significant grid dependence when the discrete solid phase flux transition ($\eta = 0$) is used. These artifacts begin to form at a grid spacing of 2 mm, accompanied with an increase in the level of positive segregation in the slurry. Although no such model is included here, it is noted that the dendritic multiphase models use the undercooling in the slurry to predict the nucleation and growth of grains. Therefore, it is not surprising that the grain structures and corresponding macrosegregation would be highly sensitive to the numerical grid. In contrast to the previous method, the diffuse solid flux transition model ($\eta = 1$) exhibits excellent qualitative grid convergence and appears to be a general improvement for numerically handling the transition from the slurry to rigid mush.

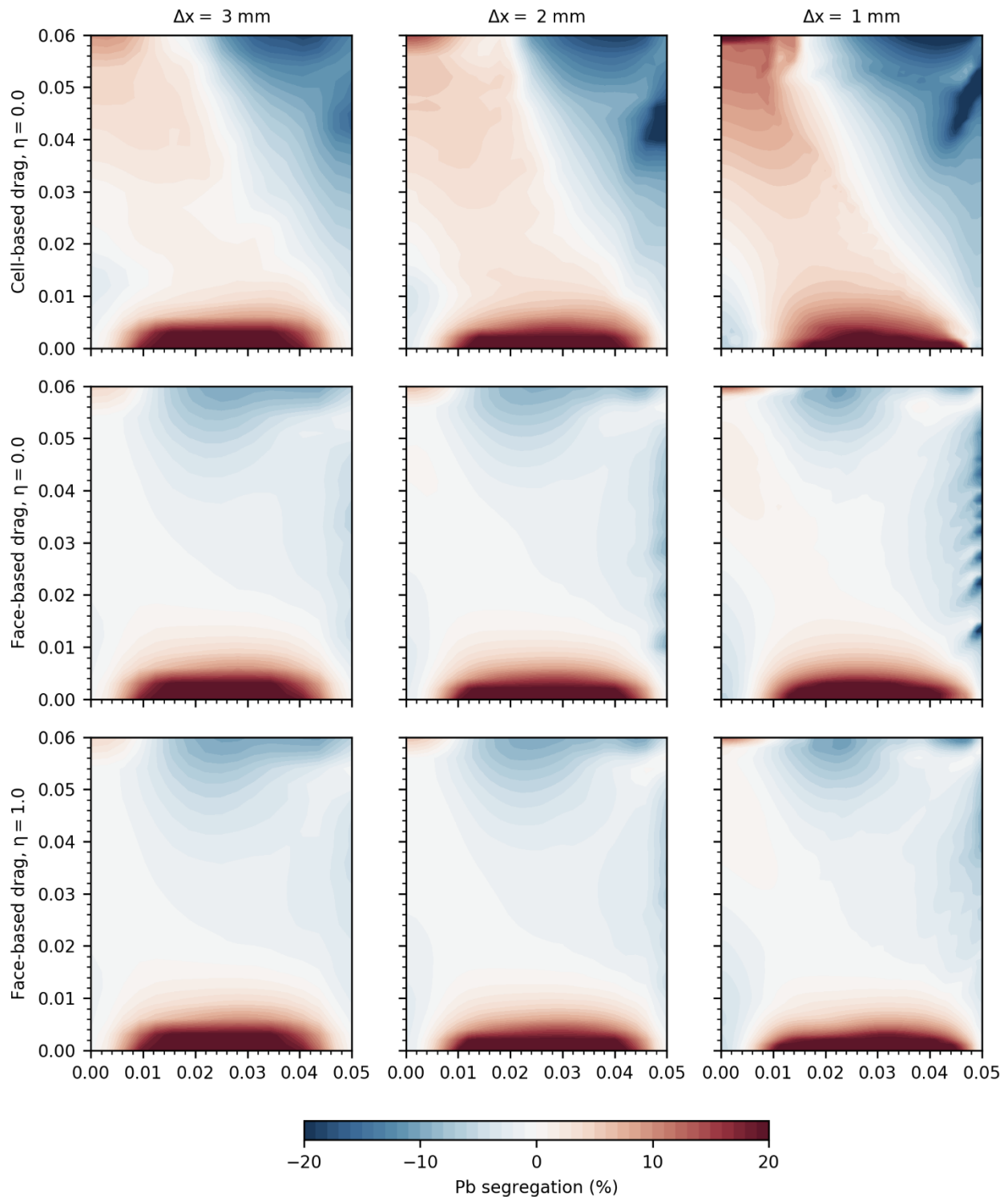


Figure 6.13: Comparison of the grid dependence of the final Pb segregation field for the cell-drag formulation and the face-based drag formulation evaluated with different levels of diffusion in the solid flux, $\eta = 0.0$ and $\eta = 1.0$. The packing fraction was $g_g^c = 0.15$ for each case.

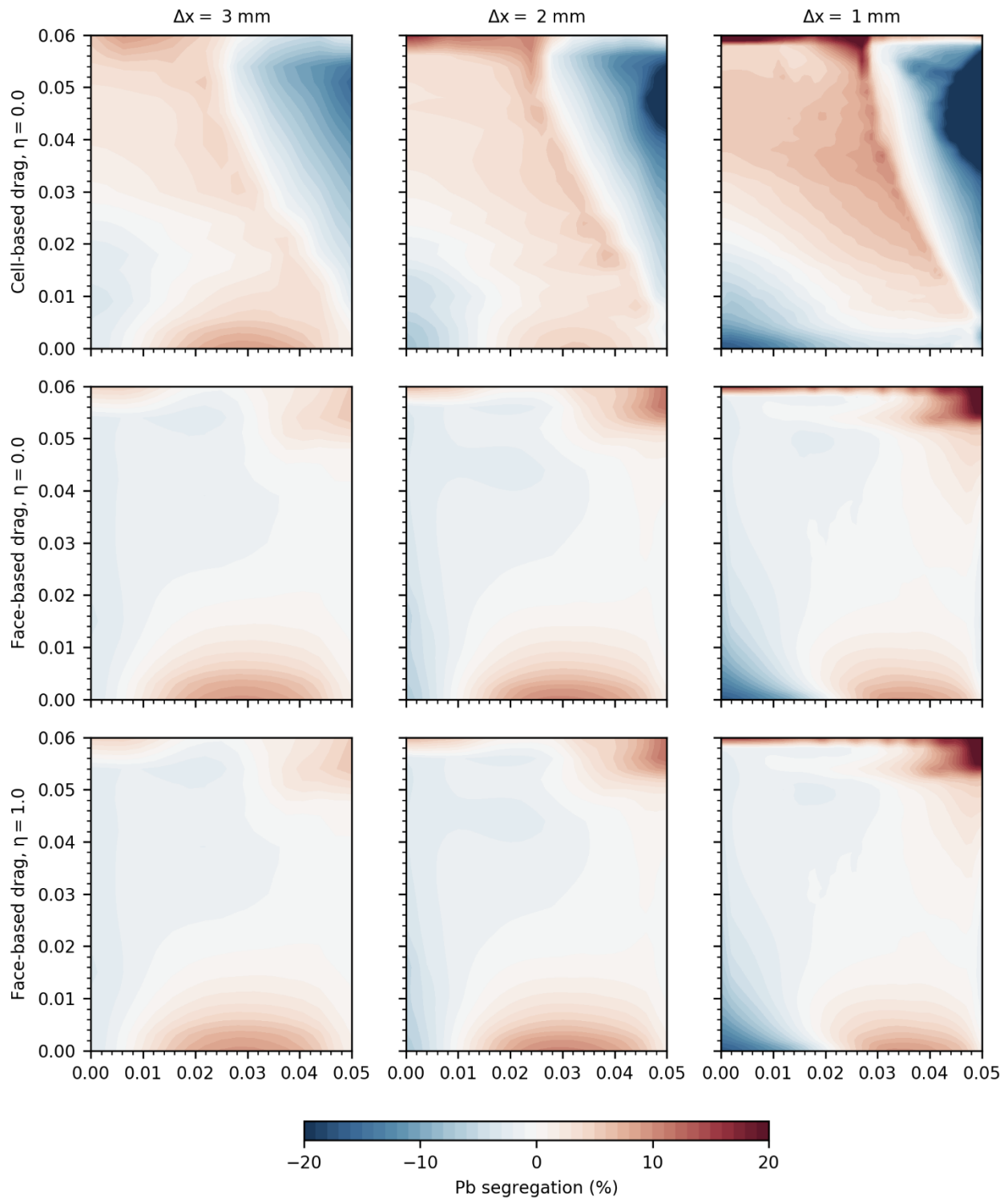


Figure 6.14: Comparison of the grid dependence of the final Pb segregation field for the cell-drag formulation and the face-based drag formulation evaluated with different levels of diffusion in the solid flux, $\eta = 0.0$ and $\eta = 1.0$. The packing fraction was $g_g^c = 0.30$ for each case.

Nature of Composition Artifact Formation

In this section, the mechanism for composition artifact formation on co-located grids with a grid spacing of 1 mm is more closely investigated by studying the development of artifacts along the packing interface. Figure 6.15 provides a series of composition field plots showing the initiation and propagation of composition artifacts along the cooled wall for the cell-based drag formulation. The problematic “stair-step” cells at the edge of the packing interface are highlighted in red with their coupled slurry cells to help visualize the outflow of enriched liquid at these locations. Once a problematic cell forms, neither the inflow nor outflow are damped using this drag formulation, even though the local solid fraction increases to high enough levels to make the cell essentially impermeable. Each “stair-step” cell has a corresponding “checker-boarding” in the local velocity field, clearly shown at $t \geq 71$ s for a packing fraction of $g_{s,p} = 0.3$. Due to this velocity “checkerboarding”, the most highly depleted cells tend to alternate every other cell along the height of the cavity, clearly demonstrating that composition formation is tied to the numerical discretization and not to some physical phenomenon. These depleted cells propagate into the cavity along the same height due to the coupled nature of the local composition field with the thermodynamic model. The advection of enriched liquid out of one stair-step cell is driven directly downward locally delaying solidification in the adjacent slurry cell, which stabilizes this packing interface orientation. This enriched liquid is then drive across another “stair-step” cell two rows below and one column over leading to the formation of another composition artifact.

Figure 6.16 provides a series of contour plots showing the initiation of composition artifacts along the right wall for the face-based drag formulation. For a packing fraction of $g_{s,p} = 0.15$, the outflow velocity from “stair-step” cells are correctly damped during solidification. Similarly, the upstream velocity is damped and has a more horizontal orientation during solidification, indicating that the flow is diverted around the “stair-step” as the cell becomes less permeable. Unlike the cell-based formulation, “checkboarding” along the packing interface cells no longer occurs. Furthermore, composition artifacts do not tend to initiate other artifacts, remaining local to individual cells. For a packing fraction of $g_{s,p} = 0.30$, the model correctly predicts negligible inflow across the packing interface and no artifacts form for this case.

Figure 6.17 provides a series of contour plots showing the initiation of composition artifacts along the right wall for the face-based drag formulation with the diffuse solid flux transition ($\eta = 1$). As the packing interface moves through control volumes, the mixture flow

across the packing interface is similar to the discrete transition model, however artifact cells no longer form due to relaxation of the requirement for the solid velocity to be zero at the packing interface. The successful removal of these artifacts without influencing the overall macrosegregation predictions confirms the suspected nature of their formation and verifies a successful method to remove them.

Based on the results from this investigation, it is suggested that the face-based drag formulation be adopted for simulations of equiaxed solidification. The cell-based drag formulation suffers from spontaneous numerical instabilities in the mixture flux that cannot be supported by physical rationale and can lead to composition artifacts. Additionally, because predictable coupling of the mixture flux and phase flux is required to suppress artifact formation, special handling of the phase fluxes to treat composition artifacts may not be effective for the cell-based drag formulation. It is further recommended to use the diffuse solid phase flux transition since it removes composition features tied directly to the numerical grid. The value of the recommended diffusion coefficient, η , is evaluated in the next section for DC casting.

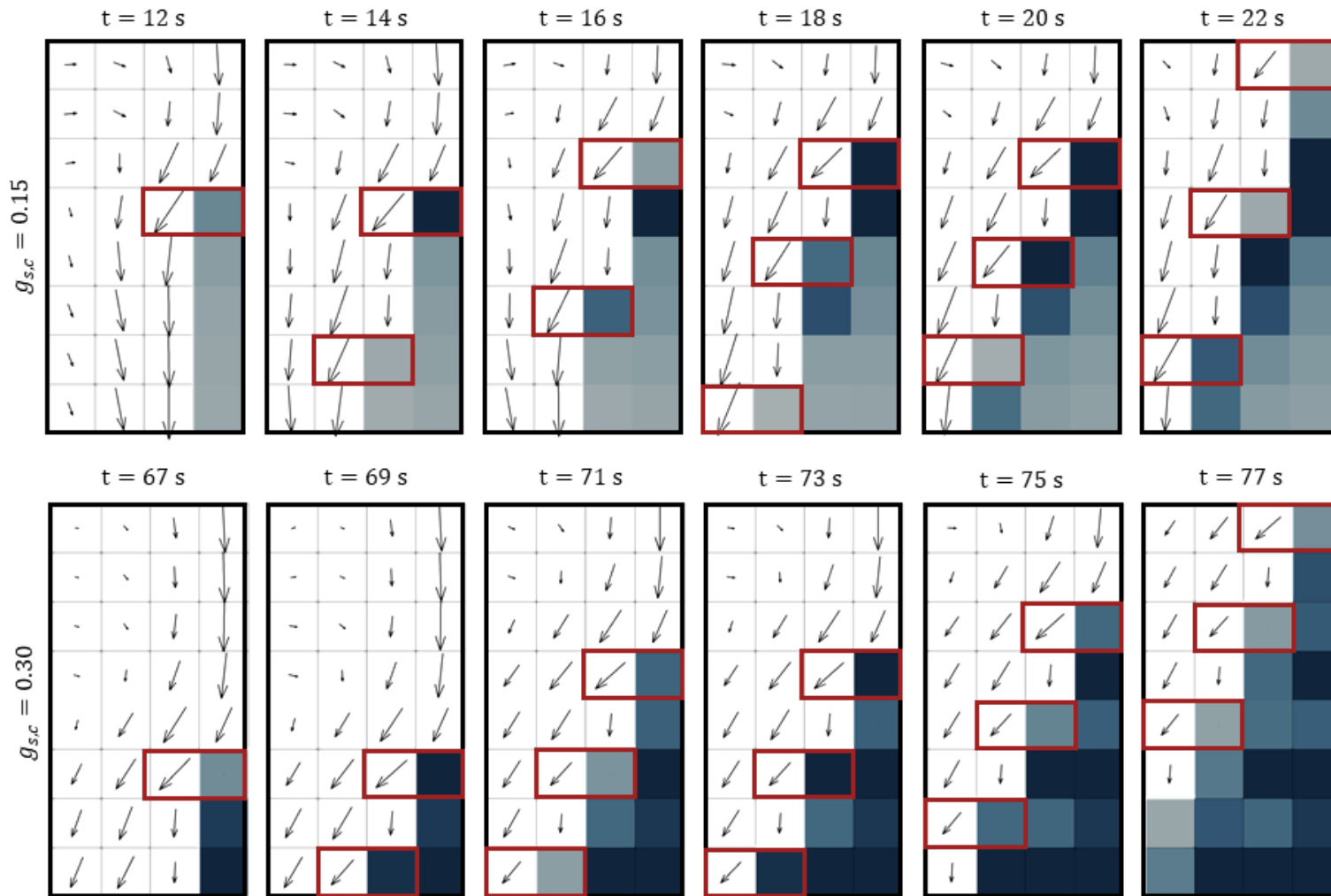


Figure 6.15: Pb composition fields in the rigid mush and velocity fields in the slurry near the packing interface for the cell-based drag formulation. Problematic “stair-step” cells which have a propensity to form composition artifacts are shown in red, paired with the outflow velocity vector. Simulations were performed with a grid spacing of 1 mm.

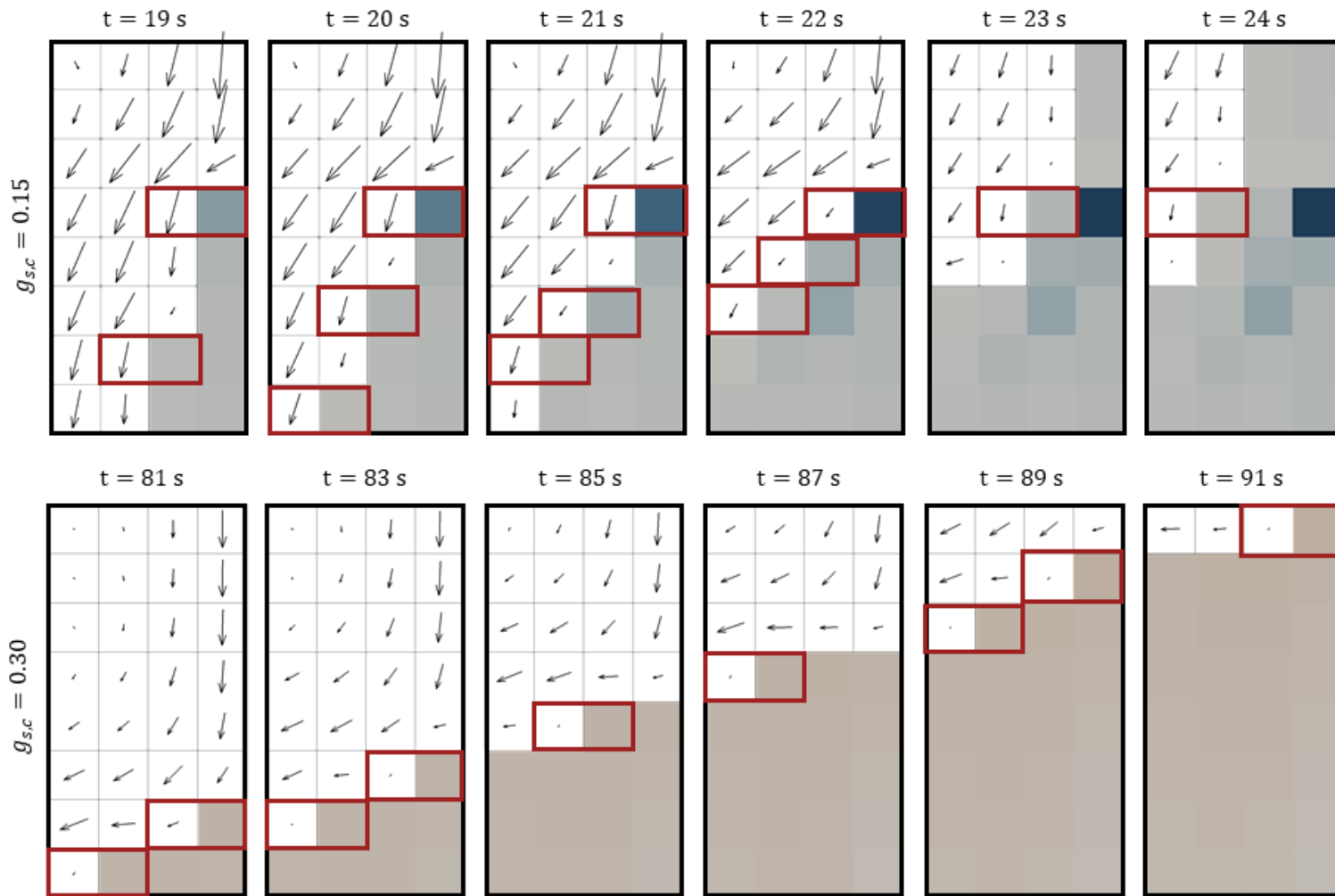


Figure 6.16: Pb composition fields in the rigid mush and velocity fields in the slurry near the packing interface for the face-based drag formulation. Problematic “stair-step” cells which have a propensity to form composition artifacts are shown in red, paired with the outflow velocity vector. Simulations were performed with a grid spacing of 1 mm.

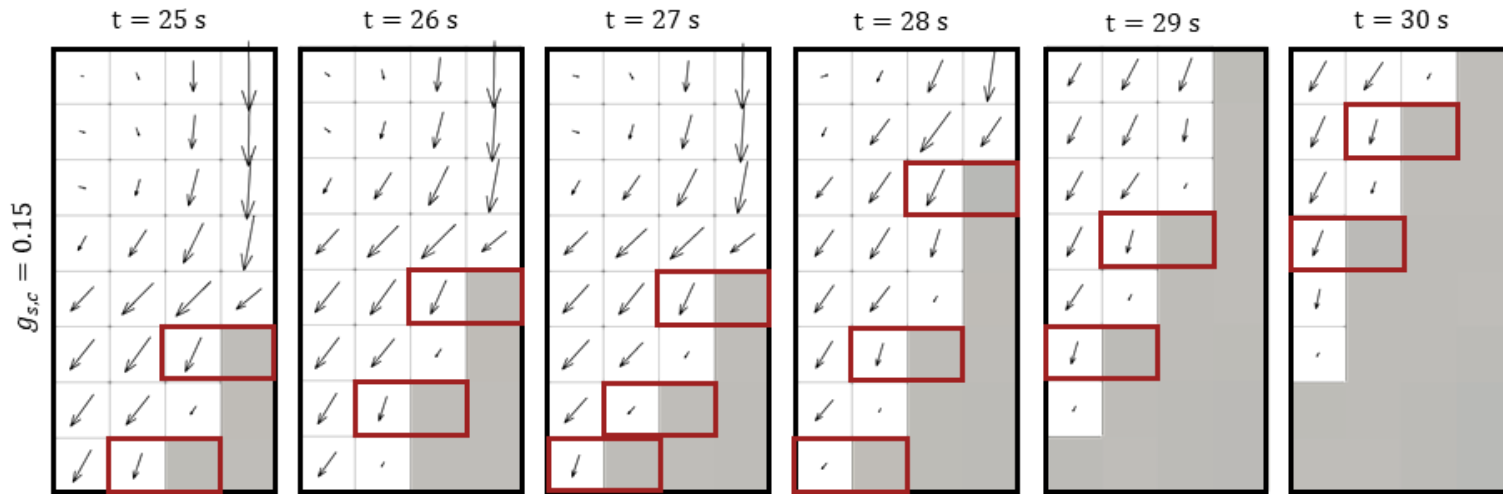


Figure 6.17: Pb composition fields in the rigid mush and velocity fields in the slurry near the packing interface for the face-based drag formulation and the blended solid-flux method ($\eta = 1.0$). Problematic “stair-step” cells which have a propensity to form composition artifacts are shown in red, paired with the outflow velocity vector. Simulations were performed with a grid spacing of 1 mm.

6.4 DC Casting Verification

The objective of this section is to directly compare the numerical predictions to data taken from an industrial scale DC casting process. In particular, the face-based drag formulation and different values of the flux diffusion coefficient, η , are evaluated. An additional source of relative phase motion compared to the previous equiaxed solidification cases is the shrinkage driven flow in the rigid mush.

Vreeman et al. [47] cast a 450 mm diameter Al-6wt%Cu billet at 60 mm/min using a hot-top mold. Grain refiner was added to promote a fully equiaxed microstructure. An aluminum rod was inserted through the top of the mold during casting to measure the sump depths, defined as the distance between the mold height and the packing interface. When the sump depth became constant, the system was assumed to be at steady state. After casting, composition was measured using X-ray fluorescence (XRF) at 10 different radial positions and two different cast lengths within the steady-state regime, for a total of 20 measurements.

To simulate this process, a 2-D axisymmetric 225 mm \times 800 mm domain is used with a uniform grid spacing of 2.5 mm. Symmetry is assumed at the centerline (the left side), while heat is extracted from the outer radius (the right side) through the mold and direct chill. Because boundary conditions were not provided in ref. [14], a mold height 70 mm is assumed with a heat transfer coefficient of 150 Wm⁻²K⁻¹. Below the mold, impingement of the water jets is assumed to occur over 10 mm with a heat transfer coefficient of 20,000 Wm⁻²K⁻¹. Film boiling is assumed to occur over the remainder of the left side with a heat transfer coefficient of 10,000 Wm⁻²K⁻¹. Additionally, an isothermal inlet (943 K) is assumed across the entire top surface. Although the casting trial fed liquid metal through a constrained inlet, the opening was wide enough that the inflow was immediately entrained to the mold. The prior assumption will not affect macrosegregation predictions since none of the mechanisms for relative phase motion are changed [49]. Finally, a zero gradient condition is assumed along the bottom of the domain. The thermophysical properties for Al-6wt%Cu used in this study are provided in Table A1.

Figure 6.18 shows the steady state solid fraction and mixture composition contours for three values of the flux diffusion coefficient $\eta = 0.0, 0.5, \text{ and } 1$. Going from top to bottom, the solid black lines mark the liquidus, the packing interface, the interface between the loosely packed and tightly packed rigid mush, and the solidus. The general macrosegregation features are similar for each case, consisting of a depleted centerline due to shrinkage driven flow in the rigid mush

and, to a lesser extent, the accumulation of solute depleted grains. For the higher packing fraction, the sump is about 5 mm shallower and the slurry more enriched due to a higher volume of grains is transported to the centerline. For a given packing fraction, the mushy zone shape is similar in the outer half of the billet for each value of the flux diffusion coefficient. However, the length of the loosely packed bed near the centerline increase with increasing diffusion coefficient. The loosely packed bed is primarily attributed to thermal and solutal stratification in the core of the sump. In this stratified layer, the packed bed retains a solid fraction close to the packing fraction until it passes through a region of accelerated cooling where solidification intensifies until completion. When the transition from slurry to packed states is diffused, stratification is enhanced, and the loosely packed region is lengthened.

In Figure 6.19, the steady state radial segregation profiles are compared to experiments. The profiles are nearly identical for a packing fraction of $g_{s,p} = 0.3$ since the mixture flow is sufficiently damped upon packing. For a packing fraction of $g_{s,p} = 0.15$, the centerline depletion tends to increase with level of diffusion introduced to the solid. This is attributed to the removal of the slightly depleted region near the surface. Because the current system is axisymmetric, small changes in the composition profiles at the periphery of the billet will have significant changes near the centerline due to the volume difference. Therefore, suppressing depletion near the surface tends to enhance depletion at the centerline according to solute mass conservation. In order to provide a solution that is not overly diffuse, but still retains the ability to suppress composition artifacts in equiaxed solidification, an intermediate value of $\eta = 0.5$ is recommended for the flux diffusion coefficient and used for the remainder of this work.

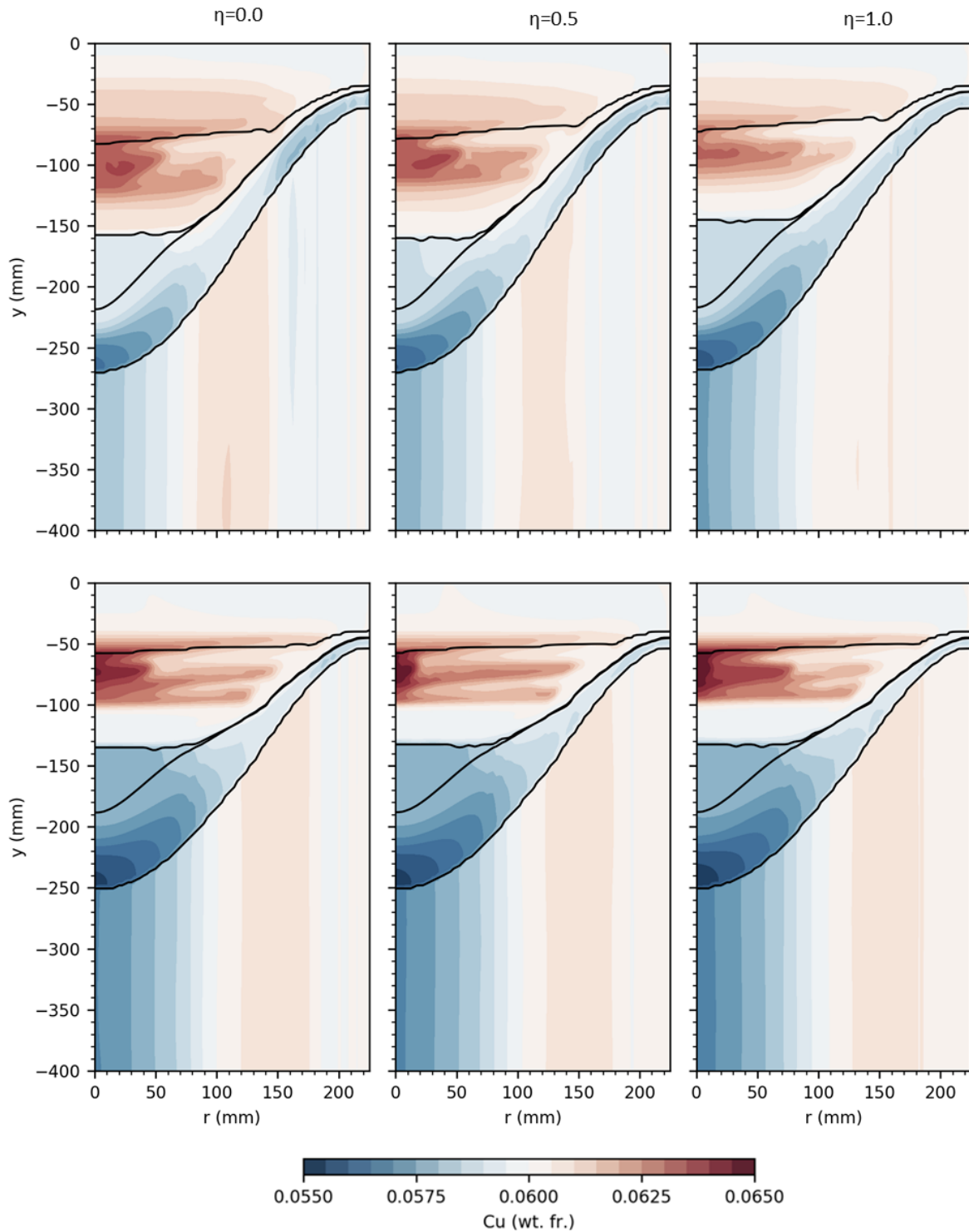


Figure 6.18: Copper (wt. fr.) for different values of the solid-flux diffusion coefficient. The contours in decreasing order of z -position are the liquidus, the packing interface, the demarcation of the loose packed grain region, and the solidus. Simulations were performed with a critical packing fraction of $g_g^c = 0.15$ (top) and $g_g^c = 0.30$ (bottom).

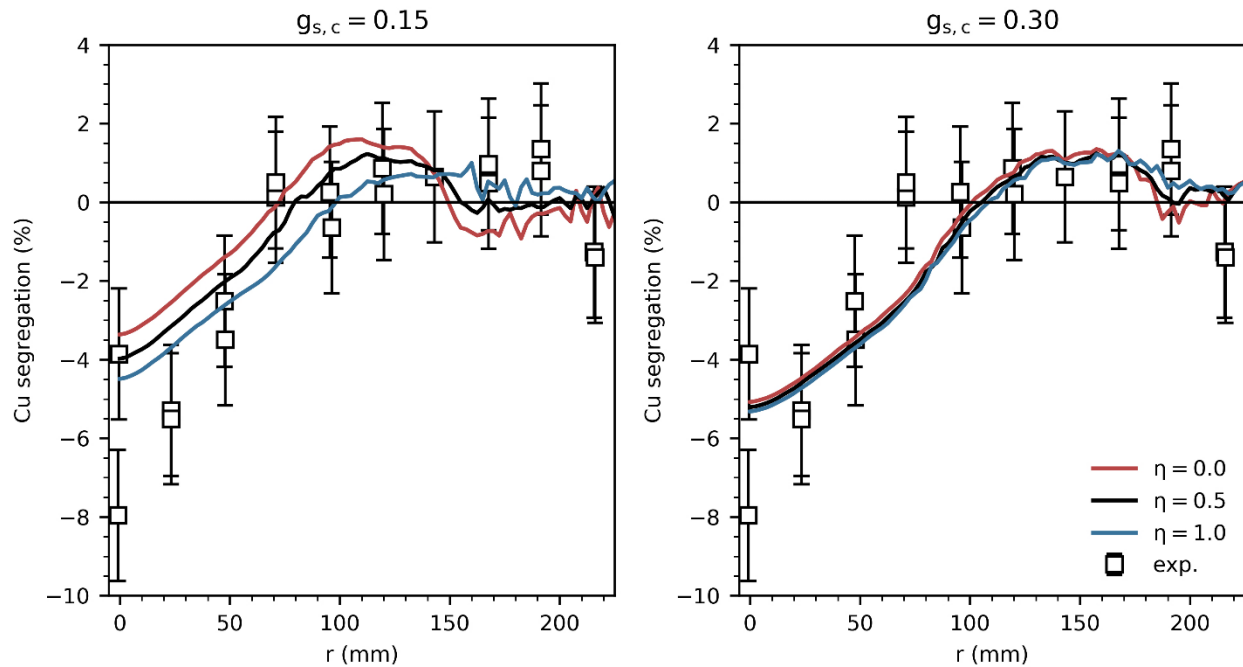


Figure 6.19: Profiles of Cu segregation from simulations with different values of the solid-flux diffusion coefficient. The model predictions are compared to the experimental profiles of Vreeman et al [47].

6.5 Summary

In this chapter, the implementation of the physical model on co-located grids was carefully evaluated through a series of incremental verification cases. First, the porous plug case verified that the cell-based drag formulation creates spurious oscillations in the flow field near discontinuous drag terms. This erroneous behavior is correct using the face-based drag formulation. Next, the settling column case verified that the Vreeman and Incropera [73] formulation of the phase flux caused inconsistent interpolations of the solid fraction, which was corrected using the phase flux formulation proposed in this work (see Section 4.3.2). Additionally, the drag model of Wang and Beckermann [35] was selected based on its conservative settling velocity predictions of spheres and extendibility to porous envelopes. Then, the solidification model was verified against the SMACS benchmark case, and while the previous developments are not necessary to reasonably predict segregation trends in simulations of columnar solidification, the face-based drag formulation and the diffuse solid phase flux formulation should be used for simulations of

equiaxed solidification. Finally, the model was verified against DC casting data from Vreeman et al. [47] and an intermediate flux diffusion coefficient of $\eta = 0.5$ was recommended.

7. SENSITIVITY OF MACROSCALE PREDICTIONS TO UNCERTAIN MICROSCALE PARAMETERS

In order to justify the use of the dendritic volume-averaged microsegregation model over the simpler analytical microsegregation model, it must be first demonstrated that this model more accurately captures the physical phenomena occurring during equiaxed. This chapter is dedicated to studying the behavior of the macrosegregation and grain structures predicted by this model in order to determine which features, if any, are necessary for modeling equiaxed solidification. First, the SMACS Pb-10wt%Sn benchmark case previously investigated in Section 6.3.2 is evaluated. Then, the DC casting case from Vreeman et al. [47] investigated in Section 6.4 is evaluated.

7.1 Description of Transport Phenomena

Before investigating the sensitivity of macrosegregation predictions to different microsegregation model inputs, the controlling transport phenomenon during equiaxed solidification are more closely investigated for the Gulliver-Scheil microsegregation model. Contour plots of the composition field, packing interface, and streamlines are shown in Figure 7.1. Since no superheat is provided and the microsegregation model assumes zero undercooling, the slurry region quickly occupies the entire domain upon cooling from the right wall. Buoyancy forces near the chill drive a clockwise flow cell and negative segregation develops near the bottom, left corner as the depleted grains accumulate. These grains become immobilized while the enriched liquid continues with the buoyancy-driven flow cell causing progressive enrichment of the slurry. A second packing interface begins to form along the chilled right wall shortly before 50 s. These two packing interfaces converge and grow vertically upwards until about 200 s when the entire domain is occupied by the rigid mush. The enriched region along the top surface, particularly near to top right wall, is the result of the progressive enrichment of the slurry until the packing interface reaches this location. At this point, the clockwise recirculation of enriched interdendritic liquid driven by solutal buoyancy widens the enrichment zone in bottom right corner and narrows the

depletion zone in the bottom left corner. The final composition field at 600 s due to this combined transport is shown in Figure 7.1.

7.2 Influence of Undercooling on Macrosegregation

To determine the total possible influence of liquid undercooling on macrosegregation development during equiaxed solidification, two primary model inputs of the dendritic multiphase microsegregation model are varied: the liquid mass diffusivity D_l and the final grain radius R_f . These inputs are varied over a range encompassing equiaxed solidification, specifically $D_l = 2 \times 10^{-9} - 1 \times 10^{-8} \text{ m}^2/\text{s}$ and $R_f = 37.5 - 500 \text{ }\mu\text{m}$. The change in predicted macrosegregation using the volume-averaged microsegregation model from the Gulliver-Scheil predictions is quantified using the mean absolute percentage error:

$$MAPE = \frac{100}{n} \sum_{P=1}^n \left| \frac{F_P - A_P}{A_P} \right| \quad (7.1)$$

where F_i is the local composition at each control volume P and A_P is the local composition predicted using the Gulliver-Scheil model. Shown in Figure 7.2, the absolute difference in the final segregation is less than 1% across the 30 calculations observing the possible parameter space for equiaxed solidification. These results indicate that liquid undercooling does not play a significant role in the final macrosegregation predictions for the current equiaxed case.

Figure 7.1 also shows contour plots of the final Pb composition fields for the volume-average model with the minimum MAPE (i.e. hemispherical tip, $R_f = 37.5 \text{ }\mu\text{m}$, and $D_l = 1 \times 10^{-8} \text{ m}^2/\text{s}$) and maximum MAPE (i.e. paraboloidal tip, $R_f = 125 \text{ }\mu\text{m}$, and $D_l = 2 \times 10^{-8} \text{ m}^2/\text{s}$). The paraboloidal tip predicts a slower growth rate than the hemispherical tip, and therefore, maintains some undercooling in the extradendritic liquid at intermediate grain radii since there is not enough interfacial area for complete mixing of the extradendritic liquid. Additionally, grain impingement, which causes complete mixing of the total liquid, does not occur until the later stages of solidification in the rigid mush. This feature of the tip model explains why there is a hump in the MAPE curve for the paraboloidal model, while the hemispherical model predicts that the deviation from Scheil decreases as R_f decreases. Although the predictions from the

paraboloidal model illustrate an interesting trend which may highlight the interplay between competing factors during grain nucleation and growth, there is no experimental evidence supporting whether this trend is realistic for the current system.

Nevertheless, these results show that some finite amount of undercooling exists in the extradendritic liquid, which slightly effects the thermal history during solidification and causes to packing interfaces to merge a few seconds before the Gulliver-Scheil model. Figure 7.3 shows the thermal and solid fraction history at the midheight, 1 mm from the chill. The thermal predictions show that the maximum MAPE case has a more pronounced recalescence curve than the minimum MAPE case and progresses with about 1 K of undercooling near the chill. Although it has been demonstrating that the volume-averaged microsegregation model can predict some physical trends that are of interest to the solidification community, these phenomena (i.e. recalescence and slight liquid undercooling) have a negligible effect of the macrosegregation predictions during equiaxed solidification. Therefore, the assumption of a well-mixed liquid phase employed in most analytical solidification paths seems reasonable.

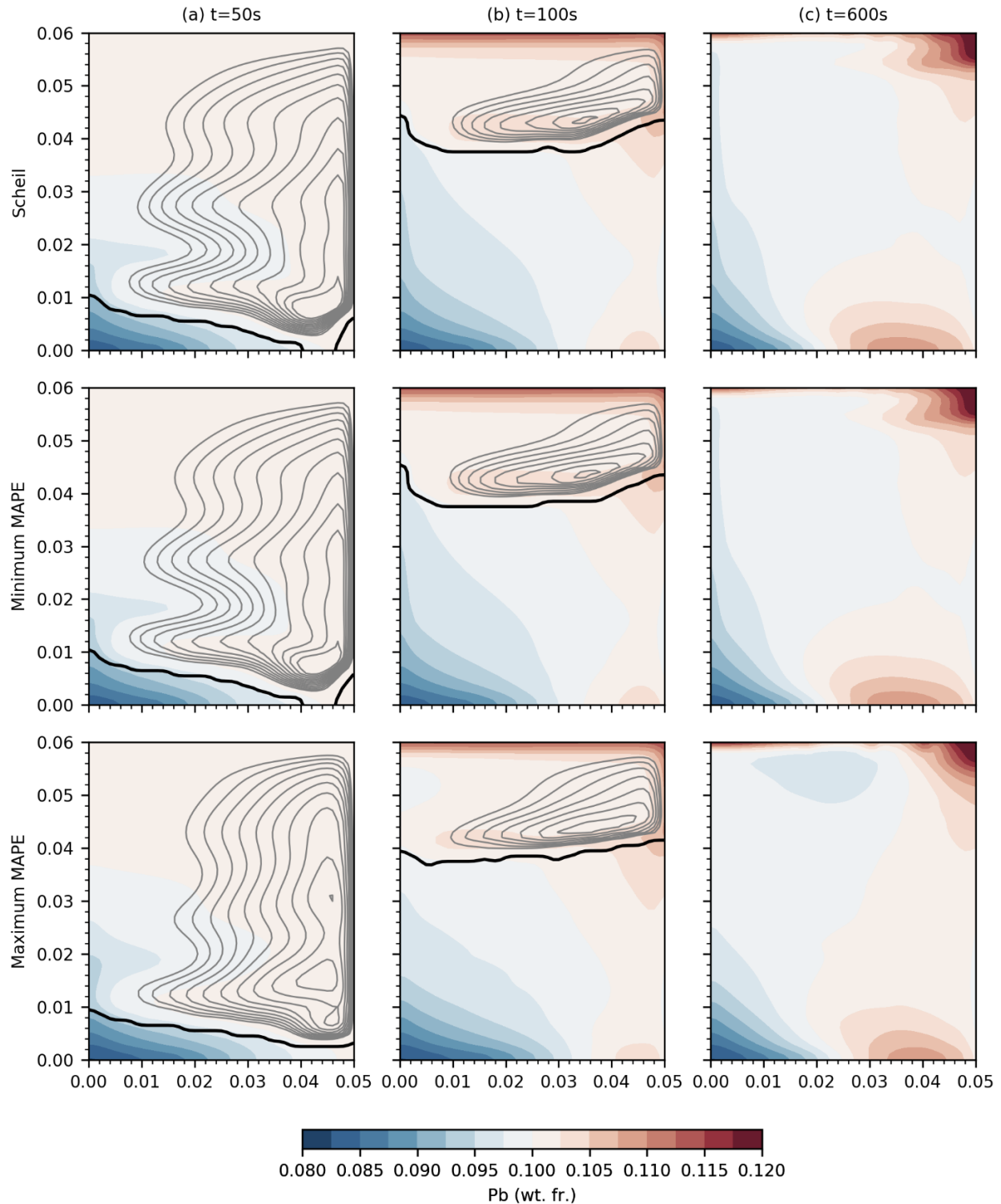


Figure 7.1: Evolution of the composition fields, flow field, and packing interface using the Scheil microsegregation model compared to volume-averaged microsegregation with input parameters showing the best agreement (hemispherical tip, $R_f = 37.5 \mu\text{m}$, and $D_l = 1 \times 10^{-8} \text{m}^2/\text{s}$) and input parameters showing the poorest agreement (paraboloidal tip, $R_f = 125 \mu\text{m}$, and $D_l = 2 \times 10^{-9} \text{m}^2/\text{s}$) at different times.

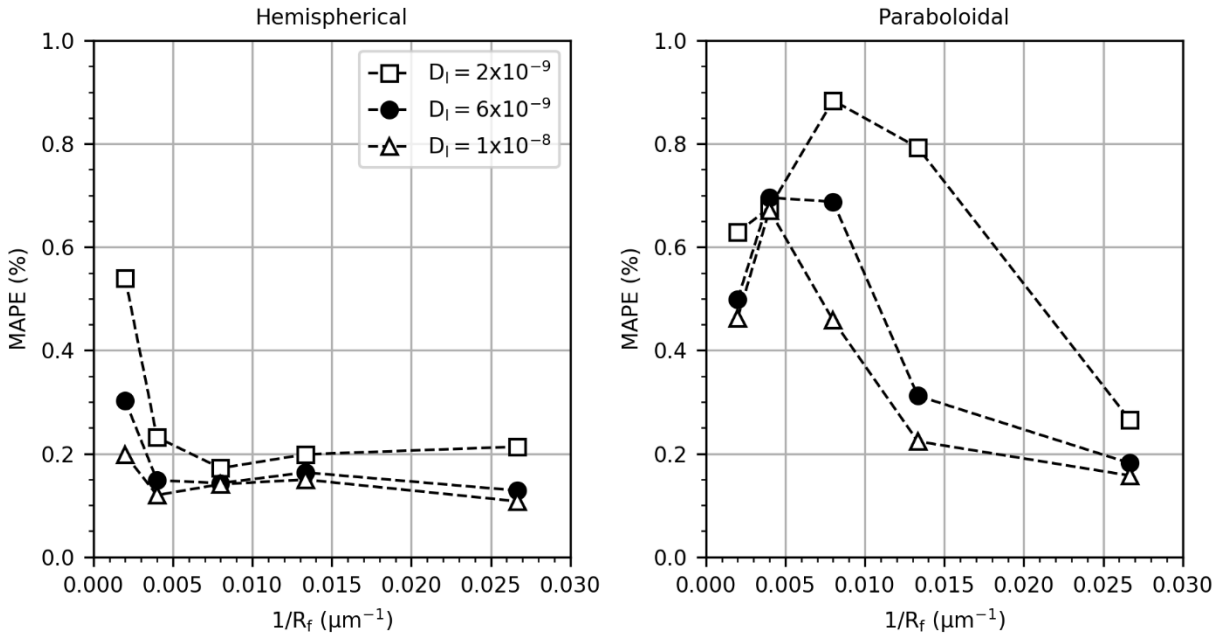


Figure 7.2: The mean absolute percent error (MAPE) measuring deviation of the macrosegregation predictions using the volume-averaged microsegregation models from the Gulliver-Scheil predictions for different values of liquid mass diffusivity and final grain size in microsegregation model.

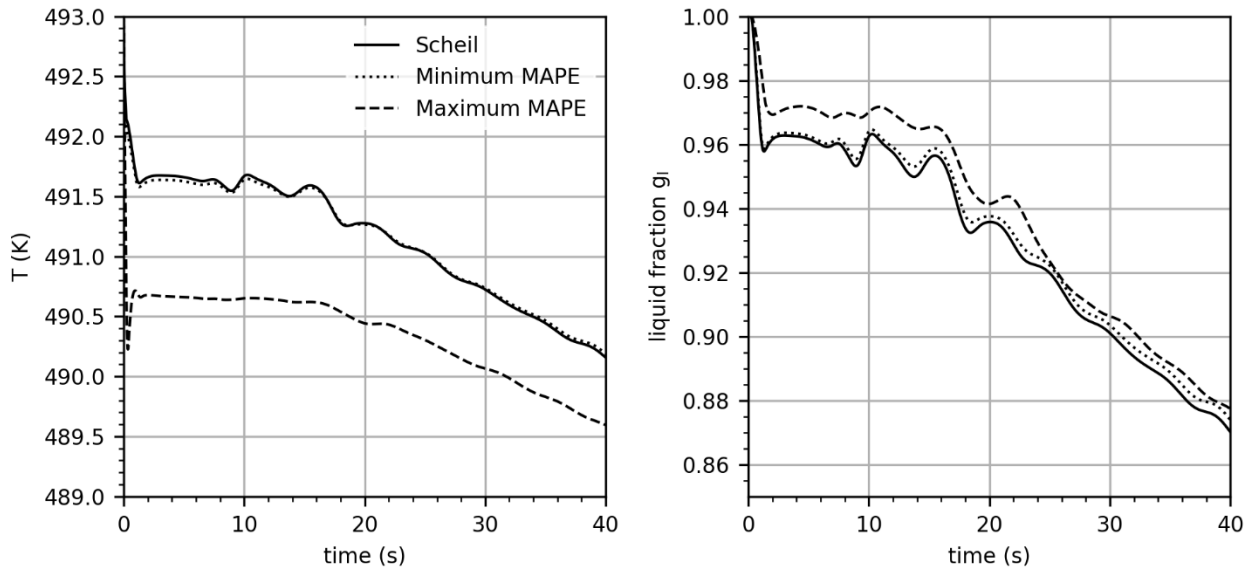


Figure 7.3: Temperature and liquid fraction histories at a location 1mm from the chill at the midheight of the cavity for a cause equiaxed solidification using variation microsegregation models. The maximum deviation from Scheil (maximum MAPE) shows a recalescence curve and about 1 K of undercooling.

7.3 Influence of Grain Structure on Macroseggregation

In the previous section, it was demonstrated that the finite amount of undercooling predicted by the microseggregation model during equiaxed solidification had a negligible effect on the macroseggregation predictions. This is not surprising since the undercoolings for equiaxed solidification are expected to be relatively small due to the amount of interfacial area supplied by the high grain number densities. However, several previous studies have advocated for the use of such models due to their ability to improve the model through grain morphology predictions. To investigate the effect of different input parameters on the grain morphology predictions, the previous calculations are repeated and the internal solid fraction upon packing is tracked.

Figure 7.4 shows contour plots of the internal solid fraction at packing for both tip geometry models using different values of R_f . For large grain radii ($R_f = 500 \mu m$), the hemispherical tip model predicts highly dendritic grains with little variation, while the paraboloidal tip model predicts intermediate grain morphologies that tend to coarsen as solidification progresses towards to symmetry plane. For intermediate grain radii ($R_f = 125 \mu m$), the hemispherical model predicts grain morphologies transitioning from dendritic to globular as solidification progresses to the upper corner of the symmetry plane, while the paraboloidal tip model predicts a completely globular structure. For smaller grain radii ($R_f = 75 \mu m$), the hemispherical model predicts intermediate to coarse grain following the same coarsening path as the intermediate case, while the paraboloidal tip model still predicts a fully globular structure.

Since the internal solid fraction directly influences settling tendency of the grains and the solid fraction at packing, it is important to know its value to some degree of certainty. It is well-understood that the packing fraction is one of the most important parameters for macroseggregation predictions since it determines the volume of solute-depleted grains in the slurry and the range of permeabilities in the mushy zone which restrict the transport of enriched interdendritic liquid. Figure 7.5 shows that the macroseggregation predictions noticeably change when the local grain morphology prediction can change the hydrodynamics. These results show different tip geometry models attempting to model the same system for the same input parameter, $R_f = 75 \mu m$. It is reminded that these same of parameters previously predicted macroseggregation fields in near perfect agreement when the grain morphology predictions were neglected the hydrodynamics model.

Probabilities densities of the internal solid fraction at packing for the two tip models are compared in Figure 7.6. It is shown that the hemispherical model predicts a somewhat wide range of intermediate morphologies (0.6 ± 0.21) while the paraboloidal model predicts a narrow range of globular morphologies (0.96 ± 0.04). Therefore, the hemispherical model tends to pack more quickly than the paraboloidal model, reaching the top surface nearly a minute before the paraboloidal model, resulting in a significantly smaller depletion region along the bottom surface. Comparison to the permeability of the rigid mush near the packing interface indicate that the hemispherical model will have a more permeable rigid mush, and as a result, the enrichment region along the bottom region is more pronounced. While the trends in these transport phenomena are physically correct, it is concerning that the macrosegregation predictions are significantly influenced by a highly uncertain closure relationship in the model [115]. The choice of one model over another appears to be circumstantial with conflicting justification.

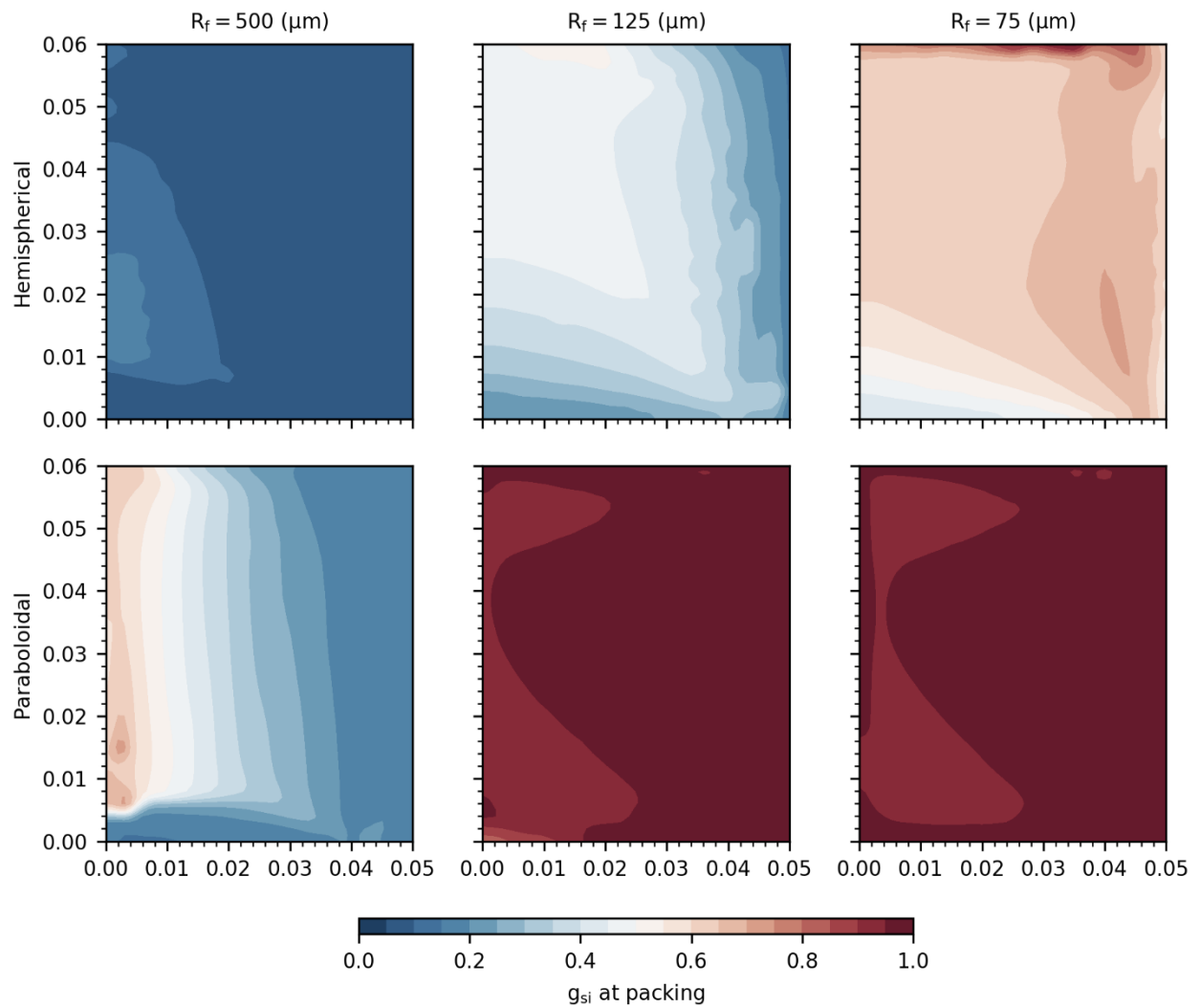


Figure 7.4: Internal solid fraction at packing for each tip geometry models for different final grain radii.

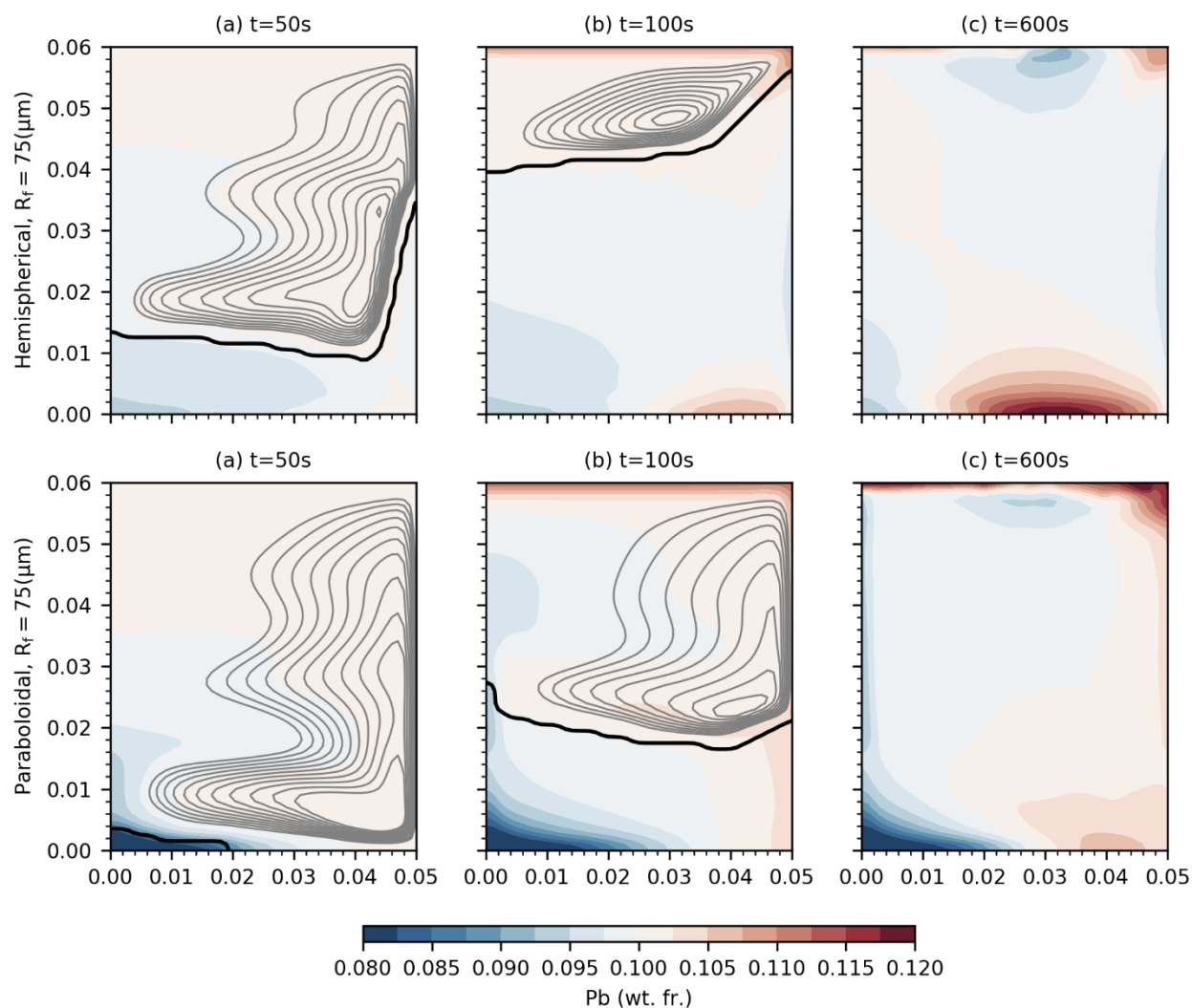


Figure 7.5: Evolution of the Pb composition fields, flow field, and packing interface using the hemispherical tip and paraboloidal tip models to control the grain morphology using $R_f = 75 \mu\text{m}$, and $D_l = 2 \times 10^{-9} \text{m}^2/\text{s}$.

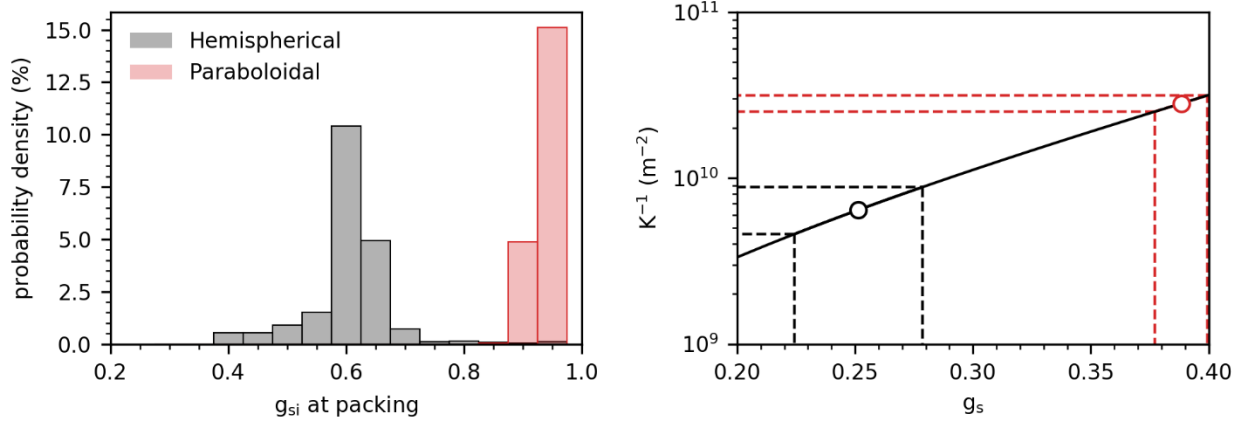


Figure 7.6: Probability density of the internal solid fraction at packing predicted by each tip geometry model for $R_f = 75 \mu\text{m}$ and $D_l = 2 \times 10^{-9} \text{m}^2/\text{s}$ (left) and the range of inverse permeabilities restricting interdendritic liquid flow across these packing fractions.

7.4 Simplified Grain Morphology Model

In an attempt to establish trends more clearly in the grain structure prediction, the internal solid fraction at packing is plotted against $1/R_f$ for both the hemispherical and paraboloidal tip models, shown in Figure 7.7. The hemispherical tip model consistently predicts more dendritic grain morphologies compared to the paraboloidal model. From these numerical results it is shown that the morphology at coherency predicted by the model is inversely related to the assumed final grain radii used as input to the numerical model. This same trend appears to fit a selection of data taken from experiments relating coherency fraction vs. grain size for aluminum foundry alloys cooled at 0.7K s^{-1} with different level of grain refiner additions. While this data was originally reported for different rheological experiments by Arnberg and coworkers [31,32], the values here were collected by Yuan et. al [116]. Despite the experimental data having some scatter because of the different types and concentrations of alloying elements, there is still a relatively strong correlation of the internal solid fraction to $1/R_f$, with an R^2 value of 0.72.

To determine if the transient variation of the grain morphology significantly effects the numerical predictions, and further, if more pragmatic closure laws for the grain morphology could be used in future work, the following linear fits were determined for each tip geometry:

$$g_{si}^H = 0.05 + 36.27 \left(\frac{1}{R_f} \right) \quad (7.2)$$

and

$$g_{si}^P = 0.11 + 107.72 \left(\frac{1}{R_f} \right) \quad (7.3)$$

The R^2 values for the proposed fits are 0.988 for the hemispherical and 0.962 paraboloidal curves. Although the hemispherical tip data appears to be in better agreement with the experimental trends, there are too many differences between experiments and calculations to draw any conclusions. However, it is noted that this is the first time that this specific relationship has been observed by the kinetics-based models and may inspire future investigations.

Using the above relationships, the evolution of macrosegregation, packing interface, and flow field are compared to the full microsegregation and grain structure prediction models for the most dendritic and most globular cases. Figure 7.8 shows the results from the most dendritic case (i.e. $g_{si}^H = 0.048$) corresponding to a hemispherical tip model. These results are similar to the columnar solidification case previously reported in ref. [117] since the grains are immobilized at low solid fractions. A vertical packing interface progress from the right wall and a clockwise recirculation cell driven by solutal buoyancy transports a significant amount of solute from the top to the bottom of the domain causing a depletion on the top surface and enrichment of the bottom surface region. All three methods for solving the features of the sub-grid scale phenomena appear to be equally valid due to the excellent qualitative agreement between cases. Similar agreement is found for the most globular case (i.e. $g_{si}^P = 1$) corresponding to the paraboloidal tip model. These results suggest that the transient evolution of grain morphologies does not significantly affect the macrosegregation results, and constant values may be used to capture the correct qualitative trends in transport phenomena.

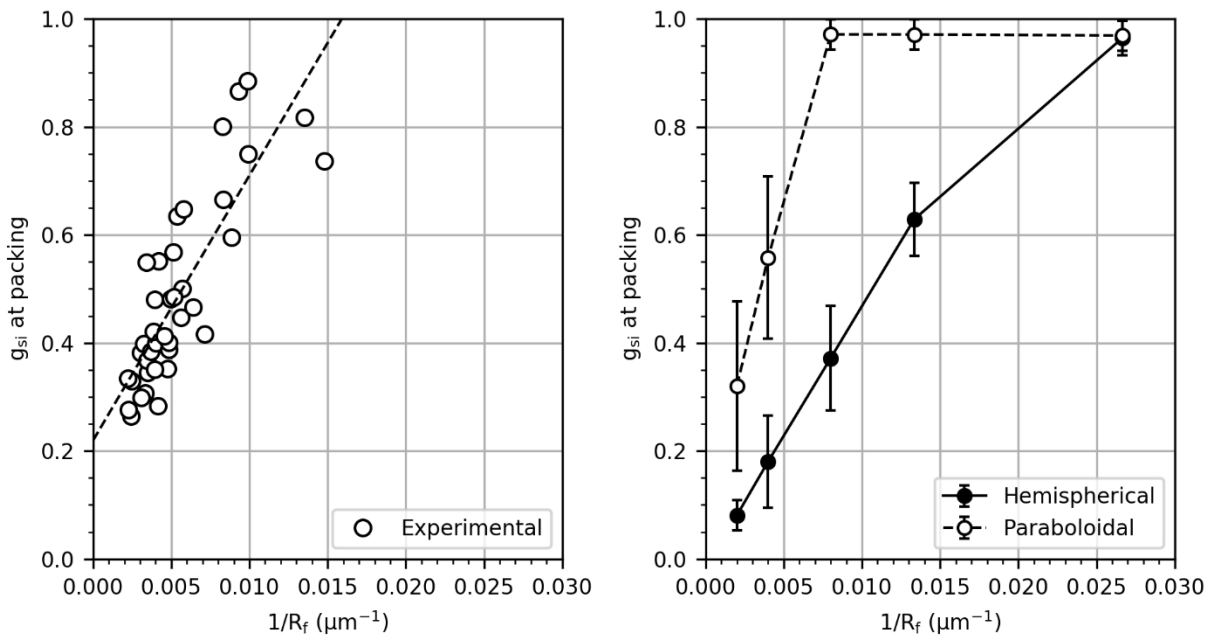


Figure 7.7: A. Experimental grain morphologies taken from ref. [117] B. Average calculated internal solid fraction at the onset of packing for both tip geometry models and the primary inputs to the microsegregation model (R_f, D_l).

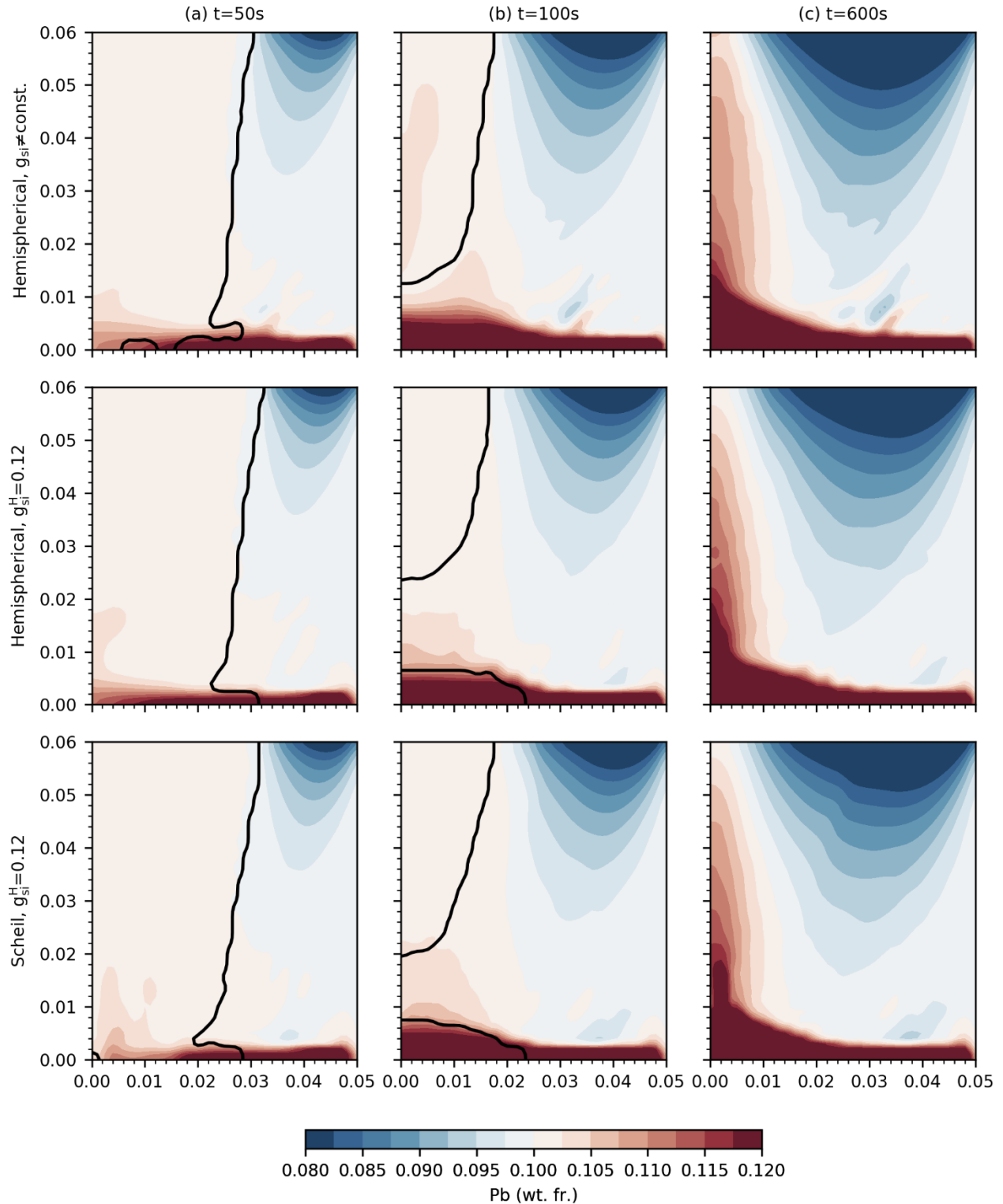


Figure 7.8: Evolution of the composition fields and packing interface using the hemispherical tip model $R_f = 500 \mu\text{m}$, and $D_l = 6 \times 10^{-9} \text{m}^2/\text{s}$ with the calculated morphological conditions compared using a constant packing fraction obtained from the linear fit in Eqn. (7.2) for the equivalent volume-averaged and Scheil microsegregation models.

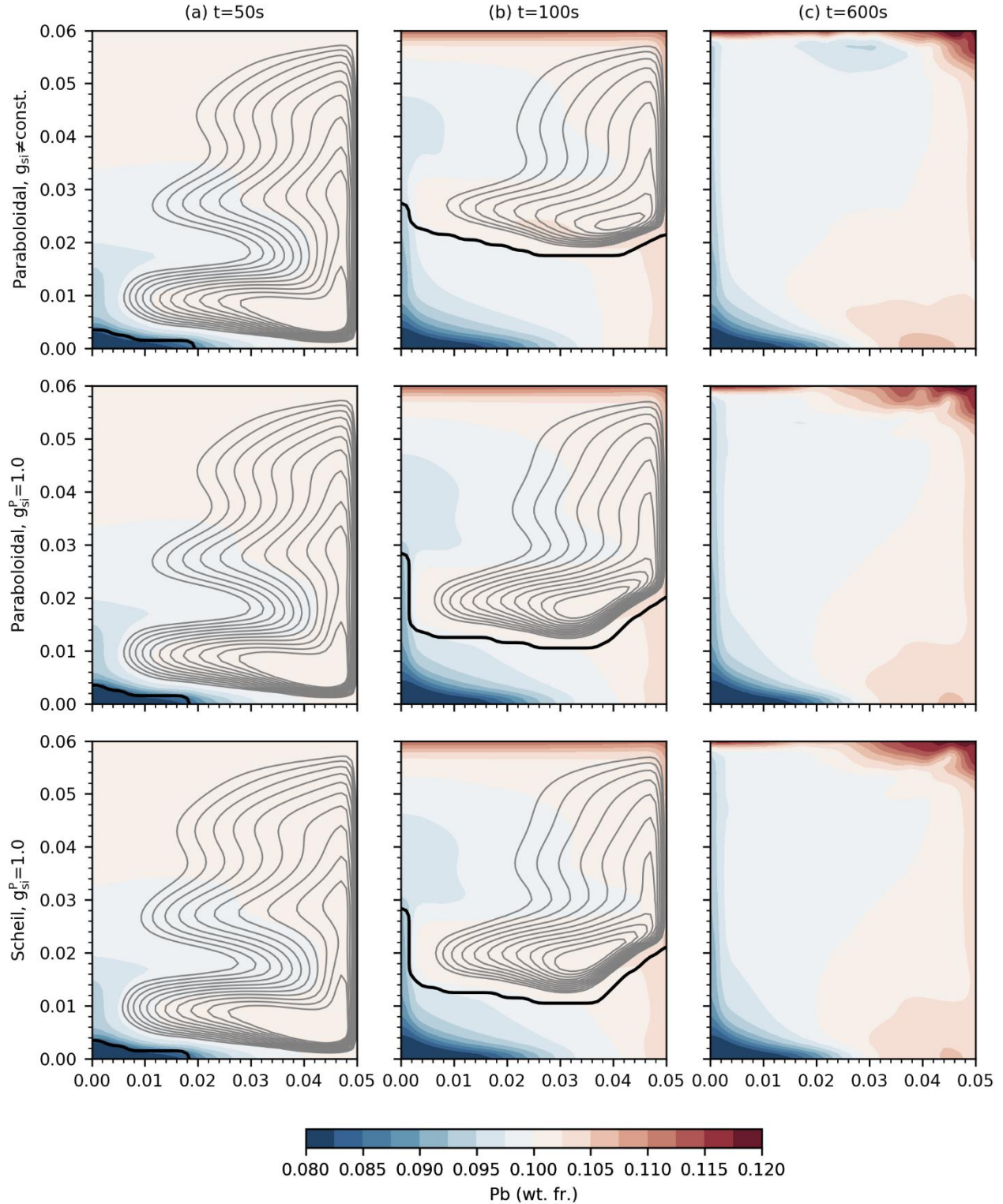


Figure 7.9: Evolution of the composition fields and packing interface using the paraboloidal tip model $R_f = 37.5 \mu\text{m}$, and $D_l = 6 \times 10^{-9} \text{m}^2/\text{s}$ with the calculated morphological conditions compared using a constant packing fraction obtained from the linear fit in Eqn. (7.3) for the equivalent volume-averaged and Scheil microsegregation models.

7.5 Sensitivity Study

Up to this point it has been established that finite undercooling in the liquid does not significantly affect the macrosegregation predictions for equiaxed solidification simulations. Instead, it is the influence of the grain morphology prediction on the hydrodynamics of the system which has a significant effect on macrosegregation. The relative sensitivities of the outputs to changes in the input parameters are determined using the Elementary Effects Method (EEM). An elementary effect is calculated for an input parameter by independently varying it over a constant step change while other parameters remain constant, and thus, measures the change in the output over some fraction of the input range. A distribution of elementary effects is then calculated for each input parameter and the mean sensitivity μ^* is used to estimate the sensitivity of the output over the input range, i.e.:

$$\mu^* = \frac{1}{r} \sum_{j=1}^r \left| \frac{\Delta Y_j}{\Delta X_j} \right| (X_{max} - X_{min}) \quad (7.4)$$

Figure 7.10 shows that the internal solid fraction at packing is very sensitive to the value of R_f used in the hemispherical model, and a lesser extent, the liquid mass diffusivity for intermediate grain radii of practical importance for industrial castings. In this range, the paraboloidal model predicts a fully globular structure so its sensitivities are significantly smaller. However, if the model tends to uniformly predict globular grains under these conditions, then there is no need to attempt modeling the grain structure further supporting the claims for simplified models made in this chapter.

Figure 7.11 shows that the macrosegregation index is very sensitive to R_f and D_l for the hemispherical tip model due to the significant changes in grain morphology prediction, and insensitive to these values for the paraboloidal tip model due to constant grain morphology prediction. When the approximate relationship for the hemispherical grain morphology is used (g_{si}^H), this model sensitivity is almost completely removed. Therefore, it can be stated that if a characteristic internal solid fraction can be determined to a higher degree of certainty than the inputs and closure laws used to the grain growth model, then those relationships should be used in place of the more complicated models. This appears to be the case for equiaxed solidification in

DC casting, where the packing fraction in the range of 0.2-0.3 has historically produces good agreement with casting experiments.

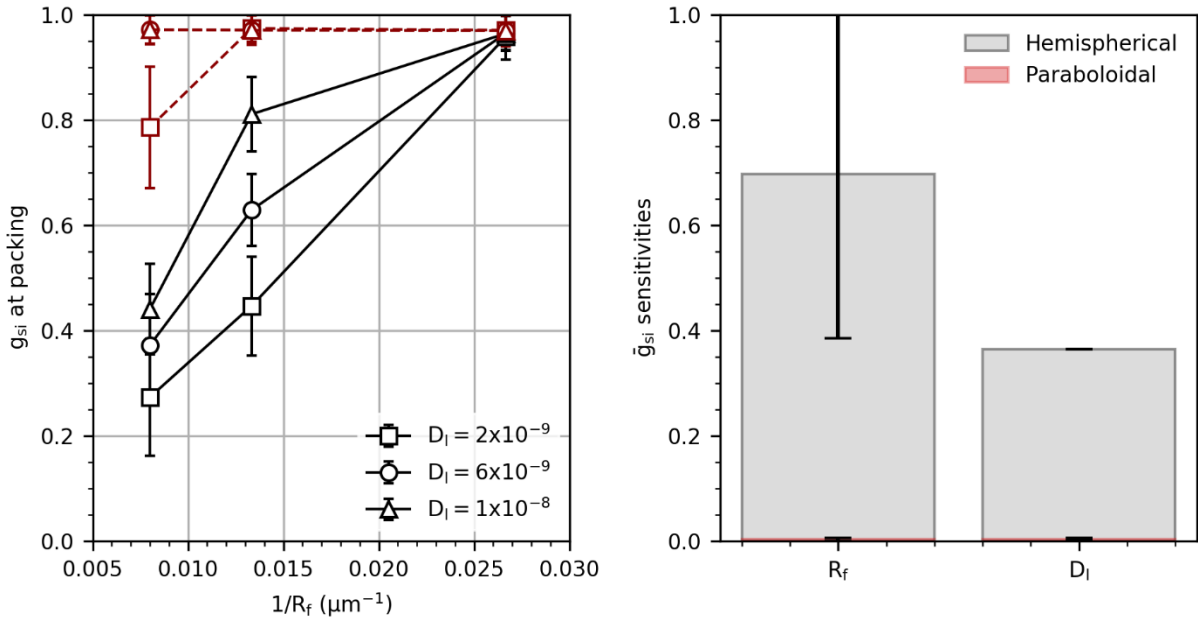


Figure 7.10: Sensitivities of the internal solid fraction at packing to the grain growth model input.

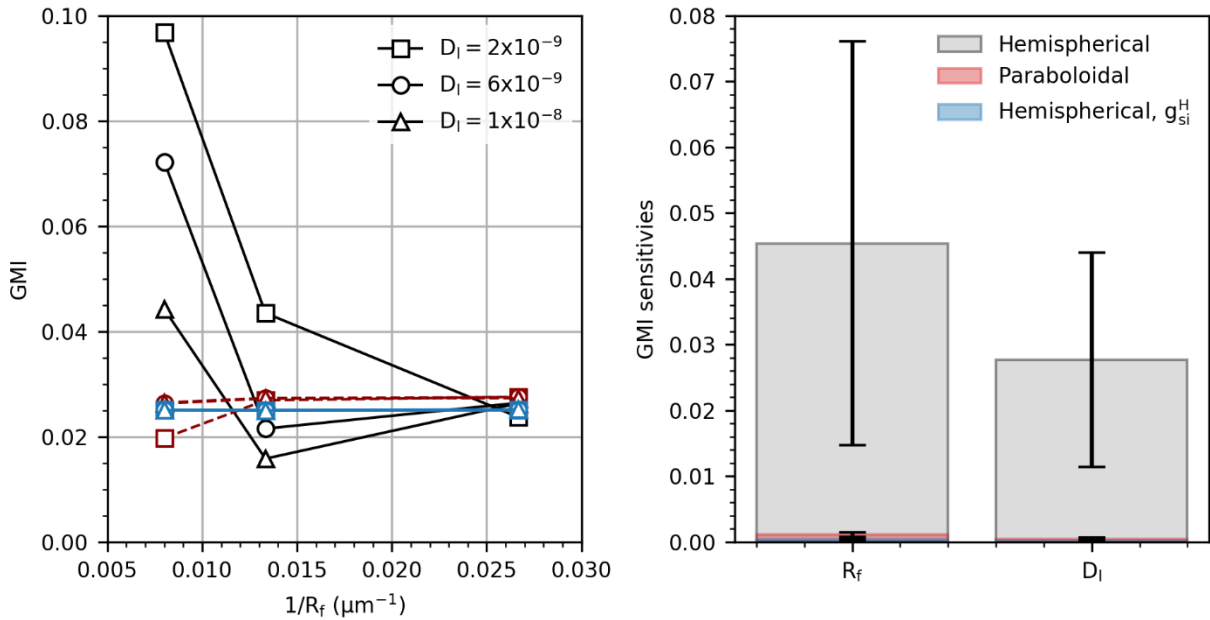


Figure 7.11: Sensitivities of macrosegregation predictions to uncertain microscale model input.

7.6 Influence of Undercooling on DC Casting Predictions

Because the level of undercooling in the extradendritic liquid tends to increase with the cooling rate, its influence on macrosegregation should be more pronounced for DC casting than the previous static casting cases. A description of the DC casting case used for this comparison has already been provided in Section 6.4. In addition to the macrosegregation measurements, Vreeman et al. [47] inserted a thermocouple rake into the sump to record the temperature histories at different radial positions during casting. The rake was solidified into the billet and thermal profiles were obtained near the centerline ($r = 10$ mm), midradius ($r = 106$ mm), and the surface ($r = 220$ mm). The predicted temperature profiles are also compared to observe any differences caused by finite undercooling.

Figure 7.12 compares the steady state solid fraction and mixture composition contours for the Scheil, hemispherical tip, and paraboloidal tip microsegregation models. Going from top to bottom, the solid black lines mark the liquidus, the packing interface, the interface between the loosely packed and tightly packed rigid mush, and the solidus. The dotted lines indicate the position of these flow regime demarcations for the Scheil model to aid comparison. The general macrosegregation features are similar for each case, consisting of a depleted centerline due to shrinkage driven flow in the rigid mush and, to a lesser extent, the accumulation of solute depleted grains. The most significant qualitative change is the segregation is the absence of the enrichment zone in the slurry for the volume-averaged microsegregation models. It is not clear if this is due to the handling of remelting by the different models, due to the Scheil model overpredicting the segregation along the packing interface at the outer- and midradius causing a larger volume of enriched liquid to be advected into the slurry, or a combination of these two factors.

Figure 7.13 shows the radial segregation profiles and temperature profile along the pool depth. The volume-averaged microsegregation models predict more positive segregation near the surface, and therefore, less positive segregation at the midradius. Because the solid fraction contours in the rigid mush are similar for each case, so is the centerline depletion which is mostly dependent on shrinkage induced flow. For all cases, the predicted segregation profiles are within the uncertainty of the experimental data and the temperature profiles are indistinguishable.

As expected, the worst agreement between the position of flow regime demarcations is the liquidus surface where recalescence occurs and delays solidification in the mold causing the liquidus to shift down about 15 mm for the volume-averaged models. In the region between the

liquidus and the packing demarcation, the volume-averaged models predict a wider and flatter rigid mush, attributed to finite undercooling that occurs in this region due to the relatively high cooling rates enacted by the direct chill. Despite these differences at the outer radius, the percent change in the predicted sump depth when the microsegregation model considers undercooling is only $\approx 3.5\%$. Since the final grain radius used here ($R_f = 125 \mu\text{m}$) is approaching the largest interfacial structures found in grain-refined DC casting, it also represents the maximum effect of undercooling on the model predictions. For comparison, Fezi and Krane [118] showed that the uncertainty in the sump depth for a similar alloy and casting parameters was $\approx 14.1\%$. Therefore, it appears that the total epistemic uncertainty in the microsegregation model is within the aleatoric uncertainty of the thermophysical property inputs and the Scheil approximation of the microsegregation behavior is sufficient for modeling grain-refined DC casting.

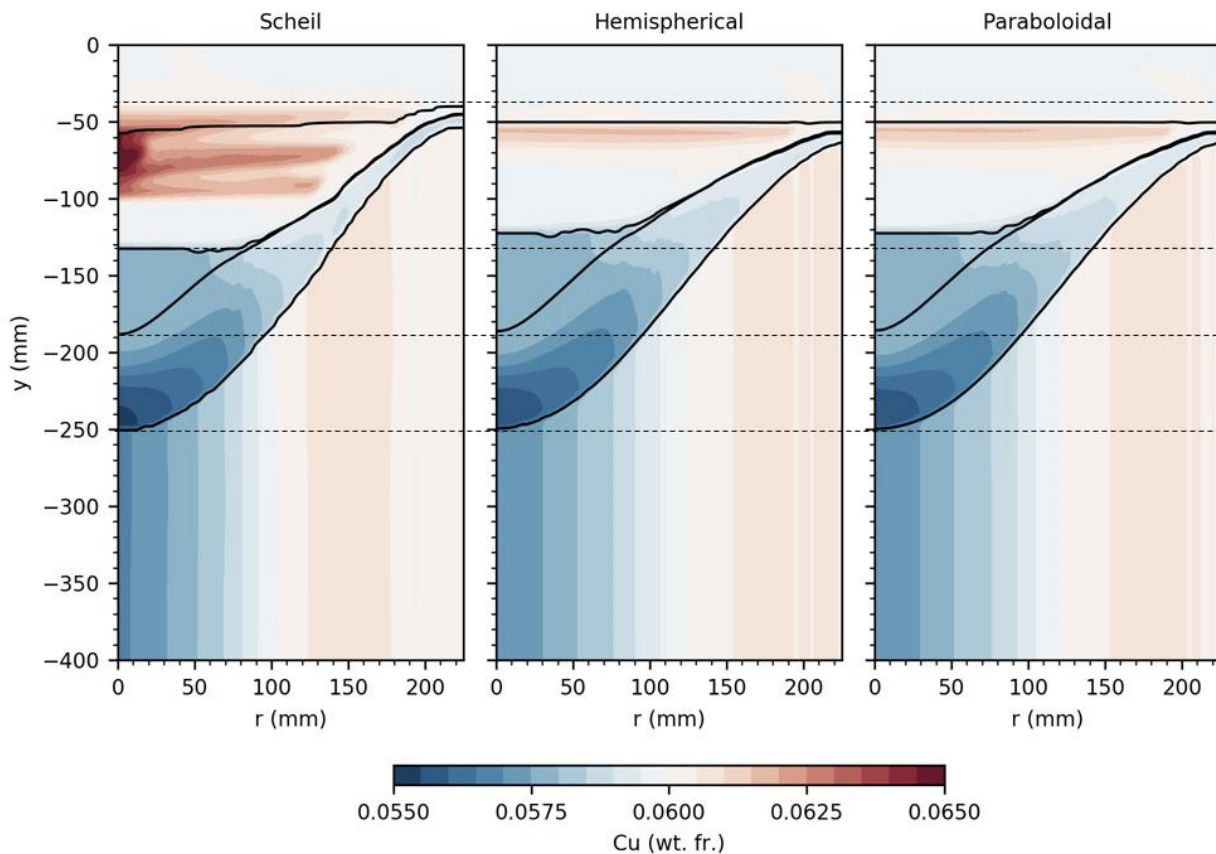


Figure 7.12: Copper distribution in the billet for different microsegregation models. The contours in decreasing order of y -position are the liquidus, the packing interface, the demarcation of the loose packed grain region, and the solidus. Simulations were performed with a critical packing fraction of $g_g^c = 0.30$ and volume-averaged calculations used a final grain radius of $R_f = 125 \mu\text{m}$.

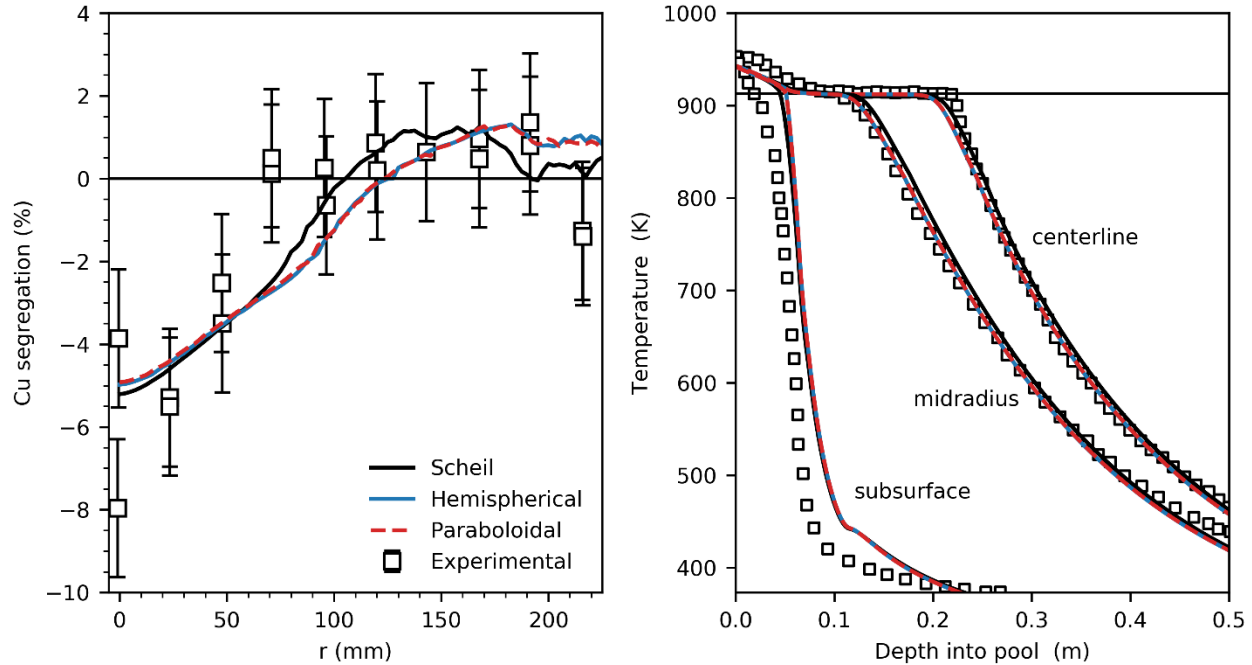


Figure 7.13: Profiles of Cu concentration from simulations with different microsegregation models. The model predictions are compared to the experimental profiles of Vreeman et al. [47] (left). Comparison of predicted and measured temperature profiles (right).

7.7 Summary

In this chapter, the Scheil microsegregation was compared to the more complicated volume-averaged microsegregation models to characterize the difference in macroscale predictions. First, the effect that finite undercooling in the extradendritic liquid had on equiaxed solidification benchmark was determined to have a mean absolute percent error of less than 1% over the entire parameter range for equiaxed solidification. Then, it was demonstrated that the grain structures predicted by the volume-averaged models are largely unreliable and can significantly affect the macrosegregation predictions. Comparing the models to DC experiments showed that the difference in the model predictions were within the experimental uncertainty and the aleatoric uncertainty of thermophysical property inputs. These results suggest that it is not necessary to include complicated microsegregation models to obtain reasonable predictions of the macroscopic transport occurring in equiaxed solidification. Therefore, the analytical model will be used, and the grain size and morphology will be prescribed for the remainder of this work.

8. INVESTIGATION OF GRAIN TRANSPORT IN HORIZONTAL DIRECT CHILL CASTING

In this chapter, the role of forced convection on the transport of solute-depleted grains during equiaxed solidification is investigated for horizontal direct chill (HDC) casting. The mixture model summarized in Table 2.3 and Table 2.4 is used with the face-based drag formulation (Section 4.2.3) and diffuse solid flux transition model with a numerical diffusion coefficient of $\eta = 0.5$ (Section 4.3.2). Additionally, the analytical microsegregation model (Section 3.1) is used assuming no back-diffusion into the solid phase ($\beta = 0$) during solidification (i.e. the modified-Scheil assumption). The grains are assumed to be fully globular $g_{s,i} = 1$, the grain volume fraction upon coalescence is $g_g^c = 0.4$, and the characteristic length scale of the rigid mush is $\lambda = 65 \mu\text{m}$

8.1 Background

Although vertical direct chill casting (VDC) is the most common technology to produce wrought aluminum alloy ingots, HDC allows for ingots to be cast without interruption. Since there is no requirement for deep casting pits and expensive hydraulic rams, the startup cost is significantly lower than VDC. Additionally, the increased casting rates in HDC (due to thinner slabs) allow for a higher annual throughput per strand, making it an economically viable alternative for certain wrought products [2]. However, because the casting axis in HDC casting is perpendicular to gravity, the natural convection driven flows in the melt are not symmetric about the casting axis as in VDC. In the case of equiaxed solidification, there will be a tendency for grains to settle along the bottom of the slab causing a region of negative segregation. Numerical simulations are used to provide estimates of inflow conditions which tend to suspend these grains for an Al-4.5wt%Cu slab. Thermophysical properties for Al-4.5wt%Cu are provided in Table A1.

The numerical domain is similar to that of Krane and Vušanović [119], extended to 3-dimensions, shown in Figure 8.1. The slab is 80 mm thick and terminates 300 mm from the inlet. Three different slab widths are investigated: 200 mm, 400 mm, and 600 mm. Liquid metal enters the model through a constrained inlet that is 20 mm thick and 80 mm wide. The mold is 45 mm long and secondary cooling is applied over the rest of the top, bottom, and side surfaces. Due to the assumption of symmetry along $z = 0$ mm, only half of the physical domain is modeled for 3-

D calculations. The heat transfer in the mold varies linearly with position from mold contact, $h = 1500 \text{ W/m}^2\text{K}$, to air cooling, $h = 150 \text{ W/m}^2\text{K}$. The secondary cooling for the top and side surface, $h = 10,000 \text{ W/m}^2\text{K}$, and bottom surface $h = 6,000 \text{ W/m}^2\text{K}$, correspond to the ratio suggested in ref. [120].

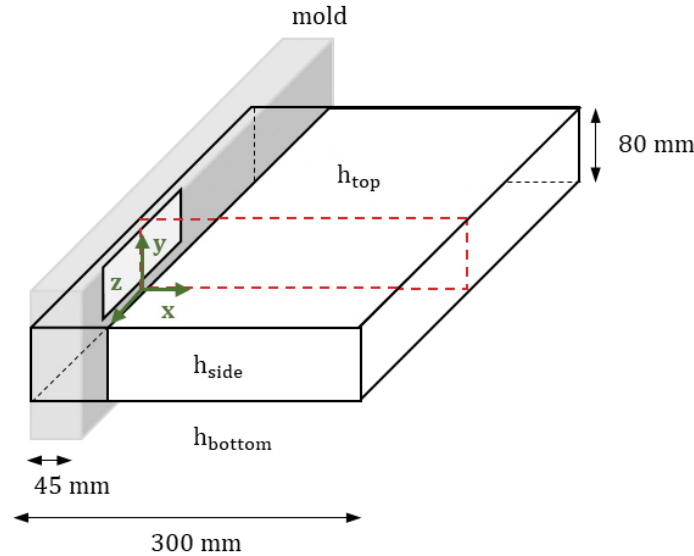


Figure 8.1: Schematic of horizontal direct chill (HDC) casting. The red outline indicates the position of the domain used for 2-D calculations.

8.2 Influence of Different Transport Phenomena

Before proceeding to the results of the 3-D model it is useful to distinguish various features of the flow field. In this section, the influence of different transport phenomena on the flow field and macrosegregation formation are evaluated for a case of equiaxed solidification, with a final grain diameter of $d_{g,f} = 150 \mu\text{m}$. According to mass conservation, the liquid metal entering the mold must compensate the mass loss due to the movement of the rigid mush at the casting velocity. The presence of body forces in the sump (i.e. buoyancy, shrinkage, and grain motion) does not change this requirement, only the path of the liquid between the inlet and the moving rigid mush. Figure 8.2 shows the different mechanisms driving flow for two different inlet positions: one at the midheight and one along the bottom of the mold. In the absence of any body forces, the inflow is initially driven into the mold by the hydrostatic head of liquid metal in the furnace. The constricted flow expands as it enters the mold to fill the volume of the moving rigid mush. The expansion of streamlines indicate that the inflow decelerates to the casting speed upon entering the

rigid mush. The final heights of the streamlines in the rigid mush are the same regardless of the inlet position. Because there are no sources of relative solid-liquid motion in this case, no macrosegregation forms.

When thermosolutal natural convection is considered, the superheated liquid metal entering the mold immediately rises towards the chilled top surface driven by positive thermal buoyancy. At the chilled surface, negative buoyancy (liquid is being cooled and enriched in Cu) drives this the fluid downwards along the rigid mush. Each streamline enters the rigid mush at the same position as the previous case. Due to the modified path that the superheated liquid metal takes, solidification near the top of the mold is delayed and solidification near the bottom of the mold is accelerated. Although it is not shown here, a shear driven recirculation cell forms in the slurry rotating clockwise. Particularly for the midheight inlet, a region of thermal stratification and relatively quiescent flow develops in the slurry below the inlet. The macrosegregation due to the natural convective flow of enriched liquid in the rigid mush is small; the relatively low permeability of the rigid structure almost prevents any liquid exchange at the packing interface.

When grain motion is considered, the entrainment rate of the inflow is higher, indicated by the more tightly spaced streamlines. This is due to the added negative buoyancy force from the mobile solid grains forming near the chill. Noticeable macrosegregation develops in the ingot as solid grains accumulate along the bottom half of the slab. The top half of the slab becomes positively segregated, while the bottom half is negatively segregated. The accumulation of depleted grains is more significant for the midheight inlet than the bottom inlet because the latter prevents the formation of a thermally stratified zone and resuspends the grains carried into this region. The resulting solute depletion along the bottom of the ingot is noticeably less for the bottom inlet.

When shrinkage is considered, the path of the inflow is nearly identical to the previous case, with the addition of a small flow induced by shrinkage parallel to the direction of the local solid fraction gradient. This is the only remaining flow deep in the rigid mush, and although small, it causes significant solute depletion in the middle of the ingot. The negative centerline segregation is due to the transport of highly enriched liquid away from this location towards the top and bottom of the ingot. From this evaluation of different transport mechanisms in HDC casting, it can be determined that shrinkage driven flow independently causes the depleted centerline, while grain motion causes the asymmetry in the final macrosegregation profile. Additionally, feeding liquid

metal from the bottom inlet improves the symmetry of the segregation by preventing the localized accumulation of depleted solid along the bottom of the ingot.

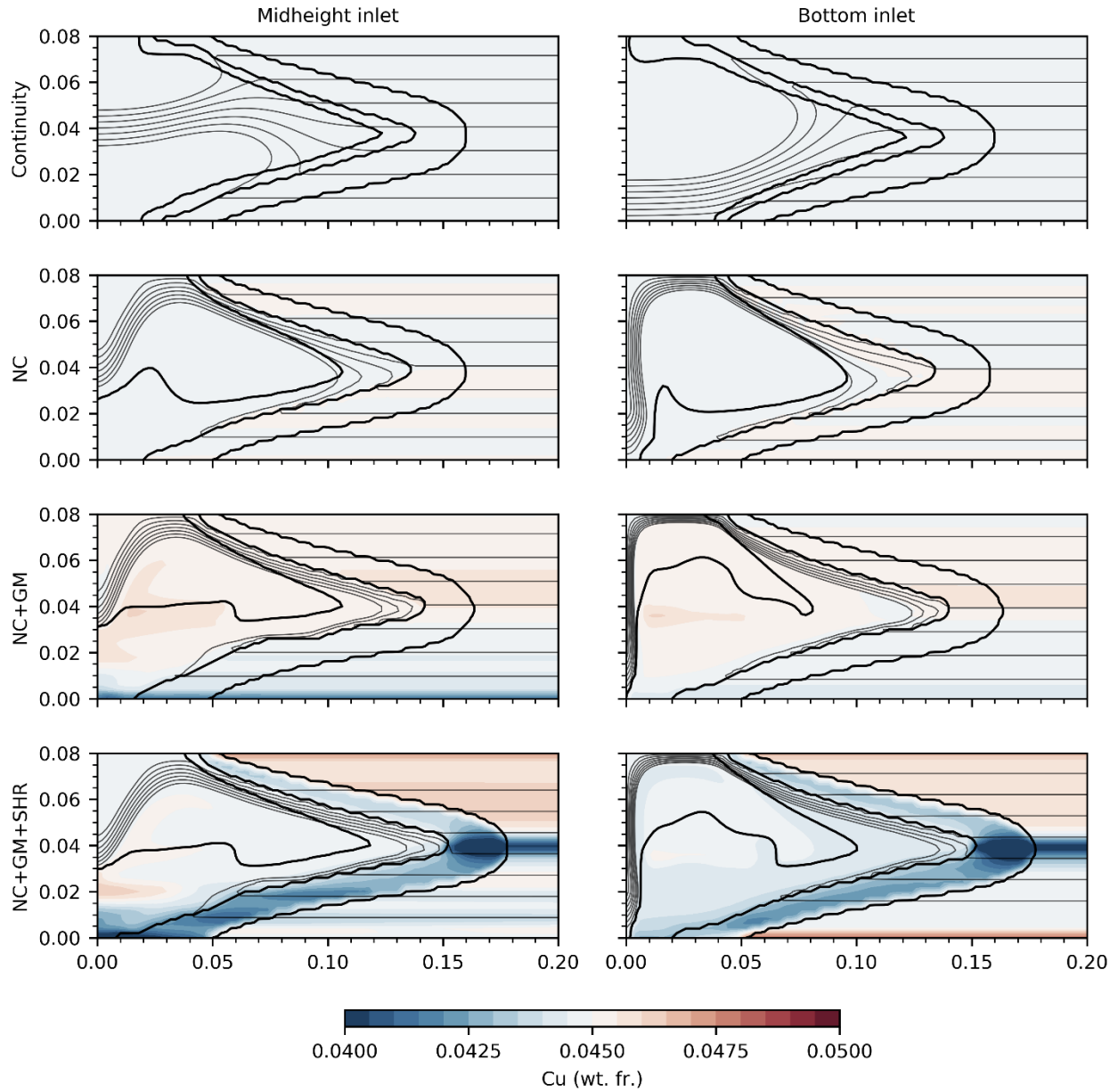


Figure 8.2: Steady state composition fields and streamlines for various transport mechanisms in HDC with two different inlet positions. Bold black lines denote liquidus, packing interface, and solidus.

8.3 Grain Suspension Due to Forced Convection

In order to better determine the competition between the grain settling due to buoyancy forces and grain suspension due to forced convection, the final composition fields for different grain sizes are provided in Figure 8.3. As the grain size increases, the macrosegregation becomes less symmetric for the midheight inlet, attributed to a larger volume of solute-depleted grains transported to the thermally stratified region below the inlet where they accumulate along the bottom. For 200 μm grains, the negative segregation near the bottom of the ingot becomes the most intense composition feature with a copper depletion of -11% . As the bottom half of the ingot becomes more depleted, the top half becomes more enriched. In Figure 8.4, the composition profiles across the thickness are compared for various grain sizes, demonstrating significant asymmetry for the midheight inlet which increases with increasing grain diameter. For the bottom inlet, forced convection from the inlet is strong enough to suspend a large volume of grains. For 200 μm grains, the negative segregation near the bottom of the ingot is only -4% compared to -11% for the midheight inlet. These results demonstrate that selective forced convection from specially designed liquid metal distribution systems can be used to suspend grains during equiaxed solidification, and furthermore, it is demonstrated that such phenomena can be sufficiently captured by the current numerical model.

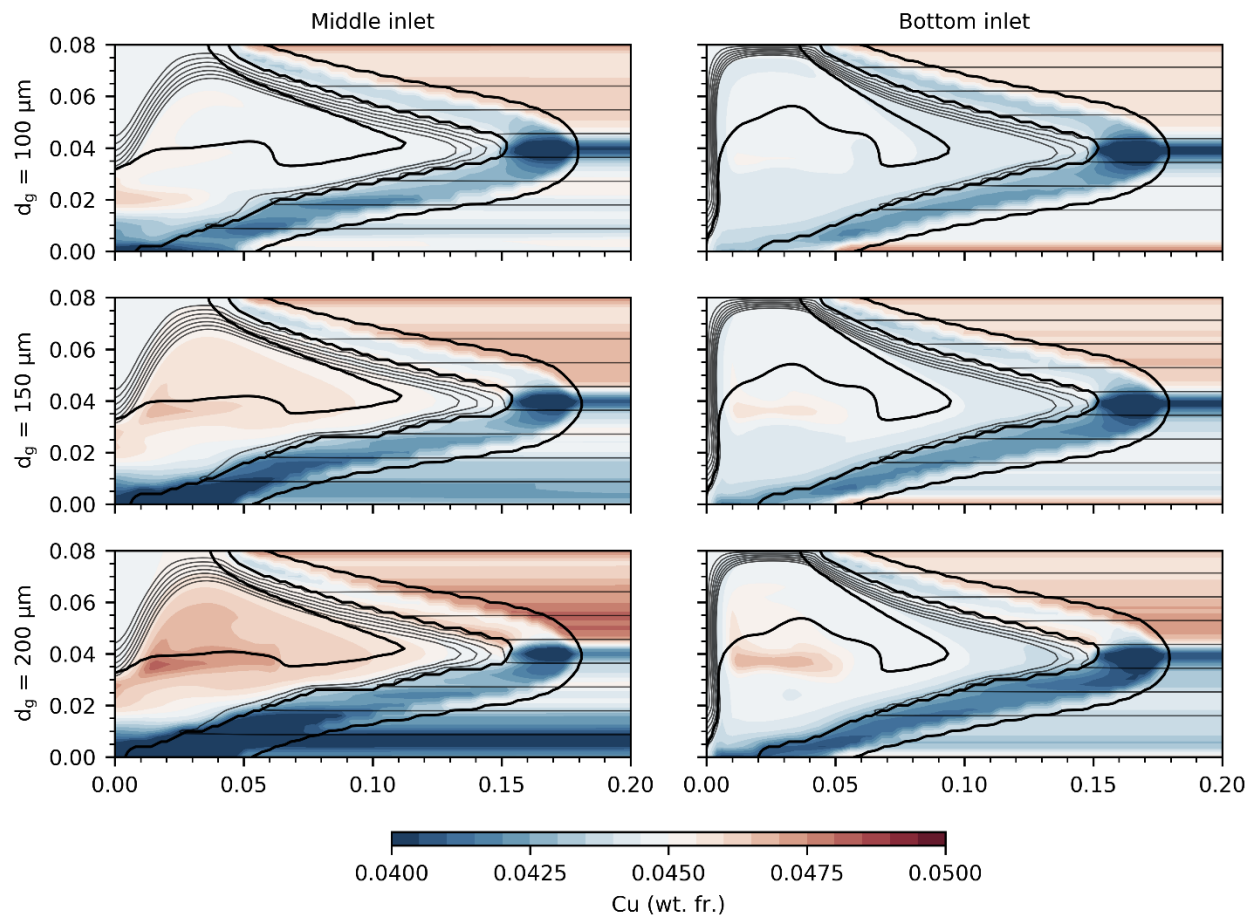


Figure 8.3: Effect of inlet position and grain size on grain suspension and the steady state composition profiles in HDC casting.

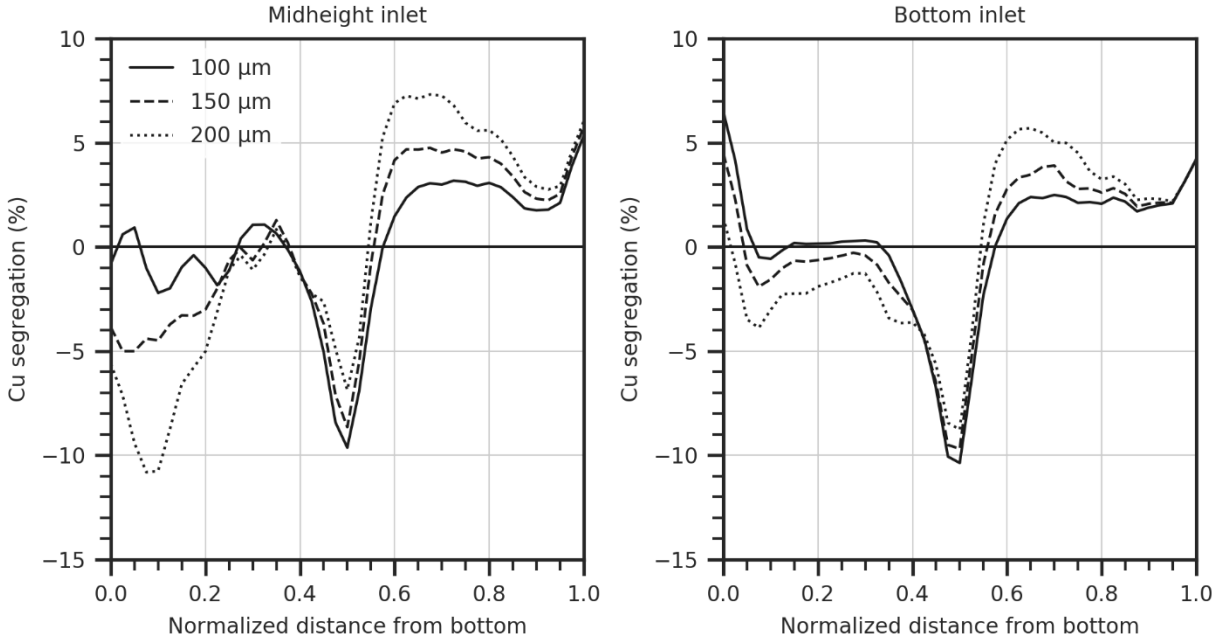


Figure 8.4: Comparison of macrosegregation profiles in HDC for a center and bottom jet. Lowering the jet position in the model significantly reduces the macrosegregation in the ingot by suspending grains.

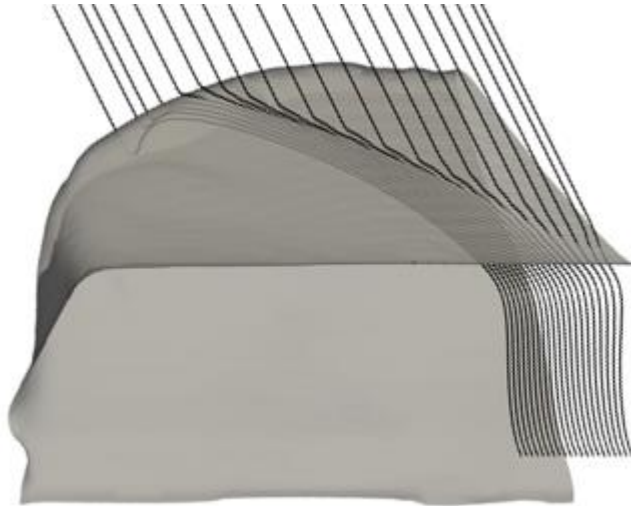


Figure 8.5: Steady state streamlines and sump shape for the 400 mm width HDC cast slab.

8.4 Comparison of 2-D and 3-D Calculations

Each of the previous 2-D calculations assumes that the dominant transport is in the x-y plane. While this assumption is reasonable for heat transfer calculations due to the aspect ratio of the slabs, it is not a valid assumption for flow calculations. Figure 8.5 shows the steady state sump profile and streamlines for a 400 mm wide slab fed with an inlet positioned at the midheight. The previously discussed continuity requirement causes a significant flow component not captured by the 2-D calculations. The effect that this flow has on the macrosegregation development is discussed by comparing the 2-D calculations to the 3-D calculations with various aspect ratios.

Figure 8.6 shows the steady-state composition, flow, and sump profiles in the x-y plane. In each case, the qualitative predictions are similar, however there are a few subtle changes. First, the inlet jet velocity increases with slab width due to mass conservation. The resulting increased penetration depth of the superheated liquid causes the sump depth to increase, albeit marginally. Despite these changes, the curvature of the rigid mush which determines the direction of shrinkage driven flow, is relatively unchanged and the predicted centerline depletion is similar for each case.

The segregation profiles between the 2-D calculation and the 3-D calculation of a 400 mm wide slab are quantitatively compared in Figure 8.7. For 2-D calculations, the flow in the slurry driven by buoyancy forces is constricted in the x-y plane. Therefore, the flow along the rigid mush is stronger in this plane and there is less of a tendency for solute depleted grains to accumulate along the bottom horizontal section of the rigid mush. Consequently, the 2-D calculation tends to underpredict the negative segregation in the bottom half of the slab and underpredict the positive segregation in the top half of the slab. Additionally, the reduced sedimentation rate of grains along the bottom horizontal section of the rigid mush shifts the packing interface down about 5 mm. These results indicate that the qualitative trends established for the transport phenomena and macrosegregation development in HDC are reasonably predicted using the 2-D model.

This point is further demonstrated by evaluating the final composition profiles across the slab slice (i.e. y-z plane) in Figure 8.8. The basic segregation features are not a strong function of the position along the slab width. The top half of the slab is enriched, the bottom half is depleted, and the most severe depletion occurs at the centerline due to shrinkage driven flow. Therefore, if the 2-D model can reasonably predict the approximate sump shape, which is primarily dependent on the heat transfer across the slab thickness, then the general macrosegregation features will be sufficiently captured. Figure 8.9 shows the comparison between the predicted sump shape for the

2-D calculation and the 3-D calculation of a 400 mm wide slab for three slab thicknesses (60 mm, 80 mm, and 100 mm) demonstrating that the 2-D model does sufficiently predict sump shape for the current system. However, if the inlet is constrained enough, the superheated liquid melt will penetrate the rigid mush causing the formation of an erosion crater at the centerline. This phenomenon must be studied using a 3-D model in order to capture the behavior of the jet. This situation is investigated in the next chapter for a variant of the VDC casting processes known as jet-stirred casting.

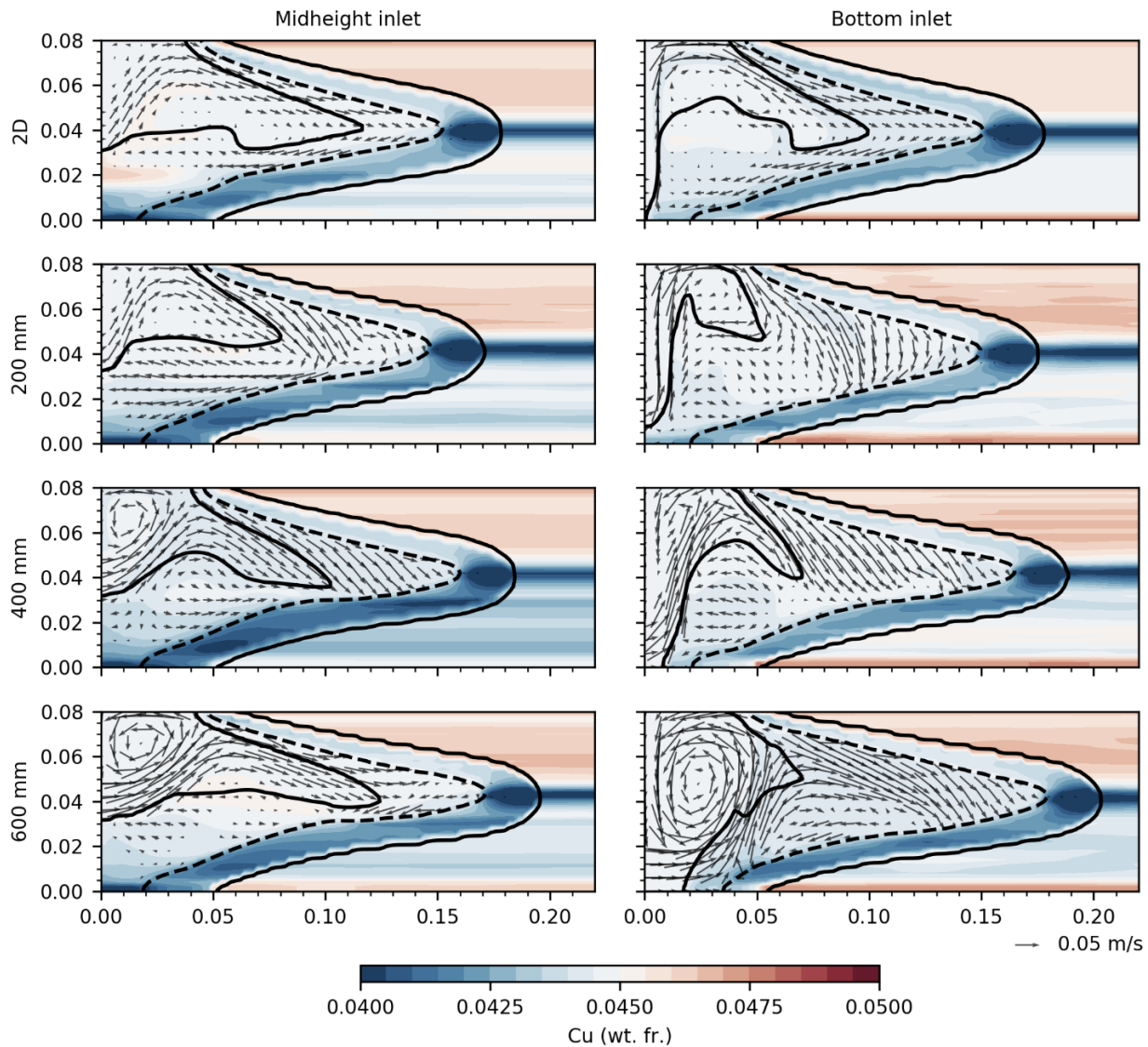


Figure 8.6: Steady state composition fields and flow vectors a 2-D simulation and 3-D simulations at the centerline slabs with increasing width. Bold black lines denote liquidus and solidus, and dotted line denotes packing interface.

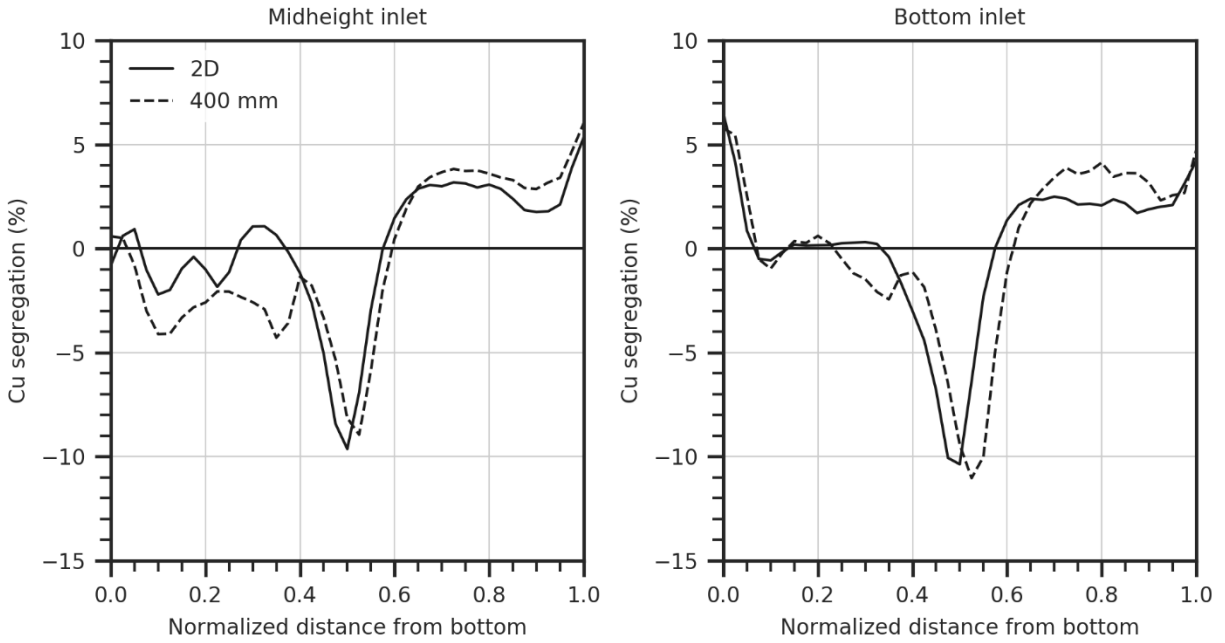


Figure 8.7: Comparison of 2-D and 3-D steady state composition profiles along the centerline of HDC cast slabs.

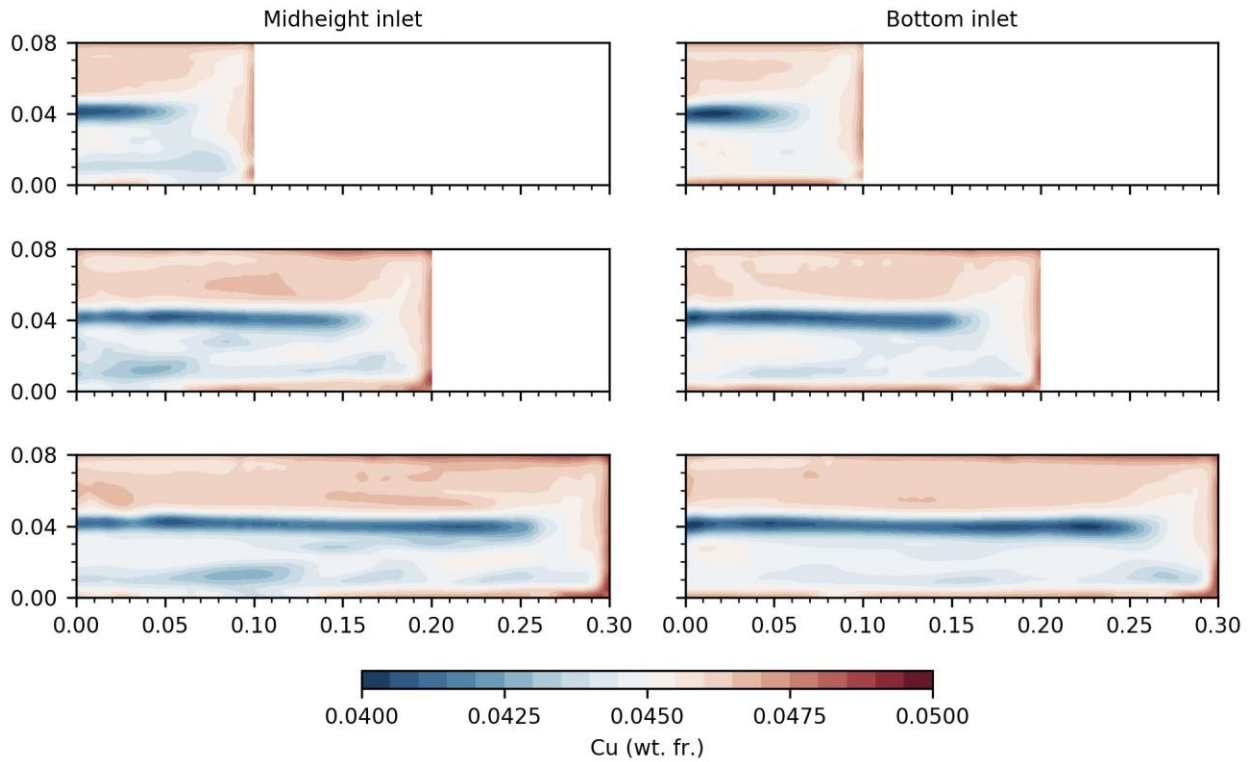


Figure 8.8: Comparison of final macrosegregation fields in the ingot slice for HDC castings with different model widths are inlet configurations.

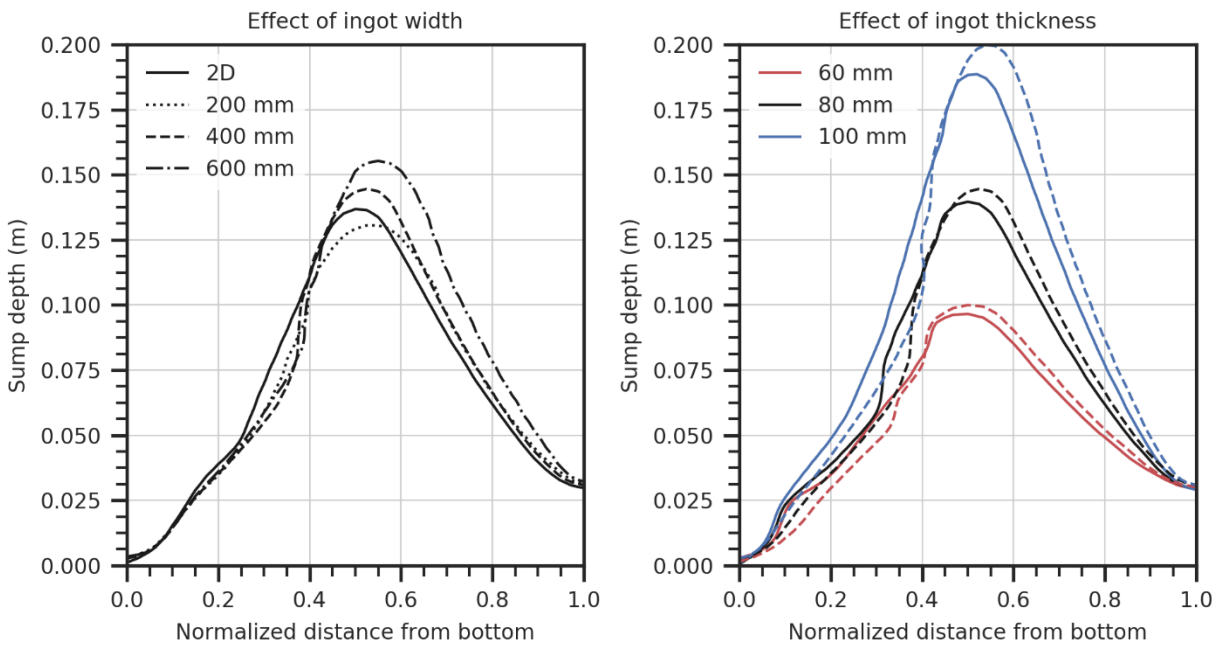


Figure 8.9: Influence of slab width on steady state sump profiles at centerline of HDC cast slabs (left). Comparison of 2-D (dotted) and 3-D (solid) results for different slab thicknesses (right). Each case have a midheight inlet.

9. INVESTIGATION OF JET-STIRRED DIRECT CHILL CASTING

In this chapter, a numerical study is performed to investigate the role that forced convection has on the macrosegregation development in vertical DC casting of large rolling slabs. The mixture model summarized in Table 2.3 and Table 2.4 is used with the face-based drag formulation (see Section 4.2.3) and the diffuse solid flux transition model (see Section 4.3.2) with a diffusion coefficient of $\eta = 0.5$. Additionally, the analytical microsegregation model is used which accounts for solidification shrinkage ($\lambda = 0.05$) and assumes no back-diffusion into the solid phase during solidification ($\beta = 0$). Numerical predictions are compared to experimental trials that were performed during Sam Wagstaff's doctoral research [121]. The experimental macrosegregation and grain structures shown in this chapter were previously published in ref. [9]. Experimental data and micrographs were courteously provided through personal communication with Sam Wagstaff.

9.1 Motivation for Jet-Stirred Casting

Fine equiaxed grains produce isotropic and uniform mechanical properties [4], which reduce hot-cracking sensitivity and permit higher casting speeds [122,123]. Such structures are generally obtained in DC casting by inoculating the melt with grain refiner particles to promote heterogeneous nucleation. The most widely used inoculants in aluminum are based on the Al-Ti-B system consisting of TiB_2 particles 0.1 to 10 μm in diameter [124]. While Al-Ti-B refiners can be used in many aluminum alloys, their effectiveness is not guaranteed in the presence of certain alloying elements [124], or for certain casting conditions [125,126]. Additionally, grain refinement in conventional DC casting promotes the formation of a quiescent zone in the slurry [53] that allows a significant number of solute-depleted grains to accumulate near the ingot centerline. The resulting chemical inhomogeneity on the ingot scale (macrosegregation) is problematic because it affects the amount of secondary phases providing mechanical strengthening to the ingot and cannot be mitigated by subsequent processing.

An alternative, or complimentary, method to melt inoculation is shear-induced grain refinement [127]. There are a number of available techniques which demonstrate refinement by this mechanism, however most use liquid motion to partially remelt existing dendritic grains or deagglomerate existing inclusions [128,129] and inoculants [124], thus creating fragments of solid

that initiate grain growth. Wagstaff and Allanore [9–12] have demonstrated the ability to promote shear-induced grain refinement using forced convection in Al-4.5wt%Cu rolling ingots. In this “jet-stirred” casting process, a narrow downward jet was used to promote dendrite fragmentation at the bottom of the sump while simultaneously preventing grain accumulation at the centerline. Despite consistent experimental observations of the reduced centerline depletion across a wide range of jet conditions, no numerical investigation has been able to confirm suspicion that macrosegregation is reduced due to locally preventing the accumulation of solute-depleted grains. In addition to grain motion, solute redistribution on the macroscale is also influenced by thermosolutal convection and shrinkage driven flow in the rigid mush [4,130]. The degree to which each transport phenomena affects the development of macrosegregation in jet-stirred casting is not yet clear. Numerical process modeling is a useful method to gain insight into the fundamental differences in transport phenomena for this new process.

The objective of this chapter is to investigate transport mechanisms influencing macrosegregation development in both jet-stirred and conventional casting of DC cast rolling slabs based on combined experimental and numerical studies. In the first section, the experimental grain structure and macrosegregation are characterized for both casting methods. The measured grain structure is used as input to the numerical model in the subsequent section. Properly accounting for the change in microstructure between the two processes enables verification of the macrosegregation predictions against experiments. With some confidence that the interplay between various transport phenomena is sufficiently captured by the model, the 3-D flow field is characterized including the combined effects of forced convection, natural convection, grain motion, and shrinkage driven flow. Finally, a parametric study is performed to further elucidate the relative importance of different physical phenomena on macrosegregation development.

9.2 Experimental Trials

An Al-4.5wt%Cu melt was obtained from a commercial gas burner furnace, and was degassed, filtered, and inoculated with 25ppm TiB₂ commercial-grade grain refiner. A bi-level pour system was used to introduce liquid metal through a 22 mm diameter fused silica downspout to a 1540 mm x 600 mm Wagstaff LHCTM (low-head composite) mold, see Figure 9.1. During the initial 500 mm cast length, the casting speed and metal level were varied using a proprietary start-up procedure to prevent hot-cracking. Two ingots were cast at 65 mm/min to a final cast length of

5000 mm: one with a combo-bag fitted around the downspout to uniformly introduce liquid metal (hereinafter referred to as conventional casting), and one with a 46 mm diameter eductor nozzle suspended about 25 mm beneath the downspout to promote stirring (hereinafter jet-stirred casting).

After casting and cooling, both ingots were sectioned into horizontal slices at cast lengths of 1200, 1800 and 2200 mm. Each cross-section was divided into quadrants and a series of 45 samples were removed using a core drill for metallographic analysis. The opposite quadrant was marked with a set of 455 points for compositional analysis using an Olympus Delta Professional Alloy Plus XRF analyzer (see Figure 9.2). The metallographic samples were etched with dilute Tetrafluoroboric acid (HBF_4) and analyzed in terms of grain size and secondary dendrite arm spacing (when appropriate) using an optical microscope and the line-intercept method at 50x magnification. The metallographic and compositional data taken at each cast length was compared to determine if time invariant trends were established in the so-called steady state regime of DC casting (considered to occur between 20% and 80% of the final cast length). For conventional casting, the grain structures and macrosegregation patterns were very similar at each cast length. However, for jet-stirred casting the centerline solute depletion at 2200 mm was more pronounced and the grains were slightly larger than at either 1200 mm or 1800 mm [9]. To simplify comparison between casting methods in the current study, a choice was made to only consider the data taken at 1800 mm. It is therefore emphasized that the transient variations in grain structure macrosegregation observed for jet-stirred casting are not considered in experimental results of this study.

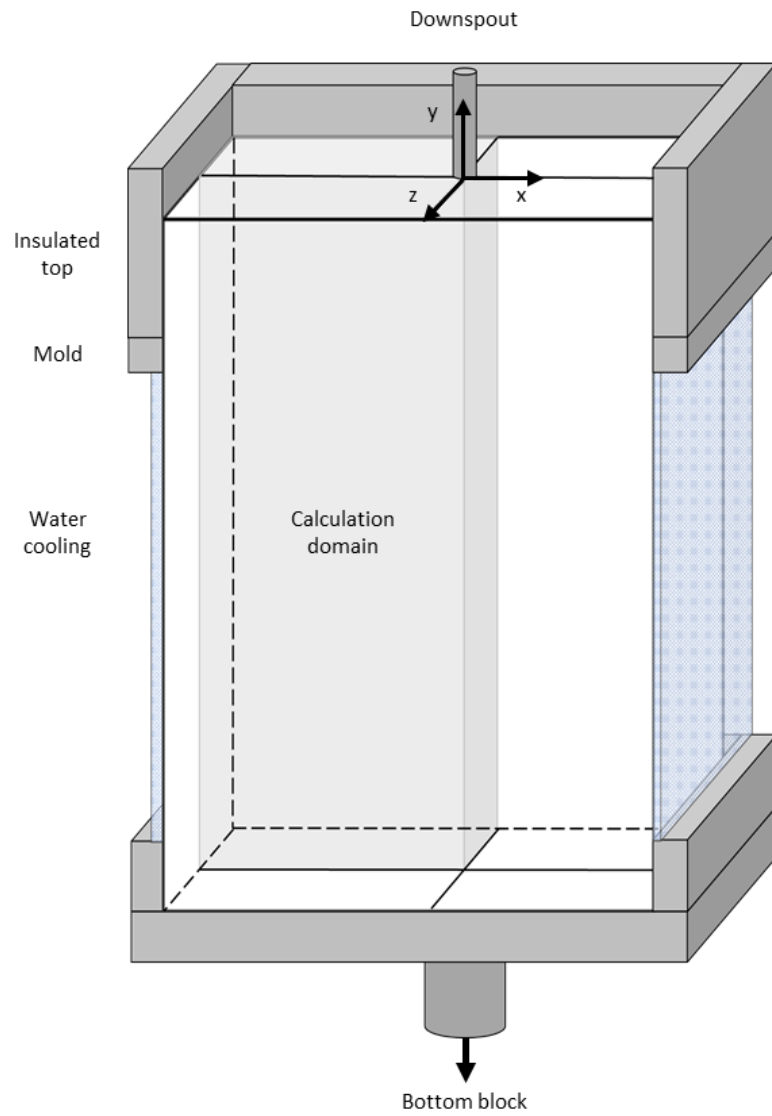


Figure 9.1: Schematic of the low-head, jet-stirred DC caster and computational domain with a bi-level feeding scheme.

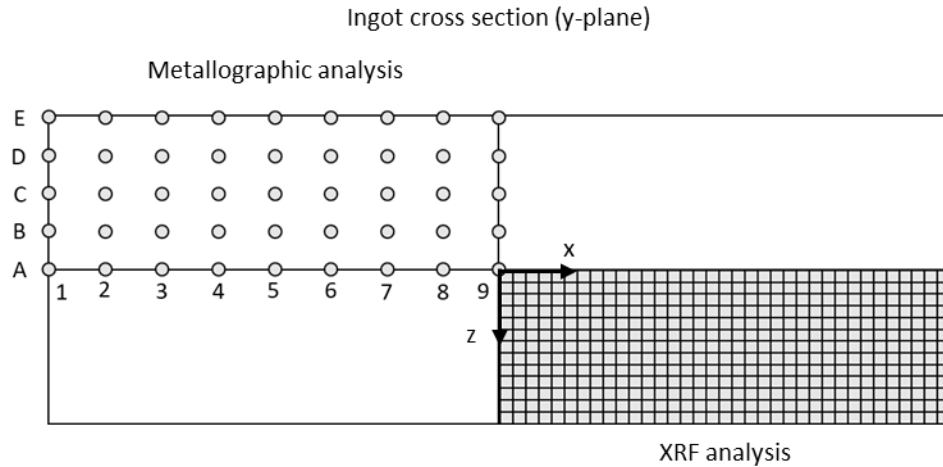


Figure 9.2: Schematic of the ingot cross section used for cutting quadrants for metallographic and XRF analysis.

9.2.1 Experimental Results

Contour plots of the final grain size and macrosegregation in the examined ingot quadrants are provided in Figure 9.3 for both conventional and jet-stirred casting. The macrosegregation profiles have been reflected across the x - and z - axis to match the orientation of the quadrant used for metallographic analysis. In Figure 9.4, micrographs along 9A-E are provided for each case.

For conventional casting, the most obvious segregation feature is the depleted region near the centerline extending 75 mm in the y -direction and 600 mm in the negative x -direction. Solute depletion is most severe ($< -10\%$) in a narrow region extending 50 mm from the centerline, and less severe (about -5% to -10%) in the remaining area. Adjacent to this depletion region is an enriched region of similar size. Results from the metallographic analysis show that large diameter dendritic grains (about $250\ \mu\text{m}$) accumulate in this enriched region. From previous numerical and experimental studies [56], it is known that the majority of grains nucleate near the mold and remain close to the packing interface as they are swept downward by buoyancy forces. Solubility undercooling in the thermal boundary layer near the packing interface promote rapid growth until their eventual coalescence. The fact that the largest grains accumulate some distance from the centerline indicates a local flattening of the packing interface in this location, otherwise it is expected for these grains to continue toward the centerline. At the centerline, the grain size is noticeably reduced (about $150\ \mu\text{m}$) indicating that smaller grains not captured by the local

flattening of the packing interface are advected into the solutally stratified core where they experience slow growth and significant coarsening until their eventual coalescence.

The micrographs along 9A-E confirm the suggested growth history of the grains for conventional casting (see Figure 9.4). In the region about 75 mm from the centerline, the grains are noticeably larger and more dendritic than at the centerline, where the grains are either globular or coarse-cell dendrites, the distinction being difficult to determine in post-mortem metallographic analysis. The progressive growth of the dendritic grains as they travel down the packing interface are supported by the increase in grain size from the rolling face until about 75 mm from the centerline.

For jet-stirred casting, the size and severity of the depletion region near the centerline is noticeably reduced. Establishing more general trends about macrosegregation in jet-stirred casting is more difficult than conventional casting since the segregation features are more randomly dispersed. Results from the metallographic analysis show that the grains are significantly refined and homogenized compared to conventional casting. Similar to conventional casting, the largest grains accumulate some distance from the centerline, however, these grains are refined by about 100 μm for jet-stirred casting. The micrographs along 9A-E further show that the grains are noticeably smaller and more globular compared to conventional casting (see Figure 9.4).

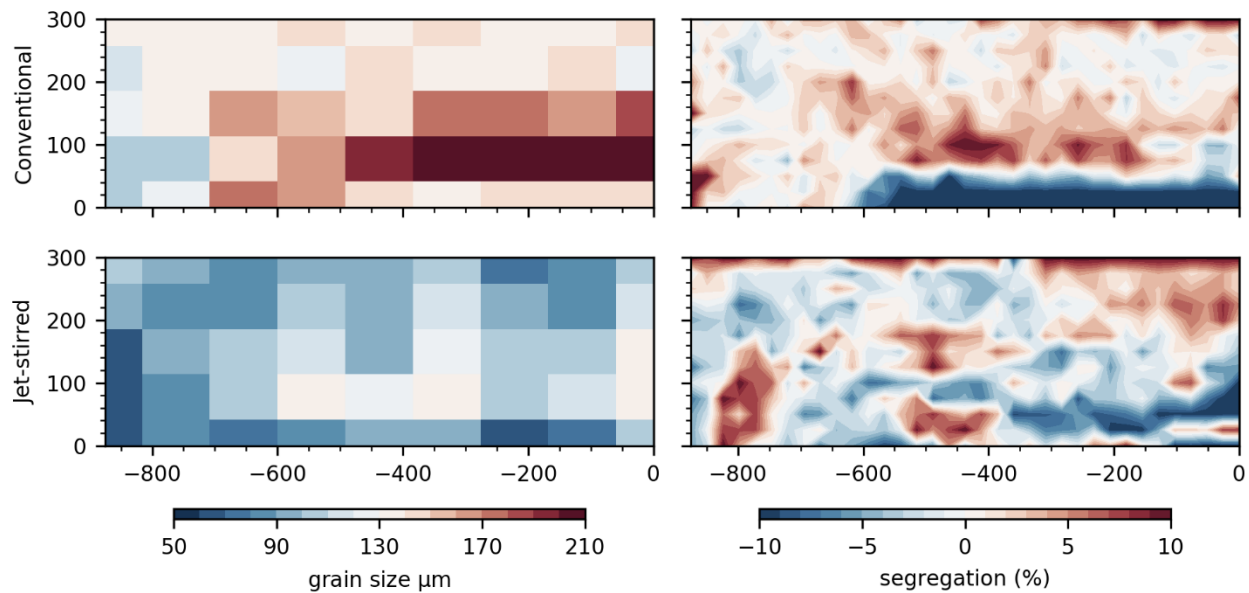


Figure 9.3: Comparison of the grain size and macrosegregation profiles for conventional casting and jet-stirred Al-4.5wt%Cu.

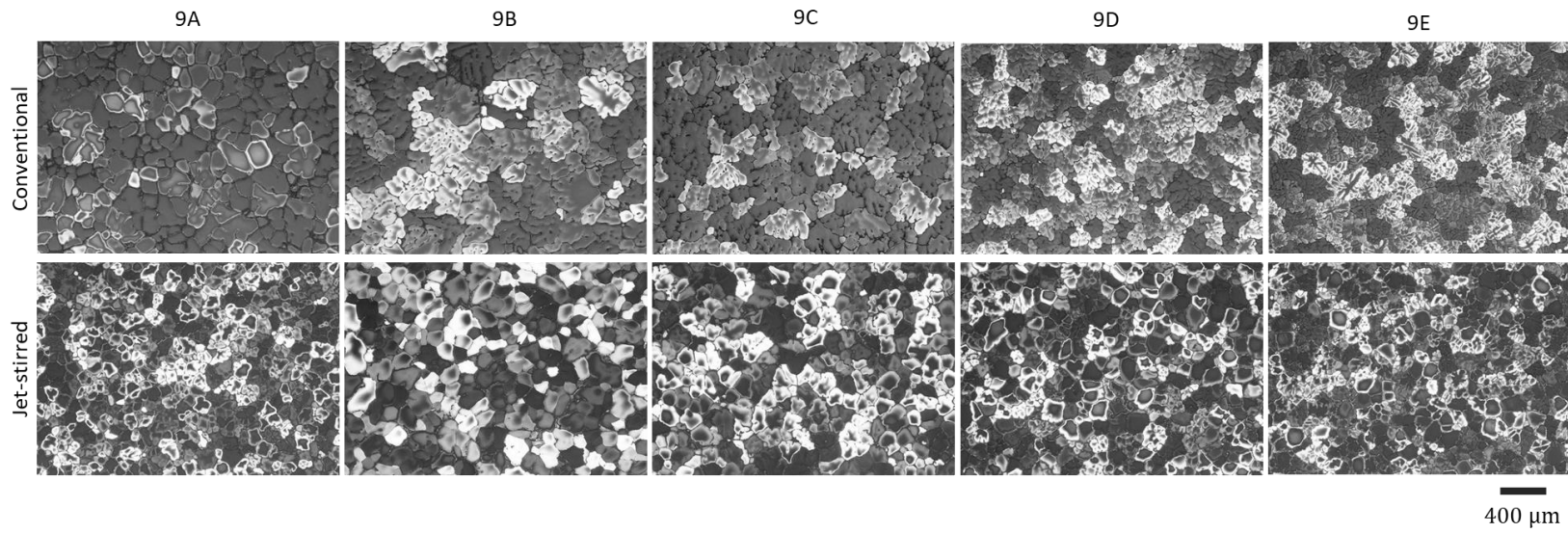


Figure 9.4: Micrographs etched with HBF₄ showing the final grain structure along the mid-length of convectional cast (top) and jet-stirred (bottom) Al-4.5wt%Cu slabs.

9.2.2 Experimental Discussion

Histograms of macrosegregation are compared for conventional and jet-stirred ingot quadrants in Figure 9.5. For Al alloy 2014 (ASTM B209), the lower and upper specification limits for copper are 3.9wt% and 5.0wt%, respectively. These limits correspond to segregation of about -13% and 11%, as indicated by the vertical lines in Figure 9.5. Although jet-stirred casting does not eliminate the formation of depleted regions, the total ingot volume below the lower solute specification limit is significantly reduced. For conventional casting, 8.1% of the ingot quadrant is below the lower limit, attributed mostly to the depleted centerline, while for jet-stirred casting this amount is only 2.0%. Although the volume below the lower specification limit is noticeably reduced, jet-stirred casting causes an increase in total ingot volume over the upper specification limit of 5.0wt%Cu. When accounting for both specification limits, the total out-of-spec volume is 9.9% for conventional casting and 6.0% for jet-stirred casting.

While this decrease does not appear to be significant at first, it is important to realize that the majority of the out-of-spec volume for jet-stirred casting is located in a narrow region along the outer surface where it can be easily removed during subsequent processing. According to conventional casting practices about 15 mm of the ingot surface would be scalped for the current ingots. Although the spatial resolution of the XRF detector (about 25 mm) is lower than required to observe details of the scalped region, the effect of scalping on the final macrosegregation can be roughly investigated by omitting the compositional data taken at the surface. In this case, the total out-of-spec volume of the ingot is 2.0% for the jet-stirred ingot compared to 8.6% for the conventional ingot.

Another significant benefit of jet-stirred casting is grain size reduction and improved grain morphology homogeneity. In Figure 9.6, the grain size probability densities are provided for conventional and jet-stirred casting. It is shown that the average grain size is reduced from $152 \pm 35 \mu\text{m}$ for conventional casting to $97 \pm 19 \mu\text{m}$ for jet-stirred casting, reported along with the sample standard deviation. Therefore, an average grain size reduction of 36% was observed for jet-stirred casting along with a 46% improvement in grain size uniformity. A measurement of secondary dendrite arm spacings could not be made for jet-stirred casting since it exhibits a mostly globular structure apart from some fine coarse-cell dendrites near the jet impact point. Nevertheless, secondary dendrite arm spacing probability densities are provided for conventional casting for completeness in Figure 9.6.

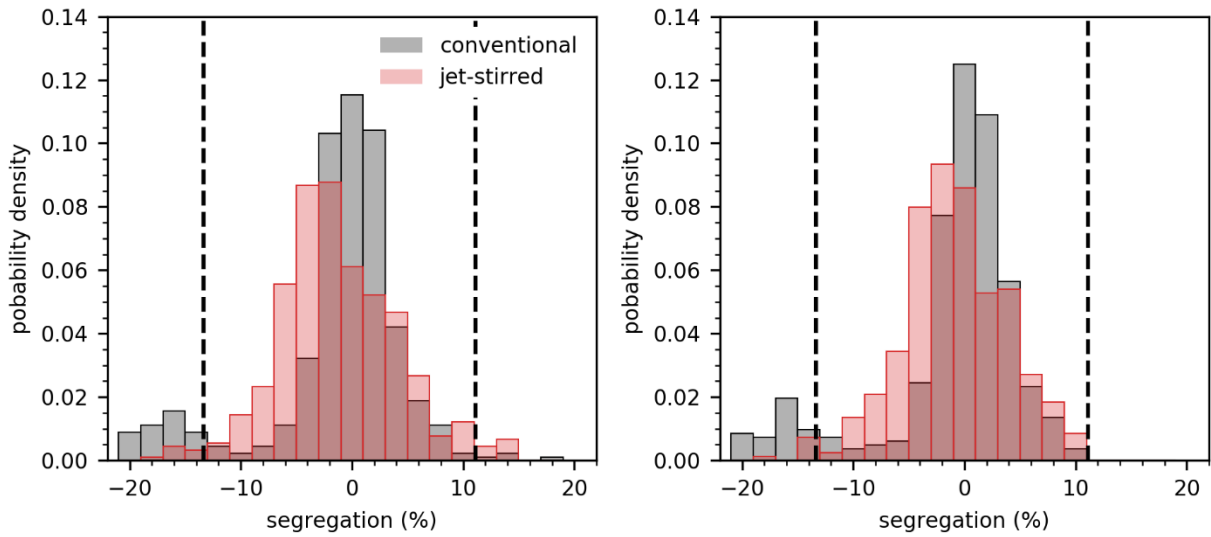


Figure 9.5: Histograms of macrosegregation measured across the ingot quadrant as-cast (left) and after scalping the surface (right).

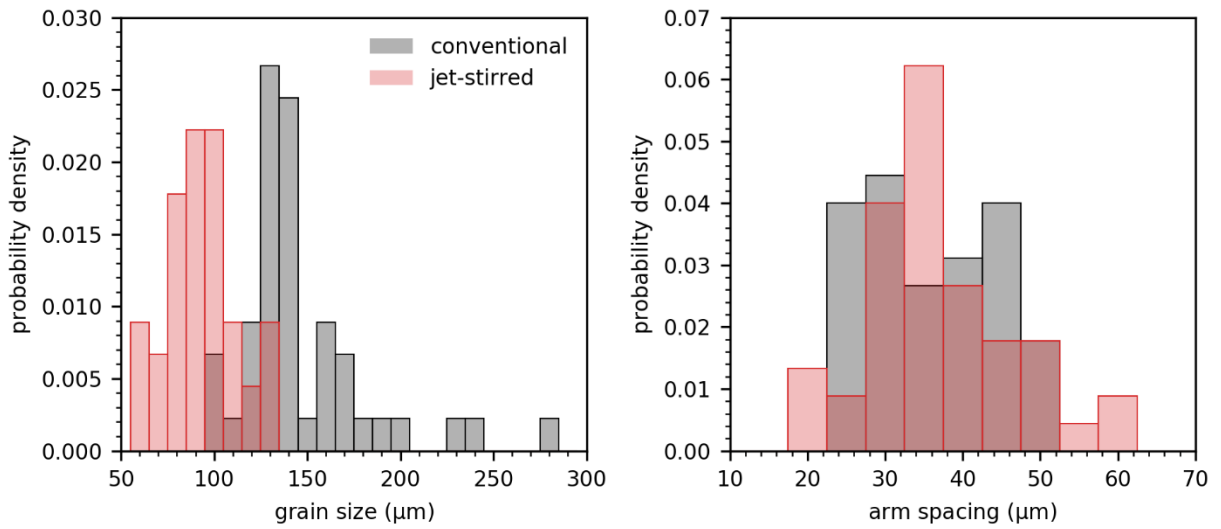


Figure 9.6: Comparison of histograms for final grain size (left) and dendritic arm spacing (right) measured across the ingot quadrant.

9.3 Numerical Investigation

In this section, a numerical study is performed to elucidate details about the transport phenomena occurring in both conventional and jet-stirred DC casting of large rolling slabs. The computation domain is $875 \text{ mm} \times 1500 \text{ mm} \times 300 \text{ mm}$ with grid spacing of about 6 mm. Because the numerical model makes no attempt to predict the grain structure, it must be supplied from the experimental trials. The metallographic data shows an average grain size of $d_g = 152 \pm 35 \mu\text{m}$ for conventional casting and $d_g = 97 \pm 19 \mu\text{m}$ for jet-stirred casting. The internal solid fraction at packing is difficult to determine from post-mortem metallographic analysis so three values are estimated here $g_{si} = 0.40, 0.55,$ and 0.70 . Therefore, a total of nine simulations are performed for each casting method to cover the experimental uncertainty band in grain structures. A characteristic length scale of $\lambda = 40 \mu\text{m}$ is used to calculate the permeability in the rigid mush based on the arm spacing reported in Figure 9.6. Thermophysical properties and phase diagram data for Al-4.5wt%Cu are provided in Table A1.

9.3.1 Characterization of the Inflow Jet

To provide insight into the basic features of the inflow and sump shape for both casting methods, solid fraction isocontours are shown in Figure 9.7. The white contours indicate the liquidus surface and the packing interface. The region between these two contours is the slurry where grains are mobile, and the region between the packing interface and the solidus is the rigid mush where grains are coalesced. While the inflow for conventional casting reaches a steady-state solution with a penetration depth of about 200 mm, two different flow states are found during jet-stirred casting indicated at “A” and “B”. In the first state, the jet penetrates the packing interface forming an erosion crater in the rigid mush. In the second state, the jet retreats from this crater, but the crater shape remains unchanged. A period for the unsteady flow in jet-stirred casting was not determined; however, “A” and “B” are 500 s apart and correspond to the maximum and minimum penetration depths of the inflow captured. The unsteady flow during jet mixing gives some insight into why the experimental composition profiles vary along the ingot length [9].

During the experimental casting trials, the location of the packing interface was monitored by inserting a steel rod through the top of the liquid metal pool near the downspout and probing for the bottom of the sump indicated by a noticeable change in resistance. The difference between

this contact point and the top liquid surface is the sump depth. For jet-stirred casting, the change in resistance was immediate at about 700 mm, whereas for conventional casting the change in resistance was gradual between 500 mm and 700 mm indicating that a loosely packed bed may form. Although there is little evidence available to explain this phenomenon due to the difficulty of determining the packed mush zone structure, it is noted that the experimental trend is supported by the predicted sump positions in Figure 9.7. Because the thickness and orientation of the rigid mush control the amount and direction of solute-enriched liquid transported by shrinkage driven flow [131], the dramatic difference in the sump shape is believed to have a significant effect on the macrosegregation. With this transport mechanism in mind, the macrosegregation predictions are compared to the experiments in the following section.

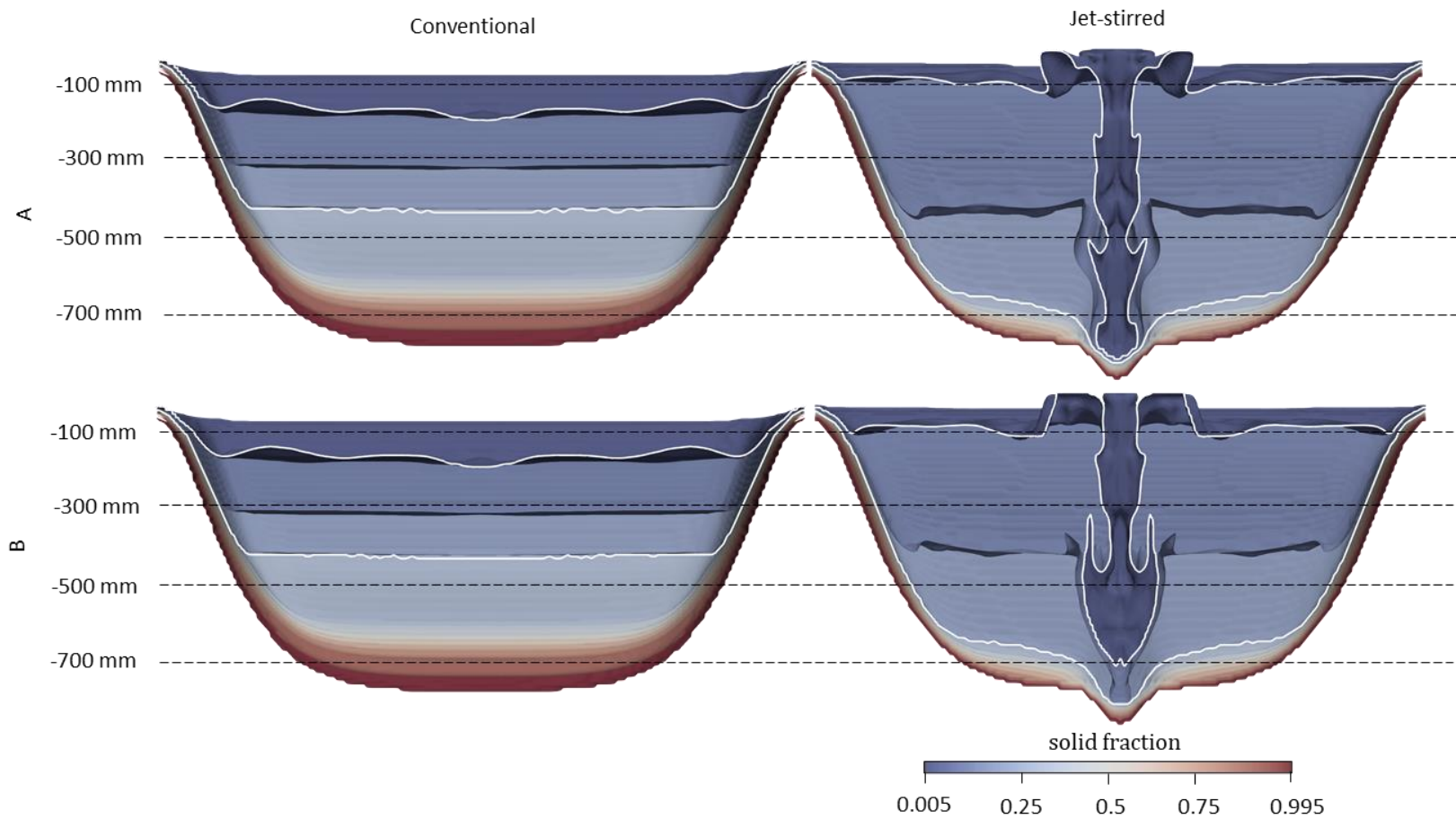


Figure 9.7: Solid fraction isocontours for conventional and jet-stirred casting. The white line surrounding the inflow marks the liquidus surface and the other white line marks the packing interface. A was taken at upon the composition field reaching steady-state and B was taken 500 s later.

9.3.2 Numerical Results

Using the values of grain diameter and internal solid fraction, final segregation maps were calculated for conventional and jet-stirred casting processes. A qualitative comparison of the numerical predictions of the composition fields to the experimental results is shown in Figure 9.8. The numerical predictions are reflected across the x-axis to aid visual comparison. Several gross macrosegregation features in the experiments are predicted by the model, most notably the reduction of centerline depletion for jet-stirred casting compared to conventional casting.

For conventional casting, the geometry of the centerline depletion predicted by the model is in excellent agreement with experiments, both extending about ± 600 mm in the -x direction and 75 mm in the +y direction. Although the level of solute depletion directly at the centerline also agrees with experiments, the area occupied by the most severe depletion ($< -10\%$) is under-predicted. Disagreement in the geometry of this depletion zone may be due to several factors. First, the spatial resolution of the XRF (about 25 mm) is lower than the spatial resolution of the numerical grid (about 7 mm) and therefore, the model will tend to predict smoother variations in composition. Second, when sectioning the ingots into quadrants, 2-fold symmetry about the geometric centerlines was assumed so it cannot be claimed with certainty that the experimental quadrants are symmetric. In a previous experimental study [8], segregation maps were extended past the geometric centerlines to ensure that a symmetric quadrant could be constructed for comparison to numerical predictions.

The model also appears to universally underpredict enrichment regions compared to the experimental results particularly near the ingot surfaces and adjacent to the centerline depletion zone when using the average grain parameters. This is not surprising since spatial variation in the grain parameters is shown to vary significantly in Figure 9.3 and can have a noticeable effect on macrosegregation development. It is shown in Section 5.1 that better agreement of the enrichment zones at the midthickness can be obtained using different grain morphology parameters in the model. Nevertheless, the general features of the centerline depletion region, of greatest concern in this study, are sufficiently captured by the numerical model using average values. A summary of the final segregation maps predicted for conventional casting over the experimental uncertainty band of grain size and morphology is provided in Figure 9.10.

It is more difficult to make direct comparisons for jet-stirred casting due to the increased randomness in experimental macrosegregation. Nevertheless, some definitive trends regarding the

centerline depletion can be established. First, the size and severity of centerline depletion for jet-stirred casting are reduced in both experiments and predictions. A narrow band of strong depletion ($<-10\%$) near the centerline between $x = \pm 200$ mm and ± 400 mm continues around the periphery of the erosion crater formed by the local penetration of the hot jet (Figure 9.8). The crater geometry predicted by the model is elliptical, 200 mm along the x-axis and 100 mm along the y-axis which agrees with the shape of the depletion regions in experiments and predictions. Directly beneath the impingement point of the jet a depletion region exists with the same diameter of the jet (about 45 mm). Between the depleted center and depleted periphery of the crater, a nominal to slightly enriched region is observed. Recalling that shrinkage-driven flow is directly related to the vertical length and orientation of the sump gives some confidence that the model accurately captures phenomena responsible for this macrosegregation feature in experiments. Similar to conventional casting, enrichment regions are found near the surfaces and adjacent to the centerline depletion region, all of which are under-predicted by the model. A summary of the final segregation maps predicted for jet-stirred casting over the experimental uncertainty band of grain size and morphology is provided in Figure 9.11.

To further demonstrate the aforementioned macrosegregation trends, experimental values are averaged along the thickness profile from the representative area between $x=-50$ mm and $x=0$ mm (Figure 9.8) and compared to the numerical predictions at $x=0$ mm along the same profile. Averaging the experimental values is done to better elucidate the basic change in macrosegregation in the presence of penetrating jet. In Figure 9.9, the average experimental profiles (indicated by the black markers with the standard deviation of the 3 readings) are compared to numerical predictions across the range of experimental grain sizes and assumed internal solid fractions. The nominal predictions are indicated by the hollow red circles and remaining predictions are indicated using solid gray circles, meant to represent the aleatoric uncertainty band of the grain morphologies used in the simplified model. For both conventional casting, the subsurface is close to the nominal composition in both experiments and predictions. The segregation increases to a maximum enrichment at about 110 mm in the model and 125 mm in the experiments. However, it is noted that if a larger representative area were taken for the experiments, agreement in these positions would improve. Moving closer to the centerline, both model and experiments show the segregation drop to a maximum depletion of about -14% . Again, the extent of this maximum depletion region is slightly larger (about 25 mm) in the experiments compared to the predictions. For jet-stirred

casting, surface enrichment is underpredicted by the numerical model. Since this enrichment is consistent across several jet-stirred ingots, it is possible that permeability of the globular microstructure is underpredicted using the current model inputs parameters. The maximum depletion regions below the jet impingement point and along the periphery of the erosion crater are in excellent agreement between experiments and prediction and have the approximately the same severity as convectional casting (about -14%). From these combined results, it appears that the numerical model sufficiently captures the transport phenomena leading the macrosegregation in both conventional and jet-stirred casting. In order to elucidate the interplay between various transport phenomena controlling macrosegregation, a more complete description of the flow field is offered in the next section.

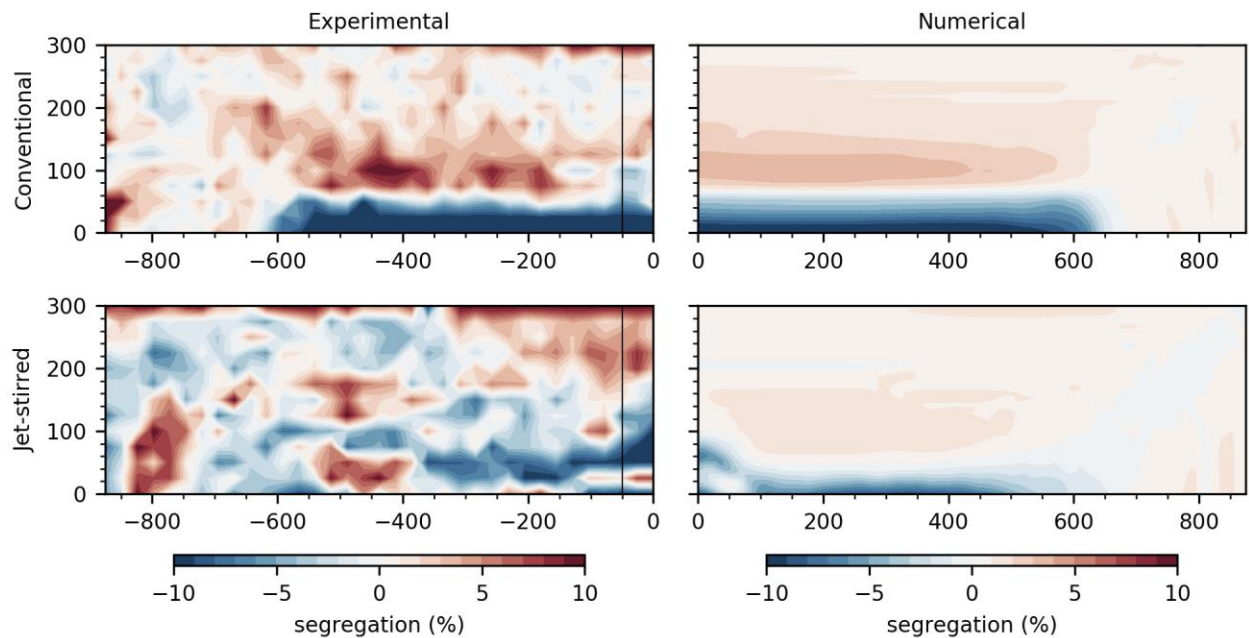


Figure 9.8: Comparison of the experimental segregation contours (left) to the numerical prediction (right) using the average grain size and morphology parameters for conventional and jet-stirred casting.

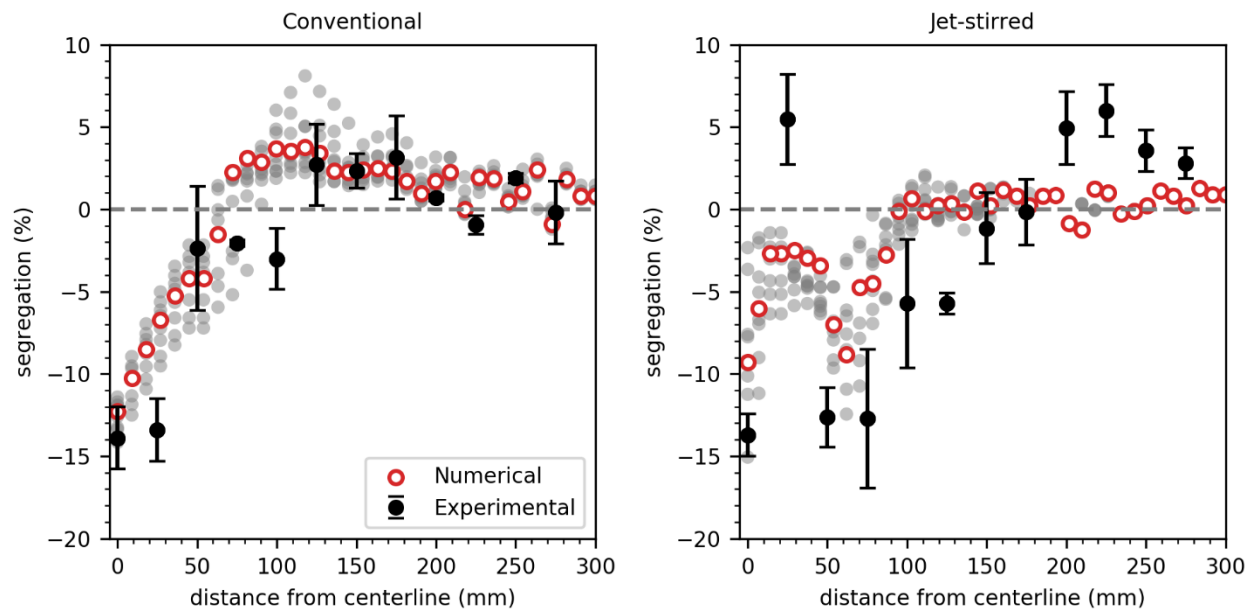


Figure 9.9: Comparison of macrosegregation profiles across the quadrant thickness for conventional casting (left) and jet-stirred casting (right). The experimental data indicated by the solid black markers was averaged over a representative area extending 115 mm from the mid-width.

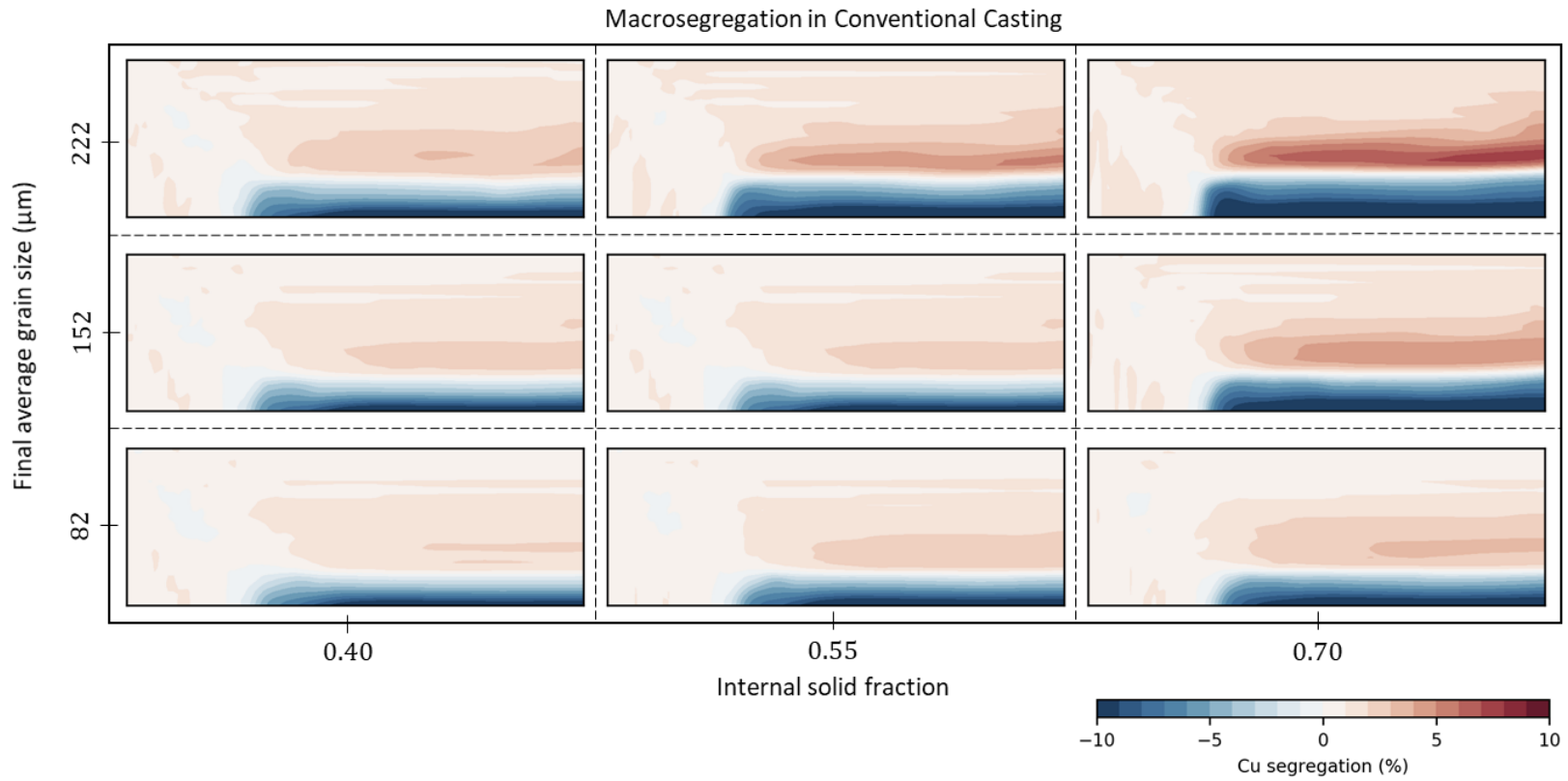


Figure 9.10: Comparison of final macrosegregation fields in the conventional ingot quadrant for various grain size and morphology parameters within the uncertainty band of the experimental data.

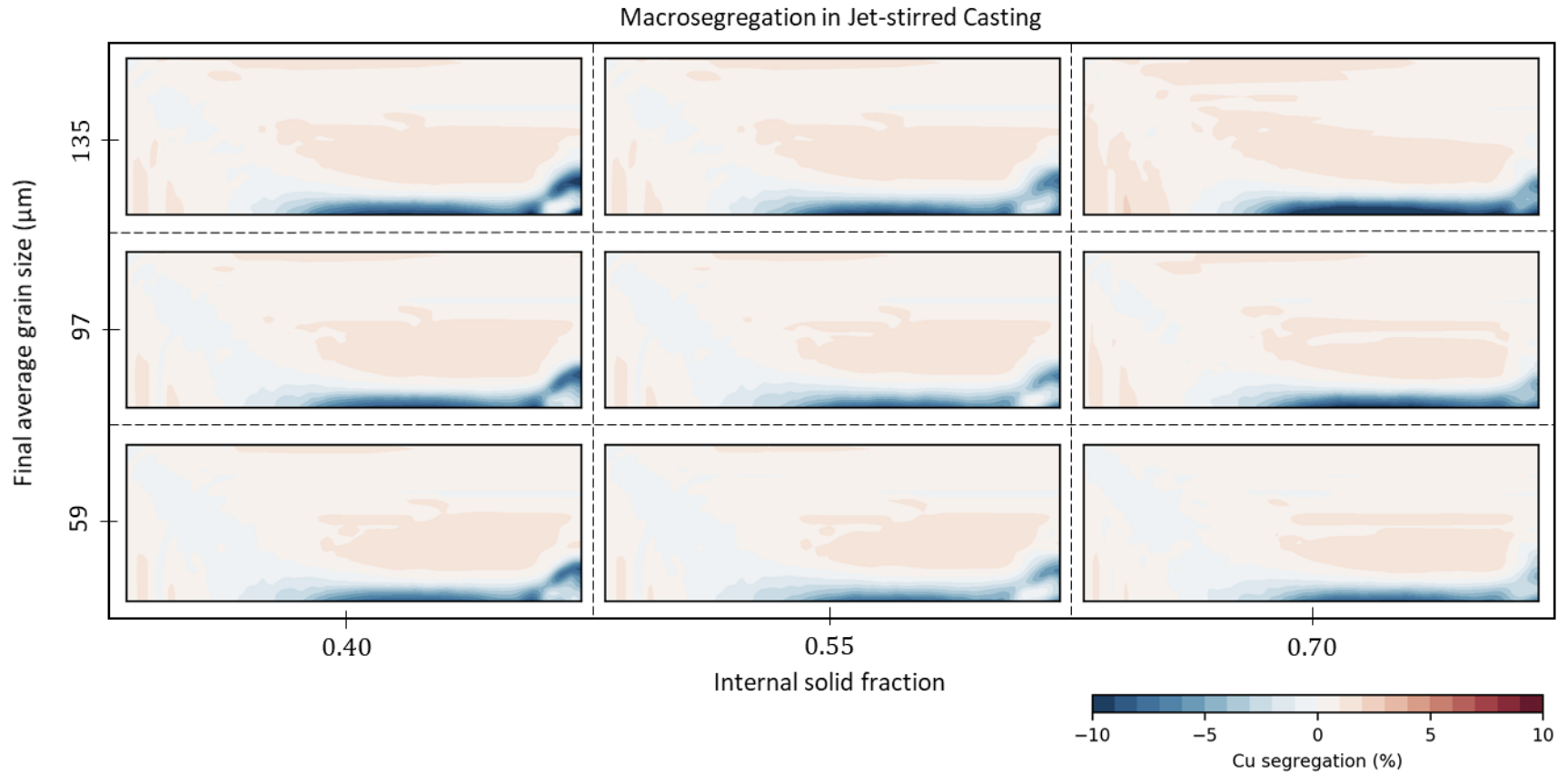


Figure 9.11: Comparison of final macrosegregation fields in the jet-stirred ingot quadrant for various grain size and morphology parameters within the uncertainty band of the experimental data.

9.3.3 Characterization of the Flow Field

Visualization of the 3-D flow field presents a unique challenge for jet-stirred casting since the velocities in the sump span several orders of magnitude and the flow field is unsteady. The same features of the jet-stirred flow field make it difficult to compare to conventional casting where the flow in the core of the sump is quiescent. For this reason, previous studies have generally omitted the 3-D flow field characterization which is crucial towards the understanding of macrosegregation development [63,64]. Figure 9.12 shows contour plots of the z-component of mixture velocity for flow field “B” at different depths in the sump previously marked in Figure 9.7. A symmetric logarithmic scaling is used for better visualization where red indicates upward flow and blue indicates downward flow in the sump. To highlight the direction of the secondary flow field, unit vectors of the x-component and y-component are shown.

For conventional casting, the inflow penetrates to a depth of 200 mm before thermal buoyancy forces drive the inflow upwards towards the top surface indicated by the strong red region surrounding the inflow at $z = -100$ mm. The secondary flow field is uniformly rotating in a consistent counterclockwise direction at various depths in the sump. Along the packing interface, negative buoyancy forces initiated near the chilled surface drive the fluid downwards where it either becomes entrained into the mushy zone or enters the recirculation cell in the slurry where it has a slight upwards component.

For jet-stirred casting, the inflow is strong enough to overcome buoyancy and shear effects and penetrated until the bottom of the sump is contacted at a depth of about -700 mm. Competition between the upward buoyancy forces in the hot jet and downward hydrostatic and electromagnetic forces persists as the jet is driven into the sump until buoyancy eventually forces the inflow towards the top surface. This is similar to the flow field reported in ref. [49] for axisymmetric billets and consistent with experimental observation of a perturbed top surface around the downspout. A counterclockwise rotation similar to conventional casting is observed for most of the secondary flow, however more lateral mixing occurs. The flow in most of the sump has a stronger upflow than conventional casting due to convergence of flow cells driven independently by forced convection and buoyancy along the chilled surface.

Figure 9.13 shows contour plots of composition and corresponding unit vectors of the mixture velocity along the $y=0$ mm and $x=0$ mm planes. Again, it is shown that in both casting methods the inflow penetrates the top surface before it is primarily entrained to the short face. For

conventional casting, only a single recirculation cell appears bounded by buoyance driven wall jets. The rigid mush formation under these conditions is about 400 mm at $x=0$ mm. For jet-stirred casting the rigid mush is only about 20 mm along the erosion crater, however the significant inclination along the short face results in a large horizontal component to shrinkage driven flow contributing the depletion in this region.

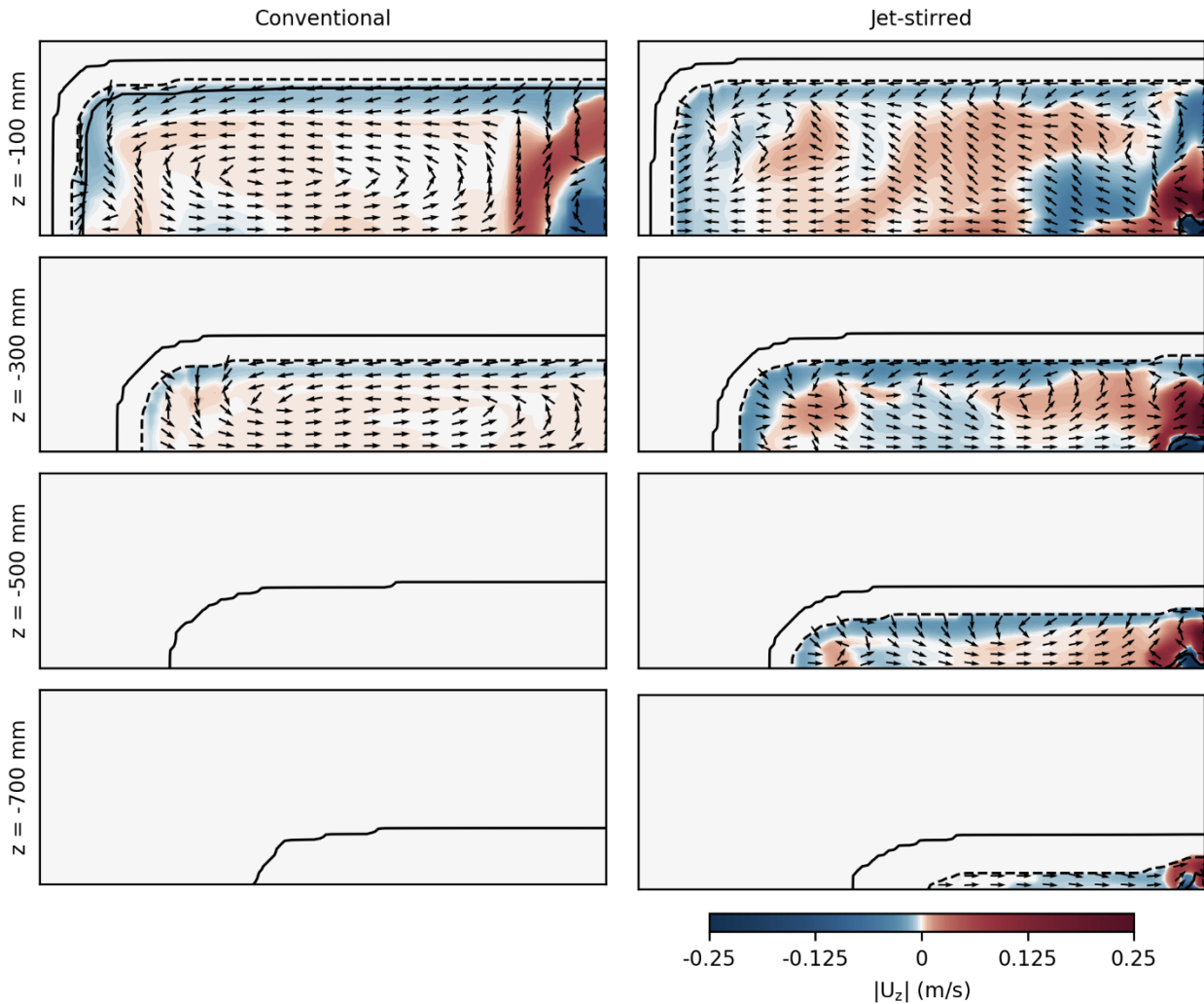


Figure 9.12: Contour plots of the z-component velocity at different depths in the sump for conventional and jet-stirred casting where a negative component (blue) indicates downward flow in the direction of casting. The vectors are plotted as unit vectors of the x-component and y-component to highlight the direction of the secondary flow field. The solid black lines mark the solidus and liquidus surfaces, while the dotted black line marks the packing interface.

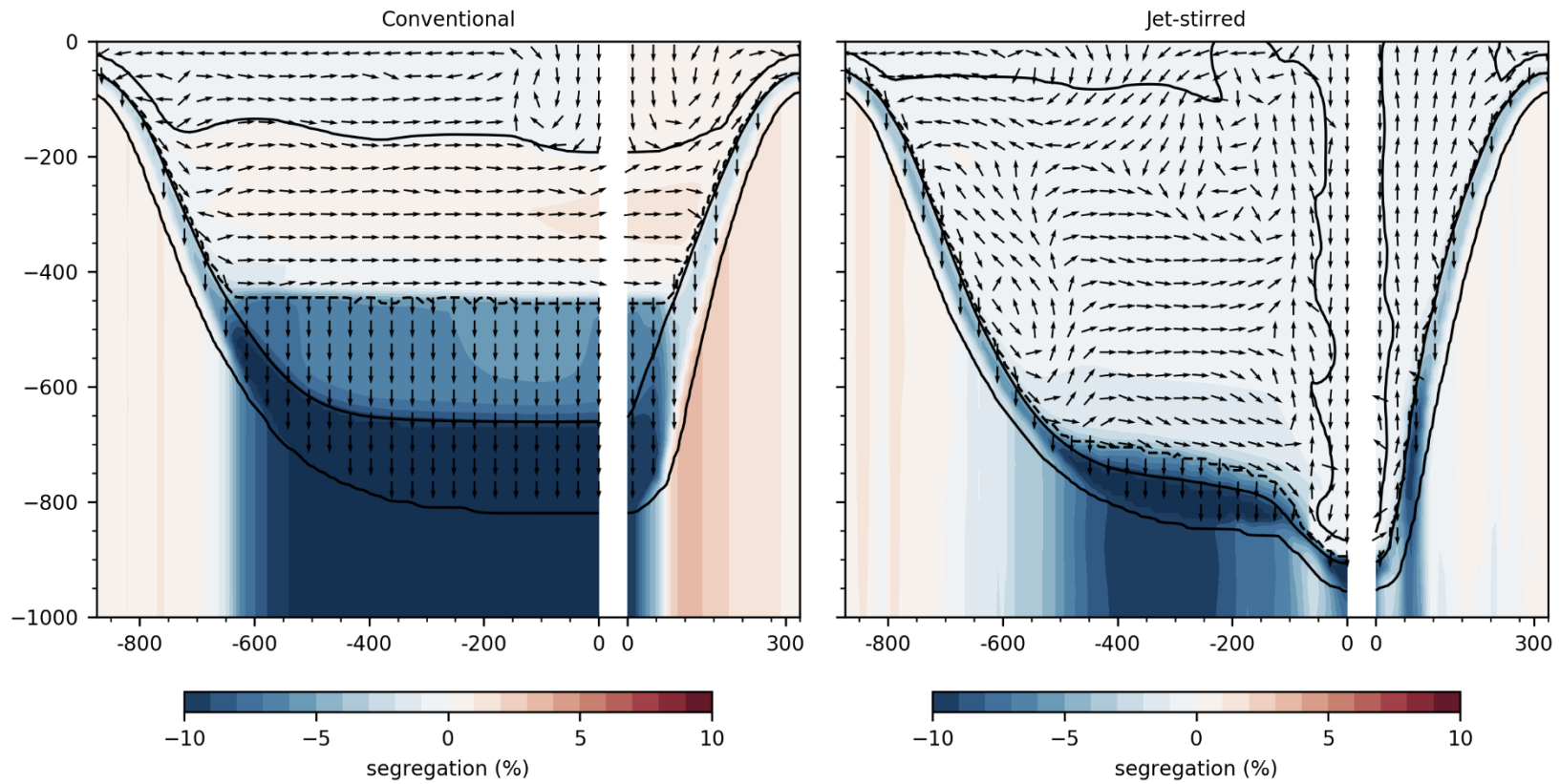


Figure 9.13: Contour plots of the segregation and solid fraction fields at the x-z plane at the centerline and y-z plane at the midwidth. The top solid line marks the liquidus surface while the bottom solid line marks the eutectic surface. The dotted line indicates the packing interface.

9.3.4 Influence of Different Transport Mechanisms

To investigate the relative importance of different transport mechanisms contributing to macrosegregation development, three cases are investigated in Figure 9.14. The first case only considers natural convection (NC) which controls the formation of the primary flow structure in the sump characterized by a recirculation cell bounded by buoyant jets driving flow down the packing interface. Figure 9.15 shows that natural convection contributes +1.5% centerline segregation through the advection of solute-enriched liquid in the rigid mush towards the centerline via negative buoyancy.

In the second case, the influence of relative grain motion (GM) is accounted for. Under these conditions, the flow in the slurry and rigid mush are essentially unchanged, however a loosely packed bed of grains accumulated near the centerline. As these grains coarsen and settle in the quiescent core of the sump, they cause negative segregation near the centerline. The accumulation of these grains enriches the slurry, which is recirculated and entrained into the rigid mush between $x=100$ and 200 m contributes to a positive segregation in this region. Thus, grain motion contributes -2.8% to centerline segregation due to the accumulation of solute-depleted grains at the centerline and +1.5% to the midthickness segregation due to the enrichment of the slurry.

Based on the difference in packing interface between the previous cases, two different mechanism for grain coalesce can be identified. The first mechanism is for grains along the inclined sump to coalesce by a rapid growth and impingement. This is supported by the micrographs in Figure 9.4, which contains dendritic grains increasing in size towards centerline. The second mechanism is for the remaining grains to coarsen and settle in the thermally stratified region near the centerline where accumulate. This is also supported from the micrographs in Figure 9.4, which contains globular grains near the centerline.

While formation of this loosely packed bed of globular grains has long been attributed as the primary cause of depleted centerlines in DC casting, it does not appear to independently cause this feature. When shrinkage drive flow is considered, a significant change in the orientation of the interdendritic liquid is observed in the rigid mush. The flow is now oriented normal to the solid fraction isocontours pulling highly enriched liquid away from the centerline and towards the midthickness. As shown in Figure 9.15, this flow field contributes the majority of macrosegregation, -10% to centerline and +2% to mid-thickness.

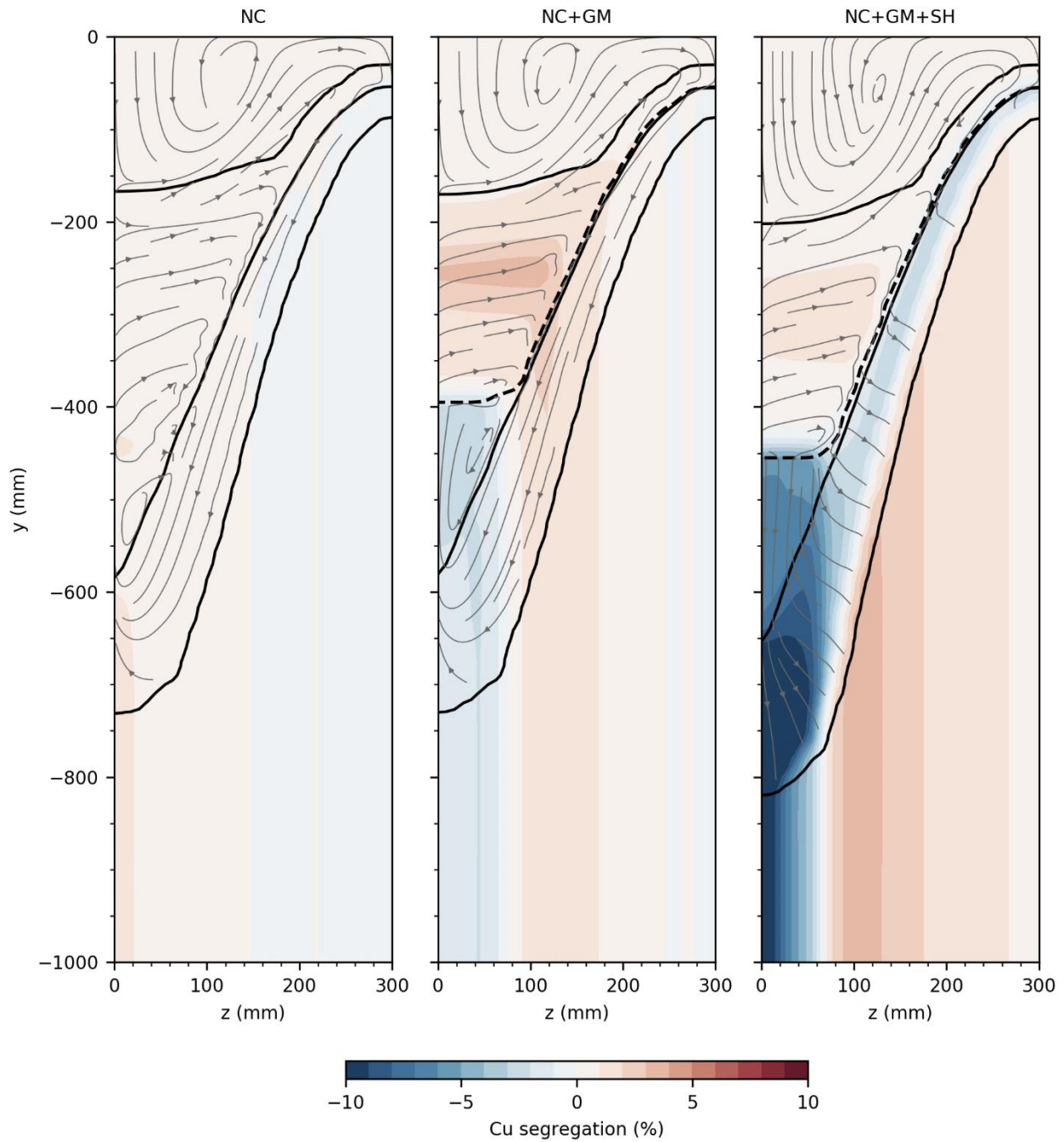


Figure 9.14: Segregation formation along the thickness for various transport mechanisms. The top solid line marks the liquidus surface while the bottom solid line marks the eutectic surface. The dotted line indicates the packing interface. Streamlines are calculated in the ingot frame of reference. Three cases are provided: natural convection only (NC), natural convection and grain motion (NC+GM), and natural convection, grain motion, and shrinkage (NC+GM+SH).

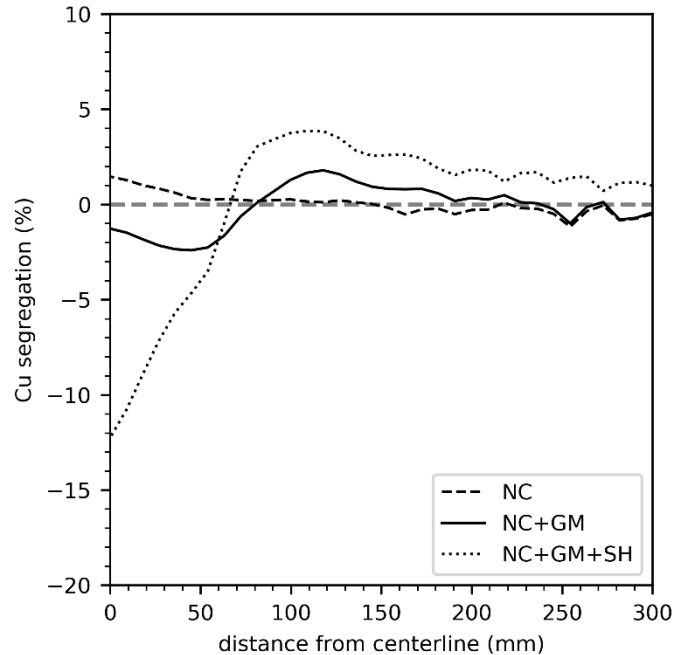


Figure 9.15: Cu segregation profiles along the thin face of rolling slabs for different transport mechanisms.

9.3.5 Conclusions

The formation of a loosely packed bed of globular dendrites, which has long been suspected to contribute to centerline depletion in conventional casting has been confirmed both numerically and experimentally. The numerical study has shown that the accumulation of these solute-depleted grains does not independently contribute to centerline depletion. Instead, the accumulation of these grains tends to increase the thickness of the rigid mush which allows for a significant volume of solute-enriched liquid to be transported away from the centerline via shrinkage driven flow. Supplying a jet down the centerline tends to reduce the thickness of the rigid mush, prevent the accumulation of grains near the centerline, and significantly refines the microstructure via dendrite fragmentation. From these studies, it appears beneficial for DC casting practices to move towards agitated or stirred melts during the steady state casting regime, and away from distribution bags which tend to promote thermal stratification and severe centerline depletion. Further design of these jets is necessary to target the optimal conditions which observed in this study characterized by the formation of a small erosion crater in the rigid mush.

10. CONCLUSIONS AND FUTURE WORK

The purpose of this work was to investigate the role that grain motion plays in macrosegregation development during equiaxed solidification, particularly in the direct chill (DC) casting process. A mixture model was rigorously derived from the microscale transport equations in a form that retained appropriate relationships for the grain structure and macrosegregation behavior during equiaxed solidification. Implementation of this model onto OpenFOAM, an open-source CFD platform based on the finite volume method (FVM) for co-located grids, ensures that this model will continue to benefit from advances in state-of-the-art developments. The use of co-located grids required a new formulation of the drag force used in the mixture momentum equation to prevent spurious velocities near discontinuous interfaces. A semi-implicit formulation that treats all body forces at the face-centers of the control volume was proposed and verified. This formulation has a general importance to the multiphase modeling community, far beyond the somewhat narrow scope of equiaxed solidification modeling. Additionally, a diffuse phase flux method was proposed and verified for reducing the sensitivity of composition predictions to the numerical grid and the orientation of the packing interface. Several previous attempts have focused on artificially smoothing the packing interface over a predefined solid fraction range; however, these methods only work under certain simulation conditions. The flux method proposed here is the first to target composition artifacts directly without changing the overall macrosegregation trends.

Once the previous issues relating to spatial discretizations on co-located grids were addressed, attention was turned towards the microscale relationships used for thermodynamic model closure. A simplified analytical model which considers finite diffusion in the solid and density change during solidification was derived and implemented using a robust and efficient semi-implicit source based numerical algorithm. This same method was applied to the volume-averaged macrosegregation models producing what is currently believed to be the fastest and most stable implementation of such a model to date. These two macrosegregation models were compared and it was determined that the undercooling predicted by the volume-averaged macrosegregation model had an insignificant effect of the transport phenomena and macrosegregation development in simulations of equiaxed solidification. Additionally, it was demonstrated that while the grain structures predicted by these models follow the correct physical trend that grain dendricity

increased as the final grain size increased, there is currently too much uncertainty in the closure relationships and model input parameters to confidently use them to predict actual casting grain structures. Although the morphology of grains is expected to differ across a casting, the spatial and transient variation of the internal solid fraction predicted by the model did not significantly affect the macrosegregation predictions compared to models where this parameter was fixed. Therefore, a more pragmatic approach was taken, and a single characteristic internal solid fraction and final grain size are supplied as inputs to the model. These parameters only affect the hydrodynamics of the system, specifically the solid fraction upon coalescence and the settling rate of grains.

This simplified grain morphology model was used to investigate the role of grain motion on macrosegregation development in equiaxed solidification, specifically in horizontal and vertical DC casting. In horizontal DC casting, the casting axis is perpendicular to gravity and there is a tendency for grains to accumulate along the bottom of the casting. Feeding liquid metal through a constrained inlet near the bottom suspends grains in the slurry both reducing the overall macrosegregation and improving the macrosegregation symmetry in the ingot. In vertical DC casting, the casting axis is parallel to gravity and there is a tendency for grains to accumulate in the center of the ingot. It was determined that a strong localized jet at the centerline can suspend grains in the slurry and reduce negative centerline segregation. The change in segregation is attributed to a combination of reducing the accumulation of solute-depleted grains near the centerline and thinning the rigid mush where solidification shrinkage pulls enriched liquid away from the centerline. The strong localized jet also causes significant refinement and homogenization of the grain structure, which improves the mechanical properties of the ingot. These studies indicate that it is beneficial for DC casting practices to move towards agitated or stirred melts, and away from conventional practices which tend to promote thermal stratification and localized accumulation of equiaxed grains.

10.1 Recommendations for Future Work

The numerical model developed and implemented in this work has demonstrated that computationally efficient 3-D models can be applied towards parametric studies of large casting operations. In a broader context of solidification processing, this model can be used in other casting operations including continuous casting of steel, vacuum arc remelting (VAR), electroslag remelting (ESR), and plasma arc melting (PAM). In some cases, it is necessary to simulate the

casting operation in a fully transient manner. Such cases require dynamic meshes. This feature has been implemented into the current model and is explained in Appendix B of this dissertation. The application of this transient model to a rolling slab cast by vertical DC casting is demonstrated. Future work on this model development should be focused on improving the parallelization efficiency of the code. Currently there is no implemented method for ensuring proper load balancing of the decomposed mesh on different CPUs as control volumes are added to the computational grid during the simulation. This feature would significantly improve the scalability of the current model. Another aspect of the model which should be tested is the use of higher order advection schemes, since it is not known how they will affect the numerical predictions.

In order to optimize the jet-stirred casting process, turbulence should be included into the numerical model. The assumption of a laminar jet used in this work underpredicts viscous mixing in the slurry, and therefore, overpredicts the jet penetration depth. It is currently believed that an optimal jet should form a small erosion crater in the rigid mush allowing enough dendrite fragmentation to occur for grain structure refinement. Because the general shape of the erosion crater manifests itself in the final macrosegregation profiles (see Figure 9.8), the behavior of the jet for different processing conditions can be investigated through numerical studies and confirmed by comparison to experimental macrosegregation profiles.

Future work should remain focused on improving the closure relationships used in the volume-averaged microsegregation and grain structure models, similar to ref. [58]. These models remain attractive since they would theoretically require less experimental trials needed to calibrate the simplified grain structure model to the actual casting microstructure. Alternatively, more pragmatic approaches to predicting grain structure may also be available following the work of Easton and StJohn [132], where simple analytical models for grain size as a function of solidification conditions in aluminum alloys are proposed. If the internal solid fraction could be related to the final grains size using the inverse relationship proposed in Section 7.4, then these simplified methods could replace the volume-averaged grain structure models altogether.

APPENDIX A. THERMOPHYSICAL PROPERTIES AND BINARY PHASE DIAGRAM INFORMATION

Table A.1 Thermophysical properties and phase diagram data for different alloys investigated in this dissertation

Property	Symbol	Al-4.5wt%Cu	Al-6wt%Cu	Pb-18wt%Sn	Sn-10wt%Pb	Units
Solid density	ρ_s	2632	2573	9250	7000	kg/m ³
Liquid density	ρ_l	2460	2490	9250	7000	kg/m ³
Solid specific heat	$c_{p,s}$	1054	1045	176	260	J/(kg K)
Liquid specific heat	$c_{p,l}$	958	950	176	260	J/(kg K)
Solid thermal conductivity	k_s	180	162	17.9	55	J/(m s K)
Liquid thermal conductivity	k_l	95	95	17.9	55	J/(m s K)
Latent heat of fusion	L_f	3.90×10^5	3.87×10^5	3.76×10^4	6.1×10^4	J/kg
Liquid dynamic viscosity	μ_l	1.3×10^{-3}	1.4×10^{-3}	1.1×10^{-3}	1.0×10^{-3}	m ² /s
Solid density for grain buoyancy	ρ_s^B	2632	2573	9250	7280	kg/m ³
Thermal expansion coefficient	$\beta_{T,s}$	1.17×10^{-4}	1.17×10^{-4}	1.16×10^{-4}	6.0×10^{-5}	1/K
Solutal expansion coefficient	$\beta_{C,l}$	-0.90	-0.90	0.49	-0.53	1/wt. fr.
Reference temperature	T_o	953	943	558.638	493.15	K
Reference liquid composition	$C_{l,o}$	0.45	0.60	0.18	0.10	wt. fr.
Solvent melting temperature	T_m	933.5	933.5	600.65	505.15	K
Eutectic temperature	T_{eut}	821.4	821.4	456.15	456.15	K
Maximum primary solid composition	C_{max}^α	0.565	0.565	0.192	0.025	wt. fr.
Eutectic composition	C_{eut}	0.331	0.331	0.619	0.381	wt. fr.
Solutal back diffusion coefficient	β	0.0	0.0	0.0	0.0	—
Shrinkage coefficient	λ	0.070	0.033	0.0	0.0	—

APPENDIX B. EXTENSION OF MODEL TO DYNAMIC MESHES

In order to simulate transient casting operations, a dynamic mesh is often required. A dynamic mesh refers to a computational grid that moves during the simulation. Implementation of dynamic meshes is not a trivial task, especially for the unstructured meshes used in OpenFOAM. The indexing of unstructured meshes is arbitrary, so the connectivity of elements (known as the mesh topology) must be defined and stored. This problem is further complicated when the mesh topology changes, and efficient parallelization is required.

A general overview of the dynamic mesh methods used for developing a transient casting model is provided here. The conservation of a general transport quantity on an arbitrary moving volume $V(t)$, bounded by a closed surface $S(t)$ is written as [133]:

$$\frac{d}{dt} \int_{V(t)} \rho \phi dV + \int_{S(t)} \rho (\mathbf{u} - \mathbf{u}_m) \phi \cdot \mathbf{n} dS = \int_{S(t)} \Gamma \nabla \phi \cdot \mathbf{n} dS + \int_{V(t)} S dV \quad (\text{B.1})$$

where \mathbf{u} is the absolute velocity and \mathbf{u}_m is the mesh velocity. The difference between these velocities, $\mathbf{u} - \mathbf{u}_m$, is the relative velocity. The relative flux is used for the dependent variable ϕ for implicit time integration of the governing equation. However, absolute fluxes must be used for any explicit terms, such as the phase mass flux in the latent heat term of the temperature equation, Eqn.(2.82). As shown in Ferziger and Perić [134], a mass source can appear in the mass conservation equation as cell faces move. To avoid this erroneous source term, the *Space Conservation Law* (SCL) [135,136] is applied:

$$\frac{d}{dt} \int_{V(t)} dV - \int_{S(t)} \mathbf{u}_m \cdot \mathbf{n} dS = 0 \quad (\text{B.2})$$

which is the relationship between the rate of change of the volume and the velocity of the boundary surface. Calculating the volume swept by a face in a time step is handled by the *meshphi()* operation in OpenFOAM, described in [133,137]. If cells have undergone topology modification, the mass fluxes on the faces must be modified to ensure continuity. To do so, a corrective pressure equation like Eqn. (4.27) is solved using:

$$\sum_f \left(\frac{[\rho_P]_f}{[a_P]_f} |\mathbf{S}_f| \nabla_f^\perp(p_{\text{corr}}) \right) = \sum_f (F_f(x, t^o)) \quad (\text{B.3})$$

where $F_f(x, t^o)$ denotes the mass flux computed at the previous time step that is remapped onto the new mesh. The mass flux can then be corrected using:

$$F_f = F_f^o - \frac{[\rho_P]_f}{[a_P]_f} |\mathbf{S}_f| \nabla_f^\perp(p_{\text{corr}}) \quad (\text{B.4})$$

With some understanding of the numerical considerations of dynamic meshing and topology changes having been established, focus can shift towards the specific implementation of these features for transient casting simulations. As shown in Figure B1, a list of cell faces is determined along a user specified reference plane, which provides the demarcation between the static and moving mesh. The cells on the moving side of the reference plane are marked for extrusion. These cells will expand to twice their original size before a topology change occurs, at which point a modified version of *layeradditionremoval* currently available in OpenFOAM is used to insert a new layer of faces in the middle of the extruded cells. For DC casting simulations, the reference plane is placed a few cells away from the top boundary and the extrusion direction is chosen in the direction of gravity.

An example of a 3-D dynamic mesh simulation with topology modification for the nominal conventionally cast Al-4.5wt%Cu rolling slab studied in Chapter 9 is provided in Figure B2. Such simulations can be used to study the start-up procedures used in DC casting. The composition profiles along the casting direction at the centerline and 50 mm away from the centerline are provided in Figure B2. Enrichment near the ingot butt is attributed to shrinkage driven flow in the direction of gravity, and the steady casting regime occurs at about 1200 mm. These results are in excellent qualitative agreement with the experimental profiles provided in ref. [121]. Figure B4 shows the sump profile 250 seconds after the start of jet-stirring with and without a combo-bag. Significant remelting of the solid shell along the bottom block occurs without the combo-bag causing a bleed-out and termination of casting. The two previous results could be used in conjugation to determine the optimal time to remove the combo-bag for jet-stirred casting.

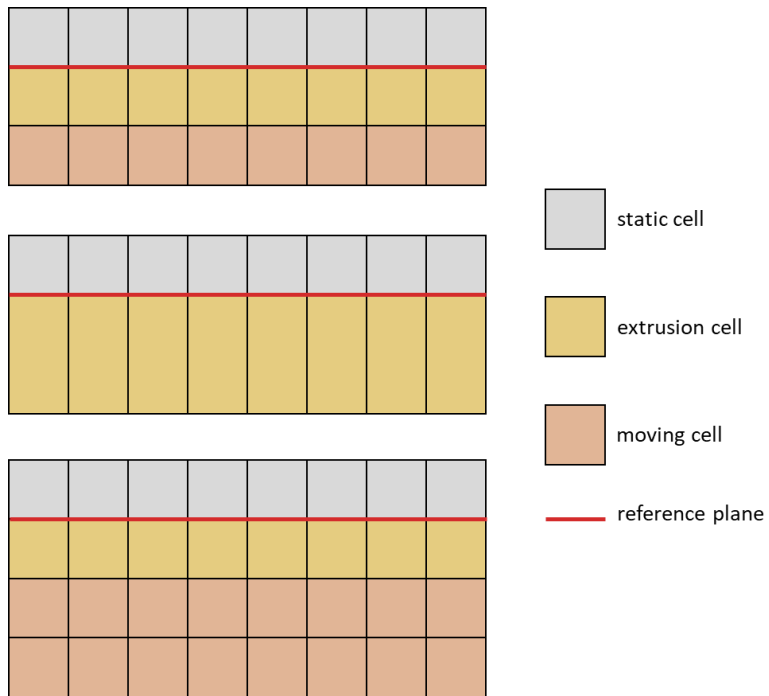


Figure B.1: Illustration of the mesh motion and topology logic used for transient casting simulations.

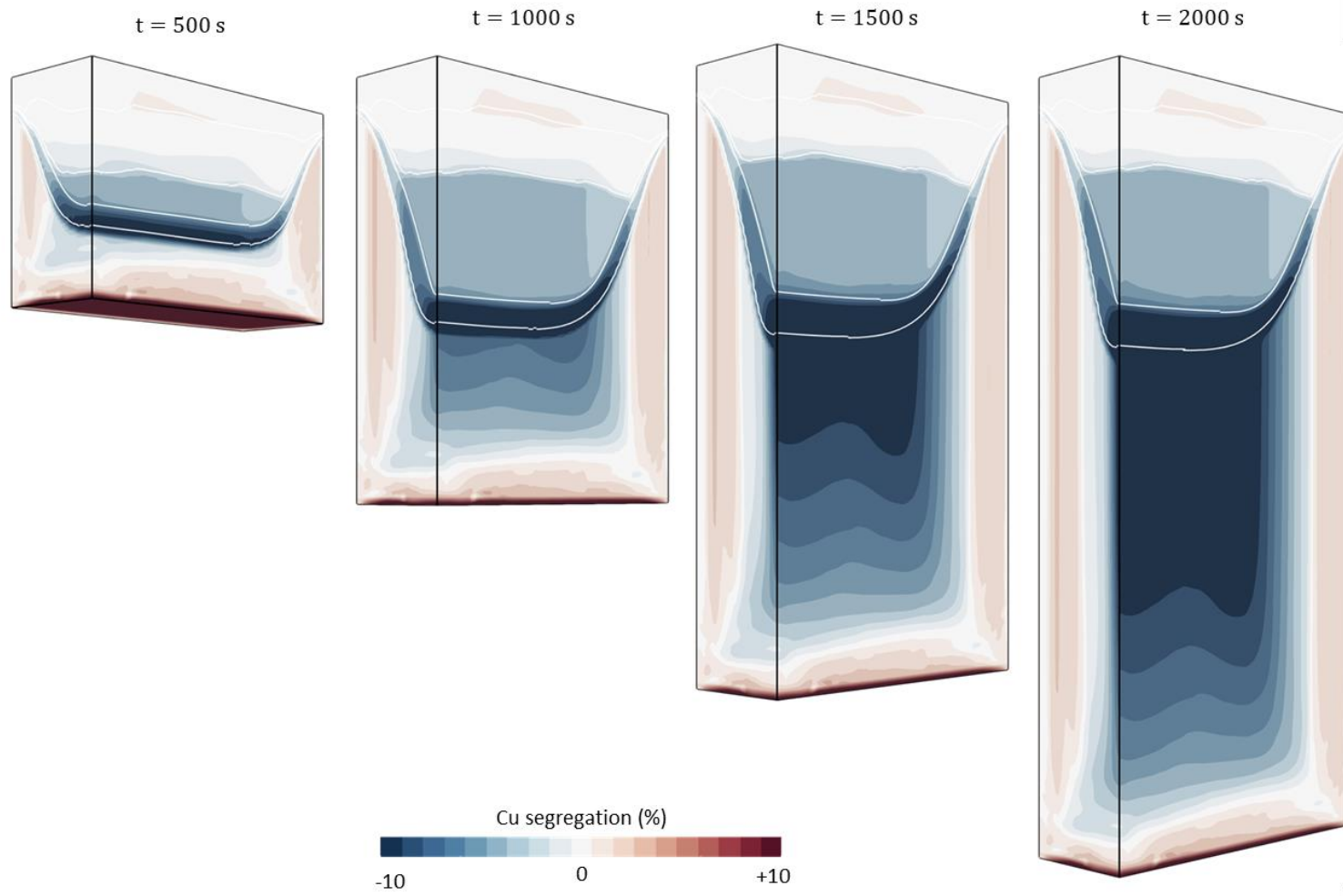


Figure B.2: Composition profiles for a transient 3-D simulation of DC casting of Al-4.5wt%Cu rolling slab (1540 mm x 600 mm).

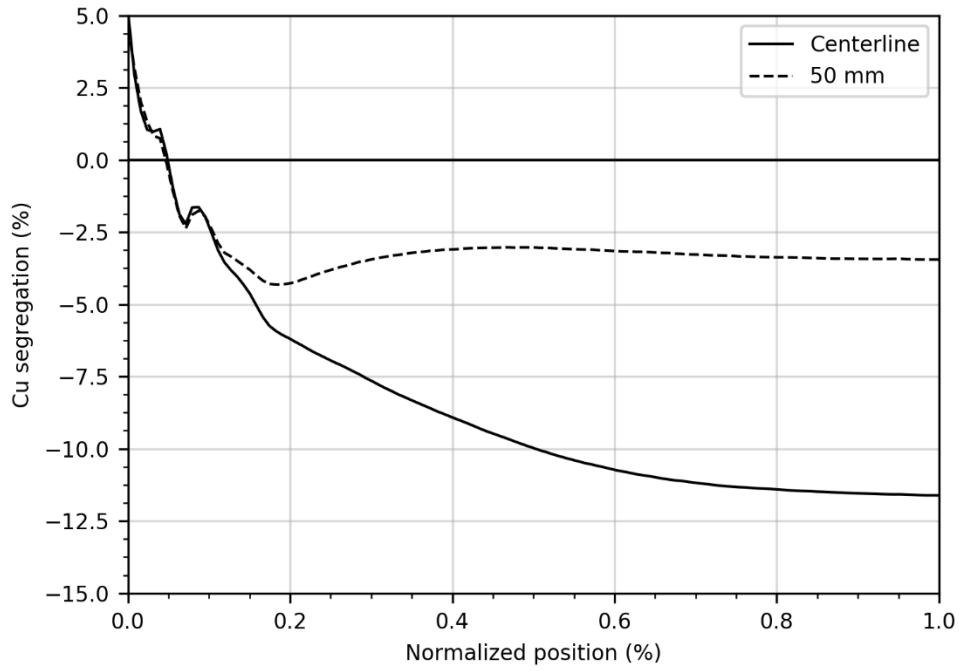


Figure B.3: Predicted development of centerline and off-centerline Cu segregation along the casting of an Al-4.5wt%Cu rolling slab (1540 mm x 600 mm).

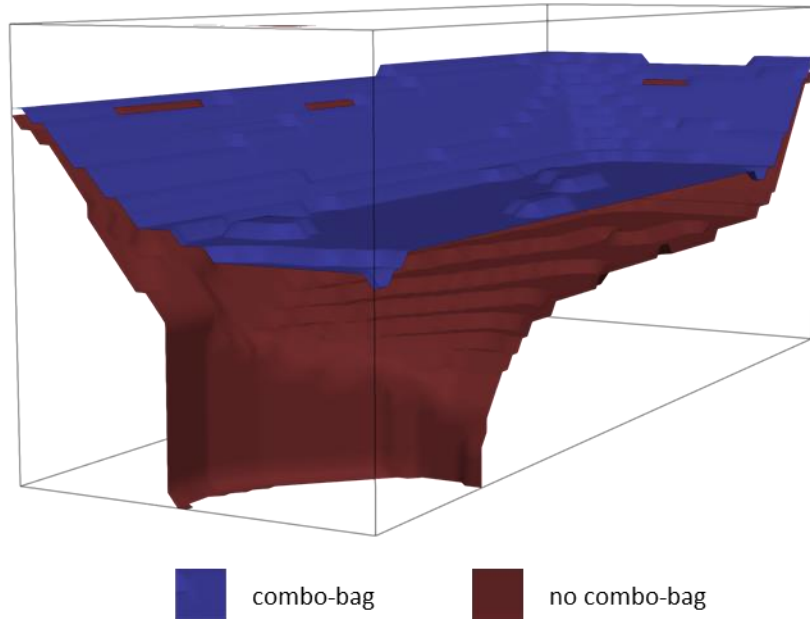


Figure B.3: Comparison of the sump profiles at 250 s after the start of casting for an Al-4.5wt%Cu rolling slab (1540 mm x 600 mm) with and without a combo-bag and fed with a narrow jet at the centerline.

REFERENCES

- [1] IAI, Statistics of the International Aluminum Institute, (2019). <https://www.world-aluminum.org>.
- [2] J.F. Grandfield, D.G. Eskin, I.F. Bainbridge, Direct-Chill Casting of Light Alloys, John Wiley & Sons, Inc., Hoboken, New Jersey, 2013.
- [3] D.G. Eskin, Physical Metallurgy of Direct Chill Casting of Aluminum Alloys, CRC Press, Boca Raton, Florida, 2008.
- [4] J. A. Dantzig and M. Rappaz, Solidification, 2nd ed., EPFL Press, Lausanne, Switzerland, 2016.
- [5] M. Rappaz, P. Thévoz, Solute diffusion model for equiaxed dendritic growth, Acta Metall. 35 (1987) 1487–1497.
- [6] H. Yu, D.. Granger, Macrosegregation in aluminum alloy ingot cast by the semicontinuous direct chill method, Alum. Alloy. - Their Phys. Mech. Prop. (1986) 17–29.
- [7] B. Garipey, Y. Caron, Investigation in the effects of casting parameters on the extent of centerline macrosegregation in DC cast sheet ingots, Light Met. (1991) 831–841.
- [8] A. Joly, G.-U. Grün, D. Daloz, H. Combeau, G. Lesoult, Effect of Grain Refinement on Macrosegregation in Direct Chill Semi-Continuous Casting of Aluminium Sheet Ingot, Mater. Sci. Forum. 329–330 (2000) 111–120.
- [9] S.R. Wagstaff, A. Allanore, Modification of Macrosegregation Patterns in Rolling Slab Ingots by Bulk Grain Migration, Light Met. (2016) 715–719.
- [10] S.R. Wagstaff, A. Allanore, Jet Mixing in Direct-Chill Casting of Aluminum: Crater Effects and its Consequence on Centerline Segregation, Metall. Mater. Trans. B. 48B (2017) 2114–2122.
- [11] S.R. Wagstaff, A. Allanore, Minimization of Macrosegregation in DC Cast Ingots Through Jet Processing, Metall. Mater. Trans. B. 47B (2016) 3132–3138.
- [12] S. Wagstaff, A. Allanore, Shear Induced Grain Refinement of a Continuously Cast Ingot, Light Met. (2017) 1005–1012.
- [13] M.C. Flemings, G.E. Nereo, Macrosegregation, Part I, Trans. Metall. Soc. AIME. 239 (1967) 41–49.

- [14] M.C. Flemings, R. Mehrabian, G.E. Nereo, Macroseggregation, Part II, *Trans. Metall. Soc. AIME*. 242 (1968) 50–53.
- [15] R. Mehrabian, M. Keane, M.C. Flemings, Interdendritic fluid flow and macroseggregation; influence of gravity, *Metall. Mater. Trans.* 1 (1970) 1209–1220.
- [16] J. Szekely, A.S. Jassal, An experimental and analytical study of the solidification of a binary dendritic system, *Metall. Trans. B.* 9 (1978) 389–398.
- [17] S.D. Ridder, S. Kou, R. Mehrabian, Effect of fluid flow on macroseggregation in axisymmetric ingots, *Metall. Trans. B.* 12 (1981) 435–447.
- [18] J. Ni, C. Beckermann, A volume-averaged two-phase model for transport phenomena during solidification, *Metall. Trans. B.* 22 (1991) 349–361.
- [19] C.Y. Wang, C. Beckermann, Equiaxed dendritic solidification with convection: Part I. multiscale/multiphase modeling, *Metall. Mater. Trans. A.* 27A (1996) 2754–2783.
- [20] W.D. Bennon, F.P. Incropera, A continuum model for momentum, heat and species transport in binary solid-liquid phase change systems—I. Model formulation, *Int. J. Heat Mass Transf.* 30 (1987) 2161–2170.
- [21] W.D. Bennon, F.P. Incropera, A continuum model for momentum, heat and species transport in binary solid-liquid phase change systems—II. Application to solidification in a rectangular cavity, *Int. J. Heat Mass Transf.* 30 (1987) 2171–2187.
- [22] P.J. Prescott, F.P. Incropera, W.D. Bennon, Modeling of dendritic solidification systems. Reassessment of the continuum momentum equation, *Int. J. Heat Mass Transf.* 34 (1991) 2351–2359.
- [23] D.A. Drew, *Mathematical Modeling of Two-Phase Flow*, MRC Tech. Summ. Rep. #2343. (1982).
- [24] M. Bedel, K.O. Tveito, M. Založnik, H. Combeau, M. M’Hamdi, A model study of the impact of the transport of inoculant particles on microstructure formation during solidification, *Comput. Mater. Sci.* 102 (2015) 95–109.
- [25] P.K. Agarwal, B.K. O’Neill, Transport phenomena in multi-particle systems-I. Pressure drop and friction factors: Unifying the hydraulic-radius and submerged-object approaches, *Chem. Eng. Sci.* 43 (1988) 2487–2499.
- [26] G.D. Scott, D.M. Kilgour, The density of random close packing of spheres, *J. Phys. D. Appl. Phys.* 2 (1969) 863–866.

- [27] C.Y. Wang, C. Beckermann, A multiphase solute diffusion model for dendritic alloy solidification, *Metall. Trans. A.* 24A (1993) 2787–2802.
- [28] G.P. Ivantsov, Temperature field around a spherical, cylindrical, and needle-shaped crystal growing in a pre-cooled melt, *Akad. Nauk SSR, Dokl.* 58 (1947) 567–569.
- [29] W. Kurz, D.J. Fisher, *Fundamentals of Solidification*, 3rd ed., Trans Tech Publications, Brookfield, Vermont, 1986.
- [30] J. Lipton, M.E. Glicksman, W. Kurz, Equiaxed dendrite growth in alloys at small supercooling, *Metall. Trans. A.* 18A (1987) 341–345.
- [31] G. Chai, L. Backerud, T. Rolland, L. Arnberg, Dendrite coherency during equiaxed solidification in binary aluminum alloys, *Metall. Mater. Trans. A.* 26A (1995) 965–970.
- [32] L. Arnberg, G. Chai, L. Backerud, Determination of dendritic coherency in solidifying melts by rheological measurements, *Mater. Sci. Eng. A.* 173 (1993) 101–103.
- [33] H.C. de Groh, P.D. Weidman, R. Zakhem, S. Ahuja, C. Beckermann, Calculation of dendrite settling velocities using a porous envelope, *Metall. Trans. B.* 24 (1993) 749–753.
- [34] R. Zakhem, P.D. Weidman, H.C. Groh, On the Drag of Model Dendrite Fragments at Low Reynolds Number, *Metall. Trans. A.* 23A (1992) 2169–2181.
- [35] C.Y. Wang, S. Ahuja, C. Beckermann, H.C. de Groh III, Multiparticle interfacial drag in equiaxed solidification, *Metall. Mater. Trans. B.* 26B (1995) 111–119.
- [36] H. Combeau, M. Založnik, S. Hans, P.E. Richy, Prediction of Macrosegregation in Steel Ingots: Influence of the Motion and the Morphology of Equiaxed Grains, *Metall. Mater. Trans. B.* 40B (2009) 289–304.
- [37] T.L. Finn, M.G. Chu, W.D. Bennon, The Influence of Mushy Region Microstructure on Macrosegregation in Direct Chill Cast Aluminum-Copper Round Ingots, *Micro/Macro Scale Phenom. Solidif.* 139 (1992) 17–24.
- [38] V.R. Voller, C. Swaminathan, General source-based methods for solidification phase change, *Numer. Heat Transf.* 19 (1991) 175–190.
- [39] C.R. Swaminathan, V.R. Voller, On the Enthalpy Method, *Int. J. Numer. Methods Heat Fluid Flow.* 3 (1993) 233–244.
- [40] C.R. Swaminathan, V.R. Voller, Towards a general numerical scheme for solidification systems, *Int. J. Heat Mass Transf.* 40 (1997) 2859–2868.

- [41] J. Ni, F.P. Incropera, Extension of the continuum model for transport phenomena occurring during metal alloy solidification-I. The conservation equations, *Int. J. Heat Mass Transf.* 38 (1995) 1271–1284.
- [42] J. Ni, F.P. Incropera, Extension of the continuum model for transport phenomena occurring during metal alloy solidification-II. Microscopic considerations, *Int. J. Heat Mass Transf.* 38 (1995) 1285–1296.
- [43] C.J. Vreeman, F.P. Incropera, The Effect of Free-Floating Dendrites and Convection on Macroseggregation in Direct Chill Cast Aluminum Alloys Part II: Predictions for Al-Cu and Al-Mg Alloys, *Int. J. Heat Mass Transf.* 43 (2000) 687–704.
- [44] C.J. Vreeman, M.J.M. Krane, F.P. Incropera, The Effect of Free-Floating Dendrites and Convection on Macroseggregation in Direct Chill Cast Aluminum Alloys Part I: Model Development, *Int. J. Heat Mass Transf.* 43 (2000) 677–686.
- [45] A. Plotkowski, M.J.M. Krane, A continuum grain attachment model for simulations of equiaxed solidification, *Comput. Mater. Sci.* 124 (2016) 238–248.
- [46] A. Plotkowski, M.J.M. Krane, The Discrete Nature of Grain Attachment Models in Simulations of Equiaxed Solidification, *Appl. Math. Model.* 47 (2017) 31–44.
- [47] C.J. Vreeman, J.D. Schloz, M.J.M. Krane, Direct Chill Casting of Aluminum Alloys: Modeling and Experiments on Industrial Scale Ingots, *J. Heat Transfer.* 124 (2002) 947–953.
- [48] K. Fezi, A. Plotkowski, M.J.M. Krane, Macroseggregation modeling during direct-chill casting of aluminum alloy 7050, *Numer. Heat Transf. Part A.* 70 (2016) 939–963.
- [49] J. Coleman, M.J.M. Krane, Influence of liquid metal feeding on the flow and macrosegregation in DC casting, *Mater. Sci. Technol.* 36 (2020) 393–402.
- [50] S.C. Flood, L. Katgerman, V.R. Voller, The calculation of macrosegregation and heat and fluid flows in the DC casting of aluminum alloys, *IOP Conf. Ser. Mater. Sci. Eng. MCWASP-5.* (1991) 683–690.
- [51] A.V. Reddy, C. Beckermann, Simulation of the effect of thermosolutal convection, shrinkage induced flow, and solid transport on macrosegregation and equiaxed grain size distribution in a DC continuous cast Al-Cu ingot, *Mater. Process. Comput. Age II.* (1995) 89–102.

- [52] A.V. Reddy, C. Beckermann, Modeling of Macrosegregation Due to Thermosolutal Convection and Contraction-Driven Flow in Direct Chill Continuous Casting of an Al-Cu Round Ingot, *Metall. Mater. Trans. B.* 28B (1997) 479–489.
- [53] P.A. Davidson, S.C. Flood, Natural convection in an aluminum ingot: a mathematical model, *Metall. Mater. Trans. B.* 25B (1994) 293–302.
- [54] T. Jalanti, Étude et Modélisation de la Macroségrégation Dans la Coulée Semi-continue des Alliages D'Aluminium, Ecole Polytechnique Fédérale de Lausanne, PhD Dissertation, 2000.
- [55] T. Jalanti, M. Swierkosz, M. Gremaud, M. Rappaz, Modelling of Macrosegregation in Continuous Casting of Aluminium, *Contin. Cast. Int. Congr.* (2000) 191–198.
- [56] M. Založnik, A. Kumar, H. Combeau, M. Bedel, P. Jarry, E. Waz, Influence of Transport Mechanisms on Macrosegregation Formation in Direct Chill Cast Industrial Scale Aluminum Alloy Ingots, *Adv. Eng. Mater.* 13 (2011) 570–580.
- [57] L. Heyvaert, M. Bedel, M. Založnik, H. Combeau, Modeling of the Coupling of Microstructure and Macrosegregation in a Direct Chill Cast Al-Cu Billet, *Metall. Mater. Trans. A.* 48A (2017) 4713–4734.
- [58] M. Torabi Rad, M. Založnik, H. Combeau, C. Beckermann, Upscaling mesoscopic simulation results to develop constitutive relations for macroscopic modeling of equiaxed dendritic solidification, *Materialia.* 5 (2019) 100231.
- [59] L. Zhang, D.G. Eskin, A. Miroux, T. Subroto, L. Katgerman, Influence of Melt Feeding Scheme and Casting Parameters During Direct-Chill Casting on Microstructure of an AA7050 Billet, *Metall. Mater. Trans. B.* 43B (2012) 1565–1573.
- [60] J.M. Reese, Characterization of the Flow in the Molten Metal Sump during Direct Chill Aluminum Casting, *Metall. Mater. Trans. B.* 28B (1997) 491–499.
- [61] L. Begum, M. Hasan, A Numerical Study of 3D Turbulent Melt Flow and Solidification in a Direct Chill Slab Caster with an Open-Top Melt Feeding System, *Numer. Heat Transf. Part A.* 67 (2015) 719–745.
- [62] M. Hasan, L. Begum, Low-head direct chill slab casting of aluminium alloy AA-6061: 3-D numerical study, *Int. J. Cast Met. Res.* 29 (2016) 137–153.
- [63] A. Pakanati, K.O. Tveito, M. M'Hamdi, H. Combeau, M. Založnik, Analysis of the Interplay Between Thermo-solutal Convection and Equiaxed Grain Motion in Relation to Macrosegregation Formation in AA5182 Sheet Ingots, *Light Met.* (2019) 1007–1013.

- [64] D. Mortensen, Ø. Jensen, G.-U. Grün, A. Buchholz, Macroseggregation Modelling of Large Sheet Ingots Including Grain Motion, Solidification Shrinkage and Mushy Zone Deformation, *Light Met.* (2019) 983–990.
- [65] D. Mortensen, A mathematical model of the heat and fluid flows in direct-chill casting of aluminum sheet ingots and billets, *Metall. Mater. Trans. B.* 30B (1999) 119–133.
- [66] T.W. Clyne, W. Kurz, Solute Redistribution During Solidification With Rapid Solid State Diffusion., *Metall. Trans. A.* 12A (1981) 965–971.
- [67] C.Y. Wang, C. Beckermann, A unified solute diffusion model for columnar and equiaxed dendritic alloy solidification, *Mater. Sci. Eng. A.* 171 (1993) 199–211.
- [68] M.. Manninen, V.. Taivassalo, S.. Kallio, On the mixture model for multiphase flow, VTT Publ. 288, Tech. Report., (1996).
- [69] A. Einstein, Eine neue Bestimmung der Molekul-dimensionen, Universitat Zurich, PhD Dissertation, 1905.
- [70] M. Ishii, N. Zuber, Drag coefficient and relative velocity in bubbly, droplet or particulate flows, *Am. Inst. Chem. Eng. J.* 25 (1979) 843–855.
- [71] C.Y. Wang, C. Beckermann, Equiaxed dendritic solidification with coNumericalInvection: Part II. simulations for an Al-4 Wt pct Cu alloy, *Metall. Mater. Trans. A.* 27A (1996) 2765–2783.
- [72] H. Combeau, M. Bellet, Y. Fautrelle, D. Gobin, E. Arquis, O. Budenkova, B. Dussoubs, Y. Du Terrail, A. Kumar, C.-A. Gandin, B. Goyeau, S. Mosbah, T. Quatravaux, M. Rady, M. Založnik, Analysis of a Numerical Benchmark for Columnar Solidification of Binary Alloys, in: *IOP Conf. Ser. Mater. Sci. Eng. MCWASP-13*, 2012: pp. 1–12.
- [73] C.J. Vreeman, F.P. Incropera, Numerical discretization of species equation source terms in binary mixture models of solidification and their impact on macroseggregation in semicontinuous, direct chill casting systems, *Numer. Heat Transf. Part B.* 36 (1999) 1–14.
- [74] R. Pardeshi, V.R. Voller, A.K. Singh, P. Dutta, An explicit–implicit time stepping scheme for solidification models, *Int. J. Heat Mass Transf.* 51 (2008) 3399–3409.
- [75] V.R. Voller, A. Mouchmov, M. Cross, An explicit scheme for coupling temperature and concentration fields in solidification models, *Appl. Math. Model.* 28 (2004) 79–94.
- [76] M. Rappaz, P. Thévoz, Solute diffusion model for equiaxed dendritic growth, *Acta Metall.* 35 (1987) 1487–1497.

- [77] M. Wu, J. Li, A. Ludwig, A. Kharicha, Modeling diffusion-governed solidification of ternary alloys - Part 1: Coupling solidification kinetics with thermodynamics, *Comput. Mater. Sci.* 79 (2013) 830–840.
- [78] Nielsen, B. Appolaire, H. Combeau, A. Mo, Measurements and modeling of the microstructural morphology during equiaxed solidification of Al-Cu alloys, *Metall. Mater. Trans. A.* 32A (2001) 2049–2060.
- [79] M. Bedel, Étude De La Formation Des Structures De Solidification Et Des Macroségrégations En Coulée Semi-Continue D’Aluminium, Institut Jean Lamour, PhD Dissertation, 2015.
- [80] M.A. Martorano, C. Beckermann, C.A. Gandin, A solutal interaction mechanism for the columnar-to-equiaxed transition in alloy solidification, *Metall. Mater. Trans. A.* 34A (2003) 1657–1674.
- [81] H. Jasak, Error analysis and estimation for finite volume method with applications to fluid flow, Imperial College, PhD Dissertation, 1996.
- [82] H. Rusche, Computational fluid dynamics of dispersed two-phase flows at high phase fractions, Imperial College, PhD Dissertation, 2002.
- [83] H.K. Versteeg, W. Malalasekera, An introduction to computational fluid dynamics: the finite volume method, 2nd ed., Pearson Education Limited, 2007.
- [84] S. V. Patankar, Numerical heat transfer and fluid flow, CRC Press, Boca Raton, Florida, 1980.
- [85] M.R. Hestenes, E. Stiefel, Methods of conjugate gradients for solving linear systems, *J. Res. Natl. Bur. Stand.* (1934). 49 (1952) 409–436.
- [86] H.A. van der Vorst, Bi-CGSTAB: A Fast and Smoothly Converging Variant of Bi-CG for the Solution of Nonsymmetric Linear Systems, *SIAM J. Sci. Stat. Comput.* 13 (1992) 631–644.
- [87] F.H. Harlow, J.E. Welch, Numerical calculation of time-dependent viscous incompressible flow of fluid with free surface, *Phys. Fluids.* 8 (1965) 2182–2189.
- [88] C.M. Rhie, W.L. Chow, Numerical study of the turbulent flow past an airfoil with trailing edge separation, *AIAA J.* 21 (1983) 1525–1532.

- [89] T.F. Miller, F.W. Schmidt, Use of a pressure-weighted interpolation method for the solution of the incompressible navier-stokes equations on a nonstaggered grid system, *Numer. Heat Transf.* 14 (1988) 213–233.
- [90] C.Y. Gu, C. Taylor, J.H. Chin, Computation of Flows with Large Body Forces, *Numer. Methods Laminar Turbul. Flow.* (1991) 294–305.
- [91] S. Zhang, X. Zhao, S. Bayyuk, Generalized formulations for the rhie-chow interpolation, *J. Comput. Phys.* 258 (2014) 880–914.
- [92] J. Mencinger, I. Žun, On the finite volume discretization of discontinuous body force field on collocated grid: Application to VOF method, *J. Comput. Phys.* 221 (2007) 524–538.
- [93] M. Nordlund, M. Stanic, A.K. Kuczaj, E.M.A. Frederix, B.J. Geurts, Improved PISO algorithms for modeling density varying flow in conjugate fluid-porous domains, *J. Comput. Phys.* 306 (2016) 199–215.
- [94] H.J. Aguerre, C.I. Pairetti, C.M. Venier, S. Márquez Damián, N.M. Nigro, An oscillation-free flow solver based on flux reconstruction, *J. Comput. Phys.* 365 (2018) 135–148.
- [95] R.I. Issa, Solution of the implicitly discretised fluid flow equations by operator-splitting, *J. Comput. Phys.* 62 (1986) 40–65.
- [96] H. Weller, Non-orthogonal version of the arbitrary polygonal C-grid and a new diamond grid, *Geosci. Model Dev.* 7 (2014) 779–797.
- [97] H. Weller, A. Shahrokhi, Curl-Free Pressure Gradients over Orography in a Solution of the Fully Compressible Euler Equations with Implicit Treatment of Acoustic and Gravity Waves, *Mon. Weather Rev.* 142 (2014) 4439–4457.
- [98] A. Kumar, B. Dussoubs, M. Založnik, H. Combeau, Influence of discretization of permeability term and mesh size on the prediction of channel segregations, *IOP Conf. Ser. Mater. Sci. Eng. ICASP-3.* 27 (2011) 1–8.
- [99] P.E. Réthoré, N.N. Sørensen, Actuator disc model using a modified Rhie-Chow/SIMPLE pressure correction algorithm. Comparison with analytical solutions, *Eur. Wind Energy Conf. Exhib.* 6 (2008) 3017–3027.
- [100] C.M. Oldenburg, F.J. Spera, Hybrid model for solidification and convection, *Numer. Heat Transf. Part B.* 21 (1992) 217–229.
- [101] M. Založnik, Modeling of Macrosegregation in Direct Chill Casting, University of Nova Gorica, PhD Dissertation, 2006.

- [102] A. Kumar, M.J. Walker, S. Sundarraj, P. Dutta, Grain Floatation During Equiaxed Solidification of an Al-Cu Alloy in a Side-Cooled Cavity : Part II — Numerical Studies, 42 (2011) 783–799.
- [103] H.G. Weller, Derivation, modelling and solution of the conditionally averaged two-phase flow equations, Technical Report, 2002.
- [104] M. Wu, A. Ludwig, A. Kharicha, Volume-averaged modeling of multiphase flow phenomena during alloy solidification, *Metals (Basel)*. 9 (2019) 1–43.
- [105] P. Thévoz, J.L. Desbiolles, M. Rappaz, Modeling of equiaxed microstructure formation in casting, *Metall. Trans. A*. 20A (1989) 311–322.
- [106] M. Založnik, H. Combeau, An operator splitting scheme for coupling macroscopic transport and grain growth in a two-phase multiscale solidification model: Part I - Model and solution scheme, *Comput. Mater. Sci.* 48 (2010) 1–10.
- [107] V.A.F. Costa, L.A. Oliveira, B.R. Baliga, A.C.M. Sousa, Simulation of coupled flows in adjacent porous and open domains using a control-volume finite-element method, *Numer. Heat Transf. Part A*. 45 (2004) 675–697.
- [108] D. Pham Van Bang, E. Lefrancoid, G. Ovarlez, F. Bertrand, MRI experimental and 1D FE-FCT numerical investigation of sedimentation and consolidation, 7th Int. Conf. HydroInformatics. (2006) 497–504.
- [109] D. Gidaspow, *Multiphase Flow and Fluidization: Continuum and Kinetic Theory Descriptions*, Academic Press, San Diego, California, 1994.
- [110] P.C. Carman, Permeability of saturated sands, soils and clays, *J. Agric. Sci.* 29 (1939) 262–273.
- [111] L. Heyvaert, *Modélisation de la formation des structures et des microporosités durant la solidification d’alliages d’aluminium*, Institut Jean Lamour, PhD Dissertation, 2015.
- [112] M. Bellet, H. Combeau, Y. Fautrelle, D. Gobin, M.A. Rady, E. Arquis, O. Budenkova, B. Dussoubs, Y. Duterrail, A. Kumar, C.-A. Gandin, B. Goyeau, M. Založnik, S. Mosbah, Call for contributions to a numerical benchmark problem for 2D columnar solidification of binary alloys, *Int. J. Therm. Sci.* 48 (2009) 2013–2016.
- [113] D.J. Hebditch, J.D. Hunt, Observations of ingot macrosegregation on model systems, *Metall. Trans.* 5 (1974) 1557–1564.

- [114] M. Torabi Rad, C. Beckermann, A truncated-Scheil-type model for columnar solidification of binary alloys in the presence of melt convection, *Materialia*. 7 (2019) 100364.
- [115] M. Rappaz, Modeling and characterization of grain structures and defects in solidification, *Curr. Opin. Solid State Mater. Sci.* 20 (2016) 37–45.
- [116] L. Yuan, C. O’Sullivan, C.M. Gourlay, Exploring dendrite coherency with the discrete element method, *Acta Mater.* 60 (2012) 1334–1345.
- [117] V.F. De Felice, K.O. Tveito, M. Založnik, H. Combeau, M. M’Hamdi, Three-dimensional study of macro- and mesosegregation formation in a rectangular cavity cooled from one vertical side, *IOP Conf. Ser. Mater. Sci. Eng. MCWASP-13*. 33 (2012) 1–10.
- [118] K. Fezi, M.J.M. Krane, Quantification of Input Uncertainty Propagation Through Models of Aluminum Alloy Direct Chill Casting, *Metall. Mater. Trans. A*. 49A (2018) 4759–4770.
- [119] M.J.M. Krane, I. Vušanović, Macroseggregation in horizontal direct chill casting of aluminium slabs, *Mater. Sci. Technol.* 25 (2008) 102–107.
- [120] J. Filipovic, R. Viskanta, F.P. Incropera, A parametric study of the accelerated cooling of steel strip, *Steel Res.* 63 (1992) 496–499.
- [121] S.R. Wagstaff, Jet Processing of Direct Chill Cast Aluminum Ingots, Massachusetts Institute of Technology, PhD Dissertation, 2017.
- [122] D.G. Eskin, Suyitno, L. Katgerman, Mechanical properties in the semi-solid state and hot tearing of aluminium alloys, *Prog. Mater. Sci.* 49 (2004) 629–711.
- [123] K. Bennett, E. Tindall, S.R. Wagstaff, K. Takahashi, A Reduction in Hot Cracking via Microstructural Modification in DC Cast Billets, *Light Met.* (2019) 999–1005.
- [124] A.L. Greer, P.S. Cooper, M.W. Meredith, W. Schneider, P. Schumacher, J.A. Spittle, A. Tronche, Grain Refinement of Aluminium Alloys by Inoculation, *Adv. Eng. Mater.* 5 (2003) 81–91.
- [125] M. Yun, S.A. Lockyer, J.D. Hunt, R. Cook, D.J. Bristow, A study of TiCAI 315TM grain refinement in a roll cast AA8111 aluminium alloy, *Light Met.* (2000) 857–862.
- [126] A.M. Bunn, P. V. Evans, D.J. Bristow, A.L. Greer, Modelling of the effectiveness of Al-Ti-B refiners in commercial purity aluminum, *Light Met.* (1998) 387–392.
- [127] M.C. Flemings, Behavior of Metal Alloys in the Semisolid State, *Metall. Trans. A*. 22A (1991) 957–981.

- [128] Z. Fan, Y. Wang, M. Xia, S. Arumuganathar, Enhanced heterogeneous nucleation in AZ91D alloy by intensive melt shearing, *Acta Mater.* 57 (2009) 4891–4901.
- [129] H. Men, B. Jiang, Z. Fan, Mechanisms of grain refinement by intensive shearing of AZ91 alloy melt, *Acta Mater.* 58 (2010) 6526–6534.
- [130] R. Nadella, D.G. Eskin, Q. Du, L. Katgerman, Macrosegregation in direct-chill casting of aluminium alloys, *Prog. Mater. Sci.* 53 (2008) 421–480.
- [131] D.G. Eskin, Q. Du, L. Katgerman, Relationship between shrinkage-induced macrosegregation and the sump profile upon direct-chill casting, *Scr. Mater.* 55 (2006) 715–718.
- [132] M.A. Easton, D.H. StJohn, Improved prediction of the grain size of aluminum alloys that includes the effect of cooling rate, *Mater. Sci. Eng. A.* 486 (2008) 8–13.
- [133] H. Jasak, Dynamic mesh handling in OpenFOAM, 47th AIAA Aerosp. Sci. Meet. (2009) 1–10.
- [134] J.H. Ferziger, M. Perić, *Computational Methods for Fluid Dynamics*, Springer-Verlag, Berlin, 2002.
- [135] P.D. Thomas, C.K. Lombard, Geometric conservation law and its application to flow computations on moving grids, *AIAA J.* 17 (1979) 1030–1037.
- [136] H. Guillard, C. Farhat, On the significance of the geometric conservation law for flow computations on moving meshes, *Comput. Methods Appl. Mech. Eng.* 190 (2000) 1467–1482.
- [137] A. Montorfano, F. Piscaglia, A. Onorati, An Extension of the Dynamic Mesh Handling with Topological Changes for les of ICE in OpenFOAM®, *SAE Tech.* (2015) 1–14.

VITA

John Coleman was born in Long Beach, California in 1992. He spent most of his childhood living in Goodyear, Arizona with his mother, father, and older sister. He and his family moved to Liberty Township, Ohio where he attended Lakota East High School from 2006-2010. He enrolled in engineering at Purdue University in August of 2010 and completed his B.S. in Materials Science and Engineering in May 2014. While in the last semester of his undergraduate education, he started graduate school in the same program. He completed his M.S. in Materials Engineering in December 2015 and started his Ph.D. in January 2016. He started at Oak Ridge National Laboratory as post-doctoral researcher in May 2020 working on computational modeling of additive manufacturing.